Synthesis of lamellar chalcogenide ultra-thin films on thermal silicon oxide by a hybrid Atomic Layer Deposition/Molecular Layer Deposition route, developed by in situ X-ray synchrotron and advanced characterization studies

Petros Abi Younes

THÈSE

Pour obtenir le grade de

DOCTEUR DE L'UNIVERSITÉ GRENOBLE ALPES

École doctorale : PHYS - Physique
Spécialité : Physique des matériaux
Unité de recherche : Laboratoire des matériaux et du génie physique

Synthèse de couches ultra-minces de chalcogénures lamellaires sur oxyde de silicium thermique, par flux alternés de molécules organiques et inorganiques. Apport des mesures in situ aux rayons X (synchrotron) et de la spectroscopie de photoelectrons au développement du procédé

Synthesis of lamellar chalcogenide ultra-thin films on thermal silicon oxide by a hybrid Atomic Layer Deposition/Molecular Layer Deposition route, developed by in situ X-ray synchrotron and advanced characterization studies

Présentée par :

Petros ABI YOUNES

Direction de thèse :

Hubert RENEVIER PROFESSEUR DES UNIVERSITES, Université Grenoble Alpes	Directeur de thèse
Denis ROUCHON INGENIEUR,	Co-encadrant de thèse
Nicolas GAUTHIER Ingénieur Chercheur, CEA	Co-encadrant de thèse

Rapporteurs :

MAARIT KARPPINEN
Professeur, AALTO Yliopisto
JOLIEN DENDOOVEN
Professeur assistant, Universiteit Gent

Thèse soutenue publiquement le **24 mars 2023**, devant le jury composé de :

MAARIT KARPPINEN Professeur, AALTO Yliopisto	Rapporteure
JOLIEN DENDOOVEN Professeur assistant, Universiteit Gent	Rapporteure
CHRISTOPHE VALLEE Professeur des Universités, UNIVERSITE GRENOBLE ALPES	Examinateur
MIKHAEL BECHELANY Directeur de recherche, CNRS DELEGATION OCCITANIE EST	Président
MURIEL BOUTTEMY Ingénieur de recherche, CNRS DELEGATION ILE-DE-FRANCE SUD	Examinatrice

Invités :

ELSJE ALESSANDRA QUADRELLI

In memory of my beloved FATHER ...

Acknowledgements

First of all, I would like to thank Professor Maarit Karppinen and Professor Jolien Dendooven for accepting to evaluate my work. I also would like to thank Professor Christophe Valée, Dr. Muriel Bouttemy, Dr. Mikhael Bechelany, and Professor Alessandra Quadrelli for accepting to be members of my Ph.D. examination committee.

I would like to express my gratitude to my thesis director, Professor Hubert Renevier, for his excellent advice and constant support. I am very grateful to you for your wise advice and for pushing me to always be a better version of myself. Secondly, I would like to thank my Co-director Dr. Denis Rouchon, for his positive mindset and for his continuous support and encouragement. I would like also to thank him for giving me the opportunity to collaborate with other people in the CEA LETI which made my Ph.D. work more noticeable. Also, I would like to express my gratitude to my supervisor Dr. Nicolas Gauthier for his guidance, his support, and for sharing his knowledge, especially in the XPS characterization technique. I really appreciated the ease of communication with you.

This thesis is part of the ULTIMED project ANR where a strong collaboration between LMGP and CEA/LETI with C2P2/IRCELYON, the SIRIUS line (SOLEIL synchrotron), and the IPVF has led to a scientific consortium composed of scientists from different fields. I would like to thank Professor Alessandra Quadrelli, Dr. Clement Camp, and Dr. Medet Zhukush for Surface Organo-Metallic Chemistry Studies. In addition, I would like to thank Synchrotron SOLEIL (SIRIUS beamline) for the general facilities placed at our disposal, and in particular, Dr. Gianluca Ciatto, Dr. Ashok Yadav, and Nicolas Aubert for this collaboration. I would also like to thank Nathanaelle Schneider for her commitment to the project. In addition, I would like to thank Marie-Ingrid Richard for her presence and her help during the beamline experiments. In memory of Dr. Dominique De Barros who played a major role in the engineering assistance of the ALD reactor. At the beginning of my PhD, I had the opportunity to collaborate with a post-doctoral fellow Dr. Evgeniy Skopin that gave me efficient training at the beginning of my Ph.D. In addition, I would like to thank my two-internship students

for their contribution to the project: Tom Iung and Hugo Menez. This Ph.D. work was not possible without financial support. Therefore, I would like to thank to acknowledge the Agence Nationale de la Recherche, ANR-18-CE09-0031 for the ULTIMED project funding and the Labex MINOS, ANR-10-LABX-55-01 for my Ph.D. work funding.

I would like to thank to acknowledge Herve Roussel for XRR and XRD measurements, and Laetitia Rapenne for TEM measurements. In addition, I would like to thank Dr. Van-Hoan Le and Dr. Raphael Ramos for their support in Raman Spectroscopy, Dr. Zineb Saghi for TEM, and Dr. Christophe Licetra for ellipsometry measurements. I would like to express my gratitude to all the technical and Human Resources staff in the LMGP. A special thanks go to Annie Ducher for her continuous support over the three years. I would like to thank Dr. Carmen Jiménez and Professor Franz Bruckert for keeping the laboratory work possible even during the difficult COVID periods. Thanks to Dr. Carmen Jiménez for being a kind and supportive laboratory director.

My sincere gratitude goes to my office mates at the LMGP Khanh, Shruti, and Carlos. I thank you all for the coffee break discussions and for keeping the office environment positive even during manuscript writing. I would like also to thank all my colleagues in the LMGP in particular Evgeniy, Bhobnibhit, Ibtehal, Rosa, Chiara, Dorina, Alexandre, Cami, Octavio, Abdou, Clement, Maxime, Tabasom, Guislain, Adrien, Etienne. Masoud, Adeel, Aditya, Olfa and Zahraa.

I would like to thank my Lebanese friends who have supported me during these three years. Thanks to my neighbor and my best friend Nadine who was always there for me, especially during the worst times I'm so lucky to have a friend like you. Thanks to my supportive and loving friends in Grenoble: Natalia, Layla, Lea, Joe, Moustapha, Rawad, Roy, Chouayb, Mrad, Rami, Toni, Christ, Louna, Joyce, Carole, Tonina and Tamara. I would like to thank my friends in Lyon in particular Maroun for sharing the lockdown COVID period with me, Dahlia for her continuous support, and Maurice for his positive attitude. In addition, I am extremely grateful for having two supportive loving and caring friends like George and Ghenwa thanks for all the lovely time spent together. I would like to thank my Lebanese community in Montpellier, the city where I started my life in France during my Master 2 internship. Thanks for making living abroad much easier. Thanks to: Cynthia, Marleine, Syreina, Sara, Maya, Ghady, Fida, Elia, Elissa and Nicole.

A special thanks go to Joelle. Joelle, thank you for making the thesis period a time of happiness. You were always a moral support and you always gave me the motivation to keep going. Thank you for believing in me and thank you for the happy moments we had together. I am so grateful to have you in my life.

Finally, I would like to thank the most important people in my life, my family. First of all, I would

like to thank my mother, Salwa, who supported me and was strong enough to encourage me to live abroad and start my future, even though it was very difficult for her. Secondly, I would like to thank my sweet and lovely sisters, Adeline, Rita, and Mariline, who believed in me and always encouraged me to be the best version of myself. I am so grateful to have you in my life and I thank you for the love and support you have filled my heart with to make me successful. I would like to thank my uncle and friend Hany who has always believed in my potential and encouraged me to continue and get this PhD. I would like to thank my two brothers-in-law Gerard and Walid for their support. A special thanks to my lovely nephew Karl, thanks to his adorable face, the writing of the thesis manuscript went much better. Finally, I dedicate all this work and this Ph.D. to my father Joseph, who passed away seven years ago. I will never forget what you did to make me a brilliant and wise man. I hope you are proud of me because you always wanted me to focus on my goals without distraction.

Abstract

Lamellar metal chalcogenides have come into the spotlight due to their semiconducting nature, which is distinct from the most studied 2D semi-metallic graphene. Over the past twenty years, researchers have focused on exploring the anisotropic physical properties of lamellar metal chalcogenides, unveiling new properties due to the thickness-dependent nature, which allows these materials to represent an ultimate level of miniaturization. The lack of scalable fabrication methods of continuous ultra-thin films on developed surfaces, at moderate temperatures, stems an obstacle for the deployment of these materials. In this context, the objective of this thesis was to obtain continuous ultra-thin film of lamellar metal sulfides on non-epitaxial substrates (thermal silicon oxide which is widely used in microelectronics) by performing a complete dissociation between growth and crystallization. For that purpose, we used an innovative two-step process approach comprising the growth of an amorphous thin film by Atomic Layer Deposition/Molecular Layer Deposition (ALD/MLD) and a subsequent thermal annealing for obtaining the crystallization. The replacement of the highly toxic H_2S co-reactant often used for growing ALD sulfide thin films with a safer organic molecule, *i.e.* 1,2 ethandithiol (EDT), permits to generate an amorphous inorganic/organic hybrid thin film at low temperature.

The process was applied for the synthesis of Titanium Disulfide (TiS_2) ultrathin films. Amorphous thin films (Ti-thiolate) were obtained by ALD/MLD process at 50 °C then, converted into textured ultra-thin films of TiS_2 upon the annealing under Ar/H_2 gas. Thanks to the high brilliance of the synchrotron, the process was monitored by *in situ* X-ray techniques, which allows to evaluate the repetitive self-limiting behavior from the first ALD/MLD cycle during the growth of the amorphous Ti-thiolate, and to observe the local structure transition during the annealing step. *In situ* measurements coupled with *ex situ* characterizations (Raman, XPS, HAXPES, and TEM) evidenced the synthesis of ultra-thin film of 5.5 nm upon annealing at mild temperature (300 °C). Four-points and spectroscopic ellipsometry mea-

surements confirmed a semi-conductor behavior with a direct band gap of 1.72 eV.

Besides, promising preliminary results on the synthesis of Gallium Sulfide (GaS_x) thin films were obtained. During this work, an ALD/MLD window has been explored with EDT and a homogeneous film has been obtained at 250 °C. By contrast, we targeted to the synthesis of Tin Sulfide (SnS_x) with EDT. However, the growth was not successful. Nevertheless, mechanistic studies were performed on a high surface area substrate that contributed to explain the result.

Key words: **ultra-thin films, lamellar, ALD/MLD, EDT, low temperature, thiolate, TiS_2, GaS_x, SnS_x**

Résumé

Les chalcogénures métalliques lamellaires ont été mis en évidence en raison de leur nature semi-conductrice, qui se distingue du graphène semi-métallique 2D le plus étudié. Au cours des vingt dernières années, les chercheurs se sont concentrés sur l'exploration des propriétés physiques anisotropes des chalcogénures métalliques lamellaires, dévoilant de nouvelles propriétés dues à la nature dépendante de l'épaisseur, qui permet à ces matériaux de représenter un niveau ultime de miniaturisation. L'absence de méthodes de fabrication évolutives de films ultra-minces continus sur des surfaces développées, à des températures modérées, constitue un obstacle au déploiement de ces matériaux. Dans ce contexte, l'objectif de cette thèse était d'obtenir des films ultra-minces continus de sulfures métalliques lamellaires sur des substrats non-épitaxiés (oxyde de silicium thermique qui est largement utilisé en microélectronique) en réalisant une dissociation complète entre la croissance et la cristallisation. Dans cette perspective, nous avons utilisé une approche innovante en deux étapes comprenant la croissance d'un film mince amorphe par dépôt en couche atomique/dépôt en couche moléculaire (ALD/MLD) et un recuit thermique ultérieur pour obtenir la cristallisation. Le remplacement du co-réactif H_2S hautement toxique habituellement utilisé pour la croissance des films minces de sulfure en ALD par une molécule organique plus sûre, à savoir le 1,2 éthandithiol (EDT), permet de générer un film mince hybride inorganique/organique amorphe à basse température.

Le procédé a été appliqué pour la synthèse de films ultra-minces de Disulfure de Titane (TiS_2). Des films minces amorphes (Ti-thiolate) ont été obtenus par le procédé ALD/MLD à 50 °C, puis convertis en films ultra-minces texturés de TiS_2 lors du recuit sous gaz Ar/H_2. Grâce à la haute brillance du synchrotron, le processus a été suivi par des techniques de rayons-X *in situ*, ce qui permet d'évaluer le comportement répétitif auto-limitant dès le premier cycle ALD/MLD pendant la croissance du Ti-thiolate amorphe, et d'observer la transition de structure locale pendant l'étape de recuit. Des mesures *in situ* couplées à des

caractérisations *ex situ* (Raman, XPS, HAXPES, et TEM) ont mis en évidence à la synthèse d'un film ultra-mince de 5.5 nm après recuit à température douce (300 °C). Les mesures d'ellipsométrie spectroscopique et à quatre-pointes ont confirmé un comportement semi-conducteur avec une bande interdite directe de 1,72 eV.

D'autre part, des résultats préliminaires prometteurs sur la synthèse de films minces de Sulfure de Gallium (GaS_x) ont été obtenus. Au cours de ce travail, une fenêtre ALD/MLD a été explorée avec l'EDT et une couche homogène a finalement été déposée à 250 °C. Nous avons également tenté de synthétiser un Sulfure d'étain SnS_x en utilisant l'EDT. Cependant, la croissance n'a pas été couronnée de succès. Néanmoins, des études mécanistiques ont été réalisées sur un substrat à haute surface qui ont permis d'expliquer le résultat.

Mots clés: **couches ultra-minces, lamellaires, ALD/MLD, EDT, basse température, thiolate, TiS_2, GaS_x, SnS_x.**

Contents

Acronymes

2D	Two-Dimensional
ALD	Atomic Layer Deposition
ALD/MLD	Atomic Layer Deposition / Molecular Layer Deposition
ALE	Atomic Layer Etching
Ar/H_2	Hydrogenated Argon
AVS	American Vacuum Society
BEOL	back-end-of-line
CMOS	Complementary Metal Oxide Semiconductor
DRIFT	Diffuse Reflectance Infrared Fourier Transform Spectroscopy
EDT	1,2 ethandithiol
EDX	Energy-Dispersive X-ray Spectroscopy
EXAFS	Extended X-Ray Absorption Fine Structure
FET	Field Effect Transistor
GISAXS	Grazing Incidence Small Angle Scattering

GPC	Growth Per Cycle
H_2S	Hydrogen Sulfide
HAXPES	Hard X-ray Photoelectron Spectroscopy
IC	Integrated Circuit
IR	Infrared
ITRS	International Technology Roadmap for Semiconductors
MoS_2	Molybdenum Disulfide
MtM	"More than Moore"
PE-ALD	Plasma Enhanced Atomic Layer Deposition
R&D	Research and Development
RF	Radio Frequency
SE	Spectroscopic ellipsometry
Si	Silicon
SiO_2	Silicon Oxide
SiP	System in Package
SoC	System on Chip
TBDS	di(*t*-butyl) disulfide
TBT	*t*-butylthiol
TDMAG	$C_{12}H_{36}Ga_2N_6$
TDMAT	Tetrakis(dimethylamido)titanium
TDT	3,4-toluenedithiolate
TEM	Transmission Electron Microscopy
TiO_2	Titanium Dioxide
TiS_2	Titanium Disulfide

XANES	X-ray Absorption Near Edge Structure
XLD	X-ray Linear Dichroism
XPS	X-ray Photoelectron Spectroscopy
XRD	X-ray Diffraction
XRF	X-ray Fluorescence
XRR	X-ray Reflectivity
ZnO	Zinc Oxide

General Introduction

The ultimate goal of semiconductor manufacturers relied on increasing electronic devices performance with continuous down-scaling of transistors dimensions. However, the down-scaling was against disastiric limitations of physics with the appearance of quantum phenomena (leakage of current by tunneling effect). Transistors based on Silicon (Si) as a channel material have encountered a serious problem during miniaturization such as the increase of charge diffusion at the interfaces of transistors that leads to a drop in the mobility of carriers in the channel.

In this context, researchers focused their attention on finding an alternative channel material such as Two-Dimensional (2D) semiconductors that lead to continuous innovation in the semiconductor valley. In particular, Lamellar metal chalcogenides have emerged as a class of exceptional materials that exhibits tunable electronic and chemical properties with the scale of ultrathin and monolayers with many potential applications. The lack of scalable fabrication methods of continuous ultra-thin films on developed substrates, at moderate temperatures, stems a bottleneck for the full deployment of these materials. The co-occurrence of growth and crystallization during Atomic Layer Deposition (ALD) process is considered a major issue that requires oriented crystalline substrates with adequate lattice parameters to be solved.

Therefore, the aim of this thesis relies on the growth of metal sulfides using an innovative 2-step process approach comprising Atomic Layer Deposition / Molecular Layer Deposition (ALD/MLD) and thermal annealing. The first step consists on replacing the highly toxic Hydrogen Sulfide (H_2S) co-reactant previously used in ALD process of sulfides growth with a safer organic molecule 1,2 ethandithiol (EDT). The use of the EDT as a molecular reactant with metallic precursor allows the generation of an amorphous hybrid organic-inorganic Metal-thiolate material while a complete dissociation of growth and crystallization is ensured. However, the second step relies on performing a subsequent annealing treatment of

the Hybrid deposit in order to obtain a in-plane crystallization. In addition, the ALD/MLD process was applied using a non-epitaxial substrate such as thermal Silicon Oxide (SiO_2) (100nm) which is widely used in microelectronics.

The mentioned process was applied for the synthesis of Titanium Disulfide (TiS_2) ultra-thin films. The ALD/MLD process succeeded to deposit at relatively low temperature (50 °C) a Ti-thiolate with a self-limiting nature of surface reactions confirmed by *in situ* synchrotron X-ray Fluorescence (XRF) studies. Ti-thiolate has been converted into textured stoichiometric ultra-thin layers of TiS_2 as thin as 5.5 nm upon the annealing under Hydrogenated Argon (Ar/H_2) gas at mild temperature (300 °C). A complete investigation of annealing strategies optimizations will be therefore discussed and confirmed by many characterizations such as *in situ* XRF, Raman, X-ray Photoelectron Spectroscopy (XPS), Hard X-ray Photoelectron Spectroscopy (HAXPES) and X-ray Absorption Near Edge Structure (XANES). Concerning the material properties four-points and spectroscopic ellipsometry measurements confirmed a semi-conductor behavior with a direct band-gap of 1.72 eV.

Promising preliminary results on the synthesis of gallium sulfide Ga_xS thin films were obtained. An ALD/MLD window has been explored with EDT showing a homogeneous film at 250 °C. A series of perspectives have been addressed in order to reach Ga_xS ultra-thin crystalline films. By contrast, we targeted to synthesis Tin disulfide (Sn_xS) with EDT. However, the growth was unsuccessful where mechanistic insights were performed on high surface area substrate to give clues for explaining such a result.

This study is within the framework of ULTiMED project funded by the French ANR. The consortium comprises a strong collaboration comprising LMGP and CEA-LETI in Grenoble for the synthesis and growth of materials, C2P2 and IRECELYON in Lyon (M. Zhukush, C. Camp, E. A. Quadrelli) for chemical experimental modeling of surface organo-metallic chemistry studies on 3D substrate-type silica nanobeads, Synchrotron SOLEIL (G. Ciatto, A.Yadav, and N.Aubert) for *in situ* X-ray studies and EXAFS simulation, and IPVF-Palaiseau (N. Schneider) for Density Functional Theory *ab initio* modeling for ALD/MLD and X-ray spectroscopy data analysis.

Therefore the following dissertation will be divided into five main chapters:

- Chapter 1 will summarize the literature review of Lamellar Metal chalcogenides materials and describe the necessity to apply the two-step process toward the synthesis of ultra-thin films.

- Chapter 2 will describe the experimental details during ALD/MLD growth inside our dedicated reactor. Moreover, the relevance of *in situ* X-ray studies performed at the SIRIUS beamline and the use of available *in situ* characterization measurements will be highlighted. In addition, this chapter will briefly describe the main *ex situ* characterization techniques combined in this work (Raman, HAXPES/XPS, XRR,..) and will remind the essential information that each of them can provide such as crystallinity (Raman), chemical composition (XPS), and thickness (XRR)...

- Chapter 3 will present the synthesis of amorphous Ti-thiolate using *in situ* X-ray studies. The thin films composed of crystalline TiS_2 layers (from the synthesis of 40 and 80-cycle ALD/MLD thiolates at low temperature followed by thermal annealing) were then characterized by *ex situ* measurements (Raman, Transmission Electron Microscopy (TEM), XANES, XPS, and HAXPES).

- Chapter 4 will focus on the enhancement of the annealing strategy to achieve ultrathin films composed of stoichiometric TiS_2. The annealing strategy was examined by tracking the evolution of the [S]/[Ti] XRF ratio coupled with quantitive XPS/HAXPES studies.

- Chapter 5 will present the progress report on the Synthesis of metal sulfides Ga_xS and SnS_x. The first part of this chapter will show the preliminary results obtained from the study targeting the synthesis of Gallium Sulfide Ga_xS thin films using *in situ* X-ray studies and *ex situ* characterizations. The second part will discuss and explain the strategy applied to grow SnS_x even if we didn't succeed to achieve Tin-thiolate clues and conclusions will be provided.

The dissertation will be enclosed with conclusions, and a series of outlooks will be initiated.

Chapter 1

Literature Review (Beyond Graphene: Lamellar Metal Chalcogenides)

1.1 Introduction

"There's Plenty of Room at the Bottom". In this title, Richard P. Feynman launched during his talk in the annual meeting of American Physical Society in 1959, the concept of the most emerging field of science nowadays, the nanoscience field. In his talk, Feynman laid the foundation stone for the nanoscience concept when he said that miniaturization down to the atomic level would be 'an invitation to enter a new field of physics´ [1].

Gordon Earl Moore co-founder of Intel was one of the first to consecrate Feynman's concept of nanoscience, when he said in 1965 his popular expression " smaller is cheaper and faster " emphasizing the importance of achieving miniaturization at the nanoscale to achieve the technological revolution in microelectronics. [2] Moore made one of the greatest predictions in human history when he estimated that the number of transistors and resistors placed on an Integrated Circuit chip will double every two years. In other words, computing power will double every two years at a low cost. Note that the Integrated Circuit (IC) are used in every device that requires a digital logic operation to be done [3].

For almost 50 years semiconductors manufacturers were following Moore's law by shrinking transistor dimensions. But transistors cannot be scaled down infinitely. [4] For this reason, an increasing awareness with Research and Development (R&D) effort and business drivers was there to push the development and application of an emerging trend the

"More than Moore" (MtM). This trend is based upon or derived from silicon technologies but do not scale with Moore's law with typical examples as Radio Frequency (RF), Power, Sensor and actuator, System in Package (SiP), heterogeneous integration, etc..

More than Moore focuses on the functional diversification of semiconductor-based devices (see Figure 1.1). These non-digital functionalities contribute to the miniaturization of electronic systems, although they do not necessarily scale at the same rate as the one that describes the development of digital functionality.[5] In other words, chip performance is no longer improved by the transistor scaling, but more by circuit design and system algorithm optimization to integrate useful new functions.[6] In addition, the MtM was partially released by the increasing social needs for high level system integration including non-digital functionalities, the necessity to broaden the product portfolio of existing wafer fabrications, and the limiting economic and time factors of advanced System on Chip (SoC) development. [7]

The International Technology Roadmap for Semiconductors (ITRS) emphasized in early editions the "miniaturization" concept and its benefits in terms of performances, as being a traditional parameter in Moore's Law. Even if the concept of the MtM was introduced, the community of microelectronics continues to find new solutions to maintain Moore's law alive addressing the "More Moore" as a direction for further progress (see Figure 1.1). This trend for increased performance will continue, while performance can always be traded against power depending on the individual application, sustained by the incorporation into devices of new materials, and the application of new transistor concepts.[6]

On device level, leading semiconductor manufacturers turned into the use of stacked nanosheets such as stacked nanosheet Field Effect Transistor (FET) architectures for Complementary Metal Oxide Semiconductor (CMOS) technology. The devices based on nanosheets were still based on Si channels.

Since the scaling of the channel length requires shrinking channel thickness by a similar factor to guarantee sufficient electrostatic control, Si channels were scaled down to the nanometer range. Dramatic limitations were observed in the form of an increase of the charge scattering at the interfaces which resulted in a dramatic drop of the carrier mobility in the channel, ruining the device performance. All these elements were putting the Moore's Law against the limits of physics, with the appearance of quantum phenomena (current leakage by tunneling effect) pushing the race of miniaturization to its limits. [8, 9] Semiconductors industries have made intense use of new materials (such as SiGe in the

source and drain) to sustain Moore's law to drive the demand for the overall industry. [10]

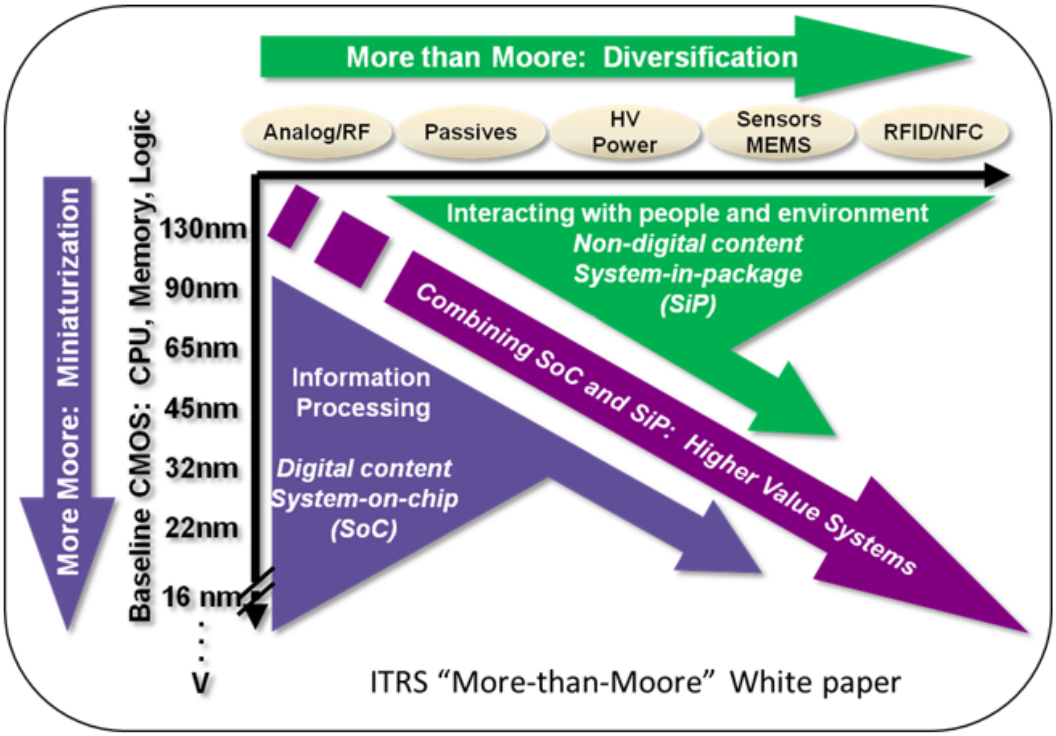

Figure 1.1: The combined need for digital and non-digital functionalities in an integrated system is translated as a dual trend in the International Technology Roadmap for Semiconductors: miniaturization of the digital functions ("More Moore") and functional diversification ("More-than-Moore"). [5]

In this context, it is very challenging to explore the properties of alternative channel material, which may give better performances than the silicon aiming to a continuous innovation in the semiconductor valley. For device engineering, at the atomistic scale 2D layered semiconductors with finite bandgap are among the best candidates to be the ultimate version of nanosheets since they are self-passivated in the third dimension. Besides, the Weak Van der Waals forces connecting layers lead the roads towards an extreme thickness-dependent property that covers a wide range of attractive anisotropic physical properties. For example, promising results obtained with Molybdenum Disulfide (MoS_2) material in the category of layered metal chalcogenides semiconductors were shown in the post-CMOS technology (Field effect tunneling transistors).[11, 12] The unique behavior of the 2D layered materials is a strong incentive for the semiconductor industry since 2D materials are able to represent an enabling device engineering technology beyond what can be accomplished by either Si

and SiGe or III–V materials. [8]

1.2 2D materials: To Graphene and beyond

1.2.1 Graphene

The full deployment of 2D materials wasn't possible if Geim and Novoselov didn't succeed to discover "Graphene" in its monolayer structure and it's novel transport properties in 2004. [13]

The isolation of graphene monolayer was obtained using the 'Scotch Tape method' denoted as a simple method for the mechanical exfoliation of graphite. [14] The discovery of Graphene and it's extraordinary properties permits to award both Geim and Novoselov the Physics Nobel Prize in 2010. The hexagonal structure of graphene presents an atomic-scale honeycomb lattice made of carbon atoms. The isolation of tightly bond one-atom thick layer of sp^2 carbon atoms, allowed to quantify and measure its exceptional mechanical, electrical and optical properties. (See Figure 1.2)

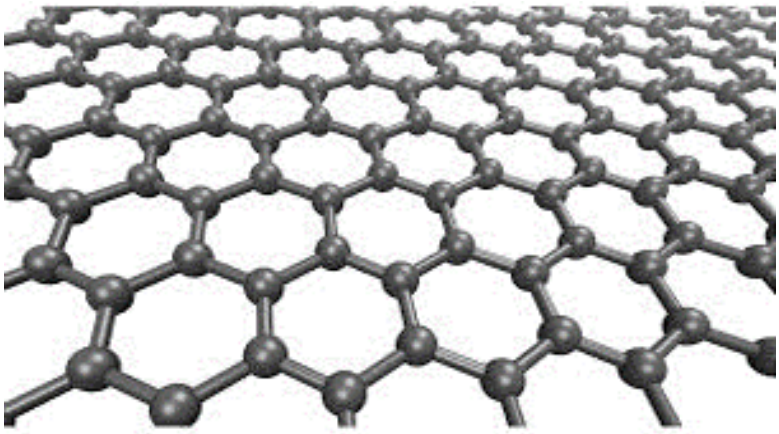

Figure 1.2: Crystallographic structure of graphene.[15]

Graphene has a high charge-carrier mobility of 2000-5000 $cm^2V^{-1}.s^{-1}$. [14] Since those early reports, the charge carrier mobility of suspended graphene solutions has exhibit charge carrier mobilities in excess of 200 000 $cm^2V^{-1}.s^{-1}$. [16, 17, 18] Moreover, graphene owns a high optical transparency (97.7%) in the visible range. [19] Other properties such as a high thermal conductivity of up to 5000 $W.m^{-1}.K^{-1}$, [20] an extraordinarily large specific

surface area of 2630 $m^2.g^{-1}$, [21] and a high breaking strength of 42 $N.m^{-1}$ were found for graphene.[19] Similar to diamond, and due to the high strength of the carbon–carbon bond, graphene is one of the strongest materials ever tested. It presents an extremely high breaking strength, 200 times higher than steel, but at the same, it is also unexpectedly flexible. [22]

Due to its amazing properties graphene opened the imagination of scientists to explore new 2D materials and it's considered nowadays the tip of the iceberg for being the first example of the 2D family.

Despite remarkable electronic transport properties, the lack of a finite electronic bandgap (zero bandgap) for graphene limited its practical use for electronic devices. Therefore, this limitation has spurred the search for another class of 2D materials with a semiconducting nature and similar structure and characteristics.[23]

1.2.2 Other 2D materials

After exploring graphene, huge efforts were made in order to explore 2D layered materials with semiconducting nature. The wide range of discovered properties has been a surge to explore the various 2D layered materials iceberg. [24]

The list of 2D layered materials started to expand in 2010 by the discovery of the runner-up h-BN (Hexgonal Boron Nitride) with a honeycomb structure, that was denoted 'white graphene'. [25] The expanded list of 2D layered materials illustrated in Figure 1.3, includes new graphene's family member: "X-enes" (mono-elemental X compound where X = C, Si, Ge, Sn etc.) like silicene, germanene etc...[26] It includes also "X-anes" (ligand functionalized derivatives of X-enes) [27] , and MXenes (prepared by extracting the A layer from the MAX phases) [28]. Moreover, the 2D metal oxides, heterostructures materials belong to the 2D family that's always expanding. [24, 29, 30]

In addition, Layered Metal Chalcongenides belong to the 2D layered family and is considered as an interesting class of material due to their outstanding electrical and optical properties. Layered Metal Chalcongenides exhibit a strong-in-plane covalent in their monolayer structure. In the case of many layers stacks, each monolayer is connected to its neighborhood by out of plane weak Van der Waals forces. The anisotropy of properties motivate the discovery of many materials for example the III-VI's and IV-VI's family such as GaS,Ga_2S_3 and SnS_2. Moreover, Transition Metal Dichalcongenides (TMD) (such as MoS_2,WS_2 and TiS_2) and Transition Metal Trichalcongenides (TMT) such as TiS_3 belong to

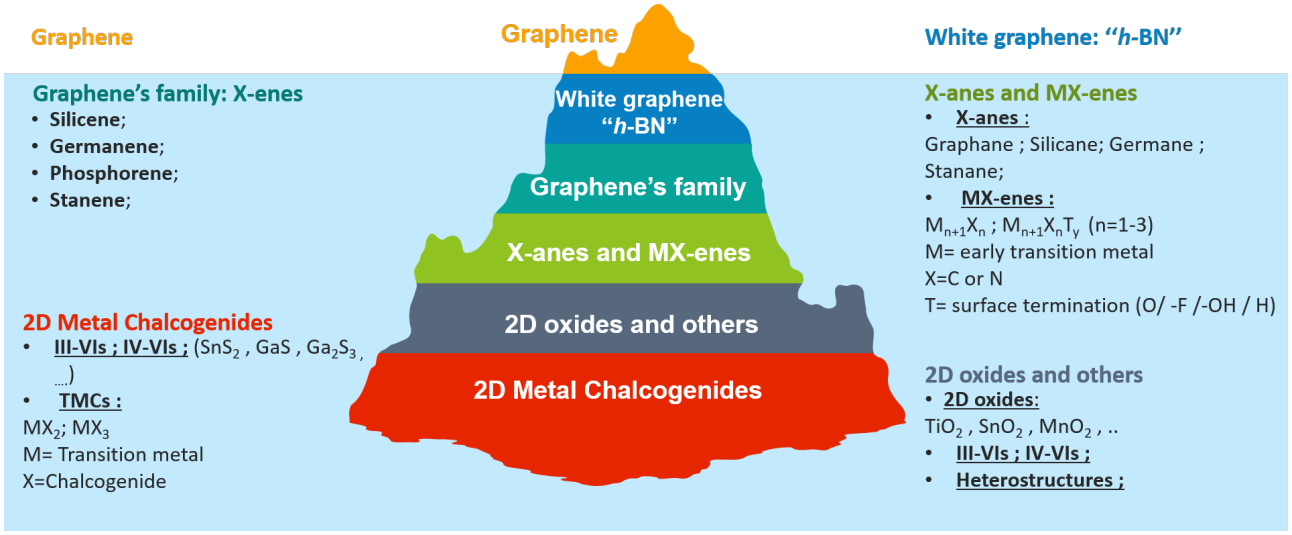

Figure 1.3: Family of 2D layered materials.

the category of Layered Metal Chalcongenides. This dissertation focus on exploring and syntheszing Layered Metal Chalcongenides materials.

1.3 Layered Metal Chalcogenides

1.3.1 Basics

Layered Metal Chalcogenides compounds are getting more attention since they are considered materials with layered structures. The layered structure with MX_n structure, where M is a metal (M=Ti, Mo, W, Ti, ...) that belongs to the group IV, V, VI, VII, IX or X in the periodic table, and X is a chalcogen atom (X=S, Se or Te) (group XVI) shows various electrical and optical properties. In addition, a wide range of electronic properties has been discovered that can go from metallic to semiconducting and even to superconducting.[23]

Among the layered metal chalcogenides, the Transition Metal Chalcogenides (TMD) presents a three-dimensional presentation of layers stacks as Figure 1.4 shows. The TMD with MX_2 structure, shows that each monolayer is based on sandwiching the transition metal (M) between two chalcogen (X) atoms. The three atom stack: X-M-X are connected to each other by strong covalent bonds in the 2D plane, whereas each monolayer is connected to its neighboring monolayer by weak van der Waals (vdW) forces. [32] The average

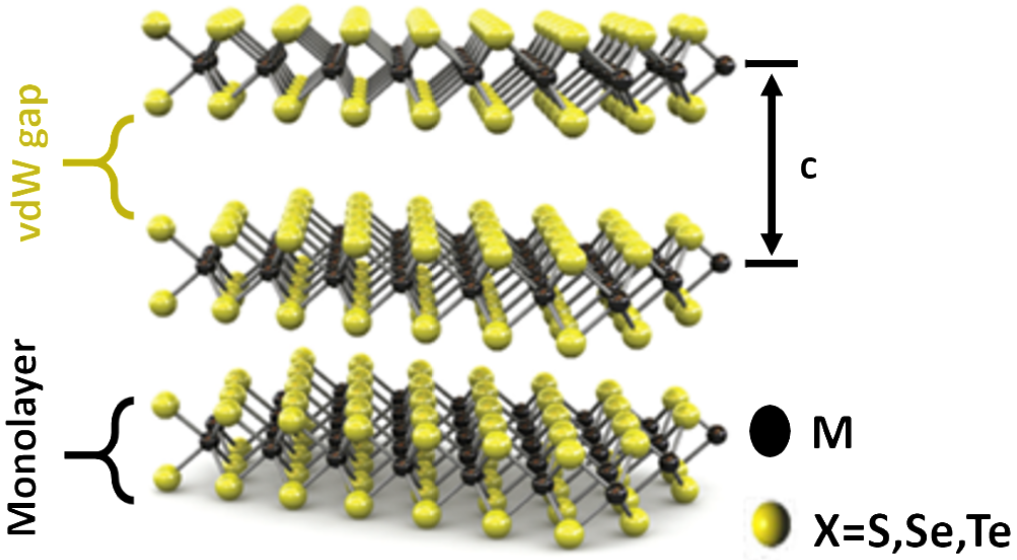

Figure 1.4: Three dimensional representation of TMD stacks (2H phase).(Adapted from [31])

distance between two layers is assigned to "c parameter".

Besides the layered crystal structure, an important feature of metal chalcogenides is their thickness dependent properties. Even though TMDs in their bulk form are not new, researchers did not pay much attention to the exploration of TMDs in monolayer structure until the 2000s. Back in 1923, the first layered metal chalcogenide discovered material was a naturally occurring MoS_2 crystals. [33] By the late 1960s, almost 60 types of TMDs were identified, with more than two-thirds of them being layered materials.[34] After the isolation of the graphene monolayer in 2004, the interest in exploring the fundamental properties and growth of layered metal chalcogenides has increased rapidly leading to exploring MoS_2 monolayer in 2005.[14] After 2010 we entered the decade of the discovery of layered metal chalcogenides.

1.3.2 Bandgap properties

In layered metal chalcogenides stacked layers, it is possible to reduce the number of layers into few or even individual layer (monolayer) due to the weak van der Waals bonding between one layer and another. The possibility of exfoliation from bulk to single-layer structure helped to explore the material properties in either its bulk or monolayer structure.

From multilayers to monolayer, the band gaps of both MoS_2 and WS_2 change from indirect to direct as shown in Figure 1.5. For example, the bulk of MoS_2 exhibits an indirect band gap of 1.2 eV [35], which gradually increases to a direct band gap [36, 37] of 1.8 eV [36] as the number of layers decreases to a single layer due to quantum confinement [37].

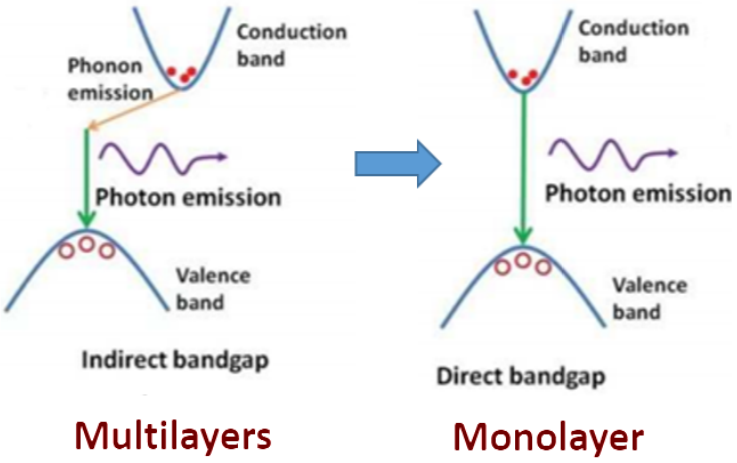

Figure 1.5: TMDs bandgap transition properties from multilayers to monolayer structure. (Adapted from [38])

The band gap engineering resulting from thickness dependency is an extremely important feature in MoS_2 and WS_2 materials. TMDs direct band gap is different from their two layers, multilayer, and bulk phases. Single layer MX_2 transistor performs much better than the available silicon transistor, when a thin dielectric film is used. Single layer MoS_2 obtained by mechanical exfoliation method shows a better photoluminescence emission response compared to MoS_2 multilayer. The transition to a direct band gap is the reason for strong photoluminescence emission in single layer MoS_2. This tunable bandgap in TMDs accompanied by a strong photoluminescence and large exciton binding energy (obtained from coupling charge carriers from different material layers), make them promising candidates for a variety of optoelectronic devices, including solar cells, photo-detectors, light-emitting diodes, and photo-transistors. [39, 40, 41, 36, 42] These results suggest that single-layer nanosheets semiconducting TMD offer innovative and stimulating opportunities for electronic industries.[24]

1.3.3 Phase-engineering

Layered metal chalcogenides, with MX_2 structure exist in several crystallographic phases, polymorphs and polytypes depending on the arrangement of the atoms. The diversity of phases in TMDs structure offer a wide range of electronic properties while containing analogous elements. For exemple, MoS_2 can exhibit both semiconducting and metallic properties, depending on its phase (2H or 1T). Therefore, by acquiring control over the materials' phase, 2H-MoS_2 can be implemented as channel material while 1T-MoS_2 can act as a source, drain and gate in the transistor device. [43]

TMDs exhibits several structural phases resulting from different coordination spheres of the transition metal atoms. Single layer TMD structures are shown in Figure 1.6. A single of layer of TMDs can be characterized by either trigonal prismatic (hexagonal,H) or octahedral (tetragonal,T) coordination of metal atoms. The trigonal prismatic phase is referred to as the 2H phase (or 1H in the case of a single layer) and can be described by a hexagonal symmetry (the D_{3h} group) and corresponds to a trigonal prismatic coordination of the metal atoms. This geometry shows that in monolayer structure, the sulfur atoms are vertically aligned along the z-axis and the stacking sequence is then AbA, where A and b denote chalcogen and metal atoms, respectively (see Figure 1.6-A).

The octahedral phase has a tetragonal symmetry (D_{3d}) and corresponds to an octahedral coordination of the metal atoms referred to 1T phase. The 1T phase is characterized by an AbC stacking sequence, where one of the sulfur layers is shifted compared to others (see Figure 1.6-B).

Depending on the particular combination of transition metal (group IV, V, VI, VII, IX or X) and chalcogen (S, Se or Te) elements, the thermodynamically stable phase is either the 2H or 1T phase, but the other can often be obtained as a metastable phase. The structure of TMDs is defined by the stacking configuration of the individual layers in the case of multilayer and bulk samples, and by possible distortions that lower the symmetry. These distortions, if pronounced, can result in the formation of metal-metal bonds as it happens, for example, in the dimerization of the 1T phase of group VII TMDs, which results in the 1T phase (see Figure 1.6-C) .[32]

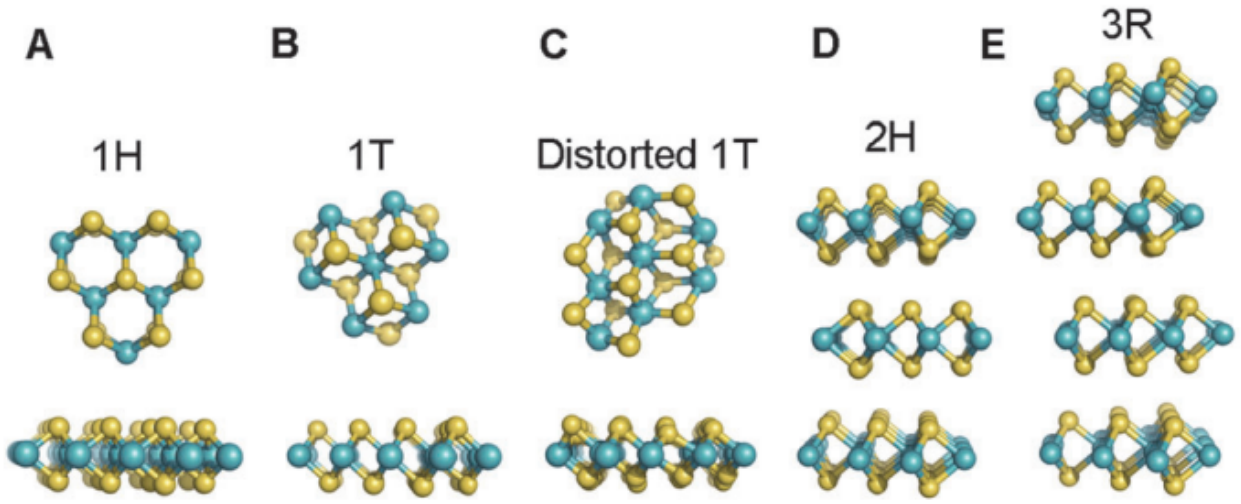

Figure 1.6: Different polymorphs or phases of single-layer and stacked single layer TMDs in their: (A) trigonal prismatic (1H) phase, (B) ideal (a a) octahedral 1T phase, (C) distorted (2a a) 1T phase (or 1T'), (D) 2H phase and (E) 3R phase. [44]

Typically, in single layer TMDs, one of the two possible polytypes is thermodynamically stable. Phase engineering can be used to change the polytype as well as the electronic properties of the materials. In addition to the 1T and 1H phases, 2 different ways of stacking the 1H layers can be achieved, imparting hexagonal symmetry (2H phase, symmetry D^6_{4h}) with a stacking sequence of AbA BaB or rhombohedral symmetry (3R, symmetry C^5_{3v}) with the stacking sequence of AbA CaC BcB ((ee Figure 1.6-D). Stacking in the 1T layer produces the AbC AbC sequence (see Figure 1.6-E). These heterogeneities in stacking order not only introduce defects, but can also lead to additional interesting new phenomena due to the breaking of symmetry.[44]

1.3.4 Titanium Disulfide: TiS_2

Titanium disulfide, TiS_2, belongs to the TMDs family and is the lightest and the least expensive candidate of this family. [45] Little is known about TiS_2 in a few monolayer form compared to other TMDs such as MoS_2 and WS_2. TiS_2 crystallize in their most stable phase, the octahedral 1T phase (see Figure 1.7 and `https://materialsproject.org/materials/mp-2156?chemsys=Ti-S`).[24] Each layer consists of edge-sharing TiS_6 regular octahedra where S-Ti-S atoms are connected by a covalent bond. The crystallographic structure

(CdI_2 trigonal structure, space group P$\bar{3}$m1) can be described as the stacking of TiS_2 layers weakly bounded by van der Waals (vdW) forces, along the [001] direction. Each layer consists of edge-sharing TiS_6 regular octahedra where S-Ti-S atoms are connected by a covalent bond. The anisotropic structure presents a lattice unit cell of a=b=3.41 Å, c = 5.7 Å, where (c-parameter) is denoted as the interlayer distance (PDF 01-070-6204 and [46]). The phase diagram of Ti-S is shown in Figure A.1 in Appendix A.

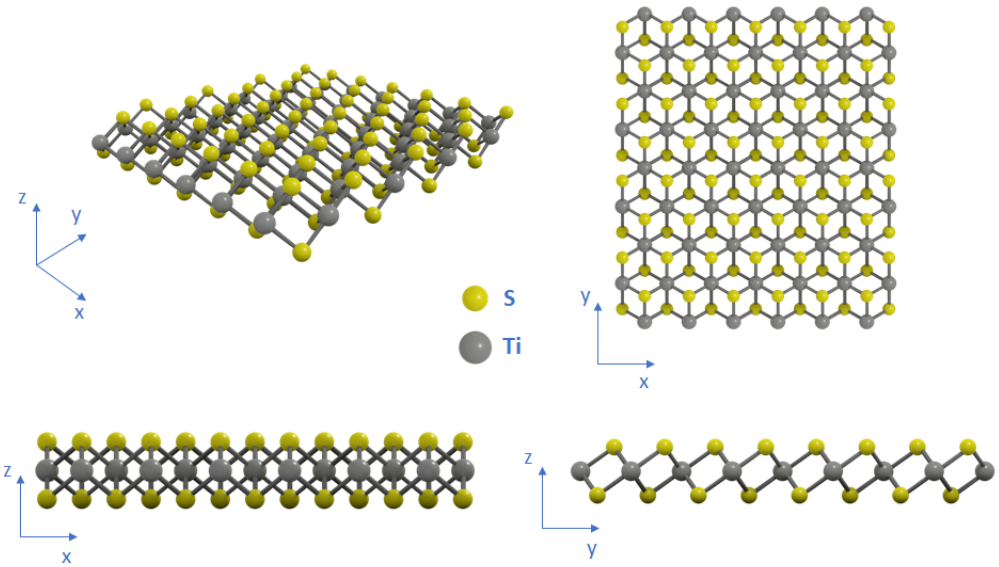

Figure 1.7: Top and side view of single-layer titanium disulfide (1T-TiS_2).[47]

However, a particular characteristic of TiS_2 is its tendency to deviate from the mentioned configuration by creating vacancies in the titanium sites in its crystal structure in favor of the migration of Ti atoms into interlayer sites. This phenomenon influences several properties of TiS_2 in non-stoichiometric ($Ti_{1+x}S_2$) and stoichiometric compounds.[48, 49]

The existence of TiS_2 was first demonstrated by Blitz et al. in 1937 along with a set of experiments that classified TiS_2 as a semimetal [50]. Since then, experiments performed on bulk TiS_2 showed either one of the two behaviors and the debate is still ongoing. The origin of its high conductivity has been under debate for several years, with theoretical and experimental results splitting between semi-metallic and semi-conductive nature. However, at the present time, researchers agree that the debate in experimental results stems from the wide range of transport properties resulting from the Ti excess in $Ti_{1+x}S_2$ (or in other words the stoichiometry variation). [48]

In addition, this behavior is believed to be present, with a different degree, both in stoichiometric and non-stoichiometric TiS_2. An extensively investigated property of TiS_2 regards its ability to be easily and reversibly intercalated with lithium, allowing it to tune its electronic properties with respect to the amount of intercalation due to a modulation in the number of carriers.[51] Such characteristic was exploited in the 1970s through its employment as a cathode in energy storage devices [52] and is currently being investigated in few-layered TiS_2 due to its potential employment in high-energy density reversible lithium batteries. [53] Other applications include thermoelectric [54, 55], optics [56], hydrogen storage [57] and photovoltaic in TiS_2/TiO_2 heterostructures. [58]

In this section we introduce two important materials that will be discussed further in this dissertation: Tin Dislufide and Gallium Sulfide (GaS_x) in their two stable forms: Gallium monosulfide: GaS and Gallium (III) sulfide: Ga_2S_3.

1.3.5 Tin Disulfide: SnS_2

Among the lamellar metal chalcogenides materials, Tin disulfide (SnS_2) is considered a promising n-type 2D semi-conductor known as a post-transition metal chalcogenide material. Its low melting point temperature distinguishes SnS_2 from other lamellar metal chalcogenides materials in general. SnS_2 exhibits a lower melting temperature (865°C) than MoS_2 (1750°C) and WS_2 (2400°C).[59] The low melting point temperature should permit to crystallize SnS_2 layers under a low thermal limit of 350 °C .[60] The low temperature process and the wafer-scale uniformity of SnS_2 validate the industrial compatibility in different applications.

Among sulfide materials from group IV only SnS_2 and PbS_2 present analogous structure of TMDs. Just like TiS_2, SnS_2 has a lamellar structure with two possible types of coordination including trigonal prismatic (H phase) or octahedral coordination (T phase). The most common polytype is the 2H-polytype ($P\bar{3}m1$) (see PDF 23-0677 and `https://materialsproject.org/materials/mp-1170?chemsys=S-Sn`). However additional polytypes such as 4H-polytypes and 18-R could be obtained under specific experimental conditions. [61]

SnS_2 with an indirect bandgap (2.2 eV) and with a bandgap of 2.6 eV in monolayer form, have been studied in many potential applications such as Field Effect Transistors (FETs), photodetectors, water-splitting catalysis, thermoelectric, batteries and gas sensors.[62]

During the synthesis of SnS_2 which appears as a natural mineral, other stable SnS_x phases are obtained that can also be found in nature such as SnS or Sn_2S_3. [63]

1.3.6 Gallium Sulfide (GaS and Ga_2S_3)

Layered gallium sulfide (GaS_x) has two stable forms: GaS and Ga_2S_3. [64] Both forms are wide-band-gap semiconductors (Eg = 3.0-3.6 eV), and can be used in optoelectronics and photovoltaics. [65]

1.3.6.1 Gallium Monosulfide: GaS

Hexagonal gallium monosulfide (β-GaS), which is the stable MX phase at any temperature, has a layered structure. It consists of four-atomic-plane monolayers (each one having two close-packed gallium atom planes and two close-packed sulfur atom planes arranged according to the stacking sequence S–Ga–Ga–S); there are strongly covalent gallium–sulfur chemical bonds within the layers, while there are weak van der Waals interactions in between neighboring bonds [66] (see for instance Figure 1.8 and https://materialsproject.org/materials/mp-2507/). The crystal structure of gallium monosulfide (β-GaS) belongs to the hexagonal system (space group $P6_3/mmc$) with unit cell parameters a = b = 3.587 Å and c = 15.492 Å, where c corresponds to the stacking of two GaS slabs.

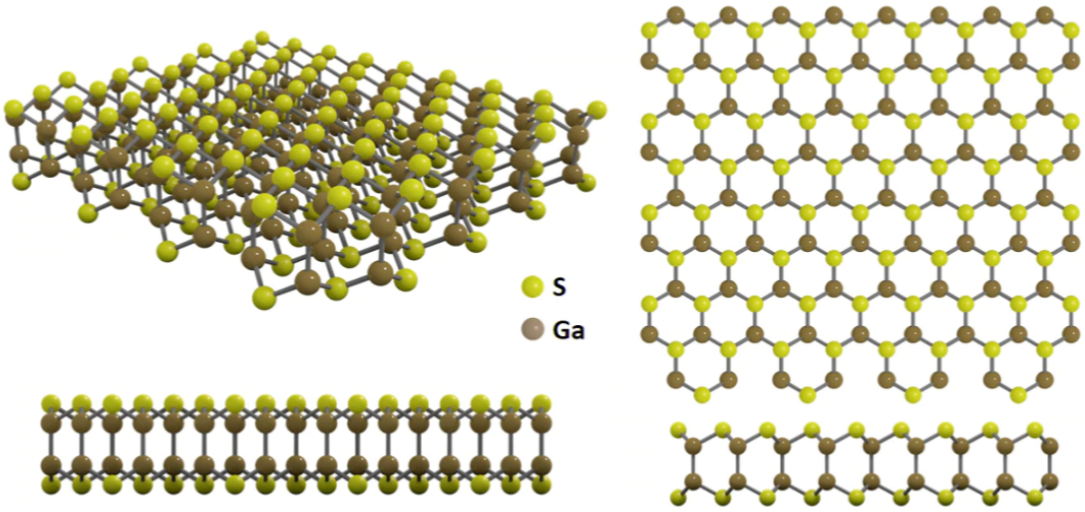

Figure 1.8: Top and side view of gallium sulfide GaS monolayer.[67]

Gallium monosulfide is a lamellar material and is a semiconductor with an indirect band gap value of 2.59 eV and a direct band gap value around 3.45 eV. [68] GaS thin films can be used in many fields such as passivation layers in III-V semiconductors [69], anodes for Li-ion batteries [70], FETs [71], Photodetectors [72] and buffer layers in Cadmium Telluride (CdTe) solar cells.[73]

1.3.6.2 Gallium (III) Sulfide: Ga_2S_3

Another stoichiometry achieved during the growth of gallium sulfide thin films is the gallium (III) sulfide: Ga_2S_3. Like gallium monosulfide, Ga_2S_3 presents interesting semiconductor properties and crystallographic structure that allow it to be useful in the fields of microwave frequencies [74, 75], photo-detection [76, 77], as a precursor for solar panels [78] and for photo-catalysis to generate hydrogen from water splitting [79].

Four different crystallographic forms have been reported for Ga_2S_3: α-Ga_2S_3, α'-Ga_2S_3, β-Ga_2S_3, γ-Ga_2S_3. In hexagonal β-Ga_2S_3 ($P6_3mc$ space group, wurtzite-type structure), Ga atoms are statistically distributed with an occupation of 2/3 on the 2b site of the lattice and are located on tetrahedral sites formed by S, with Ga–S bonds almost equivalent (3 at 2.254 Å and 1 at 2.268 Å). Hexagonal α-Ga_2S_3 (space group $P6_1$) and monoclinic α'-Ga_2S_3 (space group Cc) are superstructures of the β wurtzite with various ordering between vacancies and Ga atoms. Finally, a cubic sphalerite-type structure is also reported for γ-Ga_2S_3, (space group F-43 m). [80] The most stable crystallographic structures of Ga_2S_3 are shown in Figure 1.9 (see `https://materialsproject.org/materials/mp-539?chemsys=S-Ga`, `https://materialsproject.org/materials/mp-32616?chemsys=S-Ga` and `https://materialsproject.org/materials/mp-1224879?chemsys=S-Ga`) .

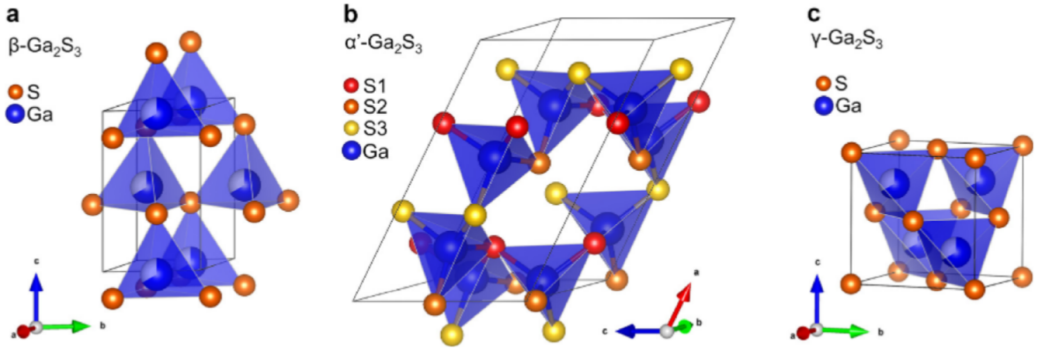

Figure 1.9: Most stable crystallographic phases of Ga_2S_3 [80]

Concerning the electronic properties, Ga_2S_3 have great similarity with GaS specially concerning the gap value. Ga_2S_3 has a direct band gap value of 3.4 eV. The attractive properties of Ga_2S_3 permits to cover various fields of applications as mentioned above.

1.4 Growth techniques: Advantages and Limitations

Exploring the features of 2D materials in general in their monolayer structure was not possible before 2005. In 2005, Novoselov and Geim discovered the 'micromechanical cleavage method' using scotch tape technique to mechanically exfoliate a graphene monolayer from graphite.[14] A scientific revolution in the field of nanoscience was started after the discovery of the 'micromechanical cleavage method' in order to increase the deployment of lamellar metal chalcogenides.

Researchers were motivated to take advantage of the interesting features of ultrathin and monolayers structure of layered metal chalcogenides materials by finding the adequate growth techniques that could produce high quality films and permit their use for large scale production in technological applications.

'Micromechanical cleavage method' was used for the first time rubbing HOPG (highly oriented pyrolitic graphite) against another surface (like using a pencil) leaving single layer flakes on the surface. On the top of an oxidized silicon substrate, a change in optical path is noticed due to the monolayer, since one atom's thick layer of any material is transparent to visible light. Therefore, the monolayer effect is enough to change the interference color with respect to the bare substrates leaving behind a phase contrast as Figure 1.10 shows. [81] Despite the simplicity of this method, an important drawback can be listed: the monolayers obtained by micromechanical exfoliation are a large minority among the accompanying thicker flakes, preventing the application of this technique as a scalable technique for coating large wafers, so it is not technologically applicable. [81]

In order to integrate 2D metal chalcogenides materials in the design of new electronic devices it is mandatory to ensure a good control in terms of the number of layers, crystal quality (defect-free, pin-hole free, grain boundaries, in-plane texture, domain size, uniformity,..), lateral dimension of grains and scalability to large area substrates. All these requirements couldn't be achieved using top down methods such as mechanical exfoliation through Scotch tape and liquid exfoliation (as an example, lithium intercalation and solvent-assisted

sonication).[82, 83]

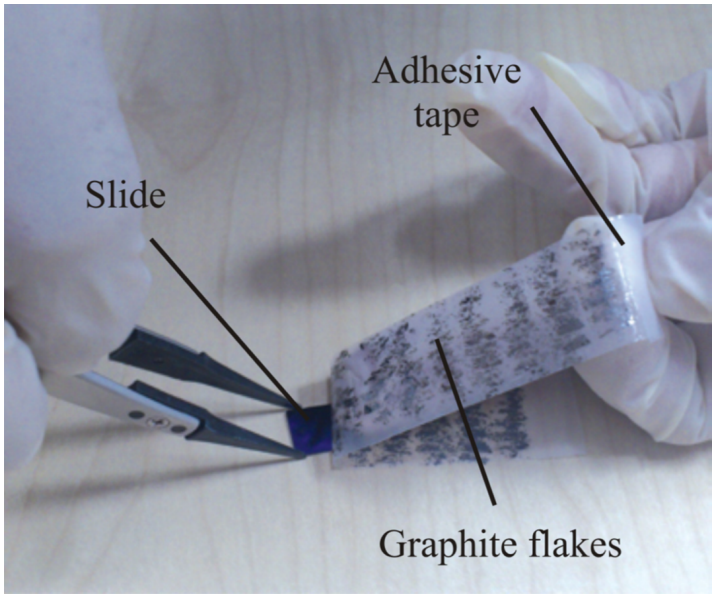

Figure 1.10: Scotch tape procedure, reported by Novoselov and Geim in 2005. [84]

The bottom up approaches aim to ensure a controllable synthesize over a large area substrate. In addition, the bottom-up approach was developed to end the limitation seen by the top-down approach. For example, the main reason behind the deployment of lamellar metal chalcogenides was the lack of scalable growth techniques.

Gas-phase growth techniques were found to be the most suitable techniques to grow these kinds of materials. The exposure of one or more vaporized sources (precursors) on a based material (substrate) permits the growth of a thin film material once the external vaporized sources react together. This principle in general, achieves a good control of the gas composition on the substrate surface since the precursors are delivered in a homogeneous way over all the substrate area: large area scalability, uniformity and thickness control could be achieved for thin films deposited using gas-phase methods.[23]

The commonly used method to grow mono to few layers of layered metal chalcogenides is Chemical Vapor Deposition (CVD). The metal and chalcogen precursors are evaporated and their vapor is delivered into the reaction chamber by inert carrier gases. Within the reaction chamber (hot zone), these precursors react to grow the final product on a target substrate. CVD offers thin films on suitable substrates with a high aspect ratio (for exemple nanotubes) whereas uniformity and the quality of the film over large surfaces significantly

depends on the flow rate of the carrier gas, concentration of the individual precursors, and their ratio along with growth temperature in the whole reactor. [85]

Despite its importance to grow thin films, CVD method suffers from limitations that prevent its use as an industrial-scale technique for the implementation of lamellar metal chalcogenides in (opto)electronics devices. Thin films grown by CVD suffer from the presence of dislocations and grain boundaries of grown crystals.[86] Moreover contamination, poor uniformity, reproducibility, and thickness control [87, 88] along with the requirement of harsh conditions such as high thermal budget or high processing temperature (> 450 °C), restricts the integration with the semiconductor device processing steps.[89] Even if some solutions such as synthesizing the target 2D material on another 2D material [85] were addressed to minimize these limitations, but this still not enough for large-scale production and for the growth of uniform monolayer or ultrathin layer. All these elements confirm the necessity to explore alternative methods to overcome all or most of these limitations.

1.5 Atomic Layer Deposition and Atomic/Molecular Layer Deposition

1.5.1 Relevence of Atomic Layer Deposition

Regardless of the advantages of the CVD approach in terms of high deposition rate (that can vary from a few nm to about ten of μm per minute), stoichiometry control, composition control, and being a reactive surface deposition, CVD suffers from many limitations such as pre-reactions in gas phase and the formation of reaction by-products that can contaminate or even degrade the deposited films. Moreover, the configuration of the reactor used can generate a thickness gradient and defects on the coverage rate along the substrate, as is the case for MoS_2 deposits by CVD. [90] Therefore, the growth of monolayer of MoS_2 and WS_2 by CVD yields to large grain size (in the micrometer range) at high temperatures.[91] The lowest substrate temperature to obtain a single uniform crystalline MoS_2 or WS_2 monolayer is 550 °C, where the process was conducted around 26 hours under high vacuum (10^{-4} torr).[92]

Atomic Layer Deposition (ALD) is a gas-phase thin film growth technique being increasingly employed in the microelectronic industry. ALD technique is derived directly from

CVD. The main difference with CVD is the absence of gas phase pre-reactions, where the precursors are sequentially introduced into the reaction chamber. Each injection of precursor in the chamber is preceded by a purge time allowing the evacuation of the different reaction products and the excess reagents in the chamber. Each exposure of the substrate to a precursor leads to the formation of a monoatomic layer of this precursor. Therefore, ALD can be considered the technique of choice for the growth monolayers. The controllable cyclic manner allows to deposit ultra-thin films of TMDs because it permits to obtain precise thickness control, large area uniformity (scalability), and excellent conformality over complex 3D structures even at low deposition temperatures, as illustrated in Figure 1.11. [93]

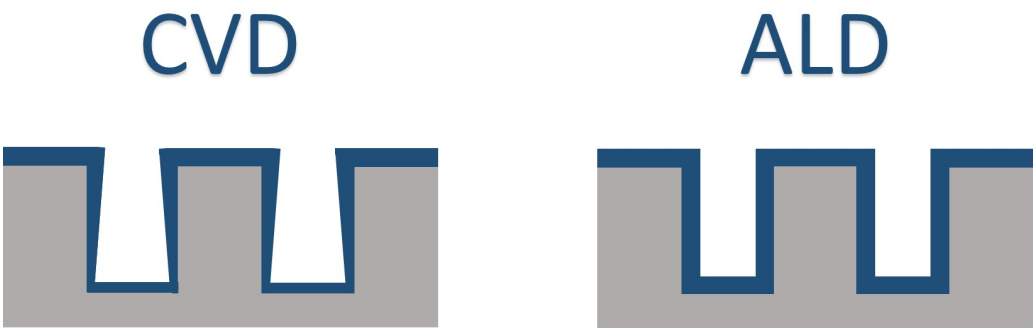

Figure 1.11: Difference between CVD and ALD in uniformity and conformality distribution over 3D substrate area.

The ALD technique was born during the decade of 1960s-1970s by combining two discoveries in Finland and in the Soviet Union. But it wasn't until 1974 that the first patent on this technology was published by the Finnish inventors Suntola and Antson. [94] The ALD process was orginally called 'Atomic Layer Epitaxy' or ALE, but since the deposition of amorphous, not epitaxial, films became more prevalent, the term ALD became the used term and it was cemented especially when it was used to name the first American Vacuum Society (AVS) ALD conference in 2001, chaired by Steven M. George. [95]

The ALD concept relies on two self saturated surface reactions of gas-phase precursor and reactant separated by an inert gas step to avoid CVD reactions. The self-limiting, alternating surface reactions gives ALD its unique advantages such as excellent reproducibility, accurate thickness and composition control, good scalability, and excellent uniformity and conformality on both large and complex substrates. [96] Beside the listed advantages, ALD

possesses a wide range of growth temperatures that can go from relatively low temperatures (room temperature) up to about 500 °C, which allows the ALD process to be useful in different fields of applications.[97, 98, 99] Moreover, the identification of precursors that present a high volatility, thermal stability, and reactivity is also considered as a key behind the success of ALD. [100, 101]

The industry began to take a deep interest in ALD in the 1990s, with the beginning of the need for conformal growth of new materials on high aspect ratio structures. As a result, in 1998, ALD was reported to be used in the production of Dynamic Random Access Memory (DRAMs) devices. [95] Intel reported the introduction of ALD grown HfO_2 as the high-K gate oxide material in FETs in 2007. [102] With the continuous drive in downscaling devices dimensions, ALD has played a crucial role in semiconductive devices fabrication process. Also ALD was implemented in other industries, one of them is the solar cell industry for depositing passivation layers. [103]

Being widely studied for oxides and nitrides, the need to study ALD for 2D materials, in particular LMDs, including TMDs has increased with the discovery of their extreme properties when as thin as one monolayer or a few layers. However, thus far, it is mostly restricted to the direct ALD approach of semiconducting and group VI TMDs in general. In addition, there is an indirect ALD approach known as chalcogenisation, where a transition metal oxide is grown by ALD and then annealed at high temperature in a targeted chalcogen environment (e.g., S, H_2S, TBT or TBDS) to form the final TMDs film. [104, 105]

1.5.2 Concept of ALD and ALD/MLD process

Since ALD is a surface-controlled synthesis method that allows to produce ultra-thin films, it is important to describe its concept in detail. The surface chemistry concept relies on the saturated or self-terminated surface of two gas-phase precursors, whereas every single layer of any material and even less can be described by one ALD cycle. Each ALD cycle can be divided into four steps, as illustrated in Figure 1.13, i) the metal pulse, in this step the metal precursor is pulsed into the substrate surface terminating with either –OH or –SH group, allowing the metal precursor molecule to react with the active sites of the substrate. ii) A purge step, in this step the excess of precursor and reaction byproducts are purged by an injection of inert gas such as N_2 or Ar flux. iii) The reactant pulse (chalcogen pulse), in this step the chalcogen precursor, for instance, H_2S, containing the nonmetal element is

pulsed to react with the remaining ligands of the metalic precursor allowing a reaction of metal/chalcogen to take place afterwards. iv) A purge step, in this last step the reaction byproducts are purged by N_2 or Ar flux.[93, 100] In order to reach the desired thickness, ALD cycles are repeated as many times as necessary. ALD process could lead to obtain an inorganic deposit of the desired compound in the form of a thin film.

An ideal ALD process can be characterized by a linear increase in the amount of material deposited as a function of the number of ALD cycles. In the ALD community, instead of talking about growth rate as it is the case in CVD, we mainly use the term Growth Per Cycle (GPC) as the amount of material deposited per ALD cycle, which is actually the ratio between the deposited thickness and the number of ALD cycles. Important information must be taken into account: the GPC value is not related to the kinetics of the chemical reaction during the deposition process, but to the number of chemisorbed sites on the growth surface, which depends on the reactivity and the number of accessible surface sites, or even on the surface morphology.[106] In addition, the GPC is directly dependent on the precursors and reagents used for the reaction. Generally, the GPC is expressed in Å/cycle because in ALD, one generally deposits atomic layers of a few Angstroms. During an ALD process, there are five growth regimes that depend directly on the temperature and the GPC. They are presented in the Figure 1.12 and detailed below:

1. For a high deposition temperature, an increase in the GPC can happen due to the decomposition of the metal precursor before reacting on the surface with the reagent.

2. For a high deposition temperature, a decreasing GPC can be observed due to desorption of the precursor, reduction of the number of active sites on the surface, or due to the sublimation of the deposited material.

3. For a low deposition temperature, the GPC can increase if the reaction rate is slow and the reaction time between precursors is higher than the cycle duration.

4. For a low deposition temperature, if a decreasing GPC is obtained it means that there is a condensation phenomenon and at least more than one monolayer is adsorbed.

5. A temperature range where the deposition rate does not depend on the temperature, but only on the density of reactive sites available on the surface and on the saturation of the surface by the precursor. This temperature range in which the GPC is constant

is called the "ALD window". To carry out an ALD deposition, one must therefore be located in this window. In addition, within the ALD window, a self-limiting surface reaction takes place where the active sites of the surface are chemisorbed.

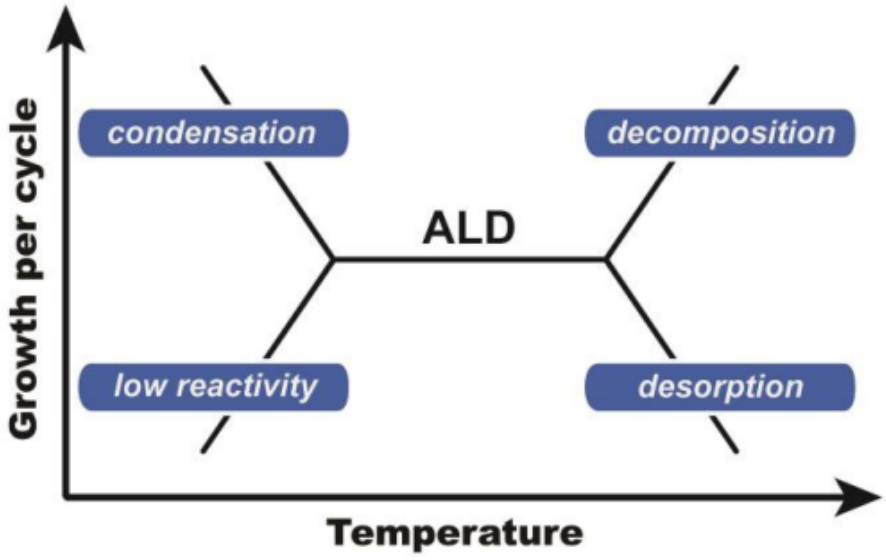

Figure 1.12: Schematic illustration representing the effect of substrate temperature on the identification of the ”ALD window”.[107]

Moreover, it was found that the GPC is substrate-dependent in the early stages of growth (first few cycles), before reaching a steady state. The reason behind such phenomena is that the chemical sites on the substrate surface can have different reactivity compared to the chemical sites on the surface of the as-grown material.[106]

ALD is already used to deposit ultrathin films, but the extreme thinness and anisotropy of lamellar TMDs and more in general LMDs bring new considerations, and despite several efforts, the deposition of as-deposited crystalline layers remains extremely challenging and possibly necessitating post-annealing steps or chalcogenization of ALD-grown metal oxides. [108, 109, 110, 111] Among the complicating factors is the co-occurrence of growth and crystallization during the ALD process which becomes particularly limiting when a predetermined crystal orientation is required. Mastering the nucleation and atomic layer-by-layer growth of a continuous crystalline ultra-thin film with layers parallel to the substrate is

a challenging task when TDMCs are involved. [112] The use of specific crystalline substrates with adequate lattice parameters is a possible strategy to overcome this problem.

To try to overcome the problem another approach, which has a larger substrate scope, is to dissociate the film deposition and its crystallization. For that purpose, one can combine the use of organic and inorganic precursors during ALD (organic molecules are for instance, alcohols (R-OH) being a generic organic fragment rather than H_2O as oxygen source). The presence of the organic chemical residues prevents the crystallization during the growth of the hybrid inorganic/organic thin film (referred as metalcones in the examples just mentioned [93, 113]) at low temperatures. A subsequent thermal treatment (an annealing which induces further chemical reactions in the film and loss of organic fragments) leads to the crystallization of the mineral phase. [114, 115]

For instance, the combination of such organic/inorganic precursor-based ALD approach, which is called herein Atomic Layer deposition/Molecular Layer Deposition (ALD/MLD) [113, 116] and post-annealing allowed to control the porosity of Al_2O_3 thin films[117], the crystallinity, composition, and electrochemical properties of SnO/SnO_2, [118] TiO_2, and V_2O_5.[119] In the field of TMDs, the value of the replacement of H_2S molecule used for sulfide phases growth by ALD, with the MLD precursor, 1,2-ethanedithiol (EDT or $HSCH_2CH_2SH$) was demonstrated by achieving atomically thin MoS_2 based layers oriented parallel the substrate, [120] with residual carbon content similar to an organic-precursor free Plasma Enhanced Atomic Layer Deposition (PE-ALD) process to MoS_2.

Concerning the growth behavior in ALD/MLD process, Karppinen et al. [116] showed that the mentioned above "ALD window" (or ALD/MLD window) can be slightly different in some typical cases of ALD/MLD (or only MLD) process. In those cases, there is no temperature range where a constant growth (or GPC) is observed. However, the process may yet be highly reproducible, and such behavior shows that the increase in deposition temperature affects the number of reactive sites or reaction mechanisms.[116]

In addition, since ALD previous studies were based on using H_2S as a reactant to grow sulfides [55, 121, 122, 123, 124, 125], it was very challenging to find an industrially relevant alternative to the H_2S reactant. Since the use of H_2S is problematic due to its flammable and highly toxic nature, researchers pushed their efforts toward the use of another reactant less dangerous and can be easily manipulated at a lab scale such as organosulfur precursors.[120, 105]

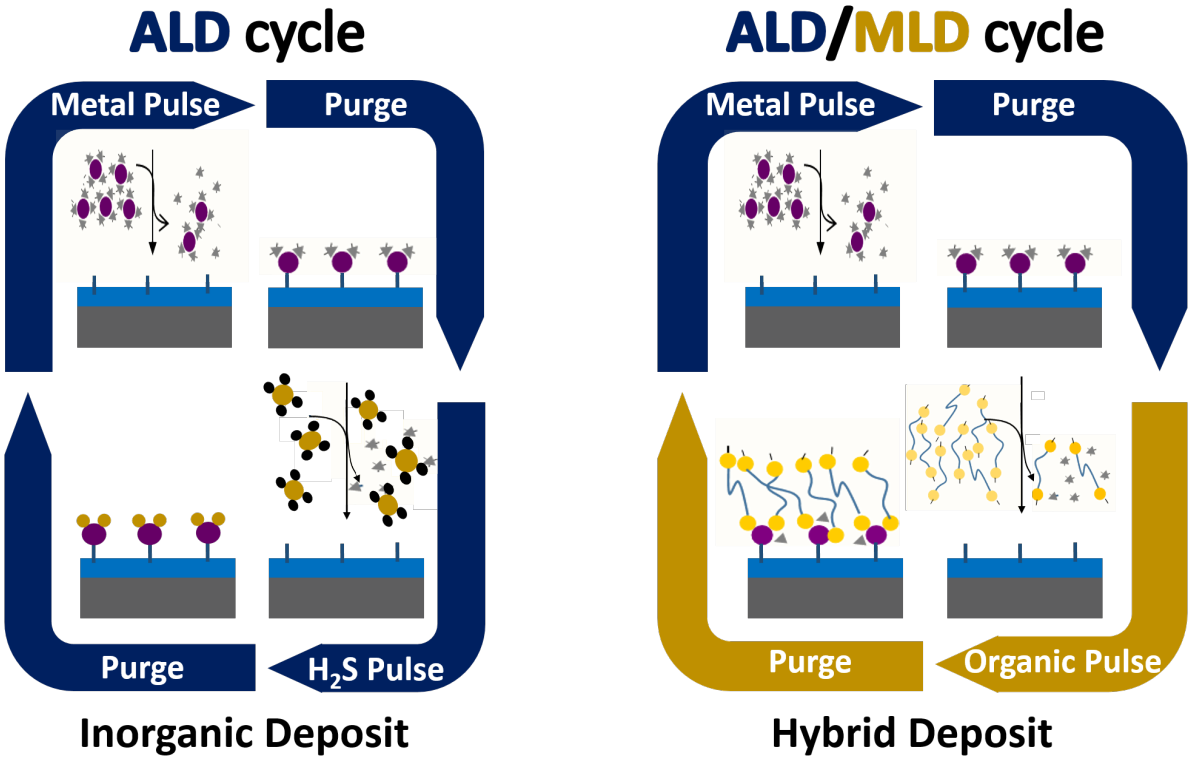

Figure 1.13: Schematic illustration of an ALD and ALD/MLD cycle.

In the context of this Ph.D. thesis work, the ALD/MLD concept illustrated in Figure 1.13 is the same as ALD, but it consists on replacing the inorganic reactant (H_2S) with an organic reactant herein 1,2-ethanedithiol (EDT, $HSCH_2CH_2SH$) aiming to produce a Hybrid (Inorganic/Oragnic) amorphous thin film hereafter called thiolate. This dissertation will be focused on the 2-steps approach (ALD/MLD and thermal annealing) in order to overcome the limitations of conventional thermal ALD, more specifically during the growth of Titanium Disulfide TiS_2 material, which will be discussed in details in 1.6.1.

Concerning the growth mechanism, an example of the deposition of Molybdenum thiolate (Mo-thiolate) is shown in Figure 1.14. [120] The proposed schematic presentation shows the suggested sequential grafting of $Mo(NMe_2)_4$ and EDT on the silica surface at 50 °C in order to obtain a molybdenum(IV) aminothiolate. Upon the first metal pulse on the substrate surface, $Mo(NMe_2)_4$ reacted with silanol surface resulting in the formation of [Si–O–Mo $(NMe_2)_3$] species (see Figure 1.14, eqn (1)). In addition during EDT pulse, the two thiols permit to substitute two $–NMe_2$ ligands by two EDT molecules, to yield a formal structure

[Si–O–Mo(NMe_2)(–S–C_2H_4–SH)$_2$] (see Figure 1.14, eqn (2)).[120]

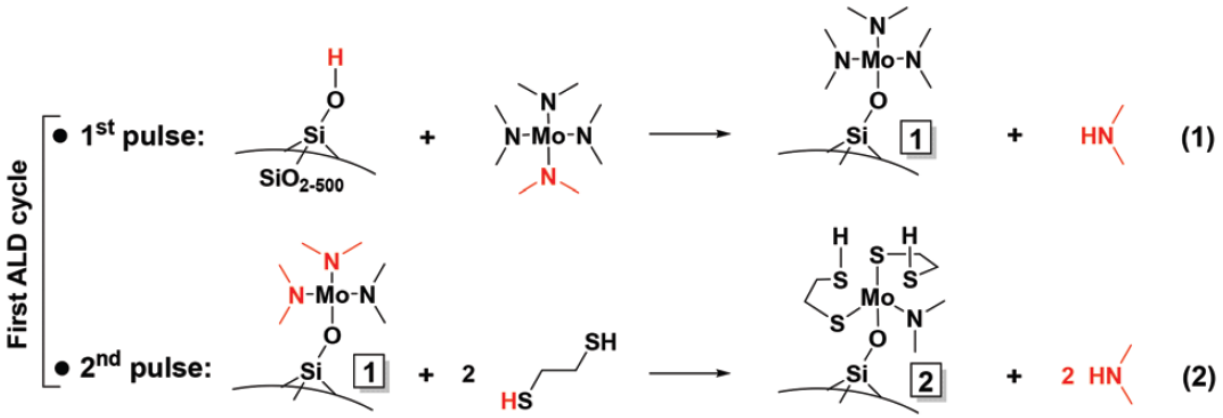

Figure 1.14: Proposed scheme for the sequential grafting of Mo(NMe_2)$_4$ and 1,2-ethanedithiol on the silica surface at 50 °C during one ALD/MLD cycle to yield a presumably amorphous surface molybdenum(IV) aminothiolate.[120]

1.6 Previous attempts

Before introducing the aim of my research work it is important to remind the reader about the previous attempts in ALD for the studied materials during my thesis work. The main focus of this dissertation is the growth of Titanium Disulfide TiS_2. Preliminary results on the growth of LMDs materials of Sn$_x$S and Ga$_x$S is also shown in Chapter 5.

1.6.1 Titanium Disulfide: TiS_2

TiS_2 has been synthesized by different growth techniques such as Chemical Vapor Deposition (CVD), [126, 127, 128, 129, 130, 131] chemical exfoliation method [132] , wet chemical synthesis [133] , and the ALD reports remain scant [122, 55, 133, 121, 124, 134, 135, 136].

The first ALD growth of TiS_2, reported in 2007 by Pore et al., was grown from $TiCl_4$ and H_2S as titanium and sulfur precursors.[55] Since then, alternative Ti (tetrakis(dimethylamido) titanium, TDMAT) [124] and S (H_2S plasma) sources [136] have been considered as well as two-step strategy (sulfurization of PEALD-TiN thin films).[135]

Film texture of ALD TiS_2 was mentioned in a few studies. In the first ALD report of Pore

et al.[55] the growth of TiS_2 using $TiCl_4$ and H_2S as precursors was performed at 400 °C on different substrates (sodalime glass, native-SiO_2/Si, ZnS, Rh, Ir, Pd, Pt, Ru, and TiN). A clear influence of the substrate on the film morphology and texture was observed with non-uniform distribution of the deposited film. Only the (001)-oriented ZnS substrate enables the growth of hexagonal (001)-oriented and stoichiometric TiS_2 layers parallel to the substrate surface, with a total film thickness ca. 100 nm. No film could be grown on native SiO_2 on Si substrate. Deposited films on soda lime glass required a rubbing step with tissue in order to obtain mechanically TiS_2-oriented crystallites with (001) planes parallel to the substrate surface.

Sayed et al. [122] reported the growth of TiS_2 by ALD with the same set of precursors ($TiCl_4/H_2S$) at lower temperature (300 °C). The deposition resulted in the formation of vertically aligned TiS_2 nanowall network along the [001] direction parallel to the c-sapphire substrate surface, as SEM and TEM reveal. In addition, the TEM observations revealed TiS_2 layers, grown on top of an amorphous TiS_2, parallel to the film-substrate interface, along with TiS_2 platelets grown away from the substrate surface. The films grown on Si(100), stainless steel and quartz substrates were amorphous.

Mahuli et al.[121] reported the growth of TiS_2 on Al_2O_3 coated native SiO_2 on Si(111) substrate, by ALD using $TiCl_4$ and H_2S as precursors. At 200 °C the as-deposited film thickness was equal to 42.5 nm and the obtained film was poorly crystalline without any presence of texture.

The TDMAT and H_2S precursors at a growth temperature equal to 180 °C, leads to amorphous TiS_2 films when grown on SiO_2/Si wafer [124], probably due to the change of the metal precursor and the reduction of deposition temperature. No specific data on film crystallinity are provided when films are grown on glass, carbon paper, or germanium.[134] Basuvalingam et al.[136] reported the growth of TiS_2 and TiS_3 thin films using both thermal ALD and PE-ALD from TDMAT and H_2S/Ar. By using the H_2S plasma at a deposition temperature of 100 °C, amorphous TiS_3 films were obtained on thermal-SiO_2/Si substrate, whereas the structural quality was improved by post-annealing step at 400 °C in sulfur-rich atmosphere. PE-ALD process showed a transition to the formation of polycrystalline TiS_2 when the deposition temperature went above 100 °C. Thermal ALD at 100 °C confirms the deposition of TiS_2 by Raman spectroscopy. In any case, the GPC was ca. 1.6 Å/cycle and film thickness 30 nm [136]. Recently Mattinen et al. [137] reported the growth of polycrystalline TiS_2 at 100 °C using PE-ALD approach through the incorporation of high H_2 ratio in

the plasma feed gas leading to sub-stoichiometry polycrystalline thin films. Van Kasteren et al. [138] reported the growth of Titanium oxysulfide thin films using a supercycle approach (m TiS_2 were alternated with n TiO_2 cycles using TDMAT, H_2S and H_2O as precursors) for specific applications.

In all cases, the material growth and properties appear strongly dependent on the nature of the substrate and no high-quality ultra-thin layered materials could be obtained. [122, 55, 121, 124, 134, 137, 138] Besides, only few applications of ALD TiS_2 thin films are reported (photo-harvesting material, Li+/Na+ intercalation, CO_2 reduction reaction), and the challenge of producing ultrathin lamellar TiS_2 still remains.

1.6.2 Gallium sulfide: GaS_x (GaS and Ga_2S_3)

In this section, the growth of gallium sulfide thin films in previous studies will be briefly summarized. Several reports described the synthesis of gallium sulfide by CVD. By using different precursors sources, authors succeeded to grow gallium monosulfide GaS [139, 140, 141] or even Gallium (III) sulfide Ga_2S_3 [142, 143, 144, 145] on different substrates types. CVD is a reliable growth technique to grow gallium sulfide thin films with both stoichiometry, either GaS or Ga_2S_3. The required high thermal budget (growth temperature ranging from 350 °C to 800 °C) limits the integration of Gallium sulfide thin films at the back-end-of-line (BEOL) technologies. In this case, ALD can be considered the technique of choice for the growth of gallium sulfide thin films since the growth temperatures are below 300 °C.

The first ALD report on the growth of Gallium sulfides phases was reported by Meng et al.[65] who described the growth of gallium (III) sulfide Ga_2S_3 using hexakis(dimethylamido) digallium $Ga_2(NMe_2)_6$ and H_2S as precursors in the growth temperature range between 125 °C and 225 °C. The obtained films were uniform and amorphous.[65]

The growth mechanism and surface chemical reactions on the results obtained by Meng et al. were examined by Schneider et al. through a computational study of this process by Density Functional Theory (DFT) studies to understand and analyze the reaction pathways favored during the injection of the different precursors.[146] Using the same precursors, Schneider et al. [147] reported the growth of gallium monosulfide GaS layer with the insertion of oxygen contamination within the film or the formation of gallium oxysulfide film in a temperature range of 125 °C -200 °C. The obtained films were amorphous even after a post-annealing strategy, at temperatures ranging from 400 ° C to 600 ° C.

The above-mentioned reports on ALD growth of gallium sulfides phases showed promising results in term of layer uniformity , conformity and even stoichiometry. However, they suffered from chemical contamination (high oxygen and carbon content) resulting in a poor crystalline structure.[65, 146, 147, 125, 70, 148] Further investigations are required in the future in order to improve the quality of these layers aiming to integrate thin films of gallium sulfide in varied fields of applications.

1.7 Synthesis process and aim of work

This dissertation deals with a novel approach to generate ultra-thin textured LMDs films on a SiO_2 thermal substrate using a two-step approach involving ALD/MLD growth of an organic-inorganic hybrid thin film at low temperature and a thermal annealing at mild temperature, to induce crystallization of the thin film toward the target material.

Since ALD growth of ultra-thin films faces difficulties, the control of the nucleation and the 2D growth of one or a few crystalline and textured MX_2 layers on non-epitaxial substrate is definitely not straightforward. As the basal planes of the crystalline MX_2 layer are chemically inert, -SH moieties are present at structural defects and edges where further chemical reactions with the metal precursor molecules will occur.[105, 112] This leads to discontinuous poorly textured, and crystalline thin films. If possible and relevant, this effect can be mitigated by depositing the 2D material on a well-chosen crystalline and oriented substrate surface that promotes the growth. The suggested approach in this thesis work aims to avoid the co-occurrence of growth and crystallization, observed during the ALD process. The use of an organic precursor (co-reactant) during the ALD process performed at a relatively low temperature, permits to generate an amorphous inorganic-organic hybrid thin film. Thus, a complete dissociation of growth and crystallization occurs.

The process was optimized in a dedicated reactor setup in LMGP, that can be installed in different synchrotron radiation beamlines allowing *in situ* monitoring of X-ray Fluorescence (XRF), X-ray Diffraction (XRD) and X-ray Absorption Fine Structure (XAFS) studies during alternating ALD/MLD pulses and annealing steps.

The major part of this work is based on applying the novel approach to obtain TiS_2 thin films on the non-epitaxial substrate thermal SiO_2. The major and advanced results obtained on TiS_2, motivates the synthesize of other materials that belong to the family of

metal chalcogenides, such as Sn_xS and Ga_xS. Intresting results were achieved from hexakis(dimethylamido) digallium, $Ga_2(NMe_2)_6$, and EDT precursors. Concerning the synthesis of SnS_2 with EDT, the growth of Tin-thiolate was not successful. Nevertheless, mechanistic studies were performed on a high surface area substrate that contributed to explain the result.

Chapter 2

Thermal ALD/MLD reactor, *in situ* synchrotron X-ray and *ex situ* characterization techniques, for the development of the synthesis of lamellar metal chalcogenides thin films

2.1 Introduction

In this chapter, we describe the growth process of 2D sulfides inside our dedicated homemade ALD reactor, called hereafter "MOON". The MOON reactor was previously used as an ALD reactor to grow oxide materials such as Zinc Oxide (ZnO) and Titanium Dioxide (TiO_2).[149, 150, 151, 152] The growth of 2D sulfides has never been performed in this type of reactor, which makes adapting an oxide reactor for their growth a major challenge. What distinguishes MOON reactor from other reactors is its capability to be moved and installed in different synchrotron centers to perform ALD process monitored by X-ray synchrotron methods. This couldn't be allowed if the reactor was not designed and built for monitoring *in situ* ALD experiment during growth.

The importance of designing a reactor that could perform such kind of experiments is actually related to the need to collect fundamental information concerning the growth be-

havior of ultra-thin films during ALD. ALD process has been known as the growth method that could deposit thin, homogeneous and conformal films for micro- and nanoelectronics at low temperatures. However, investigating the early stages of growth is crucial, since the latter can impact the quality of the obtained films especially if we aim to grow ultra-thin films. For this reason, *in situ* X-ray studies performed in synchrotron radiation centers allow the understanding of growth mechanisms. With the MOON reactor, the growth of materials at the initial stages can be studied *in situ* by various optical and X-ray methods during ALD. The MOON reactor, developed at the LMGP laboratory in cooperation with other laboratories, can be moved to different synchrotron centers to perform ALD process monitored by X-ray synchrotron methods. In the same way, some optical methods can be applied both at the LMGP laboratory and at the synchrotron centers.

In this context, the reactor allowed to study the atomistic mechanisms taking place during ZnO ALD growth on a-SiO_2 (amorphous) and c-Al_2O_3 (crystalline) substrates.[153, 154, 155] In addition it allowed a full comprehension of the early stages of the growth of ZnO ultrathin layers (1 nm) ALD on p- and n-doped $In_{0.57}Ga_{0.43}As$ substrates.[149, 150, 151] A new strategy will be presented in this chapter, the use of MOON reactor to perform the two-step process study: (1) the ALD/MLD growth by alternate additions of metalic precursor and EDT pulses to the wafer and (2) the subsequent thermal annealing of the ALD/MLD grown film. For this reason, this chapter will focus on developing the process in order to obtain reproducible ALD/MLD cycles allowing the optimization of TiS_2, SnS_2 and Ga_xS growth conditions. Furthermore, the main *in situ* and *ex situ* characterization techniques will be described herein.

2.2 Synchrotron *in situ* X-ray studies

Various *in situ* techniques can be monitored to ALD systems in order to understand reaction mechanism during deposition, for instance: mass spectrometry, quartz microbalance, infrared spectrometry, surface photo absorption, incremental dielectric reflection, surface photo interference, reflectance difference spectroscopy, optical emission spectrometry, and spectroscopic ellipsometry. [156] These methods provide information about reaction mechanisms and surface chemistry, the optical parameters of the material, the thickness of the deposited film, and the amount of deposited material. Their use in the laboratory is limited

by the design of the ALD reactor. In fact they can only be used if the ALD reactor is specially constructed and equipped with specific windows that allow the performance of *in situ* experiments.

Synchrotron techniques allow monitoring changes at the nanometer scale due to high X-ray beam brilliance. For this reason, a series of *in situ* experiments were performed during this PhD to fully understand the process. Since the wavelength of X-ray is comparable to the size of atoms, the use of X-ray techniques seems to be very suitable for probing the structural arrangement of atoms and molecules in a wide range of materials during the process.

Synchrotron-based techniques, commonly used to monitor *in situ* ALD process, can be divided into different categories according to their capabilities to probe structural or chemical properties at different scales such as X-ray Reflectivity (XRR), Grazing Incidence Small Angle Scattering (GISAXS), X-ray Diffraction (XRD), X-ray fluorescence (XRF) and X-ray spectroscopy. Several groups have already designed different ALD reactors for *in situ* experiment using synchrotron-based techniques.[157, 158, 159, 160, 161, 162, 163, 164, 165, 166, 167, 158, 168, 169, 170, 171, 172, 173]

In this work, the used *in situ* synchrotron techniques are XRR, XRF, and XANES and Extended X-Ray Absorption Fine Structure (EXAFS). XRR allows monitoring of the thickness and density of the deposited material as well as the surface and interface roughnesses during ALD/MLD growth and after annealing. Elemental analysis were provided by *in situ* XRF, allowing to monitor from the first ALD/MLD cycle the amount of deposited material. X-Ray Absorption Fine Structure (XANES and EXAFS) spectroscopy, owing to its atomic and electronic shell selectivity, gives information about the valence and local atomic environment of the absorbing atoms as well as on the empty state density above the Fermi level.

The whole ALD/MLD process on silica wafers and thermal annealing, was performed inside our custom-built portable reactor (MOON reactor) which mounts onto the 6-axis tower of the NewportTM diffractometer (Diffractometer table (20) in Figure 2.1) installed at the beamline SIRIUS [174] of SOLEIL synchrotron facility (Figure 2.2). The set-up allows using a complementary suite of *in situ* synchrotron X-ray techniques (Reflectivity, Grazing-Incidence Fluorescence, Diffraction, and Absorption).[153] The SIRIUS beamline [174] has unique characteristics that allows it to work in the tender X-ray range [1.2-5] keV, such as a variable-polarization HU36 undulator source and two monochromators. The first, a prototype multilayer grating monochromator (MGM), provides very high flux (up to $2x10^{13}$ ph/s in the tender X-ray) and optimal resolution for spectroscopy while the second, a direct Drive

double Crystal Monochromator (DCM), allows both step and continuous energy scanning modes with high energy resolution.

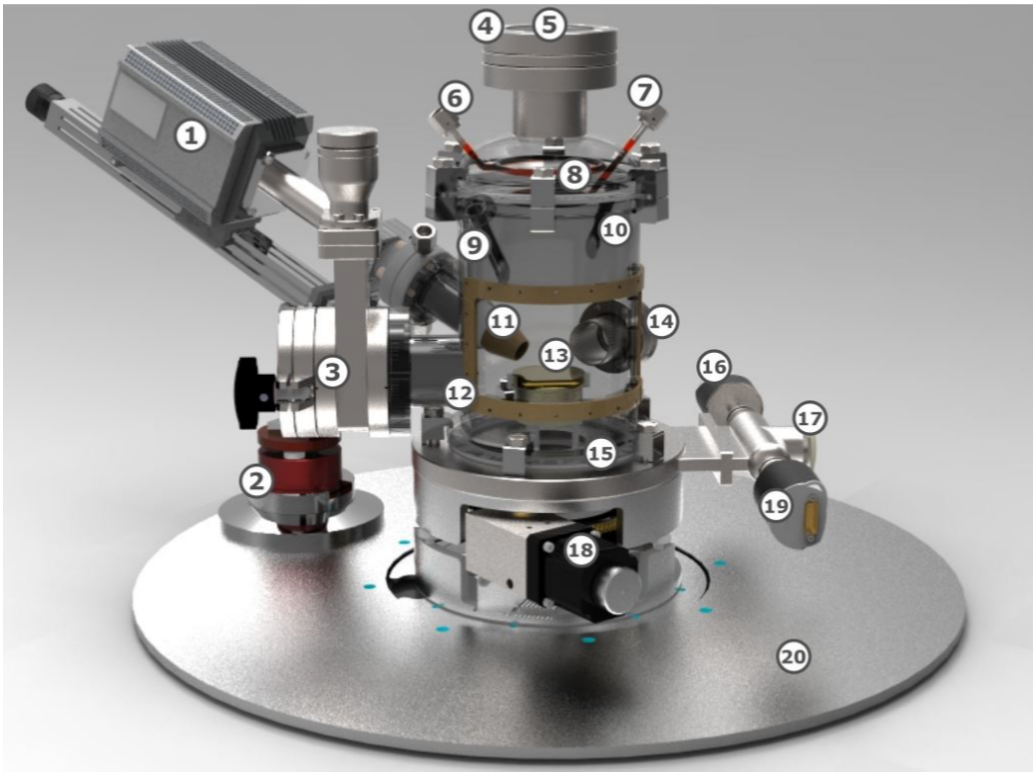

Figure 2.1: Schematic representation of the ALD reactor built for *in situ* synchrotron X-ray studies: 1 - fluorescence detector; 2 - air pad; 3 - load lock; 4- 63 mm port for inspection (stress measurements,..); 5 - quartz window; 6,7 - precursor injection ports; 8 - shower head (removed during the synthesis of Ga_xS); 9,10 - inspection ports for source and detector of the *in situ* ellipsometry; 11 - fluorescence detector nose; 12 - movable Be window; 13 - substrate holder; 14 - X-ray Be entrance window; 15 - counter rotating flange; 16,19- gauges; 17 - gas exhaust; 18 - motor of the counter-rotating flange; 20 - diffractometer table. (extracted from [175])

A four-element Silicon Drift Detector (SDD) ((1) in Figure 2.1) manufactured by Bruker (XFlash QUAD 5040) was used to measure the XRF and a 2D hybrid pixel detector (PILATUS 1M by Dectris) was used to measure the XRR (and, incidentally, the X-ray scattering). The SDD was mounted on a dedicated flange of the reactor which allows the optimization of the sample-detector distance; the detector nose (located into the reactor chamber, see (11) in Figure 2.1) was equipped with a collimator directed at the center of the sample surface and a 20 micron-thick Kapton entrance window ((11) in Figure 2.1) which separates the SDD from the chemicals in the reactor. The four-element SDD was coupled to a four-channel xMAP

DXP electronics provided by XIA. For *in situ* reflected beam intensity measurement, the X-ray beam energy was equal to 5 keV in the case of TiS_2 growth (10.5 keV in the case of Ga_xS) and the incident angle α_i was equal to 1.2°, that is above the critical angle α_c for Si (α_c=0.35° at 5 keV). For monitoring the Ti and S XRF yields, the incoming X-ray beam energy was equal to 5 keV, i.e. above the Ti and S K-edges (4966 and 2472 eV respectively). To monitor the Ga and S XRF yields, the incoming X-ray beam energy was equal to 10.5 keV, i.e. above the Ga and S K-edges (10367 and 2472 eV respectively).

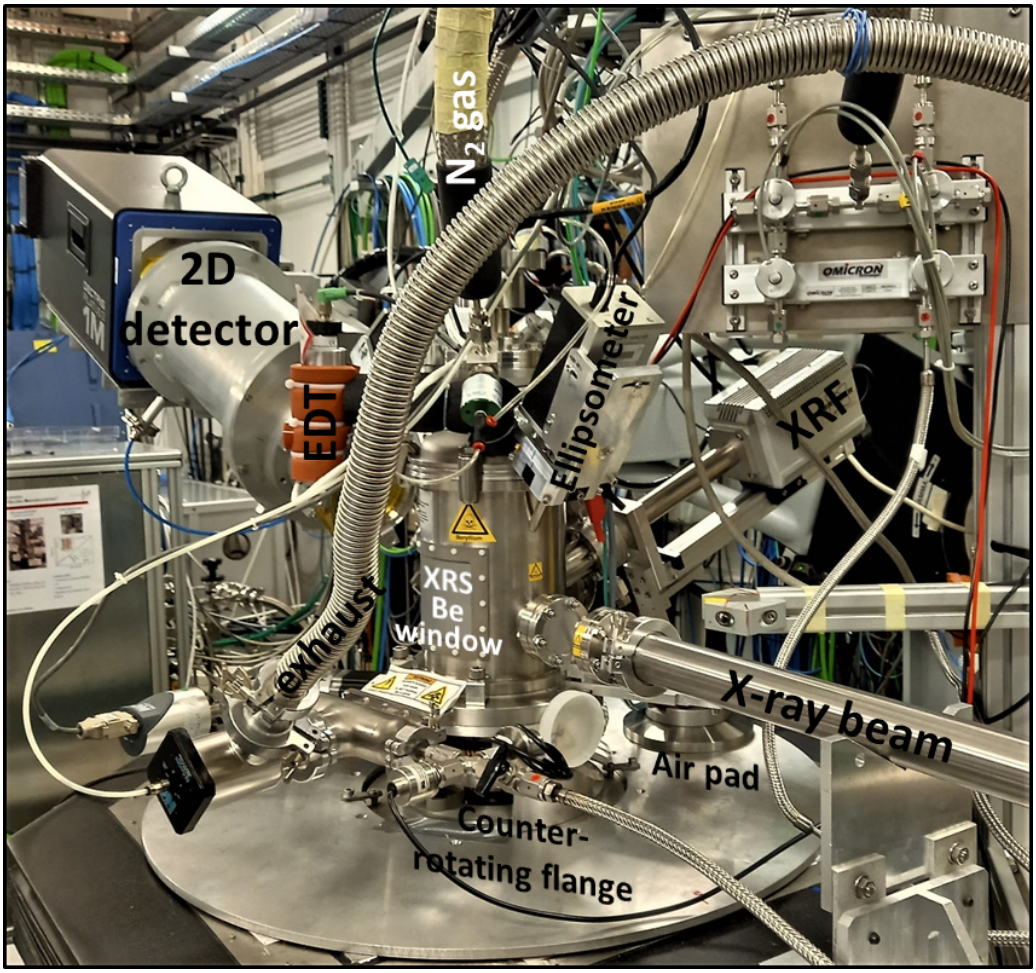

Figure 2.2: ALD/MLD reactor built for surface sensitive (grazing incidence) *in situ* synchrotron X-ray studies, installed on the tower of the diffractometer of SIRIUS beamline (SOLEIL synchrotron). As shown, the reactor has X-ray transparent windows for X-ray scattering (cylindrical 400 μm thick beryllium window) and X-ray spectroscopy (XRF,XAFS) (20 μm thick Kapton foil) with the sample in horizontal scattering geometry. The chamber maintains several ports for ALD gas injection, fluorescence and optical measurements (ellipsometry).

In situ X-ray Absorption Fine Structure Spectroscopy at the Ti and S K-edges (or Ga k edge) was performed in fluorescence detection mode using the four-element SDD described above. The incident angle was 1.2°. All XANES experiments were performed using the DCM monochromator equipped with Si(111) crystals, and by changing the beamline HU36 undulator gap simultaneously with the monochromator Bragg angle during the energy scan. A continuous energy scanning mode was used, synchronizing the speed of monochromator and undulator movements; this minimizes the acquisition dead time and takes spectra in a faster way. For Ti and Ga K-edge XANES, a couple of Pt-coated mirrors were used in order to reject high-order harmonics and focus the beam in vertical, while C-coated mirrors were used for S K-edge XANES. Grazing incidence geometry was used for all scans to limit the X-ray penetration in the substrate.

2.3 ALD/MLD process using MOON reactor

In the previous section, the installation of the MOON reactor on the SIRIUS beamline diffractometer was described, in addition, the used *in situ* X-ray techniques and their experimental details were presented. This section presents the operation of the MOON reactor and the growth parameters used during this thesis. Furthermore, insights about the understanding of the process has been achieved by the obtained results provided from *in situ* experiments performed during a campaign of synchrotron experiment in SIRIUS beamline.

Some measurements could be performed in the laboratory, due to the presence of two flanges (CF10) equipped with quartz windows ((9,10) in Figure 2.1). The two flanges are tilted by an angle of 35° with respect to the axis of revolution of the reaction chamber, and to which a laser and a detector can be connected in order to perform our spectroscopic ellipsometry measurements.

In situ ellipsometry is a versatile optical measurement technique for characterizing thin films. This technique is based on the change in the polarization of light throughout the deposited film. The polarization change is analyzed by optical models describing the grown material. In addition, *in situ* ellipsometry allows monitoring film thickness and optical material coefficients during the deposition. Usually most of ALD systems are supplied with ellipsometry viewports (at 70° angle of incidence).[176]

Our reactor design, permits to monitor our dedicated ALD/MLD reactor by *in situ* multi-

wavelength ellipsometry (MWE), using a 4-wavelengths (465 nm, 525 nm, 580 nm, and 635 nm) Film Sense FS-1™ Banded Wavelength Ellipsometer and FS-1 software for thickness calculation.

Concerning the gas flow process a scheme is presented in Figure 2.3. It shows gas lines and their connections to the reactor chamber for the deposition, or to bypass lines connected to the exhaust pump through a furnace (or scrubber) heated to temperature above the metal precursor decomposition (650 °C). The scrubber placed at the outlet of the MOON reactor aims to pyrolyse the unconsumed product (and any other molecules). If the scrubber is heated under an oxidising atmosphere (where a mixture of oxygen and nitrogen is continuously connected to the scrubber via a bypass line), the EDT molecules will be completely pyrolysed to form a mixture of SO_3, CO_2 and H_2O. These compounds are not very toxic but are corrosive (SO_3 + H_2O -> H_2SO_4).[177] In this thesis work, to avoid a backflow into the reactor (non-return valve), the oxygen supply is cut off in the scrubber. Thus, the EDT molecules are decomposed into elemental sulphur, H_2S and ethylene. In addition, we have placed impregnated charcoal (or activated charcoal) at the pump outlet, which acts as a catalyst (transforms toxic gases into less toxic pollutants by catalysing a redox reaction).

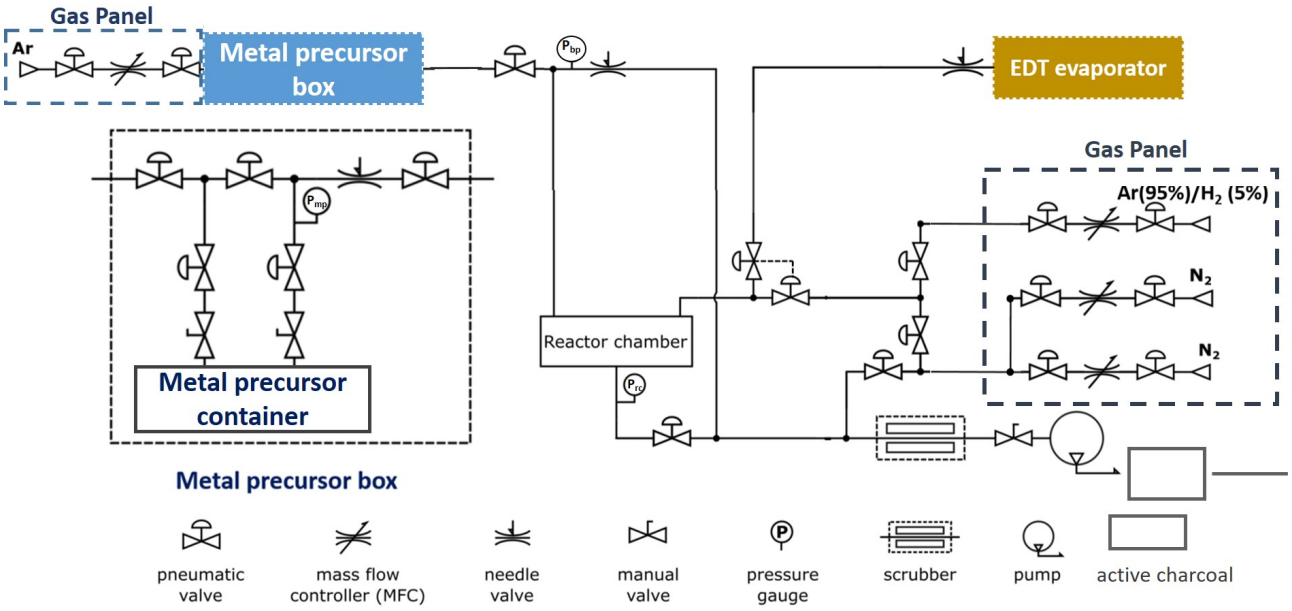

Figure 2.3: Synoptic of the gas flows. All gas flows are controlled by the mass flow controllers. Opening and closing of pneumatic valves are carried out on the control panel (adapted from [175]).

Concerning the reactor chamber, both metal precursor and EDT were reaching the substrate surface heated up to the ALD/MLD growth temperature, via the two injection ports ((6,7) in Figure 2.1). These ports are connected to a shower head ((8) in Figure 2.1) that ensures a uniform distribution of reactants in the reactor chamber above the substrate. However, the design of the reactor was changed during the synthesis of Ga_xS where the shower head was removed aiming to avoid the condensation of the gallium precursor. The gas flow through the lines was controlled by pneumatic valves and by mass flow controllers (MFCs), where the pressure inside the gas lines and the reactor chamber is controlled by pressure gauges. With some exceptions ALD/MLD experiments were performed on a 100 nm SiO_2/Si substrate. Prior to deposition, the substrate surface was pre-treated at 200 °C in a 100 sccm of N_2 flow for 30 minutes.

2.3.1 Titanium Disulfide TiS_2

2.3.1.1 Choice of precursors

For the growth of TiS_2, we used the two precursors Tetrakis(dimethylamido)titanium (TDMAT) (CAS number: 3275-24-9, 99.999% purity) and 1,2 ethandithiol (EDT) (CAS number: 540-63-6, assay greater than 99%) purchased from $Merck^{TM}$. In the following, we will justify the reason behind choosing these precursors.

2.3.1.1.1 TDMAT

Previously, the precursor Titanium tetrachloride ($TiCl_4$) has been widely used as a common source of Ti in ALD. However, several drawbacks caused by the generation of a harmfulness corrosive reaction byproduct (HCl) have limited its use.[123] Tetrakis(dimethylamino)titanium, or TDMAT, have been selected as a titanium precursor because it allows to work at a lower temperature than other precursors.[178] TDMAT is a chemical compound with the formula $Ti[N(CH_3)_2]_4$. The prefix tetrakis indicates the presence of four identical ligands, in this case dimethylamine -$N(CH_3)_2$. TDMAT is a volatile and appears as a yellow liquid at room temperature. In addition TDMAT have a low vapor pressure ($8.9*10^{-3}$ mbar at 25 °C) that requires a carrier gas to transport the TDMAT to the reactor chamber.[179] The molecule has a tetrahedral geometry and is diamagnetic (see Figure 2.4).

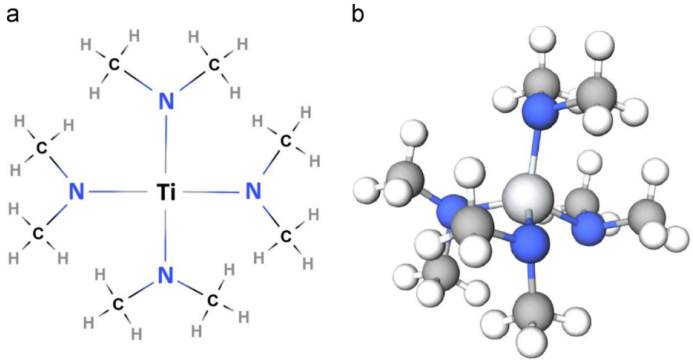

Figure 2.4: a) Chemical structure and (b) molecular formula of TDMAT.[180]

2.3.1.1.2 EDT

In order to use TDMAT for the growth of titanium disulfide, it is necessary to choose a volatile molecule that can sequentially substitute dimethylamino ligands to form Ti-S bonds. Usually, hydrogen sulfide (H_2S) is systematically used as a sulfur precursor for ALD deposition of metal sulfides. In particular, it has proven its ability to react sequentially with metal precursors. Metal ligands are substituted to form surface M-SH bonds that can in turn react with the metal precursor in the next pulse. [181]

In this work, the molecular precursor 1,2-ethanedithiol ($HSCH_2CH_2SH$) (EDT) was used to replace H_2S because it is less dangerous and can be easily manipulated at a lab scale.[120] EDT is an organosulfur molecule (see Figure 2.5) that allow the substitution of amino ligands by SH groups as it has been used in previous work for the deposition of MoS_2, WS_2 and VS_2 by ALD.[120, 182, 183]. EDT is a colorless liquid organosulfur compound, with a low vapor pressure (20 mbar at 20 °C), a metling point of -41.2 °C and a boiling point of 144 °C. [181]

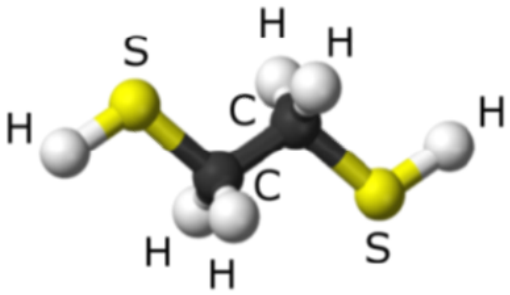

Figure 2.5: Chemical structure of the organosulfur compound: 1,2 ethandithiol (EDT).

The EDT molecule with two thiol groups (R-SH) located on the two opposite sides of the carbon chain allows sequential binding to Ti center via reaction with Ti-amido bond leading to the formation of Ti thiolate.

2.3.1.2 Growth strategy

The sample holder temperature was set at 50 °C during the ALD/MLD growth. The pre-treated substrate was sequentially exposed to TDMAT and EDT. TDMAT was carried by a 50 sccm flow of Ar gas, due to its low vapor pressure. TDMAT/Ar container box was maintained at room temperature (25 °C). The mixture of Ar and metal precursor inside the metal container is shown in the synoptic in Figure A.3. EDT evaporator was heated at 40 °C to maintain an enough pressure value (P_{EDT} = 12 mbar at the beginning of each EDT injection). The number of EDT manual valve turns was equal to 12 (additional details are presented in Figure A.2). Both precursors were sequentially injected into a closed reactor chamber. Between each precursor pulse, the reactor chamber was purged out with a 100 sccm flow of N_2 to remove reaction by-products. The ALD/MLD growth performed with various number of cycles, were followed by thermal annealing under 100 sccm flow of H_2(5%)/Ar(95%) (H_2 being known to facilitate sulfur extrusion from sulfur-rich TiS_{2+x} phases)[184]. With some exceptions, the rate of temperature increase or decrease was equal to 10 °C/min.

Figure 2.6 shows the pressure variations of precursors, reactor chamber, and bypass line measured during the ALD/MLD process. As we can see in Figure 2.6-a one ALD/MLD is composed of 5 steps. Step I is based on flowing TDMAT for 10s into the bypass line in order to stabilize the flow of the metal precursor mixed with Ar, before injection into the reactor chamber. During step II, the mixture TDMAT+Ar is injected for 60s into the reactor chamber which is closed. The injection into the reactor chamber can be clearly noticed by the pressure increases in both the reactor chamber (P_{rc} in Figure 2.3) and metal precursor box (P_{mp} in Figure 2.3) as pressures curves shows that $P_{TDMAT} > P_{reactor}$ (see Blue and Black curve in Figure 2.6-a). Step III corresponds to the purging step of the reactor chamber for 45s, with a 100 sccm flow of N_2 in order to remove reaction by-products and non consumed TDMAT molecules, whereas the reactor pressure decreases (see Black curve in Figure 2.6-a). Step IV consist on injecting EDT into the closed reactor chamber for 30s, one can see the decrease of EDT pressure during its injection in the reactor (red line in Figure 2.6-a). The last

step, step V consists on purging for 45s the reaction by-products out of the reactor chamber with a 100 sccm flow of N_2. The pressure of TDMAT stabilizes at a constant value in step III, IV, and V (blue line in Figure 2.6-a). Importantly, the value of $P_{reactor}$ must stay greater than that of P_{bypass} in order to avoid any contamination of the reactor chamber, especially during the purging step (see black and gray lines in Figure 2.6-a). In step III and V, the decrease of the reactor pressure after 30s is due to the change of N_2 flow from 100 sccm to 25 sccm (see dashed blue horizontal line in Figure 2.6-a). All the mentioned steps allow to deposit one ALD/MLD cycle of the Ti-thiolate. Figure 2.6-b shows the reproducibility and repeatability of the process.

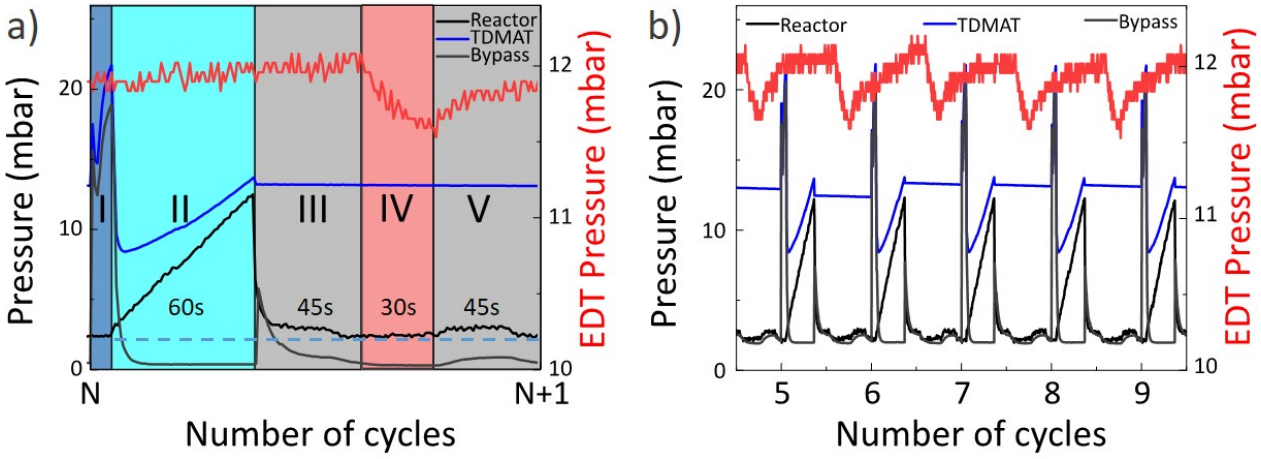

Figure 2.6: Pressures of TDMAT,EDT,reactor and bypass (see Figure 2.3) a) during one ALD/MLD cycle and b) process repeatability during several ALD/MLD cycles.

2.3.2 Tin Disulfide SnS_2

2.3.2.1 Choice of precursors

The used metal precursor for the growth of tin disulfide was the tetrakis-(dimethylamido)tin or $(C_2H_5)_2N_4Sn$ (hereafter TDMASn) (CAS number: 1066-77-9, 99.9% purity) purchased from $Merck^{TM}$. As the TDMAT precursor mentionned above, the TDMASn is liquid at room temperature and highly reactive to air, for this reason it should be kept in an Ar or N_2 atmosphere. The boiling point of TDMASn is 53-55 °C at 0.1 mbar and has a saturation vapor pressure is 0.01 mbar at 40 °C.[185, 186] For this reason, the TDMASn

container was maintained at a temperature of 40 °C during the process.

2.3.2.2 Growth strategy

The growth of tin disulfide (Sn-thiolate) consists on using the same strategy mentioned in the case of TiS_2 and on replacing the metal precursor by TDMASn. In this case, the temperature of the gas line connecting the metal container to the reactor chamber was maintained at 77 °C in order to avoid condensation of the TDMASn. In addition, The TDMASn was carried into the reactor chamber by a 50 sccm flow of Ar.

To grow the Sn thiolate thin film by ALD/MLD both TDMASn and EDT precursors were used. The process strategy is the same as the one described in Figure 2.6. As a starting point, the growth conditions used in the growth of Ti-thiolate were applied to grow Tin-thiolate. Several substrates were tested, first the amorphous 100nm SiO_2/Si substrate, then due to unsuccessful growth on SiO_2 substrate, substrate surfaces terminating by -SH groups were taken into account. The first substrate surfaces terminating by -SH groups were obtained by sulfurizing a 50 nm thick ZnO thin film deposited on 100nm SiO_2/Si substrate to obtain ZnS. The ZnO film was heated at 450 °C for 30' with a continuous flow of EDT mixed inside the reactor with a 100 sccm flow of Ar. Also, substrate surface terminated by -SH groups were obtained by the functionalization of the 100 nm SiO_2/Si substrate surface with a organic chemical molecule the (3-Mercaptopropyl)trimethoxysilane (or MPTS) aiming to replace the hydroxyl groups (-OH) with -SH terminating groups.

2.3.3 Gallium sulfide GaS_x

2.3.3.1 Choice of precursors

The metallic precursor, used for the growth of gallium sulfide was the bis(μ-dimethylamino)tetrakis(dimethylamino)digallium or $C_{12}H_{36}Ga_2N_6$ (TDMAG) (CAS number: 57731-40-5, 98% purity) purchased from STREM chemicals. TDMAG is a white solid at room temperature, with a sublimation temperature equal to 72 °C. Therefore, a heating step of the metal precursor containing the TDMAG is important in order to sublimate the solid and ensure its transport to the reactor chamber. In addition, this precursor was used to grow gallium sulfide thin films by ALD so we have insights concerning this precursor.[147, 70] Unlike, TDMAT and TDMASn, the TDMAG precursor has a different molecular structure

(see Figure 2.7). We can see the presence of dimethyl-amide bridges within the structure.

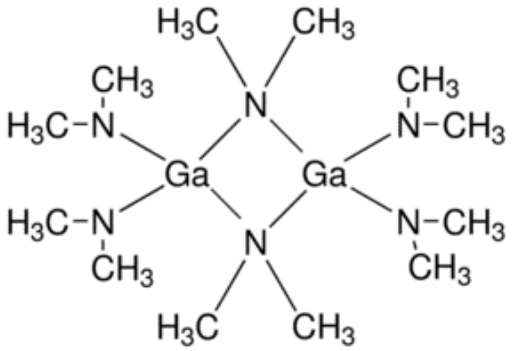

Figure 2.7: Chemical structure of the bis(μ-dimethylamino)tetrakis(dimethylamino)digallium precursor.[187]

2.3.3.2 Growth strategy

The deposition of Gallium sulfide by the ALD/MLD process relied on using TDMAG and EDT. Since TDMAG is a solid precursor at room temperature, a heating step for the TDMAG metal container and the lines connecting the metal container to the reactor chamber must be taken into account to prevent any condensation during the deposition. Therefore, we decided to heat our TDMAG container and gas lines at 90 °C, since it is mandatory to heat all the lines from the TDMAG box (see Figure A.3 in appendix A) to the reactor at a temperature higher than the sublimation temperature of the TDMAG precursor (72 °C).

Several tests were taken into account to actually reach this temperature within this box.

In particular, we added heating wires along the metal container and gas lines (pipes). In addition, thermal insulation were added around the pipes to ensure a faster and homogeneous heating. To check and verify the temperatures, thermocouples were placed on different spots between the metal container box and the reactor chamber to confirm the efficiency of the heating procedure. Therefore, we succeeded in reaching a continuous heating between the TDMAG box and the reactor chamber.

Now after finding a fixed solution that allows the maintaince of a continuous heating along the lines connecting the TDMAG container and the reactor chamber, the difficulty relies on finding an efficient way that permits to enter the TDMAG molecules into the reactor chamber during the gallium pulse. Like Titanium and Tin, Gallium precursor was carried with a continuous flow of inert gas (Ar). By using a continuous flow of Ar to transport the

heated TDMAG molecules to the reactor chamber, an condensation issue can occurs. The heated TDMAG can condense before reaching the reactor chamber, due to cooling effect generated from the continuous flow of Ar. Therefore, we decided to add an additional step before pulsing TDMAG into the reactor chamber. The additional step consists on increasing the pressure inside the TDMAG container to have enough heated molecules by flowing 25 sccm flux of argon followed by a stabilization step aiming to ensure a pressure and temperature stabilization inside the TDMAG container. However, the same flux of Ar was used during the TDMAG pulse into the reactor chamber.

Pressure curves along the deposition shown in Figure 2.8 were considered to evaluate the growth procedure upon the injection and purge steps. The different curves correspond to the pressures of TDMAG, EDT and the reactor. The process along one ALD/MLD cycle is dived into 4 main steps. The step I is based on a double pulse of TDMAG precursor to ensure enough Gallium molecule are saturating the substrate surface. Each TDMAG pulse in step I is based on: Increasing of the TDMAG pressure inside the TDMAG container, then stabilizing it and finally pulsing TDMAG into the reactor chamber. However, the repeatability of the the double pulse can be observed by the reproducibility of TDMAG pressure curves in step I (see for instance blue curves in Figure 2.8). In addition, the drop of TDMAG pressure upon the injection in each pulse (see blue curve in step I) was accompanied by an increase of the pressure inside the reactor (see gray curve in Figure 2.8).

The pressure curve of the reactor (Gray line) (a factor of 10 has been applied to it on this graph) also shows us the two injections of the TDMAG and the two plateaus that reveals that the stabilization after injection is done in a completely closed reactor. The purge (steps II and IV) also plays its full role as we can see that the reactor pressure drops to its value before injection, which is also expected. Finally, the pressure curve of the EDT (red line) also indicates that the injection of the precursor is carried out correctly in step III as observed by a drop of the pressure during the injection. Therefore, in our recipe each ALD/MLD cycle consists on: a) an injection of TDMAG with double pulse (in each pulse the TDMAG injection duration was equal to 3s), b) a purge for 90s, c) an injection of EDT for 30s or 15s (the difference is mentionned in Chapter 5), and d) a purge for 90s.

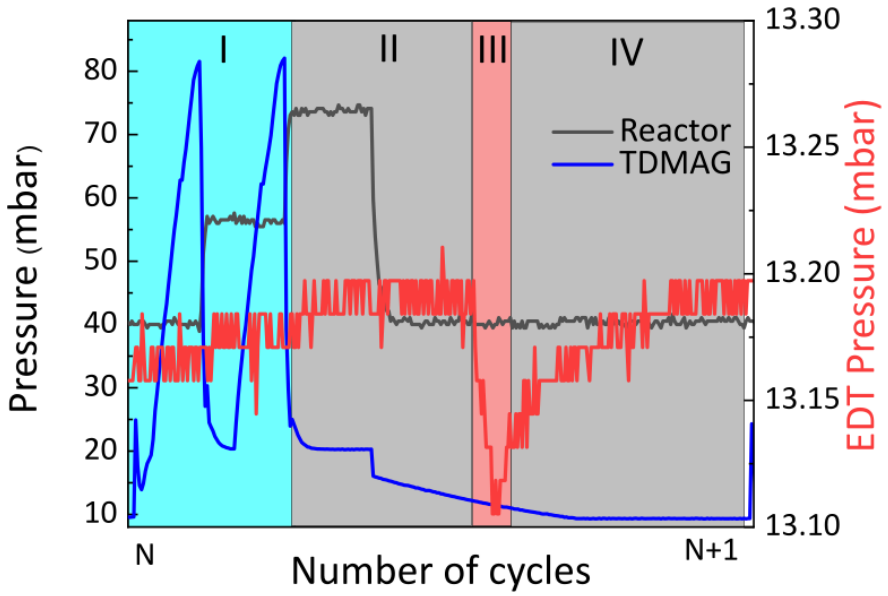

Figure 2.8: Pressure curves variation during one ALD/MLD cycle, for TDMAG (Blue curve), EDT (red curve), and reactor chamber (Gray curve applied with a scale factor multiplied by 10).

The reaction between TDMAG and EDT permits to deposit gallium sulfide thin films on various substrate temperatures (T_{sub}= [150-300] °C). Growth takes place on various substrates type such as the amorphous 100 nm SiO_2/Si(100) substrate, Si(111) etched by hydrofluoric acid (HF) to get rid of the native oxide. The use of the Si(111) substrate was taken into account to evaluate the effect of the oxide film present at the substrate surface on the deposited films.

2.4 *Ex situ* characterization

2.4.1 Raman spectroscopy

Raman spectroscopy belongs to the category of vibrational spectroscopy. Using a light source on the sample surface, a molecular vibration can be excited by the laser source that permits the analysis of a sample chemically. The principle of Raman scattering is based on inelastic scattering of a monochromatic light. For a better understanding it is important to know, that when photons (light) "strike" matter, most of the scattered light remains un-

changed in its wavelength (elastic scattering). However, also inelastic scattering processes can occur, which then lead to the emission of light with a different wavelength. This wavelength change is called: the Raman effect.

The monochromatic light could be emitted from a laser in the visible (400-700 nm), near infrared (700-1400 nm) or ultraviolet (190-400 nm) ranges. This technique permits to detect the vibrational and rotational mode in the materials. As a result a defined profile called Raman spectra is obtained in which the molecular units can be identified for any crystallographic structure. Each Raman spectra is a photon intensity as a function of energy difference between incident and emitted photons during Raman scattering. The peak positions shows the specific vibrational mode of each molecular component involved in the material. Width and shifting of vibrationnal modes from their position can be informative in term of crystallinity quality, thickness and so on. At the end we obtain a Raman spectrum that shows us characteristic signals or "bands" for the material under investigation. [188]

Raman spectroscopy is a non-destructive characterization technique. The use of which is very advantageous for the characterization of thin films. During my thesis work, all post-grown samples were characterized by Raman Spectroscopy using a Renishaw In-Via spectrometer located at CEA-LETI in the SMCP platform, equipped with a Peltier cooled (CCD) detector and 1800 groove.mm^{-1} grating. Raman spectra were recorded in the backscattering geometry. The light was focused onto the sample surface by a 100 x (0.85 numerical aperture) short working objective. The resulting spot diameter was around 0.7 µm. A 532 nm laser diode was used as a light source with a typical laser power of 0.07 mW. The acquisition time of each spectrum was 30s and the number of accumulations was equal to 5. Raman spectra were analysed using the LabSpec 5 software. As described in Chapter 3 and Chapter 4, the Raman spectra obtained for TiS_2 thin films were normalized to the intensity of the A1g mode and fitted with Lorentzian function for A1g mode, and with a Gaussian-Lorentzian function (GL(30%)) for the Eg and Sh modes.

Figure 2.9: Renishaw In-Via spectrometer for Raman Spectroscopy measurements.

2.4.2 Angle Resolved Photoelectron Spectroscopy/Hard X-ray Photoelectron Spectroscopy: AR-XPS/HAXPES

X-ray photoelectron spectroscopy (XPS) is a subsurface sensitive technique, based on the photoelectric effect, which allows quantitatively the surface composition of a material to be determined. The main feature of this technique is that it allows the identification of chemical bonds between two elements. The technique can be used in line profiling of the elemental composition across the surface, it can also probe the analysed surface at greater depths depending on the monochromatic sources used.[189, 190, 191, 192]

XPS belongs to the family of photoemission spectroscopies in which electron population spectra are obtained by irradiating a material with a beam of X-ray. Figure 2.10 schematizes the photoemission effect. The principle of XPS relies on the detection and analysis of electrons, core or valence, emitted by the sample. The energy of the incident X-ray photon ($E_{incident}$) is of the same order of magnitude but higher than the ionization energy of the core electrons. The kinetic energy of the emitted photoelectrons is measured ($E_{kinetic}$), which makes it possible to obtain the spectrum. The binding energy ($E_{binding}$) can be therefore calculated using the following formula:

$$E_{binding} = E_{incident} - E_{kinetic} \tag{2.1}$$

The binding energy allows determining the type of element, oxidation state and chemical environment. [193]

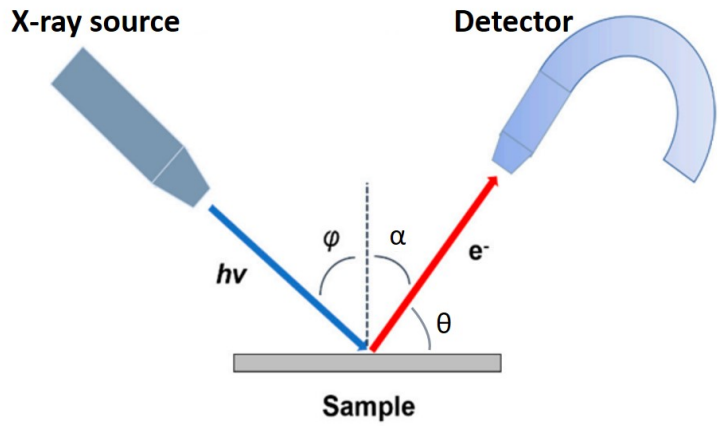

Figure 2.10: a) Schematic presentation of photoemission concept.[194]

Chemical composition and stoichiometry were examined by HAXPES and XPS using a PHI Quantes located at PFNC platform located at CEA-LETI (see Figure 2.11-a) with two different monochromatized sources, either Chromium (Cr) K_α (hν = 5414.7 eV) or Al K_α (hν=1486.6 eV). The analytical information depth using Cr K_α source is about three times deeper than with the Al K_α source (see Figure 2.11-b). For example, TiS_2 is known to be oxidised on the surface when exposed to the ambient atmosphere. In this case the large sampling depth in Cr sources opens opportunities to minimize the contribution of the upper oxidized surface of the sample, in the overall spectra. In addition, the use of Cr sources permits to have an access to supplemental core levels such as **Ti 1s** core level spectra. This leads to calculate the surface oxide depth due to the increase of the inelastic mean free path of electrons with increasing photon energy.

Samples were prepared using a metallic clamp to ensure electrical contact with the sample holder. Measurements using Cr source have been done at a fixed angle of θ=45° and for the Al one at different angles using Angle-Resolved XPS (or ARXPS) (θ=15°, 45°, and 85°), where θ is the angle between the surface and the analyzer. The thickness was calculated using the formula

$$d = 3\lambda sin\theta \tag{2.2}$$

where λ is the photoelectron mean free path using TPP2M equation.[195] Data treatment of

the measured spectra were analyzed using CasaXPS software. For spectral calibration, C 1s core peak from adventitious carbon was considered with binding energy at 284.8 eV.[136] A non-linear Shirley-type background was processed for peak fitting and the deconvolution of the peaks was obtained using the weighted least-squares calculation method of 30% Lorentzian and 70% Gaussian line shapes and Full Width at Half Maximum (FWHM) constraints.[196]

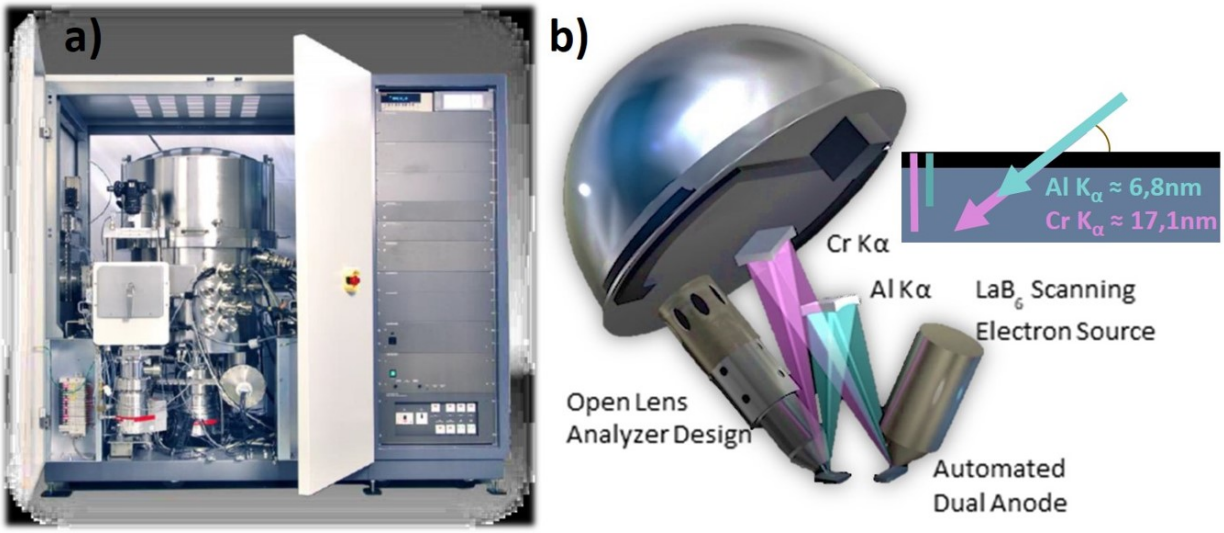

Figure 2.11: a) XPS Quantes, Physical Electronics equipment and b) Probing depth comparison for Ti2p core peaks, between XPS (Aluminium K_α, hν=1486.6 eV) and HAXPES (Chromium K_α, hν = 5414.7 eV).[197]

2.4.3 X-ray Reflectivity (XRR)

X-ray reflectivity (XRR) is a non-destructive physical characterization technique for thin-films and surface structures. It is used for determining thin film thicknesses between 1 and 1000 nm and it can also be used to determine the layer structure of a multilayer or single-layer film. In addition, XRR is also used to estimate density, surface roughness and interfacial roughness by the reflectivity law of Fresnel. [198] This technique allows analyzing both crystalline and amorphous materials. In this thesis, the XRR is employed to analyze the thickness of the obtain films.

The principle of XRR is based on impinging an X-ray beam on a sample surface with a small incident angle (θ_i). If the incident angle (θ_i) is lower than the critical angle (θ_c), the incident X-ray beam totally reflects while above the critical angle (θ_c), X-ray beam penetrates

into the sample and partially reflects at the interfaces (see Figure 2.12).

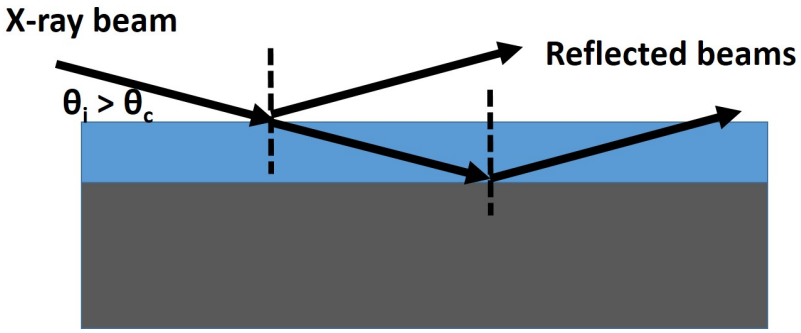

Figure 2.12: a) Schematic principle of X-ray reflectivity (XRR).

Therefore, the reflected X-ray intensity is measured as a function of the reflection angle varied from 0 to a few degrees. The analysis of the obtained XRR curves is achieved by curve simulation and fitting. To simulate an XRR we simulate our structure by considering the substrate (100nm SiO_2/Si), the thin film (TiS_2 or Ga_xS) and the oxide at the interfaces (the substrate/sulfide and the top layer coming from the hydrolysis in air). In addition, the thicknesses, densities and roughnesses are estimated by fitting the model to the experimental XRR curve.

On the other hand, a qualitative interpretation can also be made by a relative comparison of the XRR curves. The oscillation of the XRR curve indicates the thickness of the film, the shorter the period, the thicker the film. The density of the oscillation and the critical angle for total reflection also provide information on the density of the film through the amplitude of the oscillation. In the case of a multilayer structure, the contrast of the amplitude is related to the density contrast between the thin film and the substrate: the higher amplitude of the oscillations, the larger density contrast. In addition, XRR also allows the interfacial roughness to be considered: XRR curve decays faster with rougher film and the amplitude of the oscillation decreases with increasing interface roughness.[198]

During this thesis, the XRR measurement was conducted using an Empyrean diffractometer from Panalytical at PFNC or RIGAKU SmartLab at CMTC by Herve Roussel. The two equipments were equipped with the same type of Cu source (Cu Kα wavelength = 0.154184 nm). LEPTOS was used for fitting the XRR curves. In addition, during *in situ* synchrotron studies at SIRIUS beamline SOLEIL, the XRR curves were measured with an incoming X-ray energy of 5 KeV during the synthesis of TiS_2 and at 10.5 KeV during the

synthesis of Ga_xS.

2.4.4 Four-point resistivity Measurements

Four-point probe resistivity measurements were carried out at room temperature using the Lucas-Signatone Labs Pro4 and a Keithley 2400 on TiS_2/100 nm-SiO_2 thin films. The TiS_2 films were synthesized from 40 and 80 ALD/MLD cycles and annealed under Ar/H_2(5%) using different annealing strategies as discussed in Chapter 3 and Chapter 4. Five acquisitions were performed on different spots of the film surface and substrate to check the homogeneity and calculate an average of the resistivity. The mean resistivity was obtained by multiplying the sheet resistance value ($\Omega.sq^{-1}$) by the thickness of the deposited layer. The resistivity value of the bare 100 nm–SiO_2 on silicon was too high to be measured with the equipment.[199]

2.4.5 Spectroscopic Ellipsometry

Spectroscopic ellipsometry (SE) [200] measurements were performed using two Woollam ellipsometers (RC2 in the 210-2500 nm wavelength range and IR-VASE in the mid-infrared range). The complex refractive indexes of 15 and 30 nm thick TiS_2/100 nm-SiO_2 thin films obtained from 80 and 40 ALD/MLD cycles and annealed in Ar/H_2(5%) for 30 min, were derived from the ellipsometric measurement using a sum of 9 Gaussian oscillators. The complex refractive index was described as N=n+ik, where n and k are the real and imaginary part of N. The imaginary part is related to the absorption coefficient α by the formula α=4πk/λ, where λ is the wavelength. The bandgap of the samples were calculated using the Tauc-Plot [201] which can be represented by a function of $(\alpha h\nu)^n$ versus the photon energy (hν, where h is the Planck constant).

2.4.6 XANES and X-ray Linear Dichroism (XLD)

XANES at both the Ti and S K-edges were carried out after transferring the samples inside SIRIUS High Vacuum (HV) diffractometer by means of a glove box.[202] XANES spectra were recorded by scanning the incoming energy step-by-step and measuring the sample fluorescence with the four-element Silicon Drift Detector (SDD). The beamline optics setup was the same as described above for the *in situ* XANES at the Ti and S K-edges. For the

Ti K-edge X-ray Linear Dichroism (XLD) spectra, selection of the linear vertical polarization was obtained by changing the phase of the HU36 ondulator: this allows to change from linear vertical to linear horizontal polarization without changing the sample position and preserving the grazing incidence mode in all measurements.

2.4.7 Transmission Electron Microscopy (TEM)

Transmission electron microscopy (TEM) observations were carried out at SERMA technologies using 200 kV with a Tecnai Osiris TEM (Thermo Fisher Scientific) and equipped with a high brightness X-FEG gun and a Super-X Energy-Dispersive X-ray Spectroscopy (EDX) system comprising four detectors.

In addition, at LMGP, TEM observations were performed at 200 kV with a JEOL 2010 microscope (a resolution of 0.19 nm). Cross-sectioned samples were prepared by automated polishing, the latter using the MultiPrepTM system (Allied High Tech Products, Inc.). The final polishing was performed using a felt-covered disc impregnated with a silica solution until the appearance of the first extinction fringe among those of equal thickness. Ar-ion milling was then used to minimize the total thickness.

2.5 Conclusion

In this chapter, the experimental conditions and the equipment for synthesizing, characterizing by *in situ*, and *ex situ* thin films of metal sulfides were exhibited. The synthesis process was carried out inside the MOON reactor which can be used as a thermal ALD reactor and also as a furnace for post growth annealing in controlled atmosphere, i.e. where the two-step process can take place: the growth of hybrid thiolate film by ALD/MLD process, and the subsequent thermal annealing process to obtain the target material.

In the laboratory, the growth in the reactor was monitored by *in situ* ellipsometry. The deposited thin films were characterized by Raman spectroscopy and X-ray photoelectron spectroscopies. The geometric characteristics of the MOON reactor, especially the presence of dedicated windows and a flange which permits to insert an X-ray fluorescence detector, give our reactor the possibility to perform *in situ* measurements with X-ray at synchrotron centers, as well as in the laboratory by using optical methods such as *in situ* ellipsometry. Besides, the main feature of the MOON reactor relies on the presence of a counter-rotating

flange, which permits to maintain the reactor body while rotating the sample heater with the diffractometer table, around an axis perpendicular to the sample surface. This makes it possible to carry out surface X-ray diffraction and in-plane X-ray diffraction measurements at synchrotron centers.

The control of both temperature and pressure inside the EDT evaporator was controlled by the creation of a heating system to control the injected flow of EDT or its pressure. To pyrolyse the unconsumed product coming from EDT a scrubber was placed at the outlet of the MOON reactor. In addition, we have placed at the pump outlet impregnated charcoal (or activated charcoal) in order to transform the generated toxic gases into less toxic pollutants. As perspective, the replacement of the needle valve for EDT with an Mass Flow Controler (MFC) could lead to precise control of EDT flow in the future.

In order to upgrade the MOON reactor and to improve the quality of the deposited sulfide materials, we should install a vacuum chamber ("SAS" or entrance lock) at the load lock entrance of the main chamber. Indeed, we could prevent any contact with ambient conditions and avoid the hydrolysis of the as-deposited samples. Also, incrementing the reactor (beyond the present optical tool, *in situ* ellipsometry) with a residual gas analyzer (RGA) could be relevant in particular for the detection of by-product molecules at the reactor outlet; and thus allows to better understand the mechanisms of surface reactions occurring during growth and annealing.

Chapter 3

Transition Metal Dichalcogenide TiS_2 Prepared by Hybrid Atomic Layer Deposition/Molecular Layer Deposition: Atomic-Level Insights With *in situ* Synchrotron X-ray Studies And Molecular Surface Chemistry.

3.1 Introduction

In this chapter, we will apply the two-step approach to generate thin films of lamellar TiS_2. First, a molecular modeling study on high-surface area silica silica nano beads substrate will be performed to check the validity of reaction between TDMAT and EDT. Second, ALD/MLD process will be performed on silica-terminated silicon wafers (100 nm SiO_2 substrate) and monitored by *in situ* X-ray studies to evaluate the deposition of an amorphous hybrid organic-inorganic Ti-thiolate material. The as-deposied Ti-thiolate will be annealed after at a 450 °C under Ar/H_2 for 30 mins where the obtained films are characterized by various characterization tools to evaluate the crystallinity and the stoichiometry. Finally, the obtained layers were evaluated by electrical characterization methods. The presented re-

sults in this chapter were published in Chemistry of Materials journal [203]. In addition, the results presented in Section 3.2 were written and analyzed by Elsje Alessandra Quadrelli, Medet Zuhukush, and Clement Camp in the framework of collaborative work.

3.2 Molecular study of ALD/MLD process on silica beads substrate

Chemical experimental modeling on high surface area silica beads is explored to identify the appropriateness of the chosen precursors to lead to molecularly-precise ALD/MLD cycles. Selected growth steps of the proposed ALD/MLD process (see schematic overview in Figure 3.1) were carried out on silica nanobeads as a substrate (loose powder, 200 m^2/g), following an experimental molecular modeling strategy outlined elsewhere. [120]

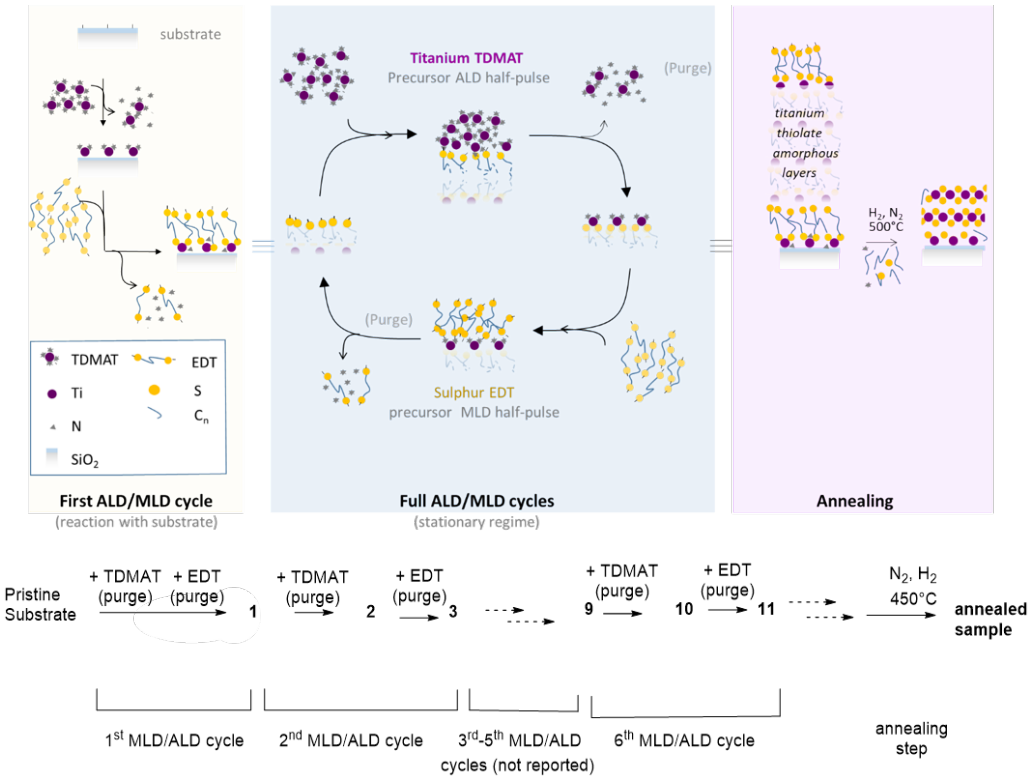

Figure 3.1: Schematic overview of the ALD/MLD step (blue background) and annealing step (pink background) of the overall process to TiS_2 reported here and numbering scheme adopted for the silica-supported solids of the modeling studies.

3.2.1 Chemical reactions between the two molecular precursors in absence of substrate

The exposure of TDMAT to EDT leads to the immediate formation of an orange precipitate in pentane, while each molecule separately is soluble in pentane at the given concentrations with no formation of solid. The formation of the orange precipitate shows the existence of a thermodynamically favorable and kinetically facile pathway reaction between the two precursors. The analysis of the orange precipitate by solid-state ^{13}C NMR (see Figure B.1 in Appendix B) displayed resonances compatible with the presence of organic moieties originating from EDT residues. The solid displays a weak Electron Paramagnetic Resonance (EPR) signal at g=1.98 (see Figure B.2 in Appendix B), assigned to titanium(III) centers.[204]

3.2.2 Successive reactions at the gas-solid interphase between the two molecular precursors and silica beads surface

The main differences between silica substrate and wafers is related to the number of actives sites between the types of experiments performed (performed on typical scales of hundreds of miligrams of silica powders having large specific surface area, typically, 200 $m^2.g^{-1}$,and much fewer milligrams of silica of non-porous wafer with geometric surface area of the order of 10^{-2} $m^2.g^{-1}$). Further insight in the ALD/MLD steps of the process was obtained by reacting the precursors with silica beads, a pertinent model for studying the reaction occurring at the gas/solid interphase between precursors and substrates such as silicon-covered wafers.[120] The modeling hereafter describes the evolution during the second ALD/MLD cycle as well as during the sixth ALD/MLD cycle to show the repeatability of the surface chemistry (see schematic overview in Figure 3.1).

3.2.2.1 Metal pulses on silica beads.

The *in situ* infrared (IR) spectra of solids **1**, **2**, and **3** (that is at the beginning, during, and at the end of the second ALD/MLD cycle (see schematic overview in Figure 3.1) are presented in Figure 3.2. The most relevant feature of the IR spectrum of sample **1** in the context of the ALD/MLD mechanism studied here is the presence of a band at 2412 cm^{-1} assigned to ν(S-H). The broad band between 2600 and 3200 cm^{-1} is assigned to hydrogen-bonded thiol moieties. Signals around 2700-3000 cm^{-1} correspond to C-H stretching vibrations arising

from organic ligands. After the metal pulse, the spectrum of the resulting solid **2** showed an increase of the IR absorption band between 2700 and 3000 cm^{-1} (see blue Diffuse Reflectance Infrared Fourier Transform Spectroscopy (DRIFT) spectrum, curve **2** in Figure 3.2), together with the reduction of the broad S-H stretching signals. Similar though shallower changes can be observed in spectra of **9** and **10** (see Figure B.3 in Appendix B)). Indeed, the analytic changes from one early cycle to the next are expected to be sharper than from a later cycle to the next, even if the surface chemistry remains similar, given the larger relative change that one single pulse is expected to bring to an early deposit than to a later one.

Furthermore, in agreement with the other analytic data presented below, the metal coverage is less efficient in the later cycles, leaving more unreacted thiols after the metal pulse thus explaining the large feature at 2412 cm^{-1} assigned to S-H, in spectrum **10** (Figure B.3 in Appendix B) with respect to its almost complete absence in spectrum **2** (Figure 3.2). The chemical composition of solids was determined by elemental analysis (see Table 3.1). The elemental analyses of the solids resulting from the metal pulses of the 2nd and 6th ALD/MLD cycles, i.e. **2** and **10**, show substantial increase in the metal content, indicating a successful metal grafting in both cases.

During the 2nd metal pulse, the volatiles released upon TDMAT addition to **1** were collected and analysed. Dimethyl amine ($(CH_3)_2NH$) was observed as the sole volatile by-product of the reaction (see 1H NMR study of the condensed volatile by-products in Figure B.4 in Appendix B), corroborating the successful reaction of the amido precursor TDMAT at the gas-solid interphase of the growing thiolate thin film.

3.2.2.2 EDT pulses on silica beads.

The sulfur pulse has been modelled by analysing the addition of EDT to the metal-terminated silica beads, **2** and **10**, followed by a purging step, leading to solids **3** and **11**, that is during the second halves of the second and sixth cycle, respectively (see schematic overview in Figure 3.1). The DRIFT spectrum for **3** (Figure 3.2, green line) exhibits a characteristic SH bond stretching (2413 cm^{-1}) which had all but disappeared in the spectrum of **2** (Figure 3.2, blue line) and broadening of the bands between 2700 and 3000 cm^{-1}, which indicates a successful chemisorption of the thiol. 1H NMR analysis of the trapped volatile by-products displayed a typical resonance corresponding to methyl protons of $HNMe_2$ (see Figure B.5 in Appendix B). The changes in elemental analysis are reported in Table 3.1. The

sulfur-containing solids are also EPR active (see Figure B.2 in Appendix B).

Table 3.1: Results of elemental analyses (expressed in weight percent, %wt) of the solids obtained during the 2nd and 6th ALD/MLD cycles using TDMAT and EDT alternating pulse on SiO_{2-700} nanobeads. See Scheme overview for numbering.

	Elemental analysis (wt%)					**Atomic ratios**		
	Ti	C	N	S	H	C/Ti	N/Ti	S/Ti
1	1.7	2.2	0.9	2.6	0.5	5.3	1.9	2.3
2	3.0	3.9	1.8	2.8	0.9	5.3	2.0	1.4
3	2.8	5.15	1.3	7.7	1.1	7.2	1.5	4.1
...								
9	4.9	9.8	2.2	15.8	2.2	8.0	1.5	4.8
10	5.5	10.3	2.4	16.1	2.3	7.4	1.5	4.3
11	5.3	10.8	2.3	17.8	2.4	8.1	1.5	5.0

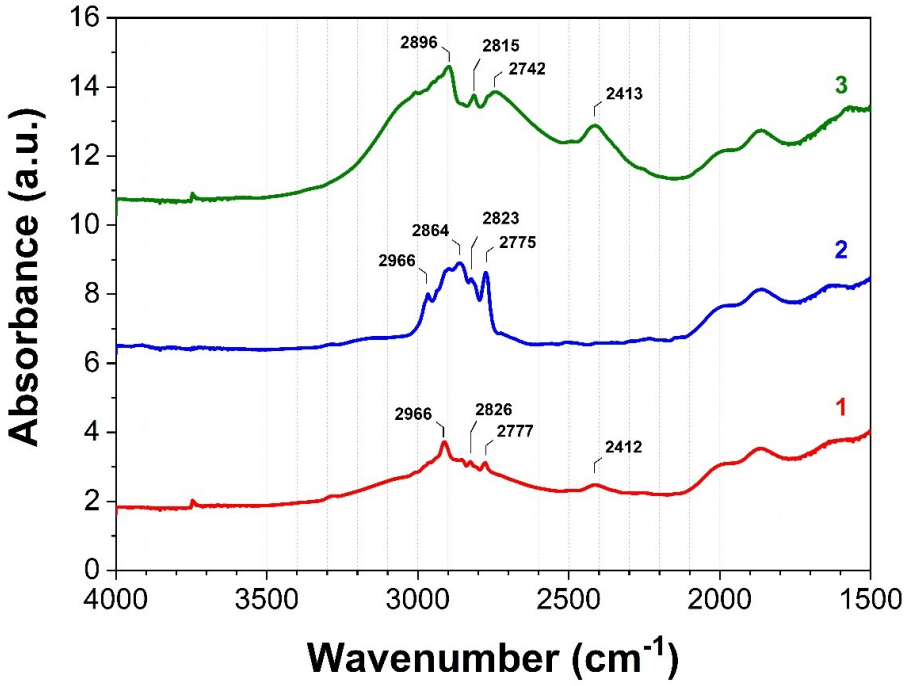

Figure 3.2: IR absorbance spectra recorded during the second ALD/MLD cycle on silica nanobeads SiO_{2-700} (spectrum of 1, red); after the ALD pulse of TDMAT (spectrum 2, blue); after the subsequent MLD pulse of EDT (spectrum 3, green), see Schematic overview for numbering.

3.3 ALD/MLD growth followed by annealing crystallization process on silica-terminated silicon wafers and monitoring with operando X-ray studies

After understanding the appropriateness of the chosen precursors thanks to the study performed by our collaborators on silica nanobeads, we will now apply the ALD/MLD growth process on wafers. Therefore, the ALD/MLD process will be based on alternating additions of TDMAT and EDT pulses to the wafer, followed by a subsequent thermal annealing of the ALD/MLD grown layer inside our dedicated reactor. The reactor allows us to understand the atomic mechanisms during the process, as observed in the previous work of our research group.[153, 154, 155, 149, 150, 152]

3.3.1 ALD/MLD growth by alternate TDMAT and EDT pulses

ALD/MLD growth of Ti-thiolate is applied on the 100 nm SiO_2 substrates at low temperature (T_{sub} = 50 °C) to have a complete dissociation between growth and crystallisation using the growth parameters mentioned in Chapter 2.

3.3.1.1 *In situ* monitoring of titanium thiolate MLD growth by MWE and XRR

Figure 3.3(a) shows thickness evolution during 40-cycle ALD/MLD thiolate growth recorded by *in situ* ellipsometry and fitted using a TiO_2/100 nm-SiO_2/Si thin film model.[152] Though such a crude model prevents a quantitative analysis of the data, the thin film final thickness value measured by *in situ* XRR (13.3 nm) is compatible with the one estimated by MWE (18.2 nm). Besides, the ellipsometry data allow to ensure that the process is robust and reproducible under SOLEIL x-ray experimental conditions. The periodic changes and saturation of the signal during the purge testify to self-limiting alternating surface reactions that insures an ALD/MLD process, as highlighted by the inset of Figure 3.3(a) showing the as-calculated total film thickness increase during a single full cycle.

Monitoring the reflected X-ray intensity provides more quantitative insights on the growth. Provided that the film roughness is not too high, the specular reflected beam intensity recorded during the deposition, at a fixed incident angle, oscillates as a function of cycle number (time) due to the film thickness evolution. A maximum (resp. minimum) of

intensity corresponds to constructive (resp. destructive) interference of the beams reflected at the growing film surface and at the film/SiO_2 interface. Then, knowing the thickness oscillation period in the steady growth regime, it is possible to relate the increase of intensity inside one half an oscillation period to the film thickness increase. Figure 3.3(b) shows the increase in film thickness with the number of cycles in the range [11-17]. Additionnal information about the RBI are provided in **Section B.1**

3.3.1.2 *In situ* monitoring of titanium thiolate ALD/MLD growth by XRF

Element-specific *in situ* analyses during the growth were obtained by monitoring Ti and S X-ray Fluorescence (XRF) during each successive ALD and MLD step, respectively, to quantify the Ti and S amount deposited on the sample surface. Figure 3.3 (c,d) shows Ti and S Kα fluorescence intensities normalized to the incoming X-ray beam intensity, respectively, as a function of ALD/MLD cycle number. The filled circles correspond to the fluorescence mean intensity at the end of each cycle (that is after the EDT purge). Overall, each fluorescence appears to increase linearly after a short transient regime of growth (see linear regression fits calculated over the last 15 cycles, in the steady linear regime of growth). The inset of Figure 3.3(c) and Figure 3.3(d) show the XRF intensity variation during the 30th to 34th cycle, representative of cycles in the steady state regime of growth, giving an insight in chemical reactions occurring at the gas-solid interphase during each pulse in the steady state. In both cases, an overall fluorescence increase is observed suggesting a successful grafting at each pulses. Some differences are also visible between the TDMAT and the EDT pulse. As for the Ti fluorescence, an initial decrease of intensity during the injection of TDMAT is observed. This drop in intensity is assigned to the presence of the TDMAT carrier gas (Ar), which leads to a significant absorption of the Ti Kα XRF because the Ti Kα energy (4509 eV) is a bit larger than the Ar K edge (3206 keV) ; upon removal of argon through the nitrogen purge the effective increase in titanium fluorescence is observed, confirming titanium enrichment of the ALD growing phase. No change in Ti fluorescence is observed after the EDT pulse, as expected since no change in titanium content is expected in the second half pulse of each cycle. As for the S fluorescence, the aforementioned drop in intensity due to the presence of argon is also observed during the TDMAT pulse but the net effect after the nitrogen pulse is null on the S fluorescence as expected. In this case, the net fluorescence increase is observed only after the EDT half-cycle. Noteworthy, the spikes of XRF inten-

sities at the S edge, notably at low cycle number, evidence the desorption of S-containing molecules, including EDT, from the surface, suggesting that physisorbed and chemisorbed EDT are present after the EDT purge and the physisorbed excess EDT (and possibly other gaseous by-products), can be correctly removed by the nitrogen purge step. To sum up, the XRF data shown in Figure 3.3 (c,d), also evidence a well-behaved self-limiting alternating deposition by ALD/MLD of a titanium-containing thiolate layer.

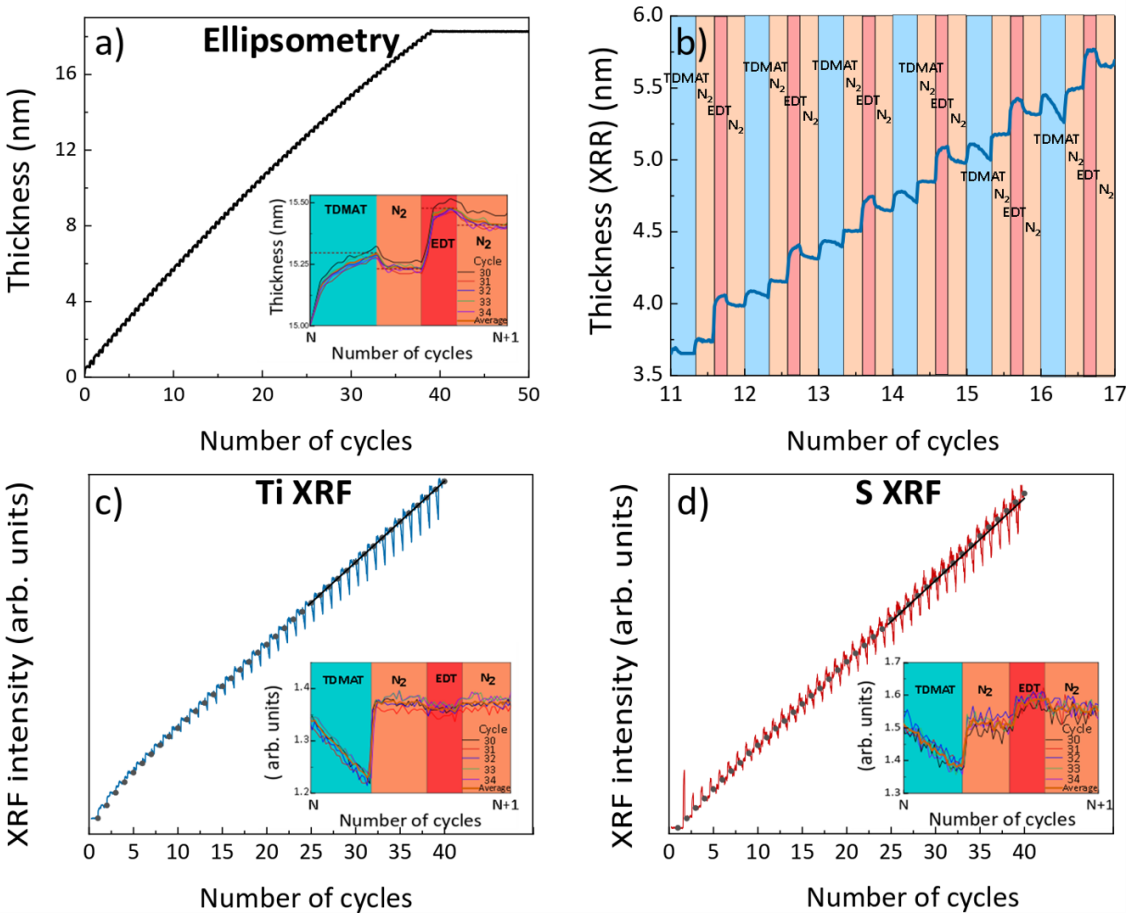

Figure 3.3: Film thickness evolution measured by (a) multiwavelength ellipsometry (b) XRR at fixed angle. Ti Kα XRF intensity (blue line, c) and S Kα XRF intensity (red line, d); in both cases, the mean intensity value at the end of the EDT purge is shown for each cycle (closed black circles) together with the regression line calculated in the linear steady state regime of growth (black lines, R^2= 0.998 and 0.992, respectively). All data were recorded *in situ* as function of the number of cycles during the Ti-thiolate deposition (Tsubstrate = 50 °C). The insets in (a), (c) and (d) show the raw data obtained during cycle numbers 30, 31, 32, 33 and 34, the curves were rescaled to be superposed.

3.3.1.3 X-ray Absorption Near Edge Structure (XANES) of Ti-thiolate sample grown by ALD/MLD

The XANES spectra recorded at the Ti K-edge of the as-deposited Ti-thiolate thin film are reported in Figure 3.4(a). The incoming X-ray beam linear polarization was set parallel to the growth surface. Its pre-edge peak position is at slightly lower in energy (ΔE=1 eV), with respect to the pre-edge peak position of the XANES spectra of the annealed samples (Figure 3.4 (b,c,d)); these overlap with the pre-edge peak position in the XANES spectrum of the reference TiS_2 powder, Figure 3.4(e). The latter is a spectrum averaged over the beam polarization orientation with respect to the hexagonal crystallographic frame of the lamellar 1T-TiS_2 structure because the sample is a powder. The higher energy pre-edge peak, observed in the energy range [4972-4973] eV (A1 feature in Figure 3.4) , is well understood with regard to the 1T-TiS_2 structure.[205] While the detailed analyses of the XANES data are beyond the scope of our discussion here, the energy difference between the feature of the as deposited thiolate sample (Figure 3.4 a) and the one of TiS_2 (Figure 3.4 e) corroborates the presence of the Ti(III) centers in the as-deposited material, as anticipated by the modeling studies reported above.

3.3.2 Characterization of TiS_2 nano domains after thiolate annealing

Two samples obtained by 40- and 80-cycle ALD/MLD thiolates, respectively, were annealed inside MOON reactor at 450 °C for 30 min under H_2(4%)/Ar(96%) gas. Indeed, H_2 being known to facilitate sulfur extrusion from sulfur-rich TiS_2+x phases.[184] The resulting phases were examined by XANES, Raman scattering spectroscopy, TEM, X-ray absorption linear dichroism, and HAXPES to study their composition, crystallinity, and microstructure.

3.3.2.1 X-ray Absorption Near Edge Structure (XANES) of the TiS_2 samples obtained by annealing

The XANES spectra of the two annealed samples are reported in Figure 3.4(c and d, respectively). In all cases, the pre-edge peak in the energy range [4972-4973] eV (see A1 in Figure 3.4), well understood with regard to the 1T-TiS_2 structure[205], is observed. Ti^{4+} atoms in 1T-TiS_2 structure (electronic configuration: $3d^0 4s^0$) sit on a 1a position (point group -3m) of the P$\bar{3}$m1 space group. The crystal has no inversion symmetry about this position, allow-

ing the local hybridization of the central Ti 4p states with near neighbor Ti 3d orbitals.[205] Since Ti first nearest neighbors comprise six sulfur atoms which form a centrosymmetric octahedron, the A1 feature intensity is ascribed mainly to the dipole transition from Ti 1s to 4p character of the 3d band. Peaks B and C arise from transitions to final Ti 4p states. Noteworthy, the pre-edge peak energy positions for all annealed samples and TiS_2 powder are the same, indicating the same formal valence of the central Ti atom (Ti^{4+}), unlike the slightly lower energy (1 eV) shifted pre-edge peak position of the sample before annealing (see Figure 3.4(a)), indicating the full conversion of the Ti(III) centers present in the as-deposited material to the expected Ti(IV) state present in TiS_2. As shown by comparing Figure 3.4(c,d), the 80-cycle sample displays significantly improved atomic local order after annealing, with respect to the 40-cycle sample after annealing, with the local density of states tending to the one of TiS_2. Such a result could indicate that the range of atomic local order and texture reached during the annealing improve upon film thickness and the relative amount of Ti atoms in oxidized regions at the sample surface and sulfide/SiO_2 interface is smaller in the case of the 80-cycle thin film (in agreement with TEM evidence below). XANES spectra was also recorded *in situ* during the annealing of the sample obtained after 40-cycle ALD/MLD sample. Figure 3.4(b) shows the Ti K-edge XANES spectra after annealing at 375 °C for 30 min under H_2(4%)/Ar(96%) gas. The quantitative analysis of the spectra before and after annealing (Figure 3.4(a) and (b), respectively) is out of the scope of this dissertation. After annealing at 375 °C the spectrum shows some substantial similarities to the TiS_2 powder spectrum, firstly the increase of the distinctive pre-edge features of TiS_2. At the same time, it is clear that the TiS_2 atomic arrangement is not yet achieved and is much poorer than the one observed by annealing at 450 °C (see Figure 3.4(c,d)). Therefore, the annealing temperature increase to 450 °C seem to significantly improve the atomic local order which tends to the one of TiS_2, as the TEM results shown hereafter will also show.

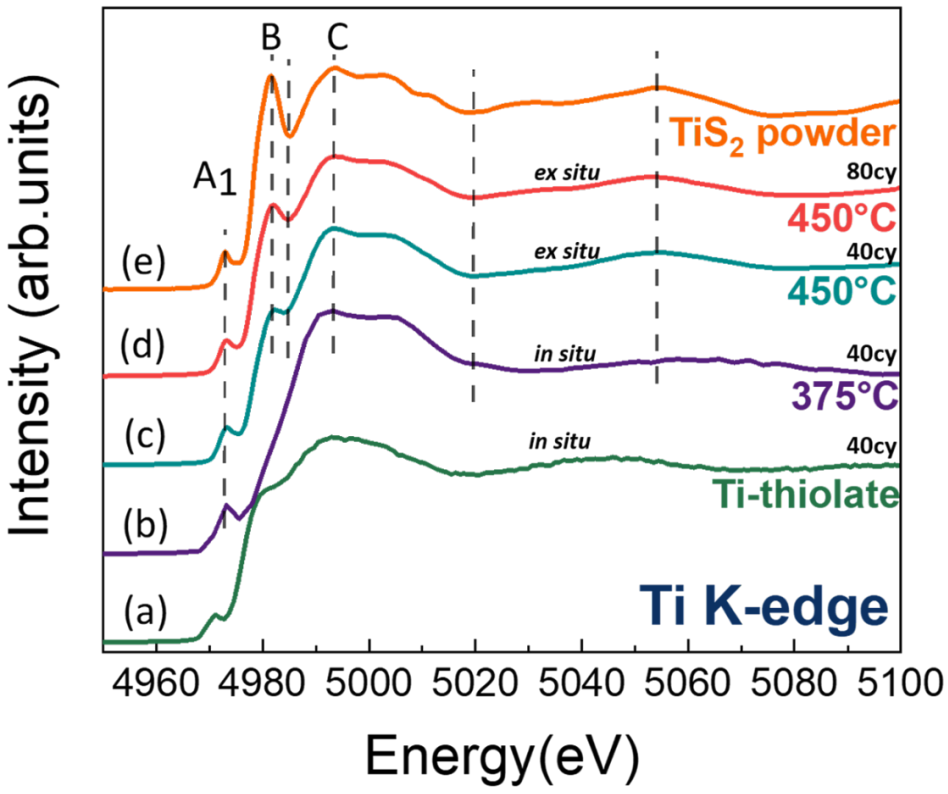

Figure 3.4: *In situ* XANES spectra at the Ti K-edge of (a) as-deposited Ti-thiolate sample obtained after 40 cycles of ALD/MLD growth and (b) after annealing under H_2(4%)/Ar(96%) gas at 375°C for 30 minutes. *Ex situ* XANES spectra of Ti-thiolate samples, obtained after (c) 40 cycles and (d) 80 cycles of ALD/MLD growth and annealing at 450°C for 30 minutes ; (e) *ex situ* XANES spectrum of a reference TiS_2 powder recorded in fluorescence mode. The linear polarization of the X-ray beam was parallel to the growth surface.

3.3.2.2 Raman scattering spectroscopy

Among the fundamental active modes in Raman spectroscopy, two modes are associated to 1T-TiS_2 (space group $P\bar{3}m1$): the Eg mode ($\approx 234\ cm^{-1}$) and A1g mode ($\approx 336\ cm^{-1}$), corresponding to vibrations of the sulfur atoms in and out of the S-Ti-S layer, respectively. An additional shoulder mode (termed Sh-shoulder or Sh herein, $\approx 372\ cm^{-1}$) appears more pronounced for S-Ti-S multilayer than monolayer structure.[132, 206, 207, 208, 209, 210, 211] The appearance of the Sh-shoulder mode is due to an excess of metal atoms between the TiS_2 layers (in the van der Waals gaps) resulting in local stiffness of the phonons.[132]

The Raman scattering spectra of the two annealed samples obtained from 40- and 80-

cycle thiolates, respectively, were measured with an excitation frequency in the visible range (532 nm), Figure 3.5(a,b). The two spectra display the Eg and A1g active modes corresponding to 1T-TiS_2. The shoulder mode (Sh) is visible at about 380 cm^{-1}. By comparison with the results found in the literature and obtained with a reference TiS_2 powder, the spectra indicate a good crystalline quality of the samples with likely some defects in between the layers as corroborated by the presence of the Sh mode.[132, 136] The frequency difference between A1g and Eg modes is correlated to the average number of stacked TiS_2 layers. However, the determination of the frequency difference with precision remains difficult due to a significant asymmetry[132] of the Eg mode intensity profile (see Figure 3.5(a,b)). For this reason, the A1g mode and the better-defined Sh-shoulder mode should be preferred for the determination of the number of layers. Indeed, it has been observed in the literature that the shoulder mode (Sh) appears being more pronounced for multilayers than for a monolayer. The ratio of the integrated intensity profiles of the A1g and Sh-shoulder (A1g/Sh) can then be used for the determination of the number of TiS_2 layers (up to 5).[132, 136, 206] The obtained values show the presence of multilayers with more than 5 layers for both samples, in line with TEM images (see Figure 3.5(c,d)). By normalizing the spectra of both samples to the T2g Si peak, the integrated intensity of the A1g peak of the 40-cycle sample is half of the one of the 80-cycle sample, in agreement with the film thickness ratio (see Figure B.7 in Appendix B).

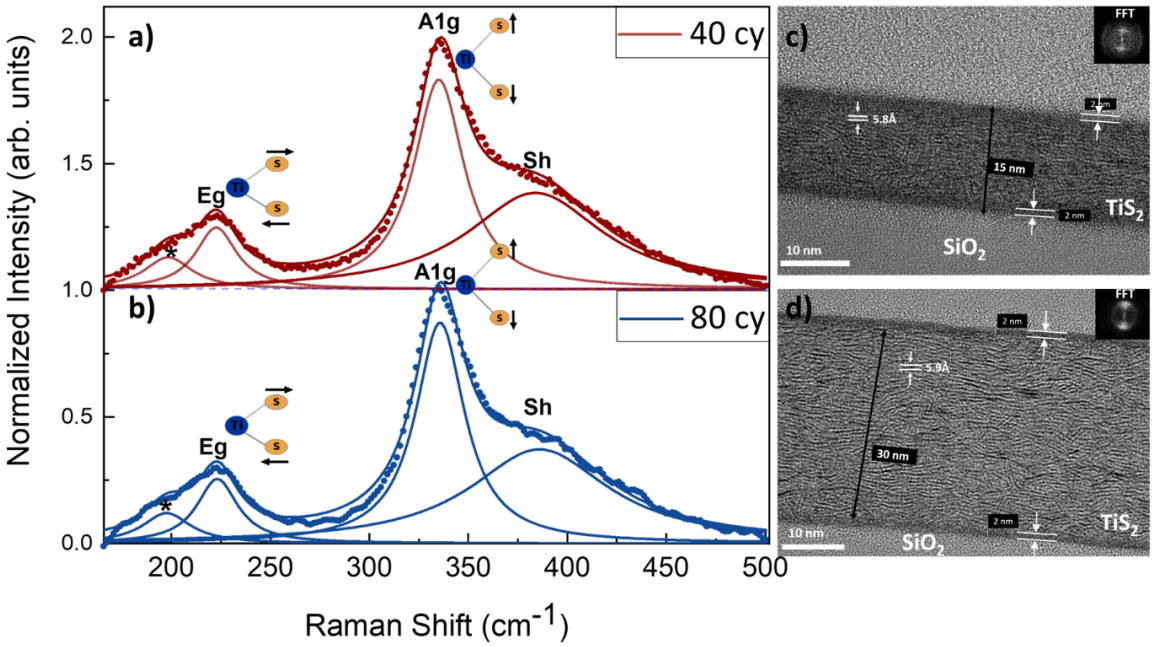

Figure 3.5: (a, b) Raman spectra (dotted lines) and (c, d) cross-section TEM images of samples resulting from (a, c) 40 and (b, d) 80 ALD/MLD cycles and an annealing at 450 °C for 30 min under H_2(4%)/Ar(96%) gas. The insets in the TEM images represent the fast Fourier transform of the sample image. Raman spectra were normalized to the intensity of the A1g mode and fitted with Lorentzian curves (solid lines in a) and b) panels).

3.3.2.3 Electron microscopy

TEM images of the two annealed samples reveal continuous thin films with low surface roughness (see Figure 3.5 (c,d)). The nanoscale structure of the bulk of the grown phase (that is not taking into account the 2 nm thick ultimate surface and the 2 nm thick interlayer surface with the wafer substrate, both discussed below) confirms the presence of partly ordered crystalline nanodomains of atomically thin stacks of TiS_2 layers, in agreement with the Raman data discussed above. The interlayer distances equal to 5.8±0.2 Å for the 40-cycles and 5.9±0.2 Å for the 80-cycles samples are close to the bulk 1T-TiS_2 c-parameter, 5.7 Å.[46] According to the TEM images, the thickness of the deposit is, as expected, almost double for the 80-cycles than for the 40-cycles sample (30 nm and 15 nm, respectively). The TEM images reported in Figure 3.5 (c,d) show some more pronounced atomic short-range order in the thicker 80-cycle sample than in the 40-cycle one. Regarding the ultimate surface, for both samples, the sulfide thin film is covered by an amorphous ca. 2 nm-thick top layer, which

presumably results from the hydrolysis and oxidation of the material exposed to air, and should therefore be titanium oxysulfide. At the bottom, the sulfide thin film/SiO_2 interface stays rather sharp. The narrowness (ca. 2 nm thick) of the interface layer, which is expected to be an oxysulfide resulting from the first pulses of the metal precursor with the pristine ultimate surface of the siliceous substrate [120], suggests a well-defined seeding chemistry from the very first pulses of the process.

3.3.2.4 X-ray absorption Linear Dichroism (XLD)

Figure 3.6 shows polarized Ti K-edge XANES spectra recorded with the incoming X-ray beam polarization parallel or perpendicular to the sample surface. The polarization effect in the XANES spectrum confirms the anisotropic nature of the obtained films.

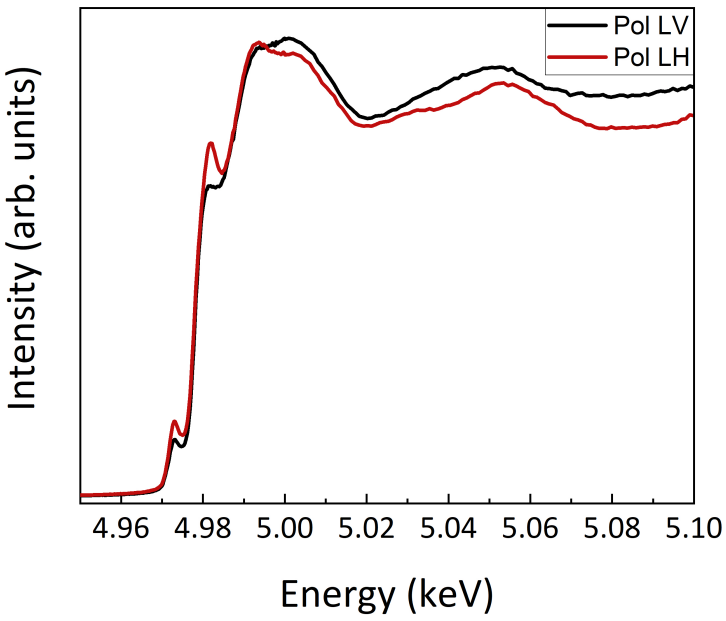

Figure 3.6: TiS_2 film obtained from 80 ALD/MLD cycles and annealed in H_2(4%)/Ar(96%) for 30 min at 450 °C: normalized XANES spectra measured with the linear polarization of the X-ray beam either parallel (Linear Horizontal (LH)) or perpendicular (Linear Vertical (LV)) to the sample surface.

This confirm at a much larger scale than that of the TEM images, that the TiS_2 monolayers are not randomly oriented, but tend to be parallel to the substrate surface, i.e. the thin films show a partial texture.

3.3.2.5 Stoichiometry study of annealed samples

3.3.2.5.1 Hard X-ray Photoelectron Spectroscopy (HAXPES) of annealed samples

In order to perform in-depth study of both the stoichiometry and chemical elemental components of the 30 nm thick TiS_2 thin film obtained from 80-cycle ALD/MLD thiolate and annealed at 450 °C, HAXPES was carried out using chromium Kα X-ray sources. The analytical information depth using Cr Kα source (hν = 5414.7 eV) is about three times deeper than with the Al Kα source. The benefit of a larger sampling depth opens opportunities to minimize the contribution of the upper surface of the sample, possibly altered by the atmosphere, in the overall spectra, TiS_2 being known to convert to TiO_x by exposure to air.[212] The presence of adventitious air oxidation and hydrolysis of the top thin film (see Figure 3.5(d)), is demonstrated in a qualitative way by comparing the Ti 1s core level spectra to the Ti-2p core level spectra presented in Figure 3.7. The mean free path of the photoelectrons calculated using TPP2M equation,[213] is found to be larger for the Ti 2p (8.1 nm) than that of the Ti 1s (1.6 nm). It follows that the analyzed thickness is about 3.3 nm with the Ti-1s core level peak instead of 15.7 nm with the Ti-2p and S-2p peaks. The Ti-1s XPS spectra shown in Figure 3.7(a) present two different environments: the strong signal at 4969.3 eV (84.7%, blue peak) is attributed to titanium oxysulfides whereas the weak one at 4966.8 eV (15.3 %, red peak) is attributed to TiS_2 layers. For the signal at 4969.3 eV, the thickness of the oxide layer on the top of the deposited TiS_2 thin film is about 2.1 nm (Additional details about the evaluation of the upper layer thickness using TPP2M calculations are provided in **Section B.2**). The latter is in agreement with the value found by ARXPS with an Al source (see Figure 3.8).[214] The Ti 2p XPS spectra shown in Figure 3.7(b) present two different Ti 2p$^{3/2}$:2p$^{1/2}$ spin-orbit doublets. The most intense (456.8 eV and 462.5 eV) corresponds to TiS_2.[206, 215, 216] The other one (459.2 eV and 464.9 eV) is assigned to the oxysulfide layer present on the top of the obtained TiS_2.[215, 217, 216, 218] The S-2p XPS spectrum shown in Figure 3.7(c) presents also two S 2p$^{3/2}$:2p$^{1/2}$ components. The intense doublet (161.6 eV and 162.7 eV, spinorbit doublet of S^{2-} species) corresponds to TiS_2.[215, 218] The weak doublet signal (163.0 eV and 164.2 eV) could be attributed to the spinorbit doublet of S_n^{2-} species (where n=2,4,6, ...) known as an S-S pair and to C-S bonds. Based on the widening of the peak component presented in Figure 3.7(c) we attribute this component to a combination of $(S_2)^{2-}$ and $(S_4)^{2-}$ species.[219] It can also be referred to titanium oxysulfide environment in

connection with the oxidized part already detected on the surface of the TiS_2 thin film.[136, 217, 220, 221] Theoretical Relative Sensitivity Factors (RSF) were used to quantify the stoichiometry of the obtained TiS_2 layers.[222] The calculated aspect ratio [S]/[Ti] calculated with the Ti2p and S2p doublets attributed to TiS_2 is equal to 2.1. This indicates that the deposited film has a stoichiometry close to the one expected for TiS_2.

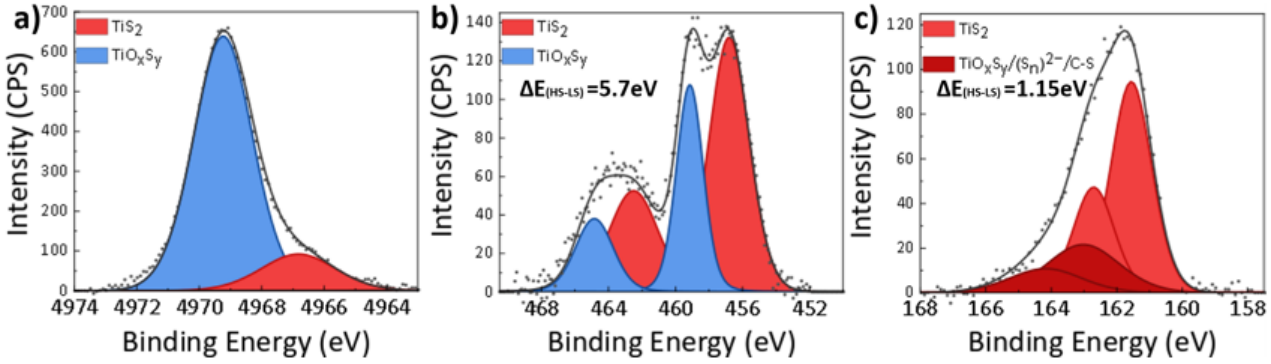

Figure 3.7: HAXPES spectra measured with the Cr Kα source: Intensity as a function of the electron binding energy a) Ti-1s core peaks b) Ti-2p core peaks (doublets) and (c) S-2p core peaks (doublets).

3.3.2.5.2 Correlation of results: Angle-Resolved X-ray Photoelectron Spectroscopy (ARXPS) analysis

To correlate and compare the results of HAXPES obtained with the Cr source, XPS spectra were measured with the conventional monochromatic soft Al source (Aluminum Kα, hν = 1486.6 eV) at three different angles (θ =15°,45° and 85° with respect to the sample surface normal) for which the depth of analysis are equal to 2.3, 4.9 and 6.8 nm, respectively. The results are listed in Figure 3.8, the calculated atomic ratio [S]/[Ti]=1.9 is in agreement with the stoichiometry obtained with the Cr source. Table B.1 in Appendix B shows the proposed chemical composition based on the XPS data obtained with the Al source, in overall they suggest the presence of the same environments for Ti-2p and S-2p core peaks for both the Al and Cr sources. ARXPS data shows large amount of carbon (21%) inside the obtained thin film (see Figure 3.8 (i)) which is not significantly affected by the change in take-off angle. The C 1s core level spectra exhibit three components originating from different sources.

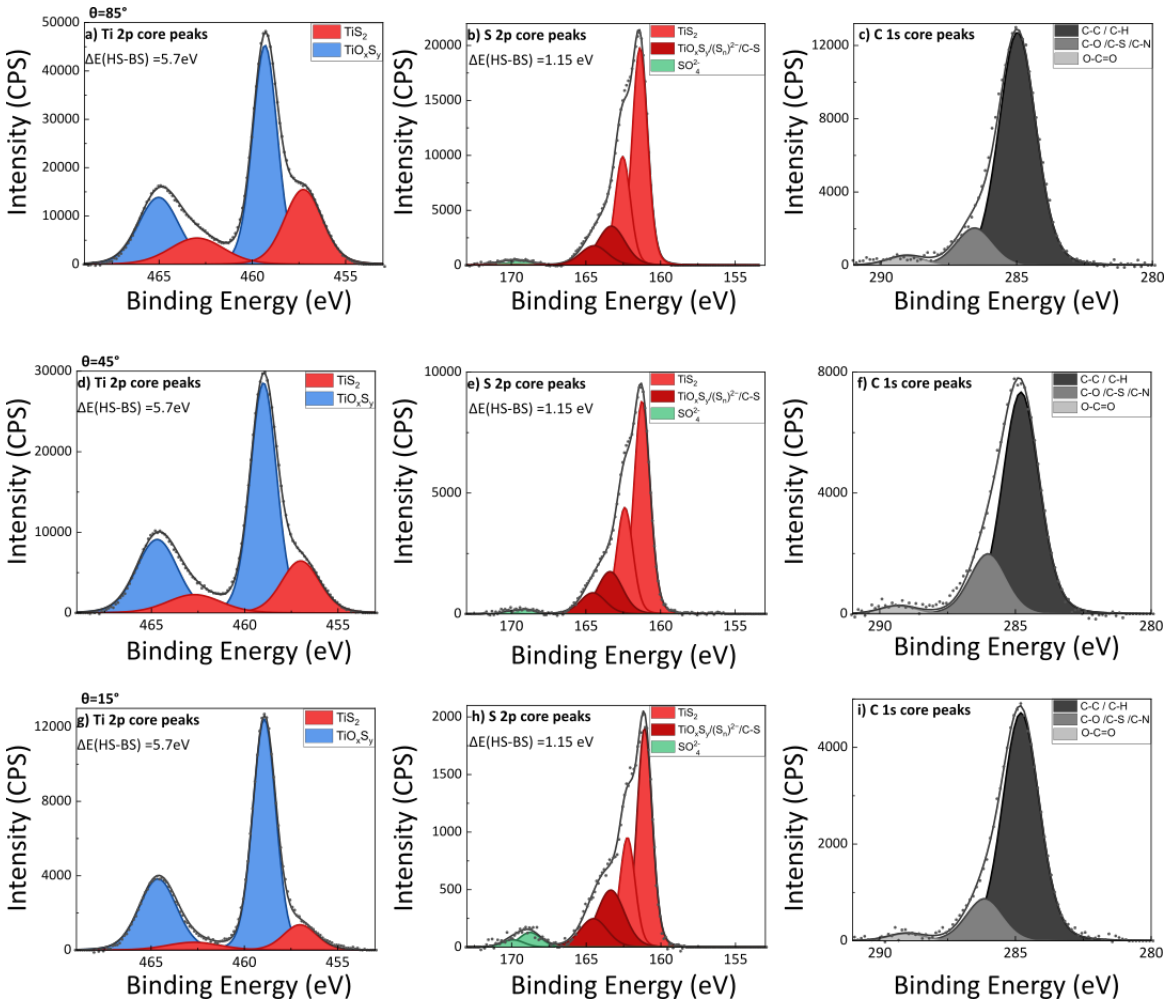

Figure 3.8: TiS_2 film obtained from 80 ALD/MLD cycles and annealed in Ar(96%)/H_2(4%) for 30 min at 450 °C. Angle resolved XPS with an Al source. XPS lines of Ti 2p, S 2p and C 1s core peaks measured at different angles (85°, 45° and 15°) with respect to the surface normal.

The major part corresponds to C-H/C-C bonding, it could originate from adventitious carbon but also from the incomplete reaction of TDMAT [124] or the presence of graphitic carbon, as it was shown in a previous study regarding the synthesis of MoS_2 by the same MLD/ALD-annealing approach.[120] The presence of oxidized carbons (C-O and C=O, attributed to the as weaker contributions at 286.6 and 289.1 eV respectively, could originate from the surface contamination due to the exposure to ambient conditions.[136] Note that the line at 286.6 eV could also be assigned to C-S bonds indicating an incomplete reaction of EDT ($HSCH_2CH_2SH$).

3.3.2.6 Annealed film homogeneity and oxidation in-depth study: ToF-SIMS and Ar ion etching in-depth profile

As discussed by HAXPES and XPS data in the previous section, the oxide environment may originate from the oxidation of the top layer of the sample. In this context, monoatomic Ar ions etching in-depth profiles were carried out to validate such theory. Importantly, the in-depth oxygen profile performed with monatomic Ar^+ beam (Ar^+ at 1 KeV 1μA 1x1 mm^2), attests the absence of oxygen contamination inside the thin film as shown in Figure 3.9-a (Dark line). Concerning the in-depth composition of TiS_2 film, the [Ti], [S] and [C] XPS profiles attest a quasi atomic percentage in-depth confirming the homogeneity of the elements distribution inside the layer. Nevertheless, the obtained results after Ar^+ sputtering could present a preferential sputtering on some elements such as oxygen and sulfur, that leads to a reduction of the titanium (from Ti^{4+} to Ti^{3+}).[223] Thus, the use of XPS profiles should be considered as qualitative analysis confirming the hypothesis of the oxygen presence only at the topmost surface of the film and at the SiO_2 interface, while the quantitative analysis of the chemical composition was confirmed by the correlation of HAXPES and ARXPS results.

Moreover, Time-of-Flight Secondary Ion Mass Spectrometry (ToF-SIMS) analyses were performed. The mass spectra were obtained using a ToF SIMS 5 Instrument, from ION TOF GmBH equipped with a 25 kV Bismuth-LMIG. For the analysis of the secondary ion, the LMIG gun was tuned to deliver Bi^+ primary ions energized at 25 kV with a direct current of 16,8 nA. The analysis area of 90x90μm^2 is described in 128x128 pixels. The etching time analyses were carried out with 500 eV Cs^+ primary sputtering ions with a 40 nA current and a raster size of 300x300 μm^2. During depth profiles, the MCs_{2+} ions were collected.[224] Figure 3.9-b shows that the distribution of S Ti C and N (where N was not clearly detected in XPS) inside the 30 nm film of TiS_2 is in agreement with the XPS results, especially as far as the oxygen is concerned which is detected (due to the high sensitivity of the ToF-SIMS [225]) in very small quantities at depth. Note that, the intensity of each element does not give any indication on atomic percentage inside layer (only XPS data give quantification results), on the other side the variation of intensity according to the depth analysis can confirm or not the presence of elements. That's why the high decreases of the oxygen profile in Figure 3.9-b beside the oxygen profile in Figure 3.9-a confirms the absence of significant oxygen content ($<$1% at) inside the layer.

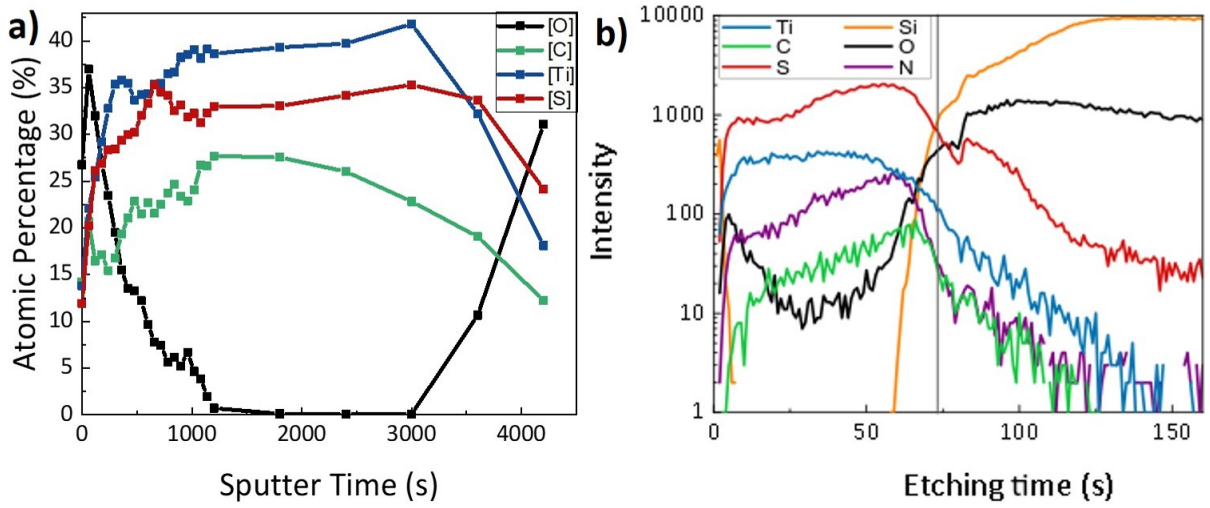

Figure 3.9: TiS_2 film obtained from 80 ALD/MLD cycles and annealed in Ar(96%)/H_2(4%) for 30 min at 450 °C: a) atomic percent profiles obtained by XPS for [O], [C], [Ti] and [S] atoms during Ar^+ sputtering (Ar^+ 1 keV 1µA 1x1 mm^2) and b) ToF-SIMS analysis as a function of etching time shows the elemental distribution profile with positive polarity for secondary ions.

3.3.2.7 Four-point probe electrical measurements and bandgap properties

Four-point probe resistivity measurements were carried out at room temperature on the 15 nm and 30 nm thick TiS_2 thin film synthesized from 40- and 80-cycle ALD/MLD thiolates and annealed in Ar(96%)/H_2(4%) for 30 min at 450°C. The mean resistivity equal to $6.61(0.4)\times10^{-3}\Omega$.cm and $8.60(0.9)\times10^{-3}\Omega$.cm for the 15 and 30 nm thick films, respectively. The small dispersion in the values from one spot to another attests to the homogeneity of the deposited samples. Such low mean resistivity value is in the range of values for a semiconductor materials at room temperature (additional details will be discussed in section 4.5 Chapter 4). We can therefore conclude that our ALD/MLD process for the growth of TiS_2 thin films allows us to synthesize a material whose resistivity is in the same order of magnitude was obtained compared to thermal ALD and PE-ALD process.

Semiconductor bandgap properties of the two samples with different thicknesses (15 and 30 nm) were also investigated by spectroscopic ellipsometry (SE)[200]. Figure 3.10 shows the experimental function $(\alpha h\nu)^2$ versus hν. The n and k curves as a function of photon energy are shown in the inset of Figure 3.10. The onset of the absorption above 1 eV indicates the existence of an optical bandgap. The linear relationship between $(\alpha h\nu)^2$ and the energy at

the absorption onset, is indicative of the existence of a direct band gap. By extrapolating the linear regime down to the cross point with the abscissa axis, a bandgap energy equal to 1.72 eV for the annealed sample obtained from 80-cycle ALD/MLD thiolate, a value which is very close to the one obtained with the 40 ALD/MLD cycles sample (Eg=1.74 eV). Noteworthy, a direct band gap equal to 1.70 eV was found in crystalline one-dimensional hybrid organic/inorganic TiS_2 (ethylenediamine) framework.[226]

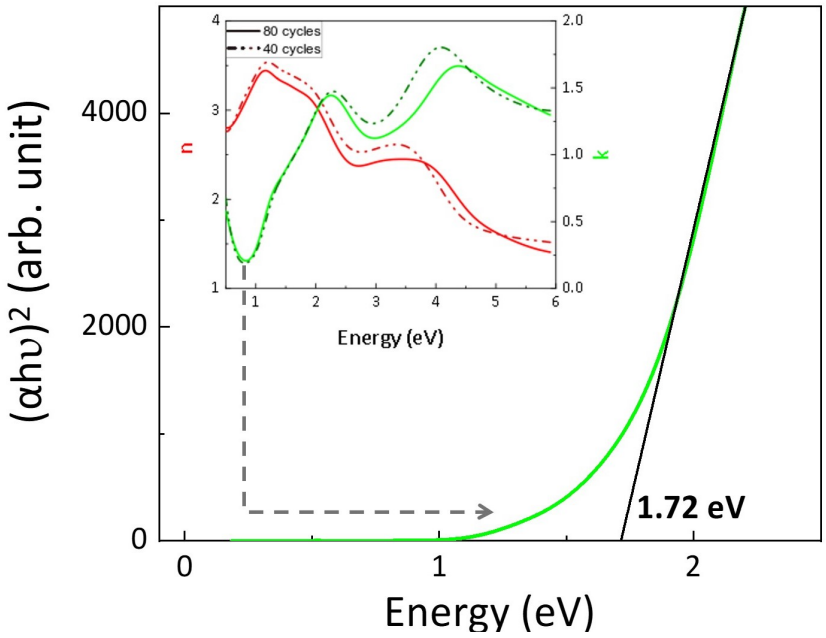

Figure 3.10: Bandgap identification from the plot of $(\alpha h\nu)^2$ vs the photon energy $h\nu$, showing an estimated direct bandgap of 1.72 eV for a TiS_2/100 nm-SiO_2/Si thin film obtained from 80 ALD/MLD cycles and annealed in Ar(96%)/H_2(4%) for 30 min at 450 °C. The inset shows the optical constants n and k of the complex refractive index as a function of the photon energy, determined by spectroscopic ellipsometry, for thin films obtained from 40 and 80 ALD/MLD cycles and annealed in Ar(96%)/H_2(4%) for 30 min at 450°C ; n and k are the real and imaginary parts, respectively.

3.4 Discussion

In this chapter, a self-limiting titanium thiolate growth by Atomic Layer Deposition/ Molecular Layer Deposition (ALD/MLD) on 100 nm-thick thermally-grown SiO_2 on Si at low temperature (50 °C) was reported. From it, lamellar TiS_2 thin films can be obtained by thermal annealing under H_2/Ar at a mild temperature (450 °C, with crystallization start-

ing at even lower temperatures). Organic carbon and bridging sulphur S_n^{2-} presence show that the annealing is not complete. The films are continuous, smooth, homogeneous, and as thin as 15 nm or even less so. To the best of our knowledge, TiS_2 material has never been obtained with an ALD/MLD approach. The electric measurements on the 15-nm and 30-nm thick thin films show a semi-conductor behavior with direct band-gap. Hereafter some other noteworthy aspects of the process are discussed, namely i) the growth mechanistic insight gained through the modeling studies on silica beads, ii) the growth mechanistic insight gained from *in situ* X-ray studies and comparison with the modeling studies and iii) the preferential orientation of TiS_2 despite the amorphous nature of the substrate.

3.4.1 Thiolate growth mechanistic insight on model silica beads

The development of ALD-grown molecularly-thin layers of MoS_2 on silica-covered silicon wafer was steered by the study of the chemical reactions between the two precursors in absence of substrate and in the presence of high surface area silica beads.[120] Herein, we successfully extended this molecular approach for studying the reaction of TDMAT and EDT, en route to the targeted ALD/MLD process toward TiS_2.

First of all, the thermodynamically accessible and kinetically facile reaction of molecular precursors (TDMAT and EDT) among themselves is insightful since it tends to suggest that an MLD/ALD process targeting TiS_2 and based on their alternate addition should lead to film growth. However, because of the absence of a substrate, this reactivity results in coordination polymers which are difficult to characterize, with no special control over their molecular weight. More importantly in the context of ALD, the presence of the self-limiting nature of the reaction cannot be investigated by studying the reactivity of the molecular precursors with each other.

The ALD reaction mechanism was therefore established by investigating the chemistry occurring at the surface of porous silica nanobeads, as a model for the flat wafer substrate. The analogy between the 3D surface of silica powders and 2D surfaces of silica-covered silicon wafer substrates was proposed 25 years ago.[227] The study showed that the ultimate surface of both 2D and 3D substrates are very close in terms of chemical nature of the reactive sites (silanols, SiO-H), and in terms of site density as a function of pretreatment temperature. More recently, Surface OrganoMetallic Chemistry (SOMC) studies [228] provided titration and reactivity studies which have further corroborated the validity of this analogy

between pristine flat and porous substrates toward a first metal pulse.[229, 230, 231] Furthermore, monitoring with IR allows to have a spectroscopic handle to gauge *in situ* the change in reaction advancement over time and hence handle possible diffusion limitations. The main differences between the two supports remains the overall number of actives sites between the types of experiments performed (performed on typical scales of hundreds of miligrams of silica powders having large specific surface area, typically, 200 $m^2.g^{-1}$, and much fewer milligrams of silica of non-porous wafer with geometric surface area of the order of 10^{-2} $m^2.g^{-1}$). It is exactly this significant order of magnitude difference in favor of the powder that allows to use spectroscopic and analytic tools on the powder inaccessible to the wafer, and yet, because density is analogous and diffusion is taken care of, the powder chemistry, with its new molecular-level insight, has a chance to mimic satisfactorily the chemistry on the wafer. As mentioned above, our first attempt to use this analogy to model a full ALD process was successful for growing ultra-thin crystalline MoS_2 nanodomains from $Mo(NMe_2)_4$ and EDT.[120]

In the present case, silica-beads model studies demonstrate the successful chemisorption of both the metal and the sulfur-containing precursors which ensures mass gain upon each respective ALD or MLD pulse in route to TiS_2. The IR monitoring of the silica beads, the analysis of the gas phase and the connected changes in elemental analyses suggest that EDT reacts, at least partially, with the Ti-NMe_2 amido moieties present at the surface of the support by protonolysis, leading to the formation of a Ti-SCH_2CH_2SH thiolate group concomitantly with release of HNMe_2 in the gas phase. This agrees with literature in molecular chemistry.[232] Elemental analysis displayed substantial increase of the S/Ti atomic ratio (from 1.4 to 4.1 during the EDT pulse of the second cycle), indicating that on average between one and two EDT ligands (that is between 2 and 4 sulfur atoms) are added per titanium center. Concurrently, the N/Ti ratio drops but is not nul suggesting that only part of the available dimethyl-amino-based ligands is substituted by EDT. Noteworthy, the C/Ti ratio also increases (from 5.3 to 7.2, see Table 3.1).

In summary, silica-beads model studies demonstrate the successful chemisorption of both the metal and the sulfur-containing precursors by a self-limiting growth of a titanium thiolate phase upon each respective ALD or MLD pulse. The approach proposed here allows having mass gain information on each element separately, through elemental analyses, for example, thus offering a well-nuanced description of the surface chemistry occurring at the interface. This could be an interesting addition to other type of mechanistic studies in ALD,

for example through QCM studies, which can obtain global, rather than element specific, mass gain at each half pulse to infer the molecular-level chemical reactions occurring at the gas-solid interface of the substrate.

3.4.2 Thiolate growth mechanistic insight through *in situ* X-ray studies

Informed in part by the insightful molecular studies presented above, we have successfully employed *in situ* X-ray techniques for assessing the quality of the new innovative two-step process to TiS_2 thin films on wafers. Both the thiolate growth and its annealing were studied inside the ALD reactor. The synchrotron brilliance enabled the study of targeted material growth, under the actual process conditions and from the first ALD/MLD pulse. The possibility to record both the S Kα and Ti Kα fluorescence yield will allow us to monitor the S/Ti ratio during the thiolate growth and during its annealing, the fluorescence yield being directly proportional to the amount of element deposited on the surface. Over the process, this S/Ti ratio clearly increases. A similar trend is observed in the molecular studies on silica beads (This study is the aim of Chapter 4).

Another example where directly comparable insight are accessible for the powder and wafer approaches is given by the observed partial reduction of Ti(IV) to Ti(III) during the sulfur pulse in both systems. The presence of S radical signature observed in EPR activity of the films grown on the silica-beads correlates to the formation of dithiol moieties identified through the HAXPES and XPS studies on wafer alongside the presence of Ti(III) center proposed based on the XANES studies. These similarities corroborate a founding tenet of our work: that the two systems (powder and wafer) display very similar surface chemistry.

X-ray reflectivity data obtained *in situ*, in real time at a fixed angle of reflectivity allowed to measure the film thickness increase as a function of cycle number (see Figure 3.3(b)). Each precursor injection leads to a clear jump in thickness which reaches a constant value during each purge, corroborating the self-limiting surface chemistry observed by MWE and XRF (see Figure 3.3 (a,c,d)). During the steady growth regime, the resulting average growth per cycle (GPC) can be estimated as 0.32 nm.cy^{-1}. The latter value, agrees with the average GPC value obtained from *in situ* XRR curve measured by varying the incident angle (usual XRR mode), after deposition of 40-cycles thin film (0.33 nm.cy^{-1}, see Figure B.6 in Appendix B). Also, the resolution of the *in situ* XRR at fixed angle of reflectivity during ALD/MLD study allows to determine the growth per each half-cycle: the thickness gain can be estimated

as 0.18 nm.cy^{-1} during TDMAT half-cycle and 0.14 nm.cy^{-1} during EDT half-cycle. As in the silica beads study, the first pulses display markedly different changes in fluorescence with respect to later ones. This datum is coherent with an expected increase of the steric hindrance upon film growth (at least in the very early stages).

The two main approaches explored here, *in situ* synchrotron-based study and ALD/MLD modeling on large surface area silica beads, lead to sharply molecularly precise insights in the ALD/MLD process mechanism on the wafer. In summary, the insightful complementarities between the two approaches comforts in pursuing such tandem approach.

3.4.3 Preferential TiS_2 orientation parallel to the substrate

The process has achieved nanodomains of crystalline TiS_2 behaving as semiconductor with direct band-gap with the TiS_2 layers preferentially oriented parallel to the amorphous substrate surface (SiO_2). Comparison with state-of-the-art shows that this achievement is a substantial novelty. Thus far, the ALD growth of crystalline TiS_2 layers parallel to the substrate surface was achieved from TiCl_4 and H_2S precursors only on crystalline substrates such as ZnS [55] and the c-sapphire substrate surface [122], albeit several substrates were tested, such as sodalime glass, native-SiO_2/Si, ZnS, Rh, Ir, Pd, Pt, Ru, and TiN by Pore et al.[55], Si(100), stainless steel, c-sapphire and quartz by Sayed et al.[122] and Al_2O_3-coated native SiO_2 on Si(111) substrate[121], carbon paper, or germanium.[134] Amorphous TiS_2 or TiS_3 films where obtained when H_2S (at 180°C) was used in combination with the TDMAT precursor used herein.[124] TiS_2 and TiS_3 layers were also obtained by using both thermal ALD and Plasma Enhanced-ALD from TDMAT. [136] Post-growing treatment such as rubbing which yields mechanical alignement[55] or exposure to sulfur rich atmosphere during post-annealing are worth mentioning as alternative routes to obtain some alignment crystallization. Noteworthy, the vertically aligned TiS_2 nanowall network obtained on the c-sapphire substrate surface grew on top of an amorphous TiS_2, parallel to the film-substrate interface, along with TiS_2 platelets grown away from the substrate surface. This shows that albeit successfully orienting the TiS_2 layers, the C-sapphire also suffers from non-well-defined initial cycles and concurrent out-of-plane crystallization which mars the quality of the process, especially if ultra-thin deposits are targeted. In our case, such ill-defined interphase does not appear to be present.

In summary, the hybrid ALD/MLD step appears to achieve complete coverage of the

starting support from the first pulse, based on the results obtained on the silica bead (the "model" system). We posit that this full coverage occurs also on the wafer (the "real" system) and contributes to the very thin interlayer between the support and the final TiS_2 phase observed by TEM on the wafer (see figure 3.5 (c,d)), and hence contributes to the quality of the final film. The fully amorphous thiolate phase is then crystallized in a separate step. We posit that the initial lack of crystalline order is beneficial to the final preferential orientation of the TiS_2 nanodomains since it prevents the coexistence of differently oriented crystallization seeds before the bulk crystallization temperature is reached. This result consolidates the pertinence of the two-step approach.

3.5 Conclusion

In this chpater, we have applied a synthesis strategy based on the combination of an ALD metal-pulse (TDMAT) with an organic-precursor MLD pulse (EDT) followed by annealing to the preparation of titanium disulfide (TiS_2). The combining of TDMAT and EDT in an ALD/MLD process has generated a thin amorphous hybrid organic-inorganic Ti-thiolate material that could be converted into lamellar TiS_2 layers by thermal annealing under H_2(4%)/Ar(96%) at 450 °C. Deep understanding and fine control of both steps could be achieved by chemical experimental modeling on high surface area silica beads, in situ synchrotron XRF, XRD, and XAFS studies during alternating ALD and MLD pulses and annealing steps in a dedicated reactor setup and ex situ characterizations for the final phase (NMR, TEM, HAXPES, and Raman scattering). The chemical reactions occurring at the gas-solid interphase in the ALD/MLD processes yield a well-behaved growth process prepared by hybrid ALD/MLD.

However, the proposed strategy didn't succeed to reach ultra-thin films (less than 10 nm). Indeed, an 20 ALD/MLD cycles was annealed also under Ar/H_2 at 450 °C for 30' and no evidence of crystallisation have been detected by Raman neither XANES. The reason behind this may be related to a significant loss of sulfur during annealing that results in the removal of all S in the case of a few ALD/MLD cycles. A thorough reflection about the annealing strategy should be performed in order to improve the understanding of the phenomena occuring this critical annealing step in order to obtain stoichiometric TiS_2 ultra-thin films afterwards. Consequently, in Chapter 4, we will follow the process by XRF *in situ*

measurements during the annealing step in order to monitor the evolution of the [S]/[Ti] ratio which could improve the structure of the synthesized ultra-thin films.

Chapter 4

Investigation Of The Transition Of Amorphous Ti-thiolate prepared by Hybrid ALD/MLD Into Titanium Disulfide Ultra-Thin Film

4.1 Introduction

The aim of this chapter is to control the transition from amorphous Ti-thiolate into crystalline TiS_2. Two different thermal annealing strategies capable of producing stoichiometric ultra-thin films of TiS_2 are presented. The necessity of using different annealing strategies depending on the Ti-thiolate thickness and sulfur content is demonstrated and discussed herein. *In situ* monitoring by X-ray fluorescence (XRF) is used to track the [S]/[Ti] ratio during the whole annealing process. Additional *ex situ* characterization such as X-ray Photoelectron Spectroscopies, elemental and structural analysis (TEM and Raman spectroscopy) were performed on the annealed TiS_2 thin films to characterize crystallinity, structure, and stoichiometry. Overall, this study has allowed the in-plane crystallization of ultra-thin lamellar stoichiometric TiS_2 at annealing temperature as mild as 300 °C. A major part of the results presented in this chapter were published in the Journal of Vacuum Science & Technology A (JVST A).

4.2 *In situ* monitoring of thiolate ALD/MLD growth by X-ray Fluorescence (XRF)

In the previous Chapter, TiS_2 layers were obtained upon the annealing of an 80 and 40 ALD/MLD cycles Ti-thiolate. The major concern of this chapter is to provide an enhancement of the thermal annealing strategy that permits to procedure ultra-thin films mainly composed of stoichiometric TiS_2. The synthesis proceeds with the growth of an amorphous Ti-thiolate at substrate temperature T_{sub}=50°C. In order to gain insight into the transition from amorphous to crystalline and control it, *in situ* experiments using the synchrotron X-ray radiation were performed and combined with other post-synthesis characterization techniques *ex situ* XPS/ HAXPES measurements. The evolution of the [S]/[Ti] ratio during the ALD/MLD step and annealing step was insightful to explore two new adequate annealing strategies.

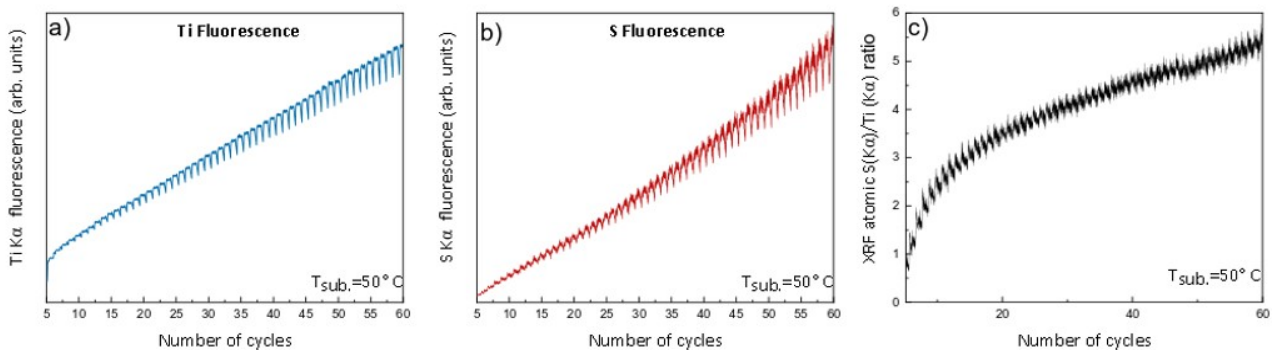

Figure 4.1: XRF intensity as a function of the number of cycles during the growth of a 60 ALD/MLD cycles Ti-thiolate (T_{sub} = 50 °C) of a) Ti Kα (blue line) and b) S Kα (red line). XRF [S]/[Ti] ratio (calibrated from XPS/HAXPES data of the 80-cycle ALD/MLD thiolate annealed under Ar/H_2 (4%) for 30').

To quantify the amounts of Ti and S deposited on the surface of the sample, *in situ* analyses were obtained by monitoring the Ti and S by XRF during each ALD/MLD cycle.[203] Note that *in situ* measurements are necessary as the Ti-thiolate is not stable in ambient conditions. The evolution of Ti and S K_α fluorescence intensity as a function of ALD/MLD cycle number is presented in Figure 4.1(a,b), for a 60 ALD/MLD cycles sample. The existence of a transient regime at the early stage of the process is due to the interaction of the thermally grown 100 nm SiO_2 substrate active surface with the first precursor pulses. Beyond, a steady XRF intensity increase of both XRF signals could be observed.

Figure 4.1-c shows the evolution of the calibrated XRF [S]/[Ti] ratio. The raw XRF intensity ratio S/Ti was calibrated with the total XRF [S]/[Ti] ratio of a stoichiometric reference sample. The reference sample was prepared from 80 ALD/MLD cycles and annealed under Ar/H_2(4%) at 450 °C for 30 min; its total thickness obtained by XRR was equal to 30 nm (see Chapter 3). For such thickness, the contribution of the oxidized regions present on the top of the TiS_2 and at the SiO_2/TiS_2 interface, is small. Indeed, XPS/HAXPES data confirmed that the S/Ti ratio, corresponding to the S bound to Ti, was very close to 2 (2.1), as expected for TiS_2 layers. One observes that S/Ti XRF intensity ratio does not stay constant and range from 0.8 (early stage) to 5.5 (higher cycle number). After 60 ALD/MLD cycles, the Ti-thiolate thickness was found to be 42±3 nm from the XRR curve fit measured *in situ*.

4.3 Thermal annealing strategies

Ar/H_2(5%) was selected as annealing gas because of the capability of H_2 to facilitate sulfur extrusion from sulfur-rich TiS_{2+x} compounds[184] (for instance, less S-S pairs were detected in the case of Ar/H_2(5%) comparing to N_2). The temperature ramp value was 10°C/min, as it prevents major sulfur loss during annealing or in other words, the formation of sub-stoichiometric layers.[233, 234] Two adequate annealing strategies, herein noted A and B, were studied by tracking the evolution of the XRF [S]/[Ti] atomic ratio aiming to produce ultra-thin TiS_2 films. Strategy A consists in increasing the temperature by steps while monitoring the XRF [S]/[Ti] ratio. Strategy B is a unique low temperature plateau, deduced from the results obtained with strategy A.

4.3.1 Thermal annealing strategy A

4.3.1.1 Strategy Description

The as-grown Ti-thiolate sample was annealed *in situ* under Ar/H_2(5%) flow (100 sccm), starting from thiolate substrate temperature (T_{sub}=50 °C). Figure 4.2 shows the evolution of the calibrated XRF [S]/[Ti] ratio along with the annealing temperature profile. The temperature plateau were decided live by checking the rate of decay of the [S]/[Ti] atomic ratio. The temperature plateau duration corresponds to the time necessary for the acquisition of Extended X-Ray Absorption Fine Structure (EXAFS) spectra (not presented in this dissera-

tion since results are under analysis) explaining the absence of experimental points in these regions.

From T_{sub} = 50 °C to 260 °C, a large decrease of the [S]/[Ti] ratio was observed ([S]/[Ti] = 5.8 to 4.0). It keeps decreasing from T_{sub} = 260 °C to 315 °C ([S]/[Ti] = 4.0 to 2.6) to reach at T_{sub} = 350°C a [S]/[Ti] ratio slightly above 2. To quickly achieve a stoichiometric sample, the annealing temperature was risen up to 385 °C. Finally after cooling down to room temperature, the [S]/[Ti] ratio remained very close to 2.

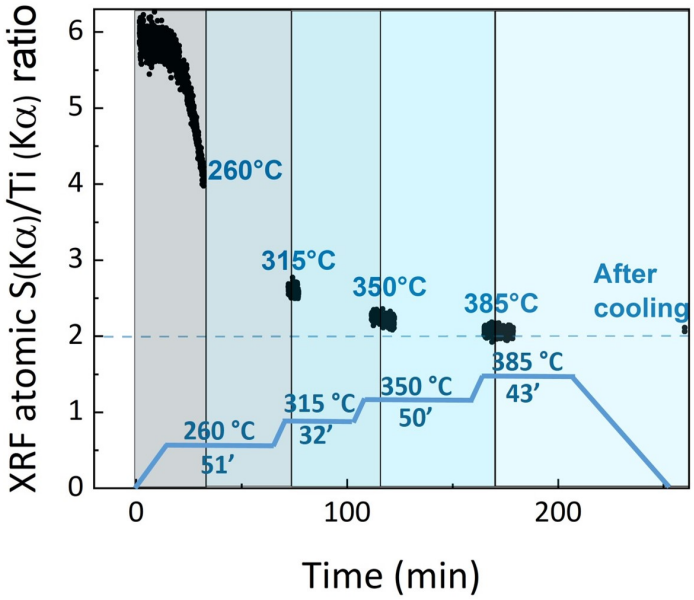

Figure 4.2: Calibrated XRF [S]/[Ti] atomic ratio as a function of time and substrate temperature, during the annealing under Ar/H_2(5%) of a 60-cycle ALD/MLD Ti-thiolate. This annealing is referred as strategy A.

When applying this annealing strategy, an important behavior was noticed, *i.e.* a major decrease of the ratio before reaching 315 °C, by about a factor of 2. This can be explained by two main reasons.

A first one, is likely related to the annealing atmosphere (Ar/H_2(5%)), since H_2 is known to improve the sulfur extrusion from sulfur-rich TiS_{2+x} phases.[184] The second one is provided by chemical experimental modeling carried on high surface area silica beads 3D substrate, herein called silica nanobeads.[120, 203] Figure 4.3 shows the *in situ* Diffuse Reflectance Infrared Fourier Transform (DRIFT) spectra of silica powder nanobeads acquired during the annealing treatment ($T_{annealing}$ = 20 °C to 500 °C) of a 2-cycle ALD/MLD Ti-

thiolate. The evolution of IR absorbance of the solid over temperature (see Figure 4.3) showed mineralization of the solid, which is the intensity decrease of all bands associated with thiolate organic fragments starting below 100°C leading to a fully inorganic sample by 300°C. Indeed, signals at around 2700-3000 cm^{-1}, assigned to organic moieties CH_x stretching vibration modes, are almost completely disappeared at 300°C, confirming that the loss of organic moieties occurs below 300°C. Over the annealing procedure, the IR component centered at 3650 cm^{-1} assigned to the vibration mode of surface hydroxyl groups, substantially increases. This datum is coherent with the fact that annealing induces densification of the phase (as expected for the thiolate to sulfide transition). As shown elsewhere, the starting amorphous thiolate achieves maximum chemical coverage.[203] The densification of such a thiolate to sulfide can thus lead to discontinuous layers and hence hydroxyl regeneration. Concomitant analysis of the gas phase (see Figure D.2 in Appendix D) showed the release of various gaseous fragments such as H_2S, ethylene, hydrogen disulfide, methylisocyanide, thiirane, and ethanethiol. Figure D.3 in Appendix D shows a schematic presentation of possible mechanistic pathways for the mineralization of the surface sites to titanium disulfide and sulfide, and fragmentation of some part of the ligands to ethylene, H_2S, thiirane, methylisocyanide. In summary, the obtained results on silica nanobeads corroborated the datum acquired on silicon wafer where the major decay of the [S]/[Ti] ratio is observed from 50 °C to 315 °C, and provide possible mechanistic pathways.

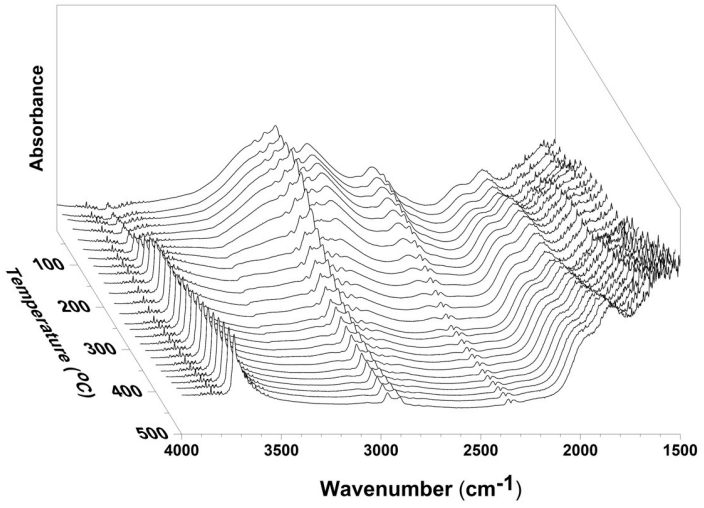

Figure 4.3: *In situ* infrared spectra of the silica nanobeads-supported Ti thiolate obtained by 2 ALD/MLD cycles recorded upon thermal treatment from 20 °C to 500 °C.

The annealing strategy A gives insights on the process to apply en route to stoichiometric TiS_2 layers. Nevertheless, additional analyses were required to validate its efficiency. Hence, elemental and structural analyses were performed on the annealed TiS_2 films to characterize their stoichiometry, crystallinity and structure.

4.3.1.2 Chemical composition: photoelectron Spectroscopy analyses

In order to confirm the atomic ratio determined *in situ* by XRF (Figure 4.2) and obtain further information on chemical bonding, ARXPS experiments we carried out on the annealed 60-cycle ALD/MLD films. Figure 4.4 shows the XPS spectra of Ti 2p, S 2p, and C 1s core peaks. TiS_2 is known to convert to TiO_x by exposure to air.[212] For this reason the Ti 2p XPS spectra (Figure 4.4 (a-d-g)) present two different Ti 2p$^{3/2}$:2p$^{1/2}$ spin-orbit doublets. The most intense at high binding energy (458.8 eV and 464.5 eV) corresponds to titanium oxysulfide (TiO_xS_y).[218, 217, 216, 215] The less intense doublet (457.0 eV and 462.7 eV) is assigned to TiS_2.[206, 215, 216]. The TiS_2 contribution significantly increases as the depth analysis increase, confirming that the oxide is mainly located at the topmost surface of the deposited film. Assuming that the oxidized top layer TiO_x is homogeneous, non-porous, and covering the TiS_2 film with an average composition, a simple model allows to estimate its thickness at around 2nm. [235]

The S-2p XPS spectra shown in Figure 4.4 (b-e-h) present also two S 2p$^{3/2}$:2p$^{1/2}$ components. The intense doublet (161.2 eV and 162.3 eV, spinorbit doublet of S2p species) corresponds to TiS_2. [215, 218] The weak doublet signal (162.8 eV and 164.0 eV) could be attributed to different species such as a S-S pair and/or to C-S bonds. Based on the widening of this weak peak component, we could also assign this environment, to a combination of $(S_n)^{2-}$ bridging sulfur (where n=2,4).[219] In addition, it could be referred to titanium oxysulfide environment in connection with the oxidized part already detected on the surface of the TiS_2 film.[136, 217, 220, 221] ARXPS data shows a large amount of carbon inside the thin films (see Figure 4.4 (c-f-i)) and not only at the top surface of the layer. Indeed, the C 1s core level spectra exhibit three components originating from different sources, which do not decrease with the thickness analysis. The main one, which corresponds to C-H/C-C bonding, could originate from adventitious carbon but also from the incomplete reaction of TDMAT [124]. Note that the presence of graphitic carbon is not to be excluded, as observed in MoS_2 and WS_2 thin films obtained by similar methods.[120] In addition, the C1s core spectrum

shows the presence of oxidized carbons (C-O and C=O) coming from surface contamination [136] (peaks at 286.2 and 288.8 eV respectively). Importantly, the component at 286.6 eV could also be assigned to C-S bonds indicating an incomplete reaction of EDT.

Binding energies (BE) and atomic concentrations (at.%) of the different chemical environments identified by XPS are reported in Appendix C (Table C.1) for better clarity. The quantitative results permit to calculate the atomic ratio of [S]/[Ti] considering the Ti2p and S2p doublets attributed to TiS_2. It is equal to 1.9, confirming that the deposited film is composed of stoichiometric TiS_2.

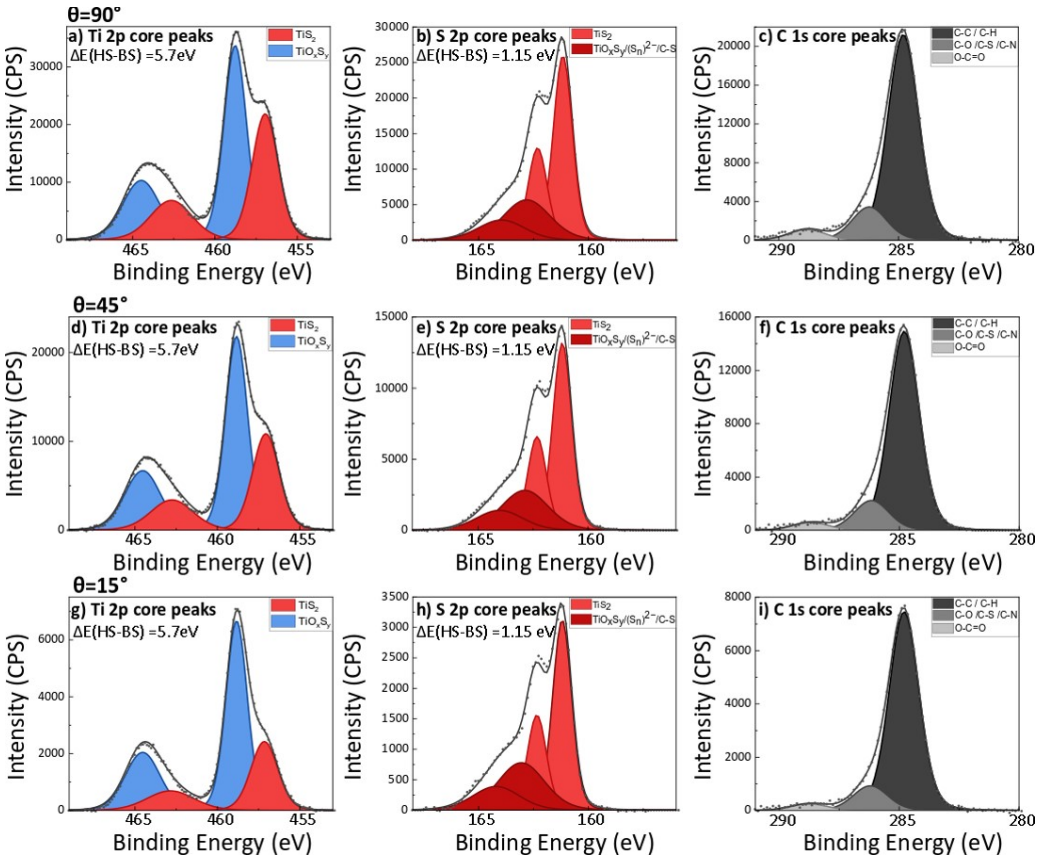

Figure 4.4: XPS lines of Ti 2p, S 2p and C 1s core measured at different angles (θ = 90°, 45° and 15°) with respect to the surface normal for the annealed 60-cycle ALD/MLD Ti-thiolate sample using annealing strategy A.

The small depth analysis of XPS remains a major limiting factor to study buried interfaces, since the obtained TiS_2 thin films are oxidized in ambient conditions. For this reason, HAXPES measurements were conducted to investigate the in-depth chemical composition

of the TiS_2 film. Both Ti 2p and S 2p spectra are presented in Figure 4.5. Binding energies (BE) and atomic concentrations (at.%) of the different chemical environments identified by HAXPES are also reported in Table 4.1. The doublets position and attribution are the same as those previously discussed in the ARXPS study. Noticeably, the most intense doublet in Figure 4.5-a is assigned to TiS_2; thus HAXPES measurements limits the contribution of oxidized layer at the surface of the TiS_2 and leads to an accurate deconvolution of the titanium spectra. Concerning the S-2p XPS spectrum presented in Figure 4.5-b, the amount of bridging sulfur and sulfur residues from EDT characterized by components at higher binding energy does not decrease meaning that the mentioned sulfur species are located throughout the thickness of the film.

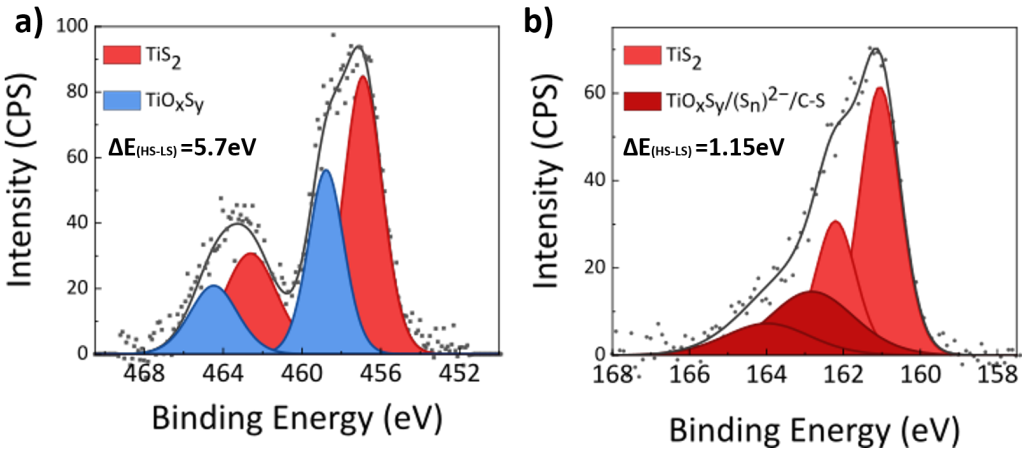

Figure 4.5: HAXPES spectra measured with the Cr Kα source for the annealed 60-cycle ALD/MLD Ti-thiolate using annealing strategy A: Intensity as a function of the electron binding energy a) Ti-2p core peaks (doublets) and (b) S-2p core peaks (doublets).

Table 4.1: Binding energies (BE) and atomic percentages (at.%) of the different chemical environments identified by HAXPES at the surface of a 60-cycle ALD/MLD Ti-thiolate using annealing strategy A.

Element	Attribution	Position (eV)	Percentage (%)
Ti 2p	TiS_2 2p3/2	456.8	6.2
	TiS_2 2p1/2	462.5	3.1
	TiO_2 2p3/2	458.8	3.8
	TiO_2 2p1/2	464.5	1.9
S 2p	TiS_2 2p3/2	161.1	14.6
	TiS_2 2p1/2	162.2	7.3
	$TiO_xS_y/(S_n)^{2-}$/C-S 2p3/2	162.8	7.2
	$TiO_xS_y/(S_n)^{2-}$/C-S 2p1/2	164.0	3.6
O 1s	TiO_2	530.5	13.9
	C-O/O-C=O/SiO_2	532.5	6.8
C 1s	C-C/C-H	284.8	25.9
	C-O/C-S	287.9	5.1
Si 1s	SiO_2	1843.9	0.5

Similarly, the carbon content is not assigned only to surface contamination. With chromium source, the atomic ratio of [S]/[Ti] obtained is equal to 2.3. The atomic ratio [S]/[Ti] using the Cr source (equal to 2.3, see deep blue column in Figure 4.6), is in agreement with the Al source (equal to 1.9, red column in Figure 4.6). The difference in values can be explained by the large sampling depth variation between the two sources (minimizing the contribution of the upper surface of the sample using the Cr source and decreasing the uncertainty on the Ti2p spectra fitting). Both XPS and HAXPES confirm that the annealing strategy A, applied affords to obtain a film composed of stoichiometric TiS_2.

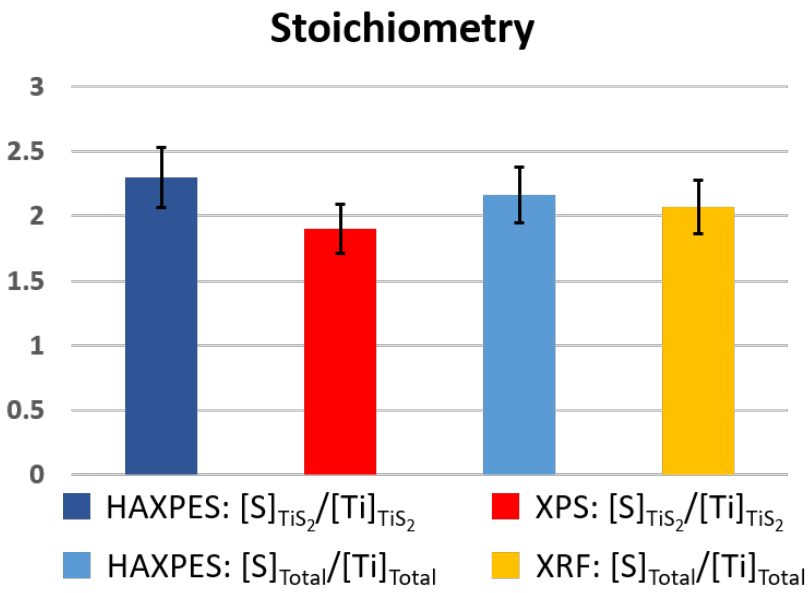

Figure 4.6: Stoichiometry study and correlation of results obtained by HAXPES, XPS and *in situ* XRF for 60-cycle ALD/MLD Ti-thiolate annealed with using strategy A. Black vertical segments represent error bars.

Since XRF cannot identify the elemental composition and attribution of each element, the total amount of S over the total amount of Ti, determined by HAXPES, was calculated (light blue column in Figure 4.6). Additional quantitative details are presented in Table 4.1. In Figure 4.6, the HAXPES (blue columns) and *in situ* XRF (yellow column) [S]/[Ti] ratio are almost the same, confirming the calibration method of the XRF [S]/[Ti] ratio by the ratio calculated by XPS/HAXPES with a thicker stoichiometric crystalline TiS_2 reference film.

4.3.1.3 Microstructural-crystallinity analysis of 60-cycle and 40-cycle ALD/MLD annealed thiolates: Raman scattering spectroscopy and Electron microscopy

Since the thermal annealing strategy A succeeded to give stoichiometric TiS_2 thin films from a 60-cycle ALD/MLD Ti-thiolate, the capacity of obtaining ultra-thin stoichiometric TiS_2 thin films using this strategy was further explored. Hence, 60-cycles and 40-cycles ALD/MLD Ti-thiolates were grown and annealed with strategy A. After annealing, the thicknesses of the 60-cycle and 40-cycle ALD/MLD films determined by the fitting of XRR curves, were 19.4±0.4 nm and 13.3±0.2 nm, respectively (See Figure D.4-(a,b) in Appendix D).

The Raman spectra of these two samples are shown in Figure 4.7-a,b). The Eg, A1g and Sh- characteristic modes of 1T-TiS_2[203, 132] are observed close to 218.2 cm^{-1}, 336.8 cm^{-1} and 375.0 cm^{-1} for the 60-cycle, and close to 224.3 cm^{-1}, 337.6 cm^{-1} and 378.0 cm^{-1} for the 40-cycle sample. The observed Raman shift in the position of the Eg mode is assigned to the thickness variation of the thin film.[132] By comparison with the results found in the literature and obtained with a reference TiS_2 powder, the overall spectra indicate the good crystalline quality of the samples with likely some defaults in between the layers as indicated by the presence of the Sh mode.[132, 136]

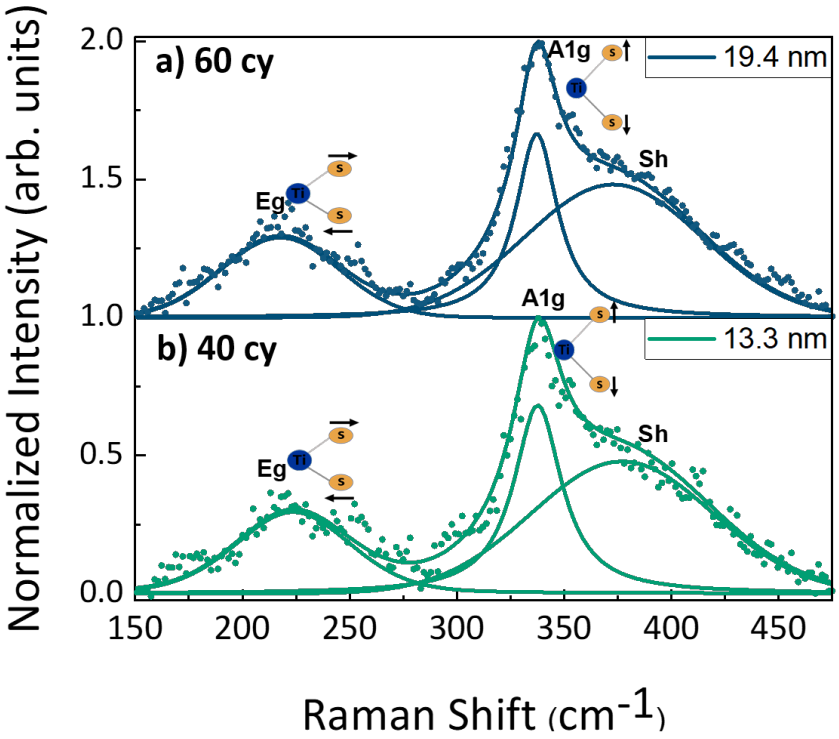

Figure 4.7: Raman spectra (dots) of samples resulting from a) 60-cycle and b) 40-cycle ALD/MLD Ti-thiolates using annealing strategy A. Raman spectra were normalized to the intensity of the A1g mode. Lorentzian function was used to fit the A1g mode and Gaussian-Lorentzian function to fit the Eg and Sh modes (solid lines in a) and b) panels).

TEM images (Figure 4.8-a) reveal a continuous thin film, with low surface roughness. The nanoscale structure shows the presence of textured nanodomains made of a few TiS_2 layers, in agreement with the Raman data discussed above. The interlayer distance between TiS_2 layers is equal to 5.8±0.1 Å close to the bulk 1T-TiS_2 c-parameter, 5.7 Å (PDF 01-070-

6204, and [46]). The lamellar sulfide is covered by an amorphous 2 nm-thick top layer, which presumably results from the hydrolysis and oxidation of the material exposed to air, and should therefore probably be titanium oxysulfide. At the bottom, the sulfide film/SiO_2 interface is not sharp. The interface regions, about 2 nm thick (can be corroborated with the ARXPS results related to surface oxide thickness estimation), are likely to be oxysulfides resulting from chemical reaction with oxygen from the air on one hand; and precursors with the silicon oxide substrate surface on the other.

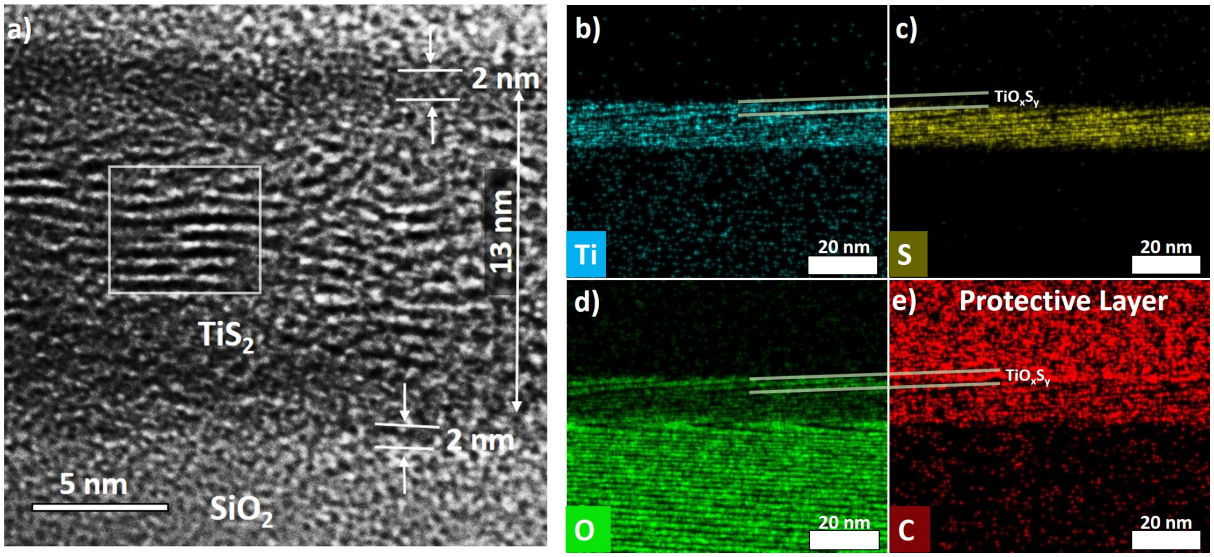

Figure 4.8: a) Cross section TEM images and b-e) element mappings (EDX) of b) Ti, c) S, d) O and e) C elements of a sample obtained from 40 ALD/MLD cycles and annealed under $Ar/H_2(5\%)$ using the annealing strategy A.

TEM-EDX element mapping in Figure 4.8 b-e shows the distribution of the elements inside the thin film. The oxidized layer is evidenced by the difference in thickness of the Ti and S maps (Figure 4.8 b and c, respectively) and the O mapping (Figure 4.8 d). C elemental mapping (Figure 4.8 e) suggests an important carbon content inside the thin film, in agreement with HAXPES analysis (about 25% of carbon content).

In addition, to protect the thin film integrity during TEM preparation a carbon film was deposited on top of the sample (see Figure 4.8 e). Concerning the stoichiometry, HAXPES study of the annealed 40-cycle ALD/MLD sample still shows an atomic ratio [S]/[Ti] close to 2.3 in agreement with the value obtained for the 60-cycle (Binding energies (BE) and atomic concentrations (at.%) of the different chemical environments identified by HAXPES

are listed in Table C.3 in Appendix C). All those data confirm the global stoichiometry of the obtained TiS_2 layers domains, even for a film as thin as 13.3 nm.

4.3.2 Thermal annealing strategy B

4.3.2.1 Strategy description

While annealing strategy A has allowed to synthesize thin films composed of good quality TiS_2 layered domain, the deposit is however composed of a significant quantity of carbon and of bridging sulfur which probably hinder a large scale crystallization and explain the presence of amorphous areas in the film (observed in TEM). Several questions are pending:

- At which temperature does the transition from amorphous to crystalline occur?
- Does the time of annealing play an important role in terms of enhancing the quality of the annealed film?
- Strategy A has allowed to obtain good quality TiS_2 layers at 385 °C, compared to 450 °C in the previous study.[203] Is it necessary to anneal at temperature as high as 385 °C ?, or is it possible obtain TiS_2 by annealing at even lower temperature?

To try to answer these questions, a second annealing strategy, referred to **annealing strategy B**, was applied.

In the section 4.3.1 the fast decrease of the [S]/[Ti] ratio in the temperature range of 50 °C-315 °C confirms that the loss of organic moieties occurs below 300°C and a fully inorganic sample is reached by 300°C (Figure 4.3). For this reason annealing temperature was kept at 300 °C and the evolution of the [S]/[Ti] ratio monitored by *in situ* XRF (Figure 4.9). As in the case of annealing strategy A, the annealing as perfomred in a 100sccm Ar/H_2 flow.

Annealing strategy B was applied on a Ti-thiolate thin film obtained from 40 ALD/MLD cycles. The thickness of the as-deposited film, equal to 32±3 nm, was determined by fitting an XRR curve measured *in situ*. The [S]/[Ti] ratio rapidly decreased while the annealing temperature reached 300 °C at the rate of 10 °C/min. After 135 min at 300 °C, the [S]/[Ti] ratio stabilized near the value of 2. Then the sample was cooled down to room temperature. After annealing, the sample thickness as determined by XRR was equal to 13.9±0.3nm (see Figure D.4-c in Appendix D) and the XRF [S]/[Ti] ratio was about 2.

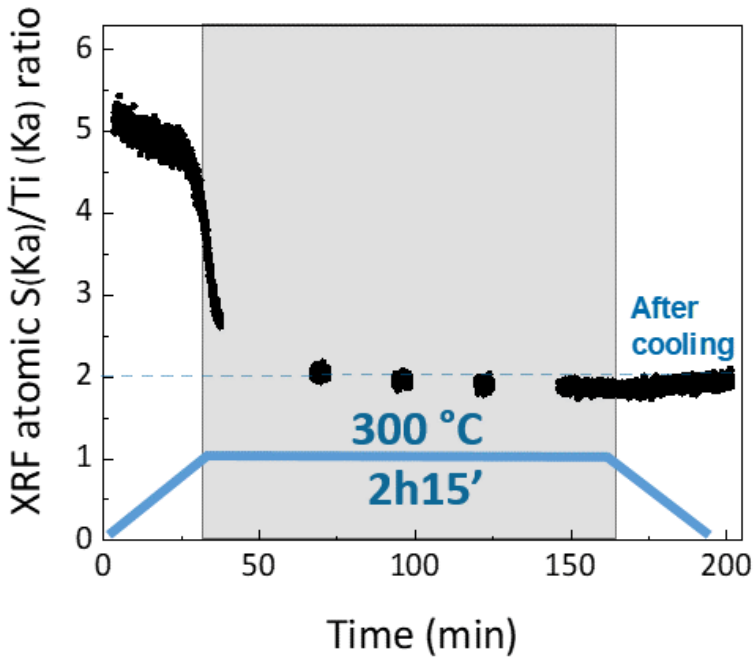

Figure 4.9: Calibrated XRF [S]/[Ti] atomic ratio as a function of time and substrate temperature during the annealing under $Ar/H_2(5\%)$ of a 40-cycle ALD/MLD Ti-thiolate. This annealing is referred as strategy B.

4.3.2.2 Toward ultra-thin thin films: A major challenge

The same strategy (B) was applied to anneal a 20-cycle ALD/MLD Ti-thiolate aiming to lower even further the number of TiS_2 layers. After annealing, the thickness of the sample as determined by XRR was 5.5±0.4 nm (See Figure D.4-d in Appendix D). Then, the efficiency of the annealing was further evaluated by elemental and structural characterizations of the thin film. Raman spectra were performed on both annealed 40-cycle and 20-cycle ALD/MLD samples to evaluate their crystallinity (Figure 4.10-a&-b, respectively). They show the presence of Eg, A1g and Sh- characteristic modes of 1T-TiS_2 close to 222.7 cm^{-1}, 337.7 cm^{-1} and 376.0 cm^{-1}, for the 40-cycle, and close to 234.0 cm^{-1}, 336.7 cm^{-1}, and 390.0 cm^{-1} for the 20-cycle. In the case of the 20-cycle, the spectrum shows the contribution of the silicon-substrate at $\sim$ 300 cm^{-1} (corresponding to the 2nd order mode of silicon) (see inset in Figure 4.10-b). The presence of the signal of the underlaying substrate attests that the penetration depth of the excitation laser (532 nm) is higher than the thickness of the thin film. In other words, this confirms the low thickness of the annealed 20-cycle ALD/MLD

sample. The difference between the Raman spectra for TiS_2 samples of different thicknesses is discussed in an additional study presented in Section D.1 in Appendix D.

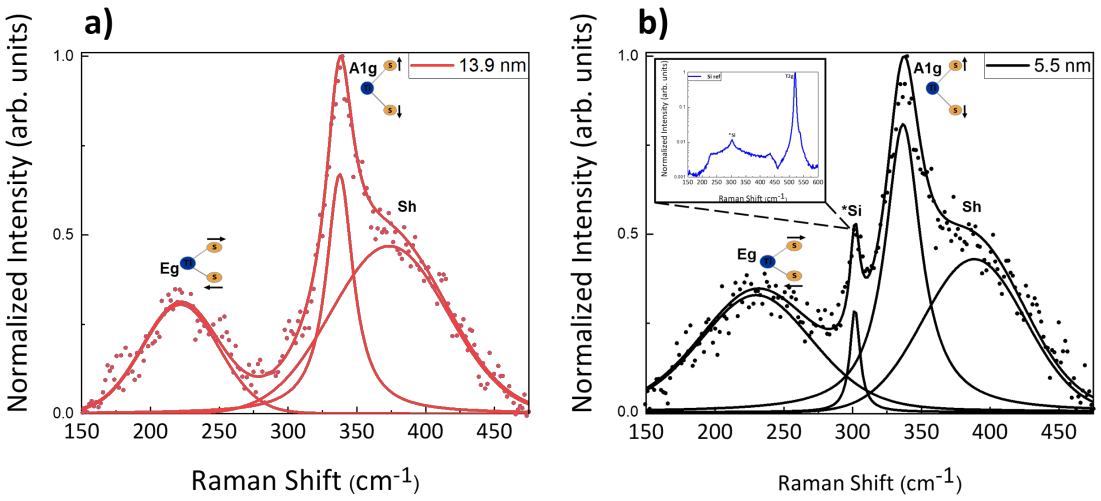

Figure 4.10: Raman spectra (dots) of a) 40-cycle and b) 20-cycle ALD/MLD Ti-thiolates annealed using annealing strategy B. Raman spectra were normalized to the intensity of the A1g mode and fitted with Lorentzian function (A1g and *Si modes) and Gaussian-Lorentzian function (Eg and Sh modes) (solid lines panels). The inset in b) show Raman spectrum of Silicon substrate.

TEM image of the annealed 20-cycle ALD/MLD sample, shown in Figure 4.11-a, reveals a continuous thin film with low surface roughness. TiS_2 layers are not visible, which seems contradictory to Raman observations. This could be due to the presence of oxygen or electron beam damage, since the sample is only few nanometers thick (5.5 nm).

Elemental distribution inside the ultra-thin film was provided by EDX mapping as shown in Figure 4.11 b-e. The Ti and S mapping (Figure 4.11 b and c, respectively) show a Ti containing thin film with an upper S depleted region. The latter, was also confirmed by the O mapping in Figure 4.11-d, demonstrating the presence of an oxidized region. The evidence of an upper oxide thin film is in agreement with the EDX observations performed on the 40-cycle ALD/MLD sample annealed with strategy A (see Figure 4.8-b-c).

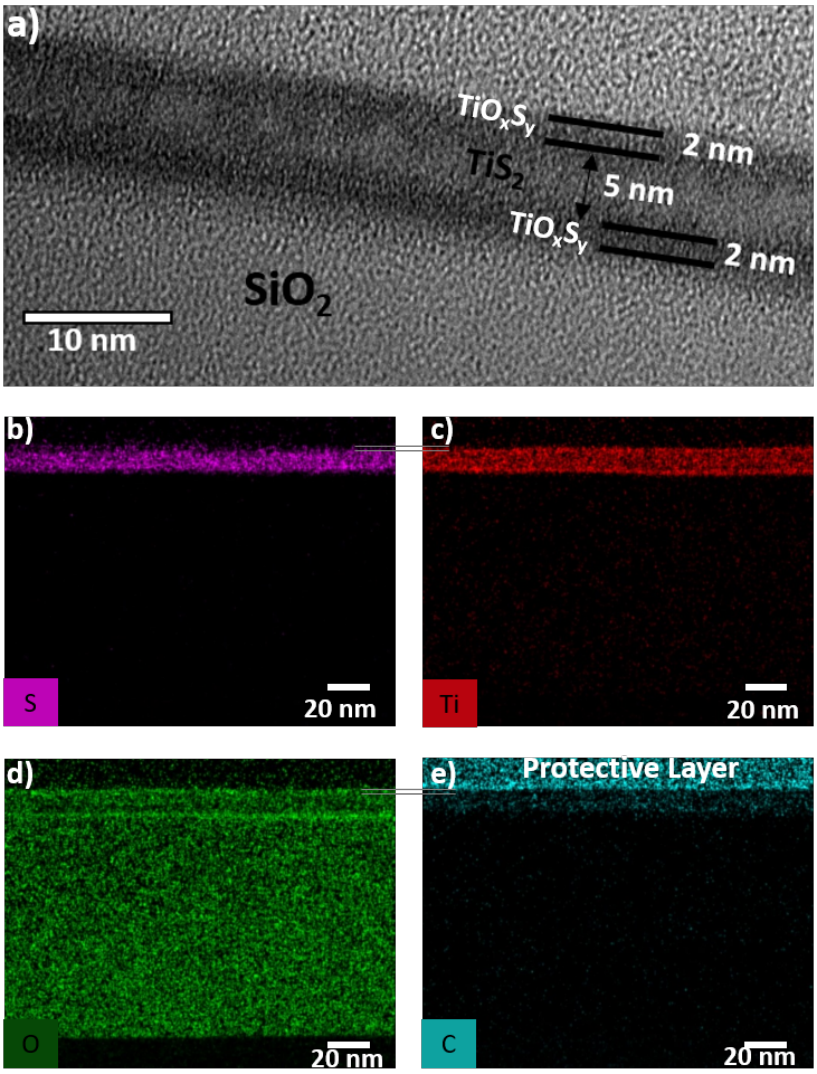

Figure 4.11: a) Cross section TEM images and element mapping (EDX) of b) S, c) Ti, d) O and e) C elements of a 20-cycle ALD/MLD sample annealed using annealing strategy B.

HAXPES measurements were performed on both films to check their chemical composition. Binding energies (BE) and atomic concentrations (at.%) of the different chemical environments identified by HAXPES are reported in Appendix C (Table C.4 and Table C.5). As reported above, the atomic ratio [S]/[Ti] considering the Ti2p and S2p doublets attributed to TiS_2 were calculated and found equal to 2.3 for both samples, confirming the synthesis of quasi-stoichiometric TiS_2. Although the 20-cycle ALD/MLD sample annealed, is very thin

(less than 6 nm thick), a significant carbon content is still detected (around 15% according to HAXPES). Finally, the thickness of the oxidized layer on the top of TiS_2 is almost the same (about 2 nm), no matter what annealing strategy was applied (also in agreement with our results presented in Chapter 3 [203]).

To obtain additional information about the local structure of the annealed samples as a function of annealing treatment and film thickness, we measured XANES spectra at the S K-edge (2742 eV) with the X-ray beam polarization vector parallel to the sample surface. Some of them are represented in Figure 4.12. Note that the contribution to the XANES spectra of the oxidized regions, which are present at the sample surface and sulfide/SiO_2 interface, must be small at the sulfur K-edge, because sulfur atoms were mostly removed out of these ill-ordered regions (see Figure 4.8a, 4.11b). On contrary, the XANES spectra recorded at the Ti K-edge are sensitive to these regions, the thinner the film the more these regions contribute to the XANES spectra.

In a previous XANES study at the Ti K-edge, we demonstrated that the XANES spectra of the 40-cycle and 80-cycle ALD/MLD samples annealed at 450 °C for 30 min, showed close similarities (features) with the reference XANES spectrum of a TiS_2 powder.[203] The same behavior is observed at the S K-edge (see (b), (c) and (d) spectra in Figure 4.12). Figure 4.12 (a) and (e) show the XANES spectra measured at the S K-edge of a 20-cycle ALD/MLD Ti-thiolate after two different annealing: at 450 °C for 30 min (Ar/H_2(4%) gas, temperature ramp of 10°C/min), and using thermal annealing strategy B. The thicknesses of the two films were 8 and 5.5 nm, respectively. The XANES spectrum of the sample annealed with strategy B presents close similarities to the spectrum of TiS_2 powder reference, while that of the sample annealed at 450 °C is very different. These XANES results allows us to conclude that the thermal annealing strategy B led to atomic local order which tends to the one of TiS_2 layers. Also, it confirms that the strategy to adopt for the mineralization of the Ti-thiolate and obtain the desired crystalline phase depends on the target film thickness. The quantitative simulations of these spectra is under progress by our collaborators at SOLEIL.

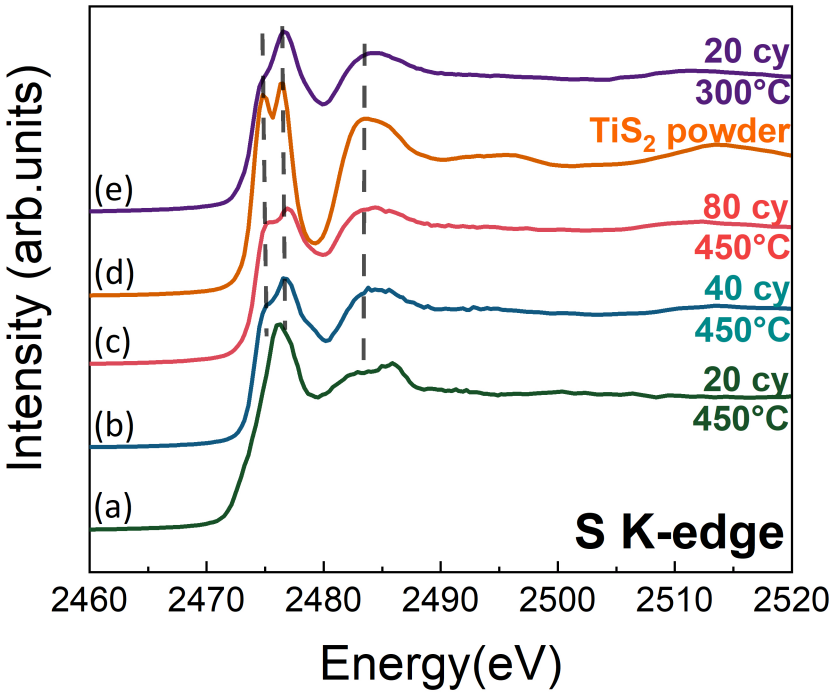

Figure 4.12: XANES spectra recorded at the S K-edge of Ti-thiolate thin films further annealed under $Ar/H_2(4\%)$ gas at 450 °C for 30 minutes, obtained from (a) 20-cycle ALD/MLD, (b) 40-cycle ALD/MLD and (c) 80-cycle ALD/MLD; (d) XANES spectrum of a reference TiS_2 powder recorded in fluorescence mode; (e) XANES spectrum of a 20-cycle ALD/MLD thin film annealed using thermal annealing strategy B.

4.3.3 Gas Effect study: $Ar/H_2(5\%)$ versus N_2

In previous sections we have shown the importance of *in situ* XRF, to optimize the annealing strategy. Stoichiometric oriented TiS_2 layers parallel to the substrate direction have been obtained when growing either a 40-cycle or a 60-cycle ALD/MLD film further annealed under $Ar/H_2(5\%)$ using annealing strategy A (confirmed by XPS, HAXPES, RAMAN, and TEM images). Moreover, TEM images showed that the texturation of the TiS_2 monolayers has improved compared to the one presented in Chapter 3.

In order to evaluate the impact of the gas used during the annealing, which could affect the outcoming material quality, we performed another annealing under a second gas. Indeed, the $Ar/H_2(5\%)$ gas was firstly used for annealing sulfide materials since H_2 is well

known to facilitate sulfur extrusion from sulfur-rich TiS_{2+x} phases.[184, 137] Nevertheless, to validate definitively the use of Ar/H_2 gas, two 60-cycle ALD/MLD Ti-thiolates were grown and annealed using strategy A under Ar/H_2 and under N_2.

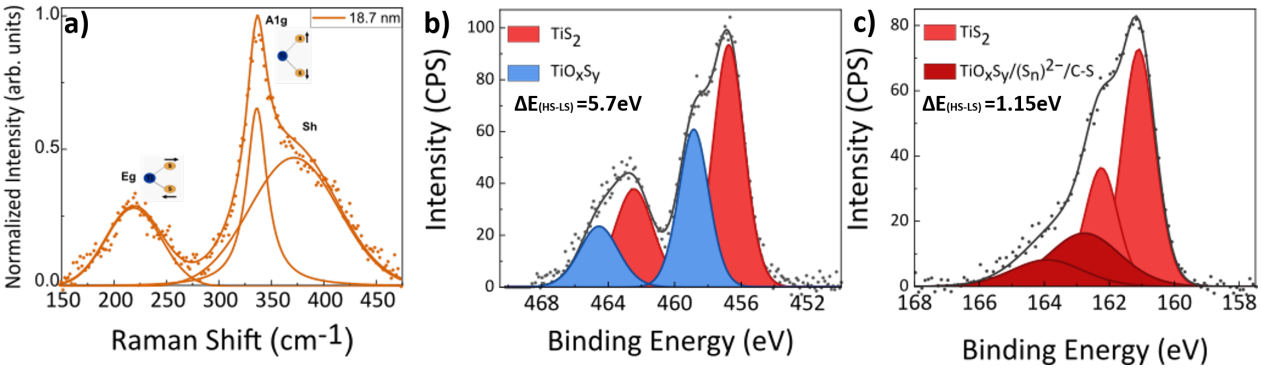

Figure 4.13: a) Raman spectrum normalized with the intensity of the A1g mode (dots). b-c) HAXPES spectra measured with the Cr Kα source: Intensity as a function of the electron binding energy of: b) Ti-2p core peaks (doublets) and c) S-2p core peaks (doublets) for the 60 ALD/MLD cycles annealed under N_2 using the annealing strategy A. Lorentzian function was used to fit the A1g mode and Gaussian-Lorentzian function to fit the Eg and Sh modes (solid lines in a) panel).

After annealing under N_2, the thickness measured by XRR, equal to 18.7±0.3 nm, was found to be about the same as the one obtained for the sample annealed under $Ar/H_2(5\%)$, 19.4±0.4 nm. The Raman scattering spectrum of the sample annealed under N_2, presented in Figure 4.13-a, reveals the presence of Eg and A1g active modes corresponding to 1T-TiS_2. The shoulder mode (Sh) is also visible at about 373 cm^{-1}. No significant difference with the raman spectrum (Figure 4.7-a) coming from the analysis of the sample annealed under Ar/H_2 was noticed.

In addition, we performed HAXPES measurements in order to investigate the differences in term of composition of the two samples. The same environments were observed on both the Ti 2p and S 2p XPS spectra as shown in Figure 4.13-b,c. The quantitative results are presented in Table 4.2. Considering the sulfur and titanium components attributed to TiS_2, a stoichiometry equal to 2.3 can be calculated, which is in full agreement with the sample annealed under $Ar/H_2(5\%)$. However, if we compare the total (S/Ti) ratio, we notice that the value obtained for the N_2 annealed sample is slightly higher (2.3 vs 2.1) in comparison to the one obtained for the Ar/H_2 annealed sample, which means an excess of sulfur after the N_2 annealing. This decrease in the ratio in the Ar/H_2 case (5%) can be attributed to the

reduction of S-S pairs since the stoichiometry of the TiS_2 monolayers was precisely the same for both samples. Indeed, the ratio between the percentage of S-S pairs and the total amount of sulfur detected could be used to validate this finding:

$$\frac{[S]_{(S_n)^{2-}}}{[S]_{total}} \tag{4.1}$$

Table 4.2: Binding energies (BE) and atomic percentages (at.%) of the different chemical environments identified by HAXPES at the surface of a 60-cycle ALD/MLD Ti-thiolate using annealing strategy A under N_2.

Element	Attribution	Position (eV)	Percentage (%)
Ti 2p	TiS_2 2p3/2	456.7	7.1
	TiS_2 2p1/2	462.4	3.5
	TiO_2 2p3/2	458.9	4.2
	TiO_2 2p1/2	464.6	2.1
S 2p	TiS_2 2p3/2	161.1	16.3
	TiS_2 2p1/2	162.2	8.2
	TiO_xS_y/$(S_n)^{2-}$/C-S 2p3/2	162.8	9.1
	TiO_xS_y/$(S_n)^{2-}$/C-S 2p1/2	164.0	4.6
O 1s	TiO_2	530.7	15.0
	C-O/O-C=O/SiO_2	533.1	5.2
C 1s	C-C/C-H	284.8	18.4
	C-O/C-S	286.5	5.5
Si 1s	SiO_2	1844.0	1.0

The following ratio is higher in the case of N_2 annealing, 0.36 compared to 0.31 in the case of Ar/H_2(5%) annealing. Although the difference is not very large (and more samples would be needed to conclude with certainty), it is an indication in agreement with the literature and the effect of Ar/H_2 gas on sulfur. Finally, it seems that the Ar/H_2(5%) mixture is more suitable to remove excess sulfur and especially bridging S-S pairs in TiS_2 films.

4.4 Effect of injected amount of sulphur on the stoichiometry evolution during thermal annealing

The [S]/[Ti] ratio of a 40-cycle ALD/MLD Ti-thiolate annealed with strategy B (described in Figure 4.9) is resulting from the Ti and S XRF as Figure 4.14 shows. One can notice that during the annealing and cooling step (above 170 min), the S XRF intensity (Figure 4.14-b) decreases very fast comparing to the Ti XRF signal (Figure 4.14-a). The significant loss of sulfur during annealing (Figure 4.9) results in the formation of a thin film composed of monolayers of TiS_2 but also carbon and bridging sulfurs. Then, we wondered if more S was injected into the Ti-thiolate would increase the amount of sulfur and amorphous nanodomains and even lead to the synthesis of TiS_3. For this purpose, we grow Ti-thiolate by doubling the injection time of EDT, the sulfur precursor.

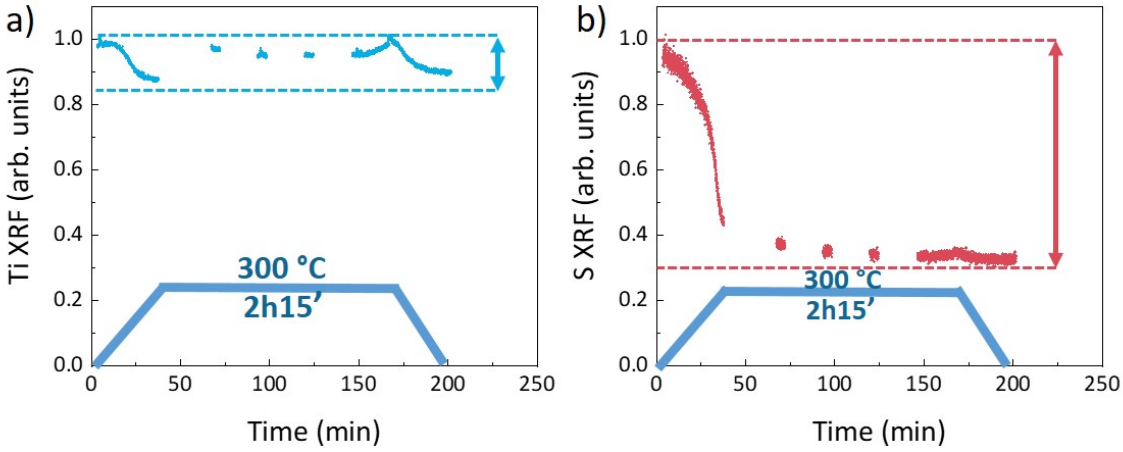

Figure 4.14: *In situ* XRF intensity of a) Ti and b) S k_α during annealing under Ar/H_2(5%) gas of a 40-cycle ALD/MLD Ti-thiolate, using annealing strategy B.

We applied adequate thermal annealing strategies (A and B) on new Ti-thiolate samples. The Ti-thiolate growth conditions were the same as usual except the duration of EDT injection which was multiplied by two. In this context, 40-cycle ALD/MLD Ti-thiolate was grown as following: $t_{injTDMAT}$=60, $t_{PurgeTDMAT}$=45, t_{injEDT}=60, $t_{PurgeEDT}$=45s.

During the growth of the 40-cycle ALD/MLD samples, we carried out *in situ* ellipsometry measurements, presented in Figure 4.15, that evidence the formation of a thicker film

when using EDT injection time of 60s time rather than 30s. In addition, in the steady state region (red line in Figure 4.15), we obtain a GPC=0.6 nm.cy^{-1} in the case of 60s injection time compared to 0.3 nm.cy^{-1} in the case of 30s injection time.

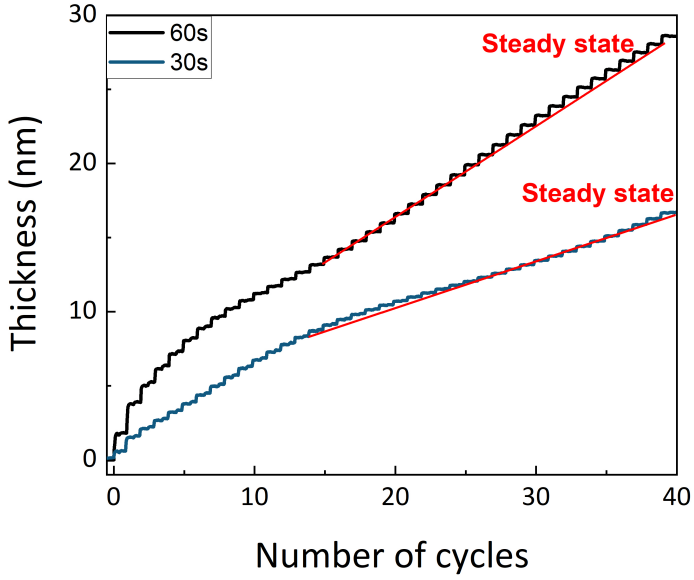

Figure 4.15: Film thickness increase measured by multiwavelength ellipsometry during the growth of 40-cycle ALD/MLD with 30s (blue line) and 60s (black line) EDT injection time.

4.4.1 Stoichiometry of the 40- and 20-cycle ALD/MLD thiolates and using thermal annealing strategy B and Ar/H_2(5%)

After annealing under Ar/H_2(5%) using strategy B of a 40-cycle Ti-thiolate grown with an EDT injection time of 60s, a thicker film was found by XRR after growing. The deposited thickness according to the simulated XRR curves was equal to 18.1±0.5nm vs 13.9±0.3nm in the case of the sample obtained with an EDT injection time of 30s. This corroborates what was observed by *in situ* ellipsometry during the thiolate growth.

HAXPES analysis were performed to estimate the stoichiometry of the film obtained with an EDT injection time of 60s. The results with the different quantitative attributions and environments are listed in Table C.6 in Appendix C. The film stoichiometry was calculated by considering the atomic ratio [S]/[Ti] with the Ti 2p and S 2p doublets attributed to TiS_2

and found to equal to 2.5 evidencing a higher value than the quasi-stoichiometric value of 2.3 for TiS_2 layers discussed earlier. The higher value suggest a sulfur over stoichiometry. In addition, the total [S]/[Ti] ratio was found to be equal to equal to 2.8 in the case of an EDT injection time of 60s comparing to 1.9 in previous cases. An 20-cycle ALD/MLD Ti-thiolate was also grown and annealed using the same annealing strategy in order to evaluate the thickness impact on the stoichiometry of the film grown with a long EDT pulse (60s). The film thickness of the 20-cycle ALD/MLD thin film obtained after annealing was found equal to 9.3$\pm$0.3nm according to the fitting of a XRR curve. As far as the stoichiometry is concerned, the HAXPES quantitatve results (Table C.7 in Appendix C) confirm that the atomic ratio [S]/[Ti] attributed to Ti_xS stays equal to 2.5, characteristic of a higher value of quasi-stochiometry even in the case of the thin 20-cycle ALD/MLD sample.

Raman scattering spectra measured with an excitation frequency in the visible range (532 nm) are shown in Figure 4.16. We can observe the presence of Eg and A1g active modes corresponding to 1T-TiS_2 in both cases: 40 and 20 ALD/MLD cycles. For the 40-cycle ALD/MLD sample, the Eg mode was visible at 220.2 cm^{-1}, A1g mode at 337 cm^{-1} and shoulder mode (Sh) at about 375 cm^{-1}. In the case of the 20-cycle ALD/MLD sample, the Eg mode was visible at 227.7 cm^{-1}, A1g mode at 338.8 cm^{-1} and shoulder mode (Sh) at about 390 cm^{-1}. Moreover, the Raman spectrum of the annealed 20-cycle ALD/MLD sample exhibits the contribution of the acoustical vibrational mode of the silicon substrate at 300 cm^{-1}, which testifies to the ultra-thinness of the film. Consequently, Raman spectra confirm that the synthesized films are composed of TiS_2 layers thanks to the appearance of vibrational modes associated with the 1T-TiS_2 despite a sulfur over-stoichiometry by HAXPES.

To conclude, we didn't succeed to obtain a better quality material or even reach TiS_3 layers by doubling the injection time of EDT. Nevertheless, by annealing under Ar/H_2(5%) with the thermal annealing strategy B, a sulfur over-stoichiometry of 2.5 was reached which could correspond to the formation of a film composed of TiS_2 and TiS_3 layers. However, the vibrational modes of TiS_3 were not observed on the Raman spectra (Figure 4.16)[136]. This result, which deserves to be further explored, may be a sign that very small amount of TiS_3 was obtained (which would explain the absence of Raman signal) or that the film is more rich in precursor residues.

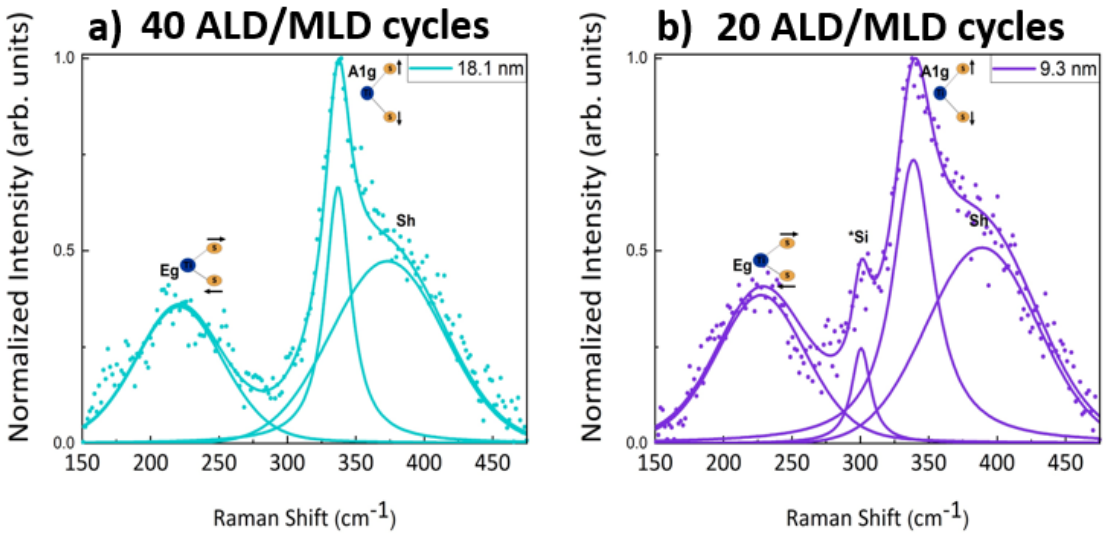

Figure 4.16: Raman spectra (dots) resulting from a) 40 and b) 20 ALD/MLD cycles of growth with t_{injEDT}=60s and annealing under Ar/H_2(5%) using thermal annealing strategy B. Raman spectrum were normalized to the intensity of the A1g mode and fitted with Lorentzian function (A1g and *Si modes) and Gaussian-Lorentzian function to fit the Eg and Sh modes (solid lines in a) and b) panels).

4.4.2 Control of the sulfur over-stoichiometry for 20 ALD/MLD cycles using thermal annealing strategy A and Ar/H_2(5%)

The annealing strategy B didn't succeed to synthesize a film composed of stoichiometric TiS_x phase when doubling the EDT injection time. Thus, we grew a 20-cycle ALD/MLD thiolate with 60s EDT injection annealed under Ar/H_2(5%) with the thermal annealing strategy A. The deposited thickness, obtained from the fitting of an XRR curve, was 7.9±0.4nm.

The calculated atomic ratio [S]/[Ti] from HAXPES measurements (see Table C.8 in Appendix C), is equal to 2.3. This result shows that the expected sulfur excess resulting from the double injection of EDT was removed during the annealing. Indeed, the film seems to be composed of quasi-stoichiometric TiS_2 layers after annealing using strategy A for which the maximum temperature reached is higher than the one of strategy B (385 °C with respect to 300 °C in the case of thermal annealing strategy B). Raman spectroscopy measurements were carried out to confirm that the film obtained after annealing is indeed composed of crystalline TiS_2 layers. The spectrum (presented Figure 4.17-a) shows the expected active modes I.e. Eg and A1g characteristic of 1T-TiS_2. The Eg mode is positioned at 230.8 cm^{-1},

the A1g mode at 335.5 cm^{-1}; as regards the shoulder mode (Sh), the latter is located at approximately 390 cm^{-1}. The observation of the mode from the silicon substrate at 300 cm^{-1} testifies to the low thickness of the film.

TEM image of the annealed sample, shown in Figure 4.17-b, reveals a continuous thin film with low surface roughness. The nanoscale structure of the grown film shows the presence of dispersed nanodomains of TiS_2 layers, in agreement with the Raman data discussed above. The sulfide thin film is still covered with an amorphous ca 2 nm-thick titanium oxysulfide film (like all the TiS_2 samples grown during this thesis work). Note that the sulfide/SiO_2 interface is also still observable. This interface layer is expected to be probably an oxysulfide resulting from the first pulses of the metal precursor with the surface of the silicon substrate. TEM image seems to be not clear compared to images shown in section 4.3.1.

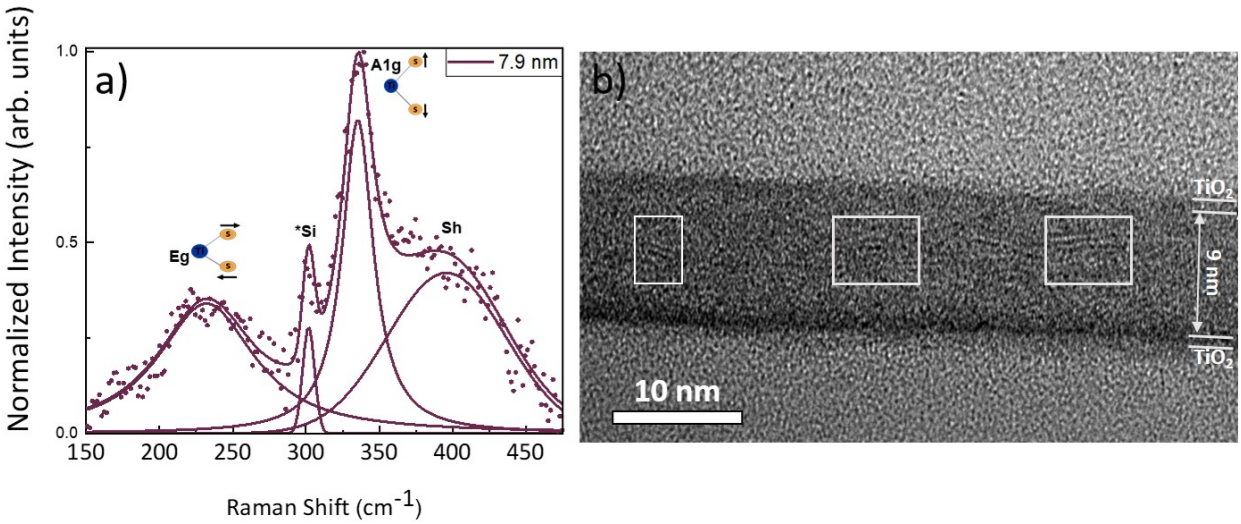

Figure 4.17: 20 ALD/MLD cycles of growth with t_{injEDT}=60s, annealed under Ar/H_2(5%) using thermal annealing strategy A. a) Raman spectrum (dots) resulting and b) Microstructural TEM image. Raman spectrum was normalized to the intensity of the A1g mode and fitted with Lorentzian function (A1g and *Si modes) and Gaussian-Lorentzian function to fit the Eg and Sh modes (solid lines in a) panel).

Despite significant work already performed to improve the process for depositing ultrathin TiS_2 films, adequate growth conditions can still be optimized.

4.5 Four-point probe electrical measurements

Four-point probe resistivity measurements were carried out at room temperature using the Lucas-Signatone Labs Pro4 and a Keithley 2400 instruments on a series of 40-cycle ALD/MLD Ti-thiolates obtained with 30s injection time of EDT, and annealed under $Ar/H_2(5\%)$ gas using different annealing strategies:

1. 450°C for 30 min (film thickness after annealing: 15.0 nm)
2. Thermal annealing strategy A that reaches a temperature up to 385°C (film thickness after annealing: 13.3 nm)
3. Thermal annealing strategy B that reaches a temperature up to 300°C (film thickness after annealing: 13.9 nm)

The three deposited TiS_2 were grown in 100 nm-SiO_2 substrate. Five acquisitions were performed on different spots of each sample to check the homogeneity and calculate an average of the resistivity. The resistivity value of the bare 100 nm-SiO_2 on silicon was too high to be measured with the equipment.[199] The mean resistivity (Ω.cm), was obtained by multiplying the sheet resistance value ($\Omega.sq^{-1}$) by the thickness of the film. The small dispersion in the values from one spot to another attests to the homogeneity of the three deposited samples.

The mean resistivity values for the three samples are presented in Figure 4.18. One can clearly see that the resistivity values decrease with the increasing of the annealing temperature. The resistivity decreases from 558.9(19.2) x10^{-3} Ω.cm at 300 °C to 6.6(0.4)x10^{-3} Ω.cm at 450 °C. Such variation in resistivity can be due to many factors. As for instance, it was observed in the literature that TiS_2 resistivity decreases with the decrease of the film stoichiometry [206, 236, 237]. The samples annealed at 300 °C and 385 °C presented a stoichiometry S/Ti = 2.3, while the sample annealed at 450 °C presented a stoichiometry of S/Ti = 2.1. In the literature, the electronic structure of TiS_2 is still debated to determine whether TiS_2 is semimetal or semiconductor. Actually, this debate is linked to the TiS_2 stoichiometry, since defects and doping are difficult to control. The existence of stoichiometric TiS_2 is still controversial.[238] In the literature, it was known and accepted that TiS_2 tends to grow metal rich and that the excess Ti atoms intercalate into the van der Waals gap, leading to the formation of $Ti_{1+x}S_2$. This excess of Ti atom is the reason behind the sub-stoichiometry.[237]

In other words it was observed that the decrease in the stoichiometry explains the different resistivity values found for TiS_2 thin films.

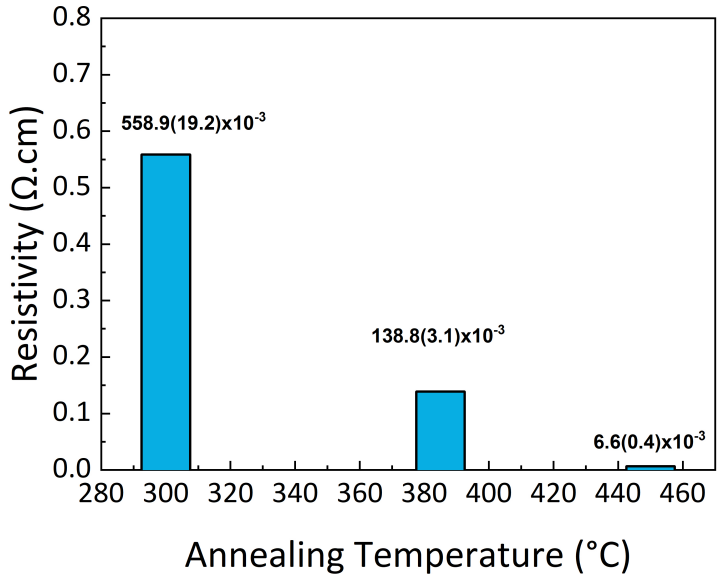

Figure 4.18: Plot of the mean resistance obtained with the four Probes measurements for 40 ALD/MLD cycles Ti-thiolate annealed at different temperatures under $Ar/H_2(5\%)$ gas. Five acquisitions were performed for each sample .

4.6 Substrate effect

Previous studies focused on enhancing the crystalline structure of TiS_2 by using various crystalline substrates. [55, 122, 121] As a first and unique try, we grew a 40-cycle ALD/MLD Ti-thiolate on 3 monolayers of MoS_2 previously deposited on SiO_2 substrate. The deposited sample was annealed under $Ar/H_2(5\%)$ gas using thermal strategy A. The same thickness is almost obtained as the one of the films deposited directly on 100 nm SiO_2 substrate (around 14 nm by XRR). Raman spectrum was performed on the annealed sample, we can see the appearance of the associated vibrational mode of the MoS_2 substrate: E^1_{2g} and A1g presented at 382.7 and 406.7 cm^{-1}, respectively. However, the presence of TiS_2 was confirmed by the contribution of the associated vibrational modes Eg and A1g. Such results confirm the successful growth of TiS_2.

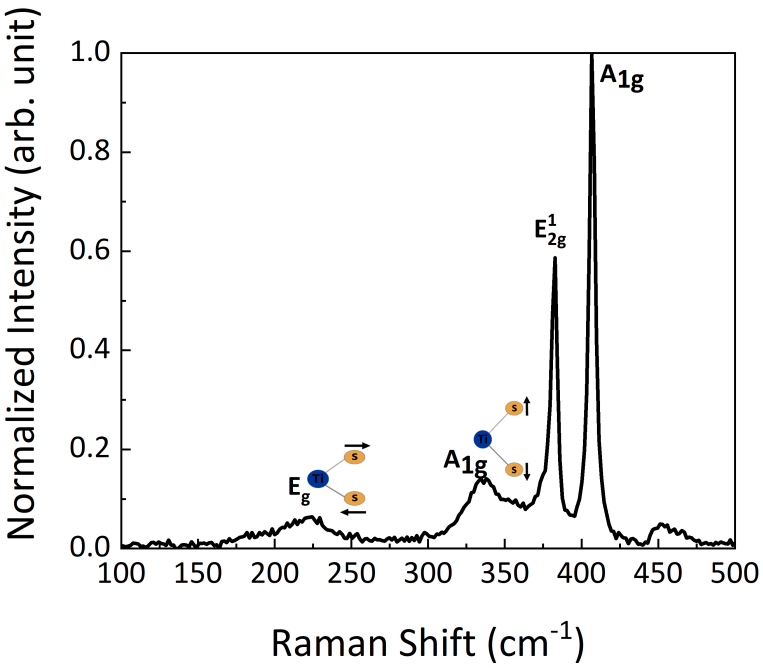

Figure 4.19: Raman spectrum of a 40-cycle ALD/MLD Ti-thiolate grown on 3 monolayers of MoS_2 substrate annealed under $Ar/H_2(5\%)$ using thermal annealing strategy A.

Furthermore, by TEM we did not succeed to see the film deposited on the MoS_2/SiO_2 substrate due to the delamination of MoS_2 film, which can be explained by the decrease of the interfacial adhesion between 2D layered metal chalcogenides with the SiO_2 substrate. [239] This initiative open the horizons toward the study TiS_2 with various substrate and better check the substrate effect on the deposited thin films.

4.7 Conclusion

The main challenge of this chapter was to understand and control the transition from amorphous Ti-thiolate thin films to ultra-thin stoichiometric TiS_2 films. Two different adequate annealing strategies were optimized using *in situ* XRF that allows a monitoring of the [S]/[Ti] ratio during the annealing step.

This work highlighted the importance of the annealing step for the synthesis of ultra-thin layered films. *In situ* X-ray synchrotron measurements performed during the annealing and *ex situ* characterizations carried out by XPS/HAXPES, TEM, XANES, and Raman scattering

confirmed that appropriate annealing conditions allow to reach an ultra-thin film (down to 5.5nm) which is composed of stoichiometric TiS_2 layers. The effect of the annealing gas (Ar/H_2 and N_2) was tested on as-deposited Ti-thiolate. In addition, a study evaluating the effect of the substrate was initiated by performing the deposition of TiS_2 film over 3 monolayers of MoS_2. The substrate and annealing gas are important parameters that should be explored further in the near future. However, the formation of a thin oxide on top of the TiS_2 film at air ambient (which was found to be a constant coverage film regardless of the annealing strategy) was also evidenced. In the future, an appropriate method to etch the top oxide layer without affecting the quality of the TiS_2 thin film or to protect it from oxidation will be required.

In addition, Four-point probe electrical measurements were performed on Ti-thiolates annealed at different temperatures. The results evidence a low resistivity in the range of semi-conductor materials for the sample that presents the lowest stoichiometric ratio: [S]/[Ti]=2.1. This property could lead to the use of TiS_2 films as 2D contact materials with 2D semiconductors in device fabrication.

The strategy followed to synthesize TiS_2 films, that is decoupling growth from crystallization, seems well adapted to lamellar metal chalcogenides and opens new possibilities for the synthesis of 2D materials in general.

Chapter 5

Progress report on the Synthesis of metal sulfides Ga_xS and SnS_2

5.1 Introduction

The deposit of textured TiS_2 films and all the work presented in the first chapters of this manuscript motivated this new study aimed at synthesizing other lamellar materials by the 2-step process: ALD/MLD growth of a metal-thiolate followed by a subsequent thermal annealing. In this context, this chapter discuss the synthesis of both Gallium sulfide and Tin disulfide synthesis. The work on the Gallium sulfide synthesis was conducted in collaboration with IPVF-Palaiseau (N. Schneider) and in the framework of the master internship of Tom Iung which I had the opportunity to supervise (Aalto university - Finland) [240]. The work on Tin sulfide was in collaboration with C2P2 and IRCELYON (M. Zhukush, C. Camp, E. A. Quadrelli) and in the framework of the master internship of Hugo Menez which I had the opportunity to supervise (Ecole d'ingénieur Denis Diderot, Université Paris Cité).

This chapter is divided into two major parts: the first part presents the promising results obtained during the synthesis of Ga_xS. These results are noticeably supported by *in situ* X-ray studies performed at SOLEIL synchrotron radiation center (SIRIUS beamline). The second part is focused on the synthesis of Sn_xS which was unsuccessful. Even though we were not able to deposit a thin film of Sn-thiolate from TDMASn and EDT, clues to explain such a result are presented.

5.2 Synthesis of Gallium Sulfide thin films

In this part, the strategy used for the synthesis of Ga_xS thin films by alternating both TDMAG and EDT on amorphous 100 nm SiO_2/Si and also on Si(111) afer etching the native oxide with Hydrofluoric acid (HF) is presented. The ALD/MLD step have been established via the development of the associated recipe, optimized for the first time, as described in section 2.3.3 in Chapter 2. After ALD/MLD process, an amorphous film was obtained confirming the necessity of the annealing step, under N_2 but mostly $Ar/H_2(5\%)$ to possibly reach a crystalline material.

In order to find the suitable deposition temperature (or the region of temperatures) in which the deposited film obtained from the ALD/MLD step is uniform and homogeneous along the substrate surface, we studied the ALD/MLD growth as a function of the substrate temperature ranging from 150 °C to 300 °C. The as-deposited films were examined by *in situ* ellipsometry, *ex situ* XRF and *ex situ* XRR. TEM allows to check the homogeneity of as-deposited films in order to find the adequate substrate temperature. XPS measurements were performed to study stoichiometry. A campaign of synchrotron experiments was performed in June-July 2022 to study the growth of gallium sulfide thin films. Thus, the use of synchrotron radiation allowed to carry out, once more, *in situ* measurements : XRF, XRR, and XANES.

5.2.1 Investigation of the ALD/MLD growth

The aim relies on alternating the TDMAG or hexakis(dimethylamino)digallium $[Ga(NMe_2)_3]_2$ and EDT on 100 nm SiO_2/Si substrate. A series of experiments were performed on various substrate temperature ranging from 150 °C to 300 °C aiming to find an the ALD/MLD window, if it exists.

Since the growth of gallium sulfide thin films by ALD/MLD have not been reported yet, the optimizations of the adequate substrate temperature were made by taking into account what was previously reported in ALD. In the literature, previous attempts in ALD showed that a constant GPC was found in an ALD window region of [120-250] °C using $[Ga(NMe_2)_3]_2$ and H_2S.[147, 65, 70].

In addition, in section 2.3.3 in Chapter 2, I have mentioned that the TDMAG and gas lines connecting the metal container to the reactor chamber were heated at 90 °C, therefore

to prevent the gas mixture (TDMAG/Ar) to cool down before reaching the substrate, we choose substrate temperatures above 90 °C. Finally, we started our optimizations from a substrate temperature equal to 150 °C. A series of experiments of 40 ALD/MLD cycles, were conducted, each ALD/MLD cycle consisting of:

1. TDMAG double pulses, a pulse duration is 3s.
2. Purge of 90s.
3. EDT injection time of 30s (15s was also tested).
4. Purge of 90s.

After the ALD/MLD growth using the parameters mentioned above, the investigation was further carried out by various characterization techniques.

5.2.1.1 *In situ* Ellipsometry

In situ ellipsometric growth monitoring allowed us to track the growth of gallium sulfide inside the MOON reactor. When *in situ* ellipsometric curves shows an increase in the film thickness signal upon the accumulation of ALD/MLD cycles, it simply means that a growth is taking place on the substrate surface. Ellipsometry was used as the first insightful technique for the growth of the series of samples deposited by 40 ALD/MLD cycles (the injection time of EDT is equal to 30 s) at 150 °C, 200°C, 225 °C. 250 °C, and 300 °C.

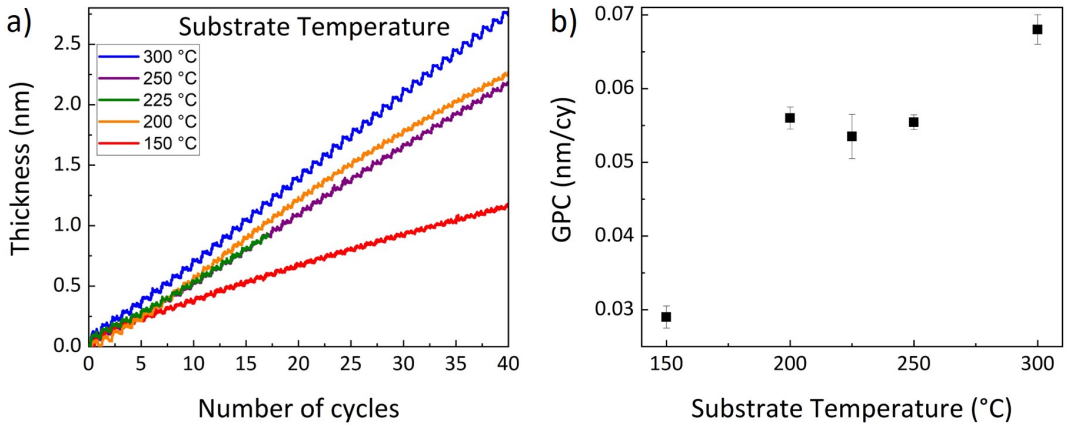

Figure 5.1: a) *In situ* Ellipsometric curves for five different temperatures of substrate with an injection time of the EDT of 30s and b) GPC as a function of these temperatures. Error bars present the calculated thickness error generated from the model during the growth.

Figure 5.1-a shows the growth of gallium sulfide at different substrate temperatures. All presented ellipsometric curves highlights a steady regime of growth after few cycles leading to the linear growth of Ga_xS thin films (see Figure 5.1-a). The variation of thickness (where the absolute values are not correct) as a function the deposition temperature can be used to calculate the GPC. The GPC is obtained by calculating the ratio of film thickness over the number of cycles. We created our ellipsometry fitting model by using the values of the pseudo refractive index <n> and the pseudo extinction coefficient <k> for 4 values of wavelengths: λ_1 = 465 nm, λ_2 = 525 nm, λ_3 = 580 nm, λ_4 = 635 nm reported in a previous work on gallium sulfide. [241] Noteworthy, *in situ* ellipsometry is used to check the evolution along the growth and not to obtain the real thickness values (quantitative analysis of data is not possible). Since this technique is based on such a crude model, an adequate optical model is required to obtain precise numerical values. For instance, our interpretation is focused on the evolution of the GPC for the deposited films. [241] Therefore, this study must be implemented by *ex situ* XRR quantitative measurements.

Figure 5.1-b confirms a constant GPC in the region of: [200 °C ; 250°C], evidencing an ALD/MLD window. To check the consistency of the GPC region, we changed the EDT injection time from 30s to 15s while growing at the same deposition temperatures. In Figure 5.2 we can observe that the same constant region is obtained (even the obtained values are higher). Of course, as explained such a conclusion cannot be definitely proven by *in situ* ellipsometry only, it requires additional characterization.

In addition, qualitative measurements was performed these samples series of 30s and 15s of EDT injection using *ex situ* XRF. XRF is not the method of choice to find an ALD/MLD window. However, XRF can define a GPC as mass concentration of a given atom deposited per cycle. Even though quantitative analysis was not possible, we used the XRF to follow the evolution of the S/Ga ratio (see Section E.1 in Appendix E).

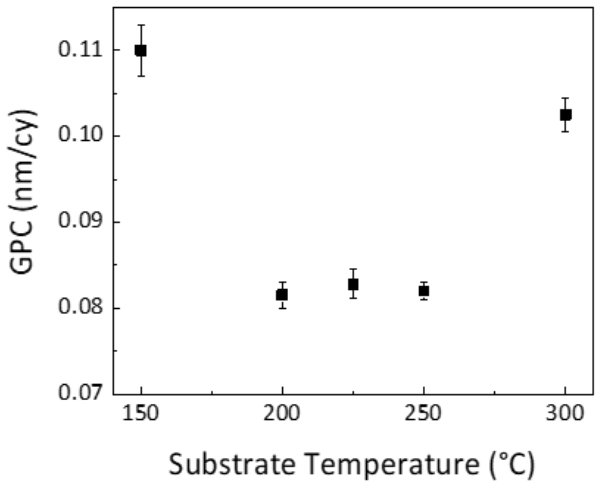

Figure 5.2: GPC obtained by *in situ* ellipsometry as a function of the substrate temperature for an injection time of the EDT of 15s. Error bars present the calculated thickness error generated from the model during the growth.

5.2.1.2 XRR

The quantitative GPC is the ratio of deposited thickness over the number of ALD/MLD cycles. Simulated XRR curves for the samples grown at different substrate temperatures with 30s of EDT injection are plotted as a function of the scattering modulus (q) as shown in Figure 5.3. The scattering modulus (q) can be obtained using the following formula:

$$q = \frac{2sin\theta}{\lambda} \tag{5.1}$$

To improve fit between simulated curve and raw data, we had to consider that the deposited gallium sulfide thin film is covered by a GaO_xS_y film which is likely coming from the exposure of the deposited sample to ambient air. These simulated XRR curves permits to obtain the final thickness of each deposited sample (additional about the thicknesses are presented in Table E.1 in Appendix E).

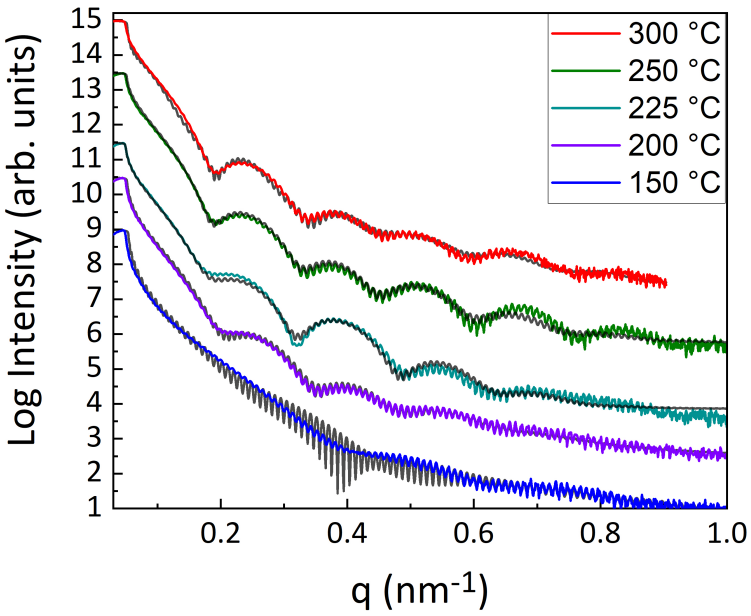

Figure 5.3: simulated XRR plots: reflected intensity as a function of the scattering modulus q for different samples deposited at various temperature with a 30s EDT injection time. Black curves represent the simulated spectra.

Figure 5.4-a shows the final thickness obtained from the fitting of the XRR curves as a function of the substrate temperature. From the quantitative thickness values, we can extract two significant informations. First, a constant GPC exists in the temperature region [200 °C ; 250 °C] as shown in Figure 5.4-b, this is in agreement with *in situ* ellipsometry and *ex situ* XRF measurements. Secondly, the obtained value in the ALD/MLD window equal to 0.16 nm/cycle is in agreement with previous studies in classical ALD process using TDMAG and H_2S (GPC around 0.1 nm/cycle).[65, 147]

From the XRR measurements we finally conclude that the ALD/MLD window (already detected by both techniques discussed above) was confirmed to be accurate in the region [200 °C ; 250 °C].

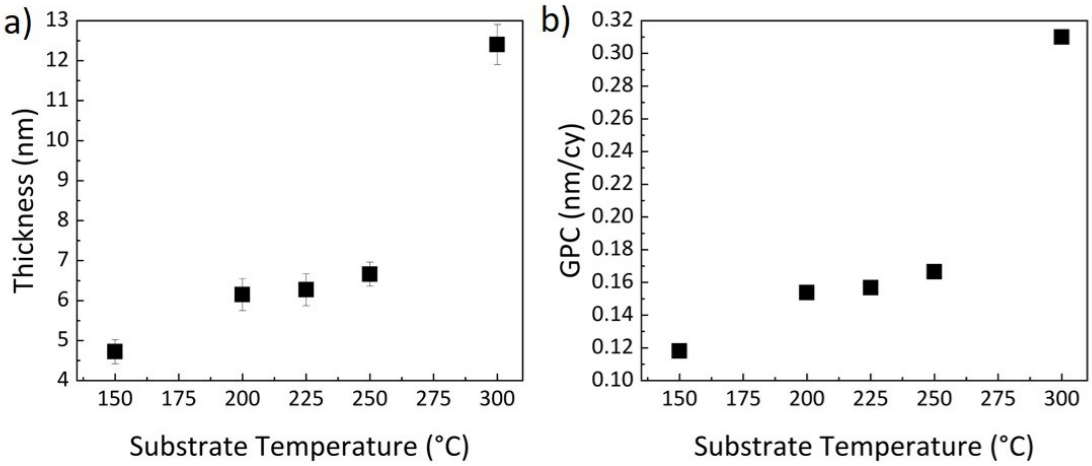

Figure 5.4: a) Thickness evolution obtained by XRR and b) GPC investigation as a function of the substrate temperature.

5.2.1.3 TEM measurements

TEM measurements were performed to check the homogeneity and the crystallinity of the deposited films, we chosen to select the two temperatures at the beginning and the end of the ALD/MLD window (200 and 250 °C). The sample grown at 200 °C, presented in Figure 5.5-a, shows that the deposited thickness is not constant along the substrate surface: indeed, an heterogeneous behaviour is clearly observed. Concerning the sample grown at 250 °C presented in Figure 5.5-b the film seems more uniform and homogeneous along the substrate.

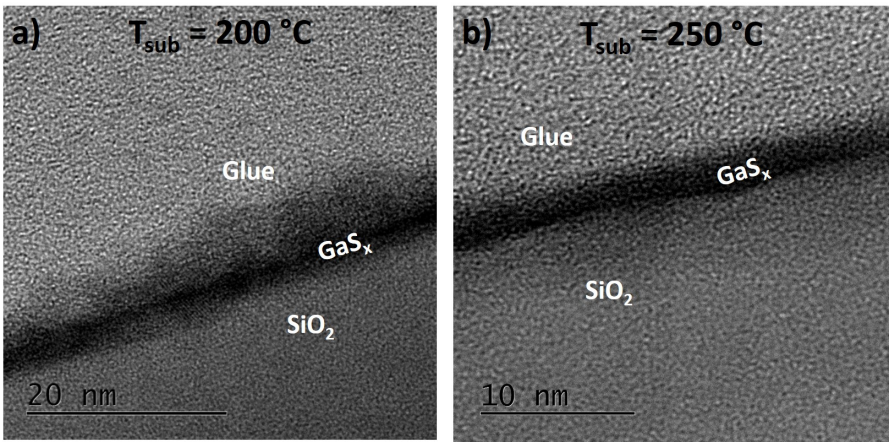

Figure 5.5: TEM images for as deposited samples with an EDT injection of 30s grown at a) 200 °C and b) 250 °C. The inset in (b) confirms the homogeneity on large scale.

In addition, Figure 5.6 highlights the homogeneity of the ultra-thin film deposited on SiO_2 surface at larger scale. No layered structure or crystallites could be observed. Note that at this stage, no annealing has been performed on the amorphous thiolate.

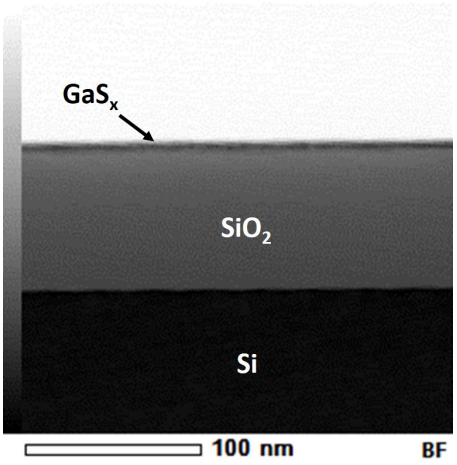

Figure 5.6: TEM image on large attesting the homogeneity of the sample with an EDT injection of 30s grown at 250 °C.

Elemental distributions inside the ultra-thin film grown at 250 °C, presented in Figure 5.7, are provided by TEM+EDX mapping. The mapping of Ga and S elements shows uniform distribution inside the thin film. The O mapping suggests that oxygen might be incorporated inside the ultra-thin film or it is present within an oxidized region on the top gallium

sulfide film. However, due to the ultra-thin film effect on large scale (100 nm) of EDX mappings in Figure 5.7, it is difficult to observe the oxygen with precision. These observations highlighting the formation of a homogeneous film on the surface of SiO_2 led us to fix the deposition temperature at 250°C.

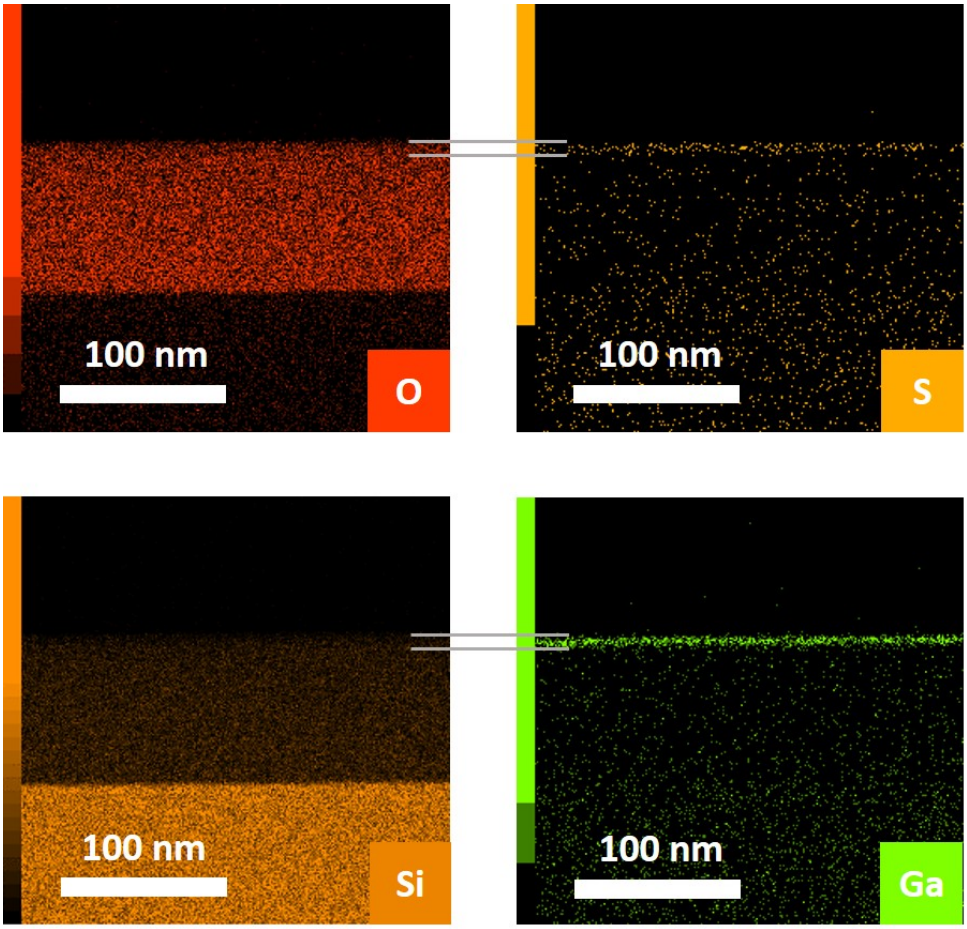

Figure 5.7: EDX mapping of Ga , S , Si , and O elements in the sample deposited at 250 °C with an injection time of EDT 30s.

The TEM+EDX evidence suggests the presence of an upper region of gallium oxysulfide due to oxidation in the ambient environment, which was also confirmed by the fittings of XRR curves.

5.2.2 Thin film chemical composition: XPS analysis

XPS analysis was performed on the sample grown at 250 °C, using the conventional monochromatic soft Al source (aluminum Kα, hν = 1486.6 eV) with θ= 45° *i.e.* analyzed thickness depth = 6.2 nm. Figure 5.8 shows the core level peaks of the Ga 3d, S 2s (S 2s was considered because an overlap between S 2p and Ga 3s is presented), and O1s. The Ga-3d XPS spectrum (shown in Figure 5.8-a) show a large peak signal at 20.4 eV, which is assigned to gallium oxysulfide layers (indicating the film is composed of interconnected Ga-S and Ga-O networks).[147] The S-2s XPS spectrum (shown in Figure 5.8-b) is also assigned to gallium oxysulfide layers at 226.3 eV. The O1s XPS spectra (shown in Figure 5.8-c) exhibit two environments: one located at 531.1 eV (green peak) is attributed to gallium oxysulfide layers, while the one at 532.3 eV (blue peak) is attributed to C-O and also to SiO_2 since the Si coming from the substrate is detected.

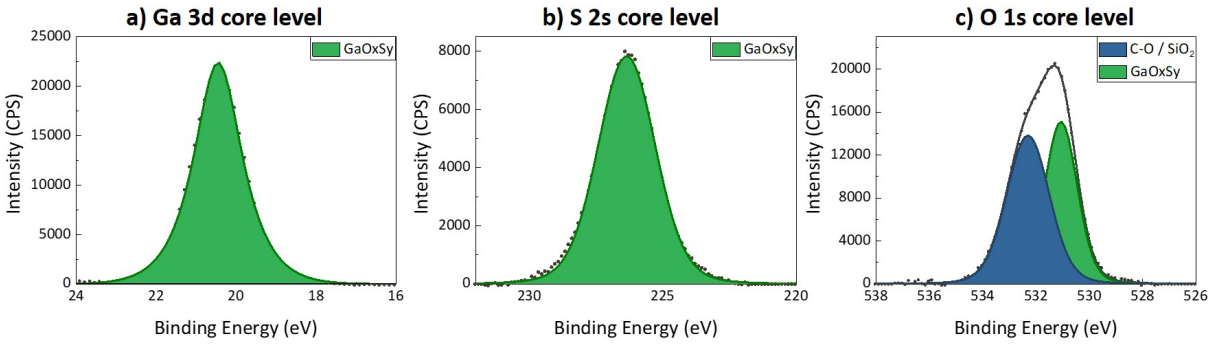

Figure 5.8: XPS spectra: Intensity as a function of the electron binding energy a) Ga-3d core peak b) S-2s core peak and (c) O-1s core peaks.

Additional informations presented in Table 5.1, permit to evaluate the film composition and to calculate the $(S_{Total}+O_{GaOxSy})/Ga_{Total}$= 1.1 atomic ratio confirming the growth of a gallium oxysulfide rather than a gallium sulfide covered by oxide. At this stage of the study, we cannot conclude on the origin of the oxygen: it could come from the substrate of from the air after exposure to ambient conditions.

Moreover, this XPS study highlights the importance of the recipe using a 30s injection time of EDT instead of 15s, since its atomic ratio S/Ga is inferior to 1 (around 0.7).

Table 5.1: Binding energies (BE) and atomic percentages (at.%) of the different chemical environments identified by XPS for the ultra-thin film deposited at 250°C with a 30s of EDT injection.

Element	Attribution	Position (eV)	Percentage (%)
Ga 3d	GaOxSy	20.4	29.2
S 2s	GaOxSy	226.3	20.3
O 1s	GaOxSy	531.1	12.8
	C-O / SiO_2	532.3	15.3
C 1s	C-C / C-H	284.8	15.9
	C-O / C-N / C-S	286.2	4.1
	O-C=O	289.0	1.7
Si 2s	SiO_2	154.1	0.8

Noteworthy, Time-of-Flight Secondary Ion Mass Spectrometry (ToF-SIMS) analyses presented in E.2 in Appendix E also highlights the presence of oxygen within the deposited films.

All *ex situ* measurements results confirmed the reason behind the absence of Raman spectra: indeed, they evidence the presence of oxygen in-depth after exposure to air ambient. Thus, our recipe of growth is not able to reach a crystalline film of gallium sulfide. A conclusion on this part require analysis on a deposited film with thickness higher than 10 nm.

5.2.3 *In situ* synchrotron X-ray studies

The preliminary results obtained in the laboratory allowed to define the necessary optimizations and to establish an experimental plan for the implementation of a campaign of synchrotron experiments carried out at the SIRIUS beamline.

5.2.3.1 Comparison between synchrotron and laboratory experiments

To obtain comparable experimental conditions between the deposition performed at the LMGP and at the SIRIUS beamline, we increased the pressure rise time in the TDMAG container from 20s to 80s (due to the length of the Ar line, the carrier gas) to reach the same final pressure of 80 mbar before pulsing the gas mixed with the TDMAG molecules into the reactor.

To compare with the sample grown in the laboratory, 40 ALD/MLD cycles at T_{sub}=250°C with 30s EDT injection and double TDMAG pulse was performed. Figure 5.9-a focuses on the *in situ* ellispometry curve during the deposition of gallium sulfide thin film, whereas the inset in Figure 5.9-a shows the deposition steps during one ALD/MLD cycle. We can see that during the injection of TDMAG the double pulses is clearly observed, and the steady states during purge is evidenced as well.

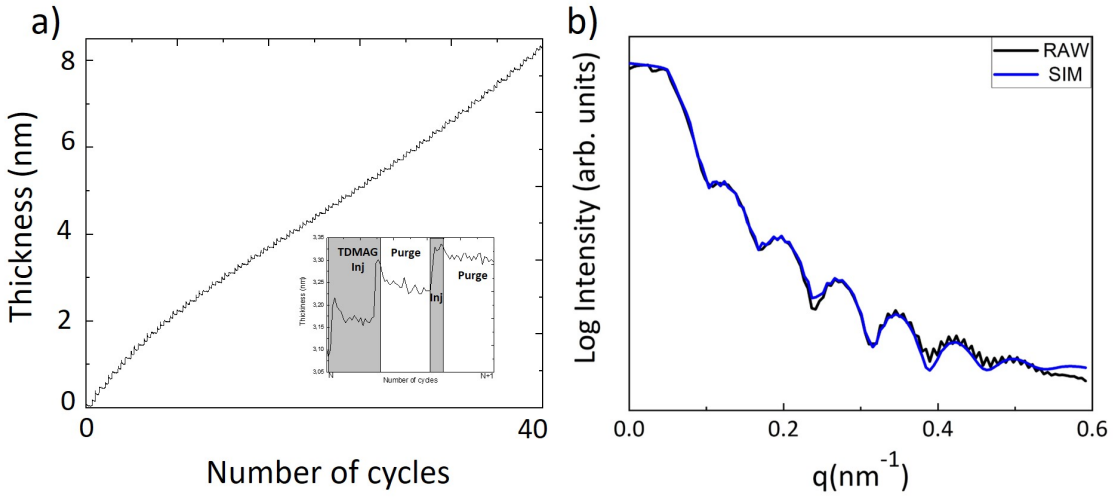

Figure 5.9: a) *in situ* ellipsometry curve and b) XRR curve ploted in reciprocal space q and b) reflected intensity curve as a function of the scattering modulus for a 40 ALD/MLD cycles deposit at 250 °C, with a 30s long injection of EDT prepared during synchrotron campaign. The inset in a) shows the injection/purge steps during one complete ALD/MLD cycle.

In addition, Figure 5.9-b shows *in situ* XRR curve performed in SIRIUS with an incoming X-ray energy of 10.5 KeV. The curve was simulated with only GaS film without considering an upper Gallium oxysulfide film. Thus, a thickness of 13.3 nm was obtained which is higher than the 6.7 nm of the sample grown in the laboratory. This result shows that it is difficult to reproduce strictly the same conditions when the reactor installation varies.

5.2.3.2 Aim of synchrotron experiments

The majority of the samples grown during the synchrotron beamline experiments used the experimental conditions mentioned above (i.e. a substrate temperature equal to 250°C, double pulsed injection of the TDMAG and an injection time of EDT of 30s). Our experi-

mental plan, attempted to answer many objectives and questions concerning the growth of gallium sulfide thin films during this synchrotron campaign. Our aim consisted on:

- Check the substrate effect on the deposited film. Such comparison can be obtained by performing the same growth on different substrate. Therefore, we managed to compare the sample grown on the conventional 100 nm SiO_2 substrate with a sample grown on Si(111) etched by Hydrofluoric acid (HF) to get rid of the native oxide. In this way, we are also able to check the effect of the oxide coming from the substrate in the contribution of oxide inside the deposited GaS_x film.

- Investigate the early stages of the growth, by tracking the variation of the S/Ga XRF ratio all along the deposition.

- Evaluate the thickness-dependent properties, using the same growth parameters, over a variable number of cycles: 35, 40 or 60.

- Reveal the importance of the thermal annealing on the as-deposited samples.

5.2.3.3 Substrate effect on the deposited films

A growth of 35 ALD/MLD cycles at T_{sub}=250 °C was performed on 100 nm SiO_2 substrate and on Si(111) etched with Hydrofluoric acid (HF) to remove the native oxide from the surface. The choice of using the Si(111) etched with Hydrofluoric acid (HF) was in the purpose of determining the influence of a crystalline surface with hexagonal symmetry effect on the grown thin film. To evaluate the growth on the Si(111) etched with HF, both XANES and EXAFS were recorded during the ALD/MLD process. Figure 5.10-a shows XANES spectra recorded at the Ga-k edge during the growth. Noteworthy, each performed EXAFS spectra spend around 40 mins (time of the scan) whereas the temperature of the sample is fixed at 250 °C under a continuous flow of N_2. The black vertical arrows marks a systematic change of peak with cycles deposition leading to a signature similar to the powder spectrum one. The Grey horizontal arrow shows an energy shift that starts from the first half-pulse until the 35th cycle growth.

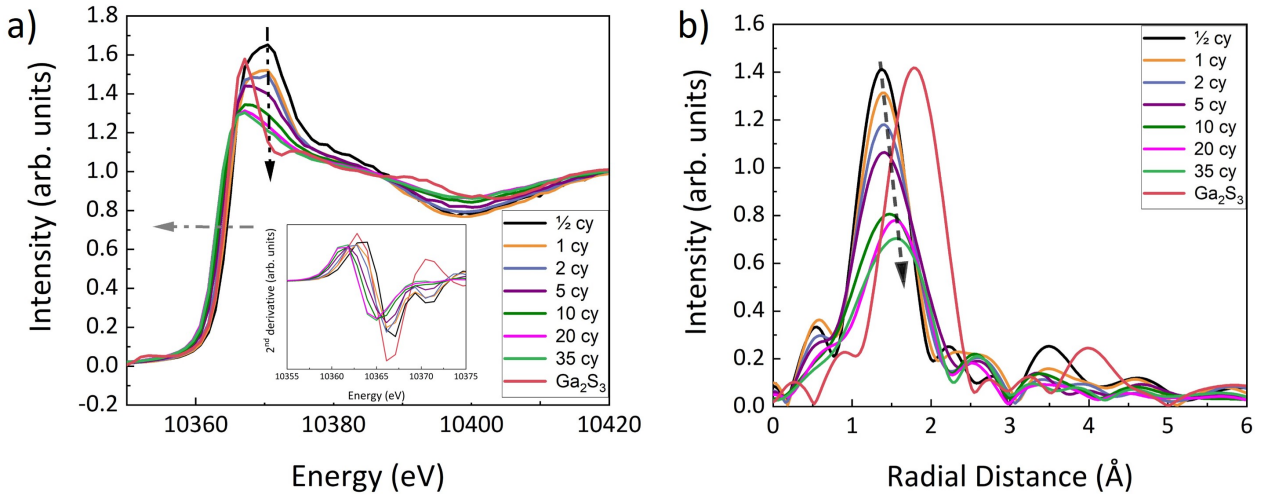

Figure 5.10: a) XANES spectra recorded at the Ga K-edge and b) Fourier transforms of the EXAFS spectra recorded during the growth of 35 ALD/MLD cycles at T_{sub}=250 °C on Si(111). The grown sample is compared to a reference spectrum of Ga_2S_3 powder. The inset in a) shows the second derivative of intensity.

A preliminary interpretation of these observations is explained by a systematic decrease of the Ga oxidation state. The gallium present in the first half-pulse can be assigned to the Gallium inside the TDMAG molecule, with an oxidation state of Ga^{3+}. However, the gallium environment after 35 cycles of growth is likely to be composed of Ga-S bonds with a Ga oxidation state belongs lower than 3+, as shown by the second derivative function of intensity (see inset in Figure 5.10-a).[242] The Fourier transformation of EXAFS spectra shown in Figure 5.10-b reveals that at the beginning of the growth the main peak corresponds to a radial distance of Ga-N bonds of the TDMAG precursor. A reduction of Ga-N peak and an increase of Ga-S (or may be adventitious Ga-O bonds [243, 244]) occur with the increasing of cycle number (see black arrow in Figure 5.10-b). [245] This result may indicate that the final material have similarities with GaS which is encouraging for our future perspectives. Further data analysis is in progress.

After a careful examination on the sample grown over Si(111) HF substrate, it is important to compare the difference in the local environment structure between the sample grown on Si(111) HF and the one grown on 100 nm SiO_2 substrate. Figure 5.11 shows the XANES spectra and Fourier transforms of EXAFS spectra from both samples to evaluate such a difference.

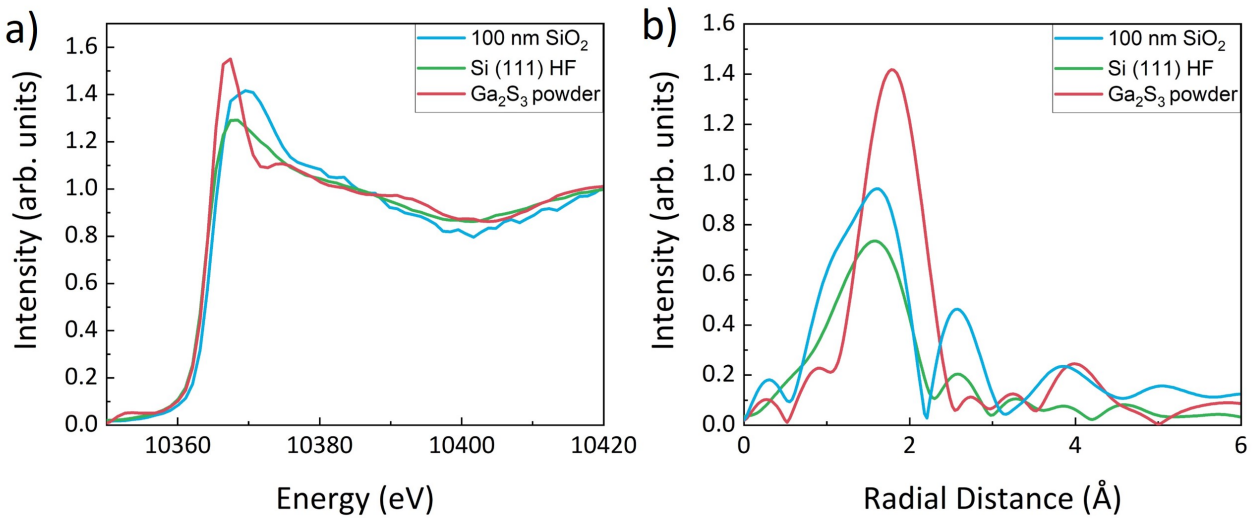

Figure 5.11: a) XANES spectra at the Ga K-edge and b) Fourier transforms of the EXAFS spectra of samples obtained from 35 ALD/MLD cycles, grown at 250 °C on 100 nm SiO_2 and Si(111). Both samples are compared to a reference spectrum of Ga_2S_3 powder.

For example, the EXAFS spectra presented in fig.5.11-b shows that the maximum intensity peaks are located at the same radial distance for the sample grown on 100 nm SiO_2 substrate (cyan) and the one grown on Si(111) etched by HF (green), indicating same Ga-S bond characteristics. These measurements require some simulations which are under progress by collaborators at SOLEIL synchrotron. Such results give the first preliminary insight that there is clear difference of growth between substrates.

5.2.3.4 Early stages of the growth investigations

After putting in evidence the substrate effect on the growth, we target to understand the growth behavior depending on the number of cycles. Usually during the growth, the substrate may inhibit or enhance the film growth depending on the compatibility of chemistries between the substrate surface and the growing film, where the GPC starts initially lower or higher before settling to a constant value. All these elements emphasized the necessity of exploring growth behavior from the early stages of growth.[116]

Therefore, we monitored the ALD/MLD process by *in situ* XRF with an incoming energy of 10.5 keV that permits to record both Ga Kα and S Kα fluoresence yields, simultaneously (see Figure 5.12) . XRF data permits to track the evolution of S/Ga ratio along the deposition,

in order to check the growth behaviour especially in the early stages.

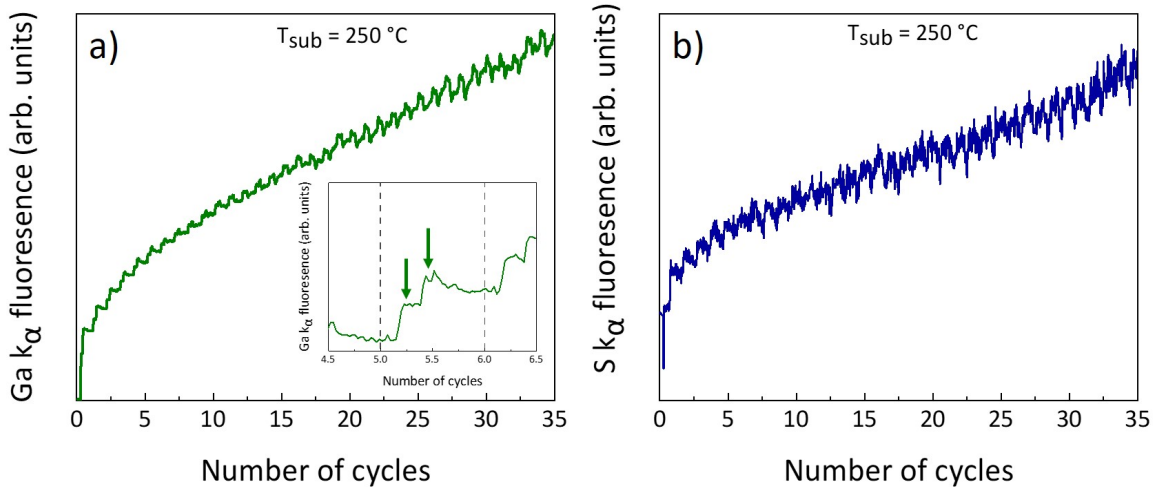

Figure 5.12: XRF intensity as a function of the number of cycles during the growth of 35 ALD/MLD cycles on 100 nm SiO_2 substrate (T_{sub} = 250 °C) of a) Ga Kα (olive line) and b) S Kα (blue line). The inset in a) shows the double injection of Gallium precursor during one ALD/MLD cycle.

The S and Ga XRF were recorded during the growth of 35 ALD/MLD cycles on 100 nm SiO_2 and Si(111) HF substrates. As shown in Figure 5.13-a, the S/Ga ratio, obtained by dividing the raw XRF intensities of the S Kα and Ga Kα start with a higher ratio value for the first five cycles, and it slightly decreases to reach a constant value till the end of the growth (after 10 cycles). The main insight that we get from the ratio evolution is that a similar growth behaviour is reached after 10 cycles growth, and the higher ratio at the beginning of growth is explained by a transient regime coming from the interaction of the -OH hydroxyl groups present on the substrate surface with first precursor pulses.

Similarly, if we look at the evolution of the ratio for the sample grown on Si(111) HF, presented Figure 5.13-b, we can observe that the same behaviour is observed in term of a constant value along the deposition. However, an important difference can be noticed in the early stages of the growth. Such difference confirm that the use of the Si(111) HF as substrate substrate lead to a constant ratio all along the process or in other words the number of deposited cycles does not have a high impact on the quality of the obtained film, contrary to the 100 nm SiO_2 substrate that requires few cycles growth before reaching a compatibility in surface chemical reactions between the surface and the deposition. The obtained data

confirms the impact of the -OH groups present on the substrate on the growth behaviour during the first cycles, which can lead to deposit a transient film at the interface. So, finally, in the current state of our analysis of the results obtained at the synchrotron, it is difficult to obtain a definitive conclusion on the impact of the change of substrate on the deposition and the final material obtained, but an important behaviour can be confirmed that both substrates permits to have a similar growth behaviour with some more advantage for the Si (111) HF substrate especially in the very first cycles.

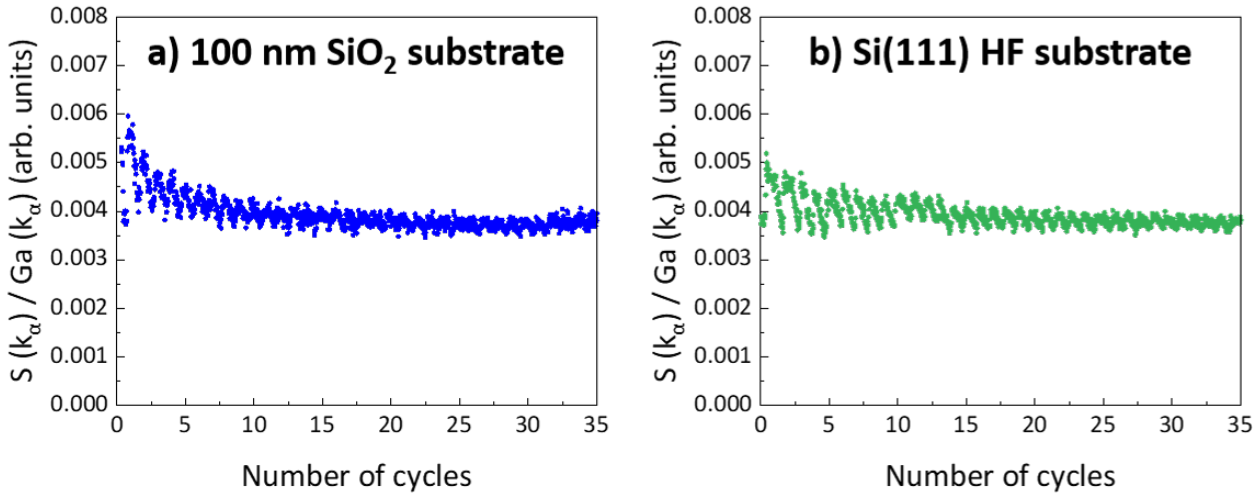

Figure 5.13: S Kα/Ga Kα XRF ratio evolution during the growth of 35 ALD/MLD cycles at T_{sub}=250 °C using a) 100 nm SiO_2 and b) Si(111) HF substrates.

5.2.3.5 Thickness dependent properties

After presenting the growth behavior and evaluating the effect of the substrate surface nature on the deposition, we focus on the thickness effect on the quality of the film. A growth of 60 ALD/MLD cycles was carried out on 100 nm SiO_2 substrate. Similar behaviour can be observed as described for the sample grown on Si(111) HF substrate (see Figure 5.10).

Figure 5.14 shows that by increasing the number of ALD/MLD cycles from 35 to 60 cycles, a systematic shift of peak with the number of cycle deposition leads to an appearance similar to the powder spectrum marked by the black arrow in Figure 5.14-a. Moreover, the Fourier transform to EXAFS spectra shown in Figure 5.14-b allow us to better evaluate the thickness effect on the film growth as marked by the black arrow. The radial distance

shift in EXAFS data corroborate with the change of gallium nearest neighbors upon the accumulation of cycles.

Once again, the data indicates that in the very first pulse (first half-cycle) the gallium nearest neighbors consist of N from the TDMAG precursor then it evolves to S atoms as the number of cycles increase.

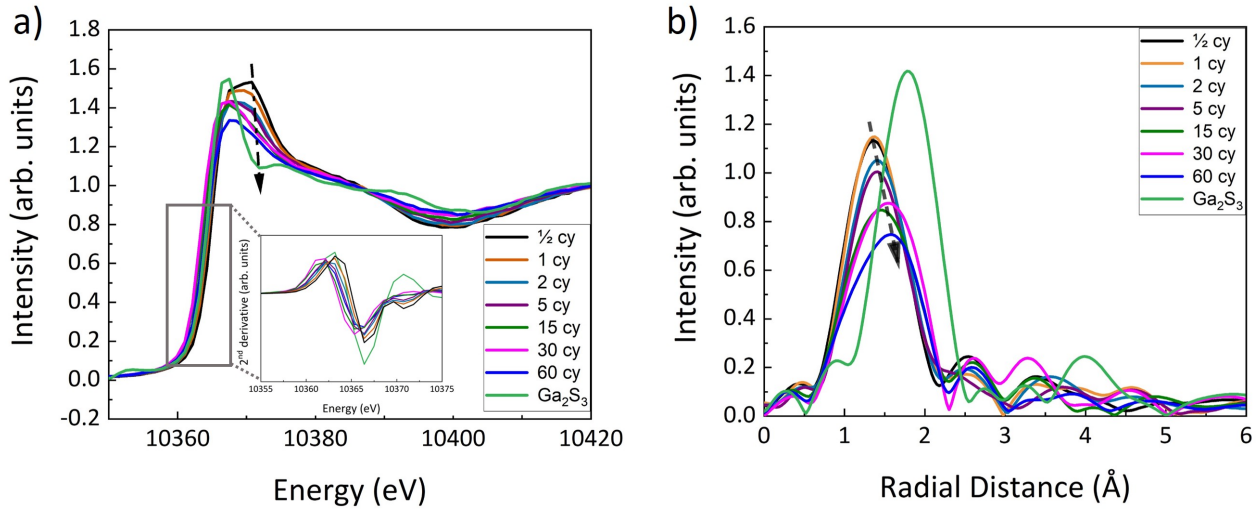

Figure 5.14: a) XANES at the Ga K-edge and b) Fourier transforms of the EXAFS spectra recorded during the growth of 60 ALD/MLD cycles at T_{sub}=250 °C on 100 nm SiO_2 substrate. The grown sample is compared to a reference spectrum of Ga_2S_3 powder. The inset in a) shows the second derivative of intensity.

5.2.3.6 Effect of the thermal annealing

Regardless the promising collected data obtained in this dissertation on the growth of Gallium sulfide, it's not possible to reach crystalline film without optimizing the thermal annealing conditions. Therefore optimizing annealing process requires additional experiments that we were in a lack of time to perform them. However, a test have been performed on the 60 ALD/MLD cycles under 100 sccm flow of N_2 at 315°C, 375°C and 415 °C with a ramp rate of 10°C/min. Both XANES and EXAFS spectra were recorded in situ after cooling the substrate once the annealing process have been performed. Figure 5.15-a shows an energy shift for the annealed sample in the opposite direction of the gallium sulfide confirming a change of the oxidation state after annealing (toward Ga^{3+} again, as seen in the case of first-half cycle). Moreover, the black vertical arrow marks a systematic change of peak after annealing where the appearance is no longer similar to the powder spectrum. EXAFS spectrum shown

in Figure 5.15-b shows a reduction of Ga-S bonds confirmed by a small shift in the radial distance shift after annealing. All the presented inputs confirm that our annealing didn't permit to enhance the structure, emphasizing the necessity to perform more optimizations on this part in the future.

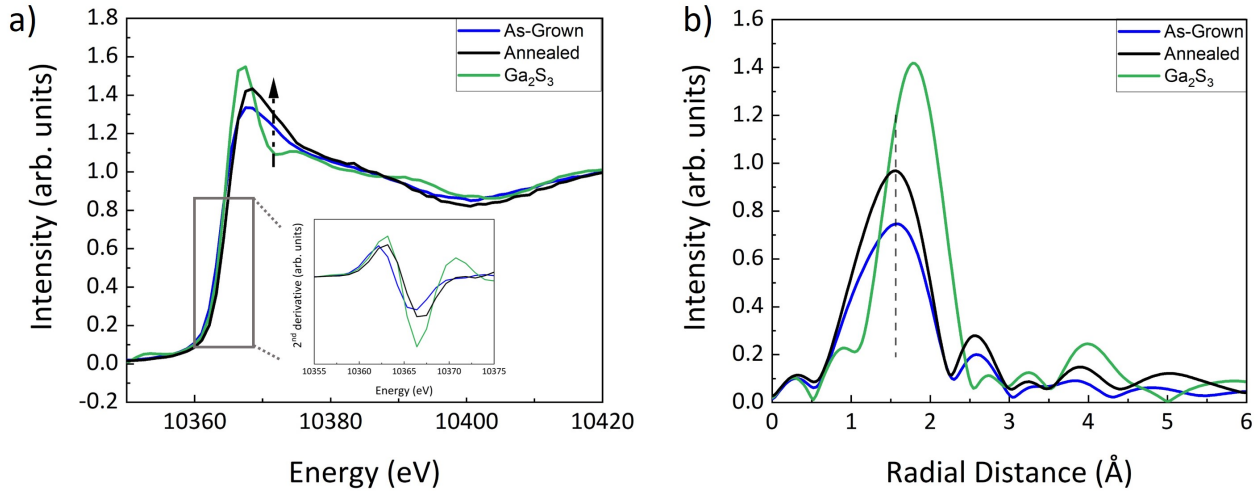

Figure 5.15: a) XANES at the Ga K-edge and b) Fourier transforms of the EXAFS spectra recorded for as grown and after annealing of a 60 ALD/MLD cycles at T_{sub}=250 °C on 100 nm SiO_2 substrate. The grown sample is compared to a reference spectrum of Ga_2S_3 powder. The inset in a) shows the second derivative of intensity.

XANES and EXAFS measurements shows the energy shift or the change of gallium oxidation state from +III to +II which could indicate that the synthesized material is getting closer to GaS.[245] The conversion of Ga-N bonds to Ga-S bonds provides also the growth of gallium oxysulfide thin films.

5.3 About the synthesis of Tin Disulfide SnS_2 thin films

The second part of this chapter, deals with a try to apply the two step strategy (ALD/MLD and thermal annealing) for the synthesis of Tin sulfide (SnS_2) by alternating TDMASn and EDT on the 100 nm SiO_2 substrate and on other substrates as well. The low melting point of SnS_2 (865 °C) comparing to other lamellar metal chalcogenides such as as MoS_2 (1750 °C) and WS_2 (2400 °C) [59] permits to crystallize SnS_2 with a lower thermal budget (T $\leq$ 350 °C). [60, 105]. Moreover, the crystallization of SnS_2 at low temperature presents

a unique property that drives us to apply the two-step process to synthesize ultra-thin film of SnS_2.

5.3.1 Studies of Sn-thiolate growth

Reactivity between TDMASn and EDT was first modelled by molecular chemistry in solution by our collaborators in C2P2 and IRECELYON (M. Zhukush, C. Camp, E. A. Quadrelli). The mixture of two solutions of TDMASn and EDT, resulted in immediate precipitation of a white solid. Elemental analysis of the isolated solid defined an empirical formula as $SnC_6NS_4H_{15}$ which matches well with calculated formula of proposed structure shown in Figure 5.16.

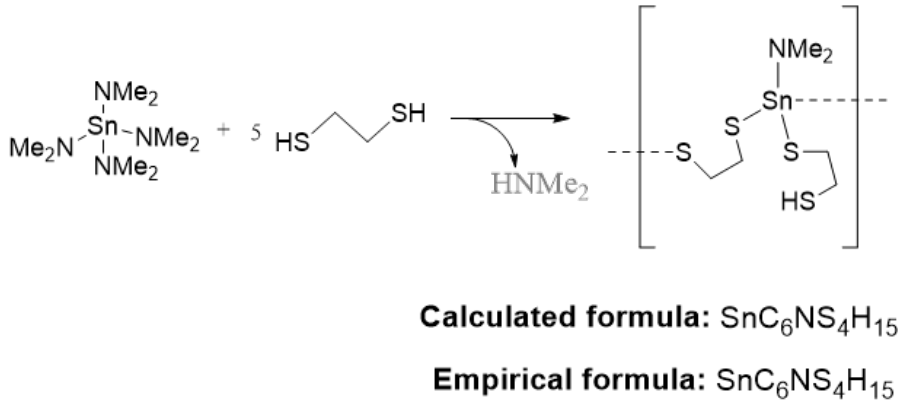

Figure 5.16: The reaction of TDMASn with EDT in excess in pentane leading to the formation of Sn (alkylamido)thiolates.

After confirming a fast reactivity between the two precursors, we decided to use these precursors for the growth of Tin-thiolate inside our reactor over on 100 nm SiO_2 substrate. During the growth, the substrate temperature was set to 50 °C using the recipe described in Section 2.3.2 Chapter 2. The growth was monitored by *in situ* ellipsometry. Ellipsometry analysis revealed a non reproducible behavior from one sample to another using same growth parameters during ALD/MLD growth, as shown by red and blue curves in Figure 5.17-a. Such observations, show that the growth of Tin-thiolate seems to be very complicated at least by *in situ* ellipsometry data. These insights were confirmed by *ex situ* XRF measurements that shows no signature of Sn and S atoms, or very few in the error of measurement. To understand what is preventing the Tin-thiolate growth to proceed with a reproduciblity,

our collaborators in C2P2 and IRCELYON studied Tin-thiolate growth chemistry via modeling on 3D type high surface area silica nano beads.

Figure 5.17-a shows the Infrared (IR) absorbance study of the powder obtained in first four pulses on pristine silica nano beads SiO_2^{500} where 500 corresponds to the pre-treatment temperature value of the silica beads. Upon the first pulse of TDMASn on the bare substrate one can observe the disappearance of the band at 3747 cm^{-1} assigned to OH bond stretching and an increase of the IR absorption band between 2700 and 3000 cm^{-1} (see red DRIFT spectrum, curve 1). Such observation confirms the full coverage of silanols group (Si-O-H) with the Tin complex provided upon TDMASn pulse. Upon the second pulse of EDT, an increase of the broad S-H stretching signal at 2412 cm^{-1} was observed. However, the re-generation of surface OH stretching bonds at 3747 cm^{-1} as shown by the blue DRIFT spectrum (curve 2), points the cleavage of previously formed Sn-O-Si bond. The re-generated silanol groups and the remaining S-H groups can further react with TDMASn during the next pulse (see green DRIFT spectrum, curve 3). This random behaviour limit the self-limiting surface reaction growth of Tin-thiolate due to unwanted surface reactions. The cleavage of the SnO-Si bond shows unstable growth and a competition between Sn-O and Sn-S bonds. Preferential reaction of EDT with the Sn-O bonds than with the Sn-S bonds explains why the growth of Tin-thiolate does not steadily continue. Besides, cleaved Tin-thiolate seems to be either volatile or easily decomposable which does not afford the following ALD cycles. [246]

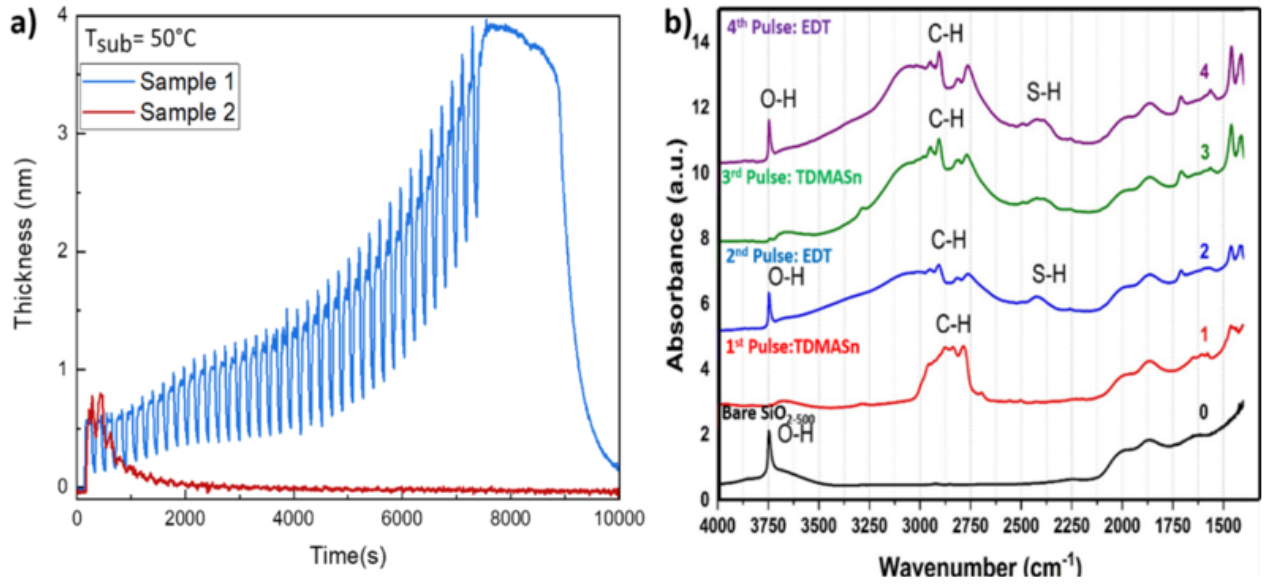

Figure 5.17: a) Ellipsometry curves during Tin-thiolate growth at 50 °C on 100 nm SiO_2 substrate using the same growth parameters ; b) IR absorbance spectra recorded for pristine silica nanobeads SiO_{2-700} (spectrum 0, black), after the 1st pulse of TDMASn precursor (spectrum 1, red); after the first pulse of EDT (spectrum 2, blue); after the second pulse of TDMASn (spectrum 3, green); after the second pulse of EDT (spectrum 4, purple).

Thermogravimetric Analysis (TGA) analysis shown in Figure 5.16 was performed to evaluate the stability of grown thiolate. TGA analysis were carried between room temperature and 400 °C under N_2 flow with a ramp rate of 5 °C/min. Sublimation of the powder Sn-thiolate was carried under a dynamic ultra-high vacuum (10^{-5} mbar). The solid has lost its weight in four main steps within the given temperature range. The first weight loss observed between 60 and 120 °C is related to the evaporation of Sn thiolate vapors upon its sublimation. Second weight loss observed between 120 and 200 °C is related to the thermal decomposition of the carbon chain present in the ethylenedithiolate ligand, -SCH_2CH_2SH, that produces ethylene (C_2H_4). The third loss between 250 and 280 °C is actually the major weight loss, that is attributed to more significant fragmentation of the molecule involving the breakage of the C-N and Sn-N bonds. We can clearly see the temperature higher than 220 °C , Tin-thiolate totally decomposes. However, at 40 °C we see white sublimed powder but the major part of solid was not sublimed.

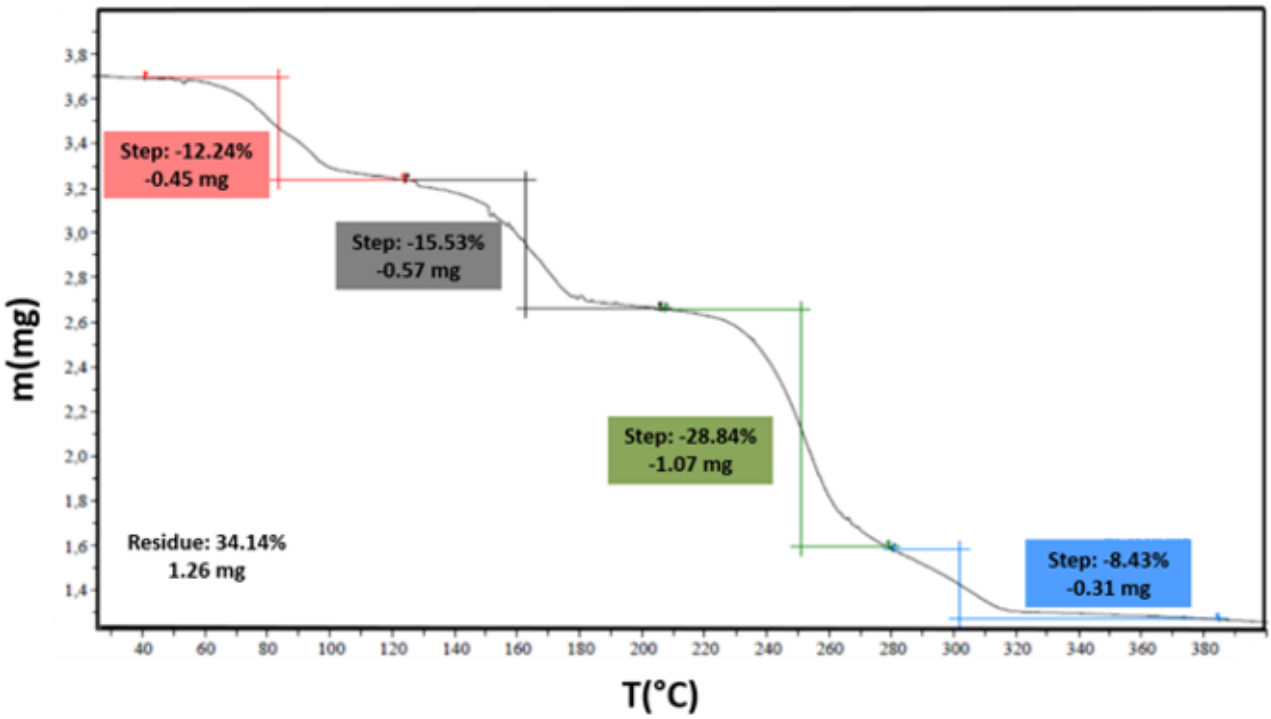

Figure 5.18: TGA anaylsis of the Sn(EDT)2(NMe_2) complex (Tin-thiolate) between 20 and 400 °C.

The data presented in this section show the complexity of the deposition of Sn-thiolate by alternating TDMASn and EDT on 100 nm SiO_2 substrate. The inputs provided from the study on high surface area substrate give clues to understand the non reproducible behaviour of Tin-thiolate growth. This may be mainly due to the preferential reaction of Sn-O bonds comparing to Sn-S bonds explaining the difficult growth of Sn-thiolate.

5.3.2 Functionalization of the 100 nm SiO_2 substrate surface

In order to steadily grow Tin-thiolate on a substrate, we need to avoid the competition between Sn-O and Sn-S bonds that prevents the growth and leads to desorption problems (*i.e.* Sn-O-Si bond breaking). Pre-functionalization of the silica surface by a protecting group could be the solution. For this reason Mercaptopropyltriethoxysilane (MPTS) was grafted on the surface dehydroxylated silica nano beads substrate following the previously published method.[247]

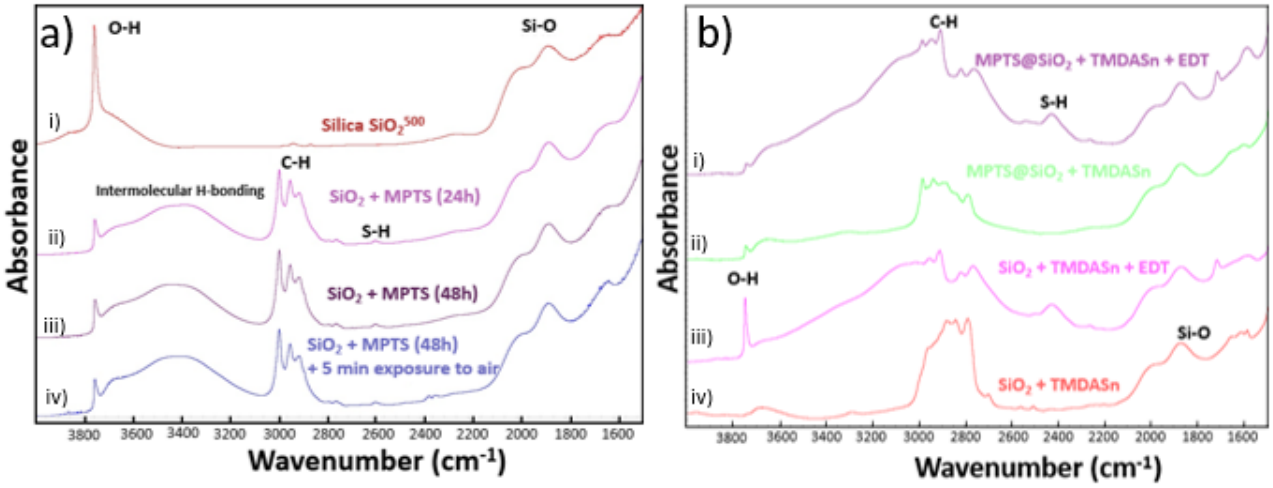

Figure 5.19: IR absorbance sprectrum for a) nanobeads substrate surface functionalization process by MPTS and b) one ALD/MLD cycle on both non-functionalized and functionalized 100 nm SiO_2 wafer.

First, to optimize the efficiency of the functionalization process by MPTS on the bare dehydroxylated silica nano beads substrate, IR spectra were taken into account to validate the functionalization process as shown in Figure 5.19-a. Therefore, we can see that after the functionalization of the silica beads for 24 hours, the peak representing the O-H bonds has not totally disappeared, indicating a partial replacement of the surface -OH by -SH. Moreover, no significant changes are observed between the 24h- and 48h-spectra (spectra ii and iii), nor after exposure to air for 5 minutes (spectra iv) which implies that the functionalized substrate is stable enough to resist the exposure to air during the sample preparation prior to deposition.

Figure 5.19-b shows the IR spectra for one ALD/MLD full cycle (after TDMASn and EDT pulses) upon the injection on SiO_2 and functionalized SiO_2 substrates. The appearance of O-H bonds after the injection of EDT (spectra iii) confirms the breakage of Sn-O in favor of Sn-S and thus, the etching of the surface by EDT. Intrestingly, we can see that upon the grafting reactions of TDMASn and then EDT on the MPTS functionalized SiO_2 surface (spectra i), the generation of a new O-H bond stretching band is not been detected, confirming that the functionalization is achieved.

The functionnalization process by MPTS was applied the 100 nm SiO_2 wafer, and Sn-thiolate growth was performed in the MOON reactor at LMGP. The obtained grown thiolate presented a similar behaviour in the non-stability as the one previously obtained before

functionalization. Obtained results confirms the complexity of the growth on 100 nm SiO_2 substrate. Therefore, we tried to replace the functionnalization process by a sulfurization process performed inside the MOON reactor to check its impact on the growth.

5.3.3 Growth on ZnS substrate

Since performing growth on MPTS functionalized 100 nm SiO_2 substrate didn't reach its target, we tried to find another solution by performing the thiolate growth over another sulfide material, We chose zinc sulfide (ZnS) [248], which was obtained by the sulfurization *in situ* of 50 nm ZnO substrates on 100 nm SiO_2 substrate. The sulfurization is obtained upon the injection of the mixture of EDT and N_2 (100 sccm) at 450°C for 30 min on the surface of the ZnO substrate.[249] The process was carried out inside the MOON reactor.

In-plane XRD data shown in Figure 5.20 shows the impact of the sulfurization process on the ZnO sample. We can see that after 30 min sulfurization we succeeded to go from polycrystalline ZnO with a Wurtzite structure (hexagonal system, space group P63mc with a lattice parameters of a=b= 3.24 Å and c=5.22 Å) (Figure 5.20-a) [250] to a ZnS with the Wurtzite-2H hexagonal system, space group $P_{63}mc$ with a lattice parameters of a=b= 3.81 Å and c=16.68 Å (Figure 5.20-b) [251]. Besides, from Figure 5.20-b we can clearly notice that the sulfurization of ZnO is not completed.

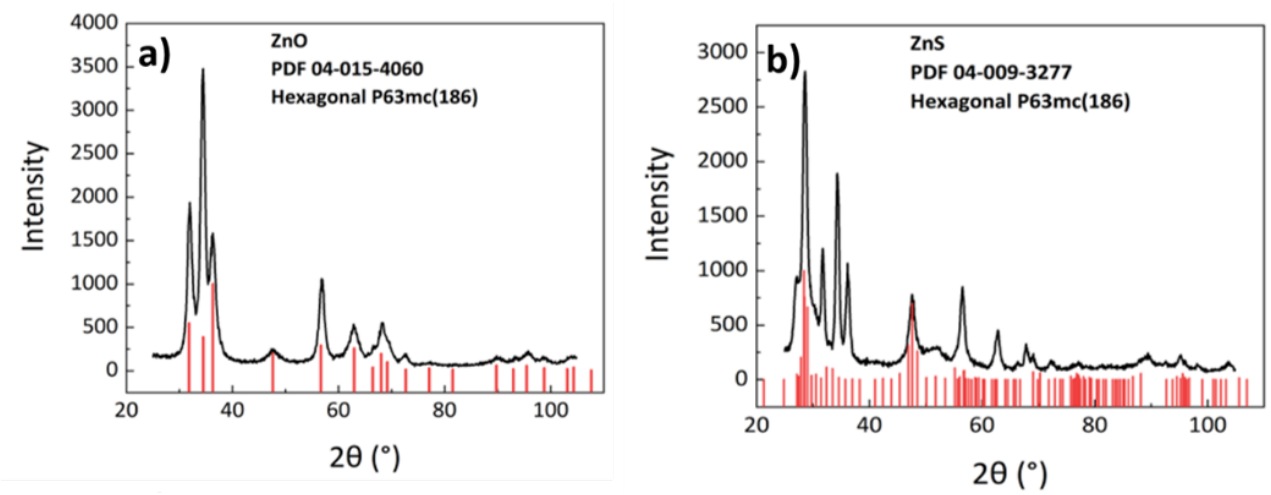

Figure 5.20: In plane XRD of a) 50 nm ZnO polycristalline thin film on 100 nm SiO_2 and b) sulfurized ZnO into ZnS.

Therefore, to confirm if a full coverage of -SH group take place on the surface of the sulfurized ZnO film, XPS measurements were taken into account. XPS performed using the Al Kα source at an incidence of θ= 45° with respect the surface normal, leading to analyzed thickness depth of 5.6 nm. Figure 5.21 shows the S 2p and Zn $2p_{3/2}$ core peaks confirming that the analyzed surface has been well sulfurized and it's fully converted into ZnS. For this reason, the sulfurized sample was used as a substrate for the growth of Sn-thiolate.

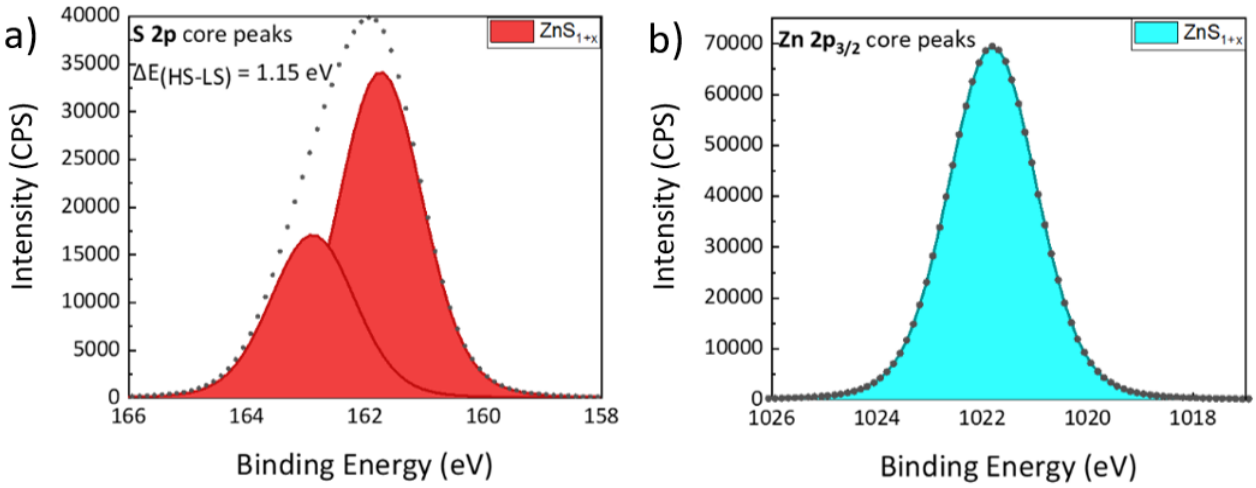

Figure 5.21: XPS data of the ZnS substrate a) S2p core peaks and b) Zn 2p3/2 core peaks.

Unfortunately, the growth of Sn-thiolate over the EDT-sulfurized ZnO substrate we obtained the same result as with the other wafers (SiO_2 and MPTS-functionalized SiO_2). These results confirm that the deposition of Tin-thiolate using TDMASn and EDT is very complex.

5.4 Conclusions

This chapter was based on applying the two-step process strategy on lamellar metal chalcogenide materials such as gallium sulfide and tin disulfide.

The obtained results regarding gallium sulfide show that we were able to obtain a conformal and uniform film at T_{sub}=250 °C as suggested by *ex situ* XRR and by TEM measurements. The growth of 40 ALD/MLD cycles on 100 nm SiO_2 at 250°C gives a film with a thickness equal to 6.6 nm, where the film might be covered by a gallium oxysulfide top film (resulting from the exposure of the deposited sample to ambient air) as XRR simluated curves

indicated.

The growth behavior was studied by *in situ* X-ray analyses on two different substrate types, i.e. 100 nm SiO_2 and Si(111) HF. The evolution of the S/Ga XRF ratio during the deposition permit to evaluate the growth behavior. The constant ratio value observed after few ALD/MLD cycles show that a similar growth behavior is achieved on both substrates. The deposition on 100 nm SiO_2 substrate start with a higher S/Ga comparing to the deposition on Si(111) HF substrate before stabilizing on a constant ratio after. The higher values at the beginning might be related to the time needed before reaching a compatibility of chemistries between the surface and the deposition. [116]

In addition, the XANES and EXAFS recorded during ALD/MLD growth showed both thickness and time dependent properties (cannot be sorted) since upon accumulation of ALD/MLD cycles, the Fourier transform showed a shift towards higher values of the radial distance between Ga and its nearest neighbors (N, S, possibly O) by accumulating the number of ALD/MLD cycles. However, XPS and ToF SIMS data show the presence of oxygen within the deposited films due to their exposure to ambient air. In addition, the oxidized gallium sulfide films are composed of quasi-stoichiometric gallium oxysulfide GaO_xS_y layers where $x+y \approx 1$.

Finally, neither the RAMAN spectroscopy nor the *in situ* XRD has given any indication of the film crystallization even after annealing. Consequently, the process and in particular the annealing step still needs to be improved.

The second part of this chapter targeted the deposition of Tin disulfide thin films. The growth of Tin-thiolate was not successful. Moreover, silica nano beads study highlighted that EDT pulses induce a re-generation of surface OH stretching bands that also suggests cleavage of the SnO-Si bond. Such results confirmed the complexity for depositing thiolate over 100 nm SiO_2 substrate. Few solutions have been proposed to overcome this obstacle such as performing a functionalization of SiO_2 substrate with MPTS molecule [247] or performing sulfurization of ZnO in order to replace the surface terminating -OH groups by -SH groups that could lead to a successful Sn-thiolate growth. Therefore, the growth of Sn-thiolate was performed on -SH terminating wafers inside our ALD reactor whereas a unsuccessful growth was also obtained. The MPTS-SiO_2 substrate functionalization was effective for the first ALD/MLD cycle but not after accumulating the cycles. We concluded

that the ALD growth of Tin-thiolate is not possible using TDMASn and EDT. Noticeably, IR absorbance studies suggest that EDT plays the role of an etching gas on the Si-Sn coverage. In addition, the difficulty of obtaining $Sn(EDT)_2$ by solvent reactions was previously reported for low melting point range.[246]

The preliminary experimental results presented in this chapter are instructive and consistent with the literature. However, the work is not completed and it requires additional data analysis and experiments to reach ultra-thin crystalline materials.

General conclusions and perspectives

Lamellar metal sulfide thin films are promising candidates to be integrated in emerging devices for various applications. However, it is important to prevent high thermal budget during their synthesis and find an industrially reliable growth method. In this context, the work presented in this dissertation focused on developing a two-step process for the synthesis of lamellar ultra-thin films of metal sulfides: first an amorphous hybrid organic-inorganic thin film is deposited by ALD/MLD, then a thermal annealing is carried out. The use of an organic molecule as sulfur precursor, *i.e.* 1,2-ethandithiol (EDT) (a safer organic molecule than the highly toxic H_2S co-reactant most often used in ALD), permits to generate an amorphous inorganic/organic thin film (thiolate), especially when the ALD/MLD is performed at low substrate temperature.

In chapter 1, the state of the art on lamellar 2D materials (and especially sulfides) as well as the methods of deposition of these materials were presented. In chapter 2, the method followed during this study was described.

In chapter 3, the two-step process was performed to synthesize ultra-thin films of TiS_2 (the lightest and the least expensive candidate of TMDs family) using TDMAT and EDT as precursors on non-epitaxial substrate (100 nm SiO_2). The growth of the hybrid thiolate film at 50 °C was studied by *in situ* X-ray synchrotron measurements (XRF, XRR, and XANES). An 80- and 40-cycle ALD/MLD Ti-thiolates were converted into lamellar TiS_2 layers upon a thermal annealing strategy under Ar/H_2 at 450 °C for 30 mins. The crystalline quality of the resulting films was assessed by Raman scattering and XANES. The chemical composition of the obtained films was quantified by ARXPS and HAXPES measurements that demonstrated that our films are composed of stoichiometric TiS_2 layers. TEM images showed the presence of TiS_2 monolayers, preferentially oriented parallel to the amorphous substrate surface. The

film texture was also confirmed by X-ray linear dichroïsm at the Ti-K edge, confirming the TEM observations at a larger scale. The formation of a thin oxide on top of the film after exposure at air ambient (which was found to be a constant coverage layer regardless of the annealing strategy) was also evidenced. Besides, the four-point probe resistivity measurements and spectroscopic ellipsometry strongly suggest the semi-conductor behavior of the obtained TiS_2 thin films with a direct bandgap of 1.72 eV. However, the proposed strategy didn't succeed to reach ultra-thin films (less than 10 nm). Indeed, an 20-cycle ALD/MLD thiolate was annealed also under Ar/H_2 at 450 °C for 30' and no evidence of crystallisation was detected by Raman neither XANES. The reason behind was likely related to a significant loss of sulfur during annealing that results in the removal of major part of the sulfur in the case of a few ALD/MLD cycles.

In chapter 4, we report on the investigation of the annealing strategy, thus highlighting the importance of the annealing step for the synthesis of ultra-thin films. Two annealing strategies were explored. *In situ* X-ray synchrotron measurements (mainly *in situ* XRF) afforded to monitor the [S]/[Ti] ratio during the process to follow the transition from amorphous Ti-thiolate to stoichiometric TiS_2. *In situ* X-ray synchrotron measurements performed during the annealing and *ex situ* characterizations carried out by XPS, HAXPES, TEM, XANES, and Raman scattering allowed to study the quality of thin films. Finally, the growth of a 20-cycle ALD/MLD thiolate then annealed with strategy B enabled to produce an ultra-thin film with a thickness of 5.5 nm composed of stoichiometric TiS_2 layers at mild temperature (300 °C).

In the last chapter (chapter 5), we reported the progress of the synthesis of Ga_xS metal sulfides (an interesting candidate as buffer layers in CdTe solar cells). This material was deposited using TDMAG and EDT. Promising results were obtained showing that an ALD/MLD window exists in the region of T_{sub}= [200 °C; 250°C], and a homogeneous deposit was obtained at T_{sub} = 250 °C. *In situ* experiments performed with synchrotron X-ray at the SIRIUS beamline (SOLEIL) showed a difference in the growth behavior in the early stages of the growth depending on the substrate, i.e. 100 nm SiO_2 and Si(111) HF (as shown by the XRF [S]/[Ga] ratio). In addition, the *in situ* XANES and EXAFS spectra recorded during ALD/MLD growth showed both thickness and time dependent properties (cannot be sorted) since upon accumulation of ALD/MLD cycles, a change in the oxidation state of

gallium from +III to +II was observed on the XANES spectra recorded at the Ga-K edge, suggesting the formation of gallium sulfide. Concommitantly, the Fourier transform showed a shift towards higher values of the radial distance between Ga and its nearest neighbors (N, S, possibly O). For a 60-cycle ALD/MLD sample grown on 100 nm SiO_2, we noticed a shift back to higher energy of the Ga-K edge when increasing the cycle number from 35 to 60, this would indicates a shift back toward Ga^{3+}. Additional simulation and fittings of the XAFS spectra are needed to conclude, the data analysis is in progress. Besides, the XPS and ToF-SIMS results (obtained *ex situ*) show the presence of oxygen within the deposited films which is likely due to hydrolisation from the sample surface and possibly oxygen diffusion from substrate. This last point is under investigation.

Also, we targeted depositing Tin disulfide thin films (a lamellar semi-conductor post-transition metal disulfide). The Tin-thiolate was intended to be grown from TDMASn and EDT. However, we didn't succeed to grow the Tin-thiolate neither on silicon wafer nor on the high surface area silica nanobeads. To solve such problem, we tried to functionalize the substrate surface with MPTS molecules, as well as to deposit on other sulfide materials as for instance polycrystalline ZnS obtained *in situ*, prior to the thiolate growth, by the sulfurization of ZnO with EDT. But all these solutions didn't allow us to grow the Tin-thiolate. Therefore, the growth of Tin-thiolate needs to be studied in more detail as it turned that EDT cleaves the Sn-O-Si bond.

The optimization and elaboration of thin films by ALD/MLD and thermal annealing on non-epitaxial substrates could not be achieved if our reactor did not have the possibility to be installed on the diffractometer of the SIRIUS beamline (SOLEIL). The *in situ* X-ray experiments performed at the SIRIUS beamline and the use of advanced characterization techniques (XPS/HAXPES, Raman, TEM...) have been one driving force to shed light and better control the process from the first pulses to the end of the annealing.

Finally, this hybrid ALD/MLD process seems particularly well adapted to explore other lamellar metal chalcogenides and opens new possibilities for the synthesis of 2D materials in general. Additionally, the successful growth of an ultra-thin stoichiometric crystalline TiS_2 on an amorphous SiO_2 substrate at mild temperature (300 °C) could present a significant advantage for the integration of such process for back-end-of-line (BEOL) technologies in microelectronics.[252]

This thesis work should be continued and some results should be improved to obtain

higher-quality materials: indeed, it leaves the field open to several perspectives:

- Careful considerations should still be taken into account during the annealing step aiming to remove S-S pairs and Carbon content that prevent to obtain an X-ray diffraction pattern, that is a crystallization at large scale. In this context, additional experiments are required such as increasing the flux of the annealing gas, the use of other sulfur precursors, and longer purge times...

- The presence of a thin oxide film on top of the TiS_2 film in ambient air, means finding a way in the future to etch the top oxide without affecting the quality of the TiS_2 thin film or covering it to protect it from oxidation or, at least to have the possibility to transfer the sample in vacuum or inert atmosphere (via the connection of a vacuum suitcase, for instance, to the moon reactor) to characterization equipment, as for instance XPS. In addition, an interesting perspective on the design of the reactor aims to implement additional precursor injection systems that would give the possibility to deposit a protective film over the annealed material.

- Additional electrical measurements are also required on the thin and ultra-thin films of TiS_2 to evaluate the electrical properties of the synthesized deposits and the possibility of integrating these thin films in emerging devices.

- As far as the synthesis of gallium sulfide is concerned, the in-depth presence of oxide stays is not yet elucidated for sure. Therefore, future experiments will target the growth of a thicker film to minimize the effect of the oxidized region on the upper part of the sulfide film which comes into contact with air.

- Although the growth of tin sulfide was not possible using TDMASn and EDT, carrying out the two-step ALD/MLD process for the synthesis of SnS_2 could still be considered by replacing EDT with another organic sulfur precursor such as *t*-butylthiol (TBT), di(*t*-butyl) disulfide (TBDS) and 3,4-toluenedithiolate (TDT) [105, 253]; in order to involve a chemical reaction between the Sn and S precursors leading to the formation of the tin thiolate film.

- Since it is confirmed that EDT is etching Sn moieties grafted on SiO_2, and most generally Tin oxide and Tin sulfides, we may suggest applying EDT in Atomic Layer Etching (ALE) process.

Bibliography

[1] Richard Feynman. "There's plenty of room at the bottom". In: *Feynman and computation*. CRC Press, 2018, pp. 63–76.

[2] George M Whitesides. "Nanoscience, nanotechnology, and chemistry". In: *Small* 1.2 (2005), pp. 172–179.

[3] Gordon E Moore et al. *Cramming more components onto integrated circuits*. 1965.

[4] Mark Lundstrom. "Moore's law forever?" In: *Science* 299.5604 (2003), pp. 210–211.

[5] Wolfgang Arden et al. "More-than-Moore white paper". In: *Version* 2 (2010), p. 14.

[6] Shuiyuan Wang et al. "Two-dimensional devices and integration towards the silicon lines". In: *Nature Materials* (2022), pp. 1–15.

[7] GQ Zhang, F Van Roosmalen, and M Graef. "The paradigm of" more than Moore"". In: *2005 6th International Conference on Electronic Packaging Technology*. IEEE. 2005, pp. 17–24.

[8] Max C Lemme et al. "2D materials for future heterogeneous electronics". In: *Nature Communications* 13.1 (2022), pp. 1–5.

[9] Klaus Schuegraf et al. "Semiconductor logic technology innovation to achieve sub-10 nm manufacturing". In: *IEEE Journal of the Electron Devices Society* 1.3 (2013), pp. 66–75.

[10] Giuseppe Iannaccone et al. "Quantum engineering of transistors based on 2D materials heterostructures". In: *Nature nanotechnology* 13.3 (2018), pp. 183–191.

[11] L Britnell et al. "Field-effect tunneling transistor based on vertical graphene heterostructures". In: *Science* 335.6071 (2012), pp. 947–950.

[12] Thanasis Georgiou et al. “Vertical field-effect transistor based on graphene–WS2 heterostructures for flexible and transparent electronics”. In: *Nature nanotechnology* 8.2 (2013), pp. 100–103.

[13] Kostya S Novoselov et al. “Two-dimensional gas of massless Dirac fermions in graphene”. In: *nature* 438.7065 (2005), pp. 197–200.

[14] Kostya S Novoselov et al. “Two-dimensional atomic crystals”. In: *Proceedings of the National Academy of Sciences* 102.30 (2005), pp. 10451–10453.

[15] Angelo Armano and Simonpietro Agnello. “Two-dimensional carbon: a review of synthesis methods, and electronic, optical, and vibrational properties of single-layer graphene”. In: *C* 5.4 (2019), p. 67.

[16] Caterina Soldano, Ather Mahmood, and Erik Dujardin. “Production, properties and potential of graphene”. In: *Carbon* 48.8 (2010), pp. 2127–2150.

[17] Kirill I Bolotin et al. “Ultrahigh electron mobility in suspended graphene”. In: *Solid state communications* 146.9-10 (2008), pp. 351–355.

[18] Kirill I Bolotin et al. “Temperature-dependent transport in suspended graphene”. In: *Physical review letters* 101.9 (2008), p. 096802.

[19] Dale AC Brownson, Dimitrios K Kampouris, and Craig E Banks. “Graphene electrochemistry: fundamental concepts through to prominent applications”. In: *Chemical Society Reviews* 41.21 (2012), pp. 6944–6976.

[20] Alexander A Balandin et al. “Superior thermal conductivity of single-layer graphene”. In: *Nano letters* 8.3 (2008), pp. 902–907.

[21] Yanwu Zhu et al. “Graphene and graphene oxide: synthesis, properties, and applications”. In: *Advanced materials* 22.35 (2010), pp. 3906–3924.

[22] Changgu Lee et al. “Measurement of the elastic properties and intrinsic strength of monolayer graphene”. In: *science* 321.5887 (2008), pp. 385–388.

[23] Matteo Bosi. “Growth and synthesis of mono and few-layers transition metal dichalcogenides by vapour techniques: a review”. In: *RSC Advances* 5.92 (2015), pp. 75500–75518.

[24] Ankur Gupta, Tamilselvan Sakthivel, and Sudipta Seal. “Recent development in 2D materials beyond graphene”. In: *Progress in Materials Science* 73 (2015), pp. 44–126.

[25] Andre K Geim and Irina V Grigorieva. "Van der Waals heterostructures". In: *Nature* 499.7459 (2013), pp. 419–425.

[26] Patrick Vogt et al. "Silicene: compelling experimental evidence for graphenelike two-dimensional silicon". In: *Physical review letters* 108.15 (2012), p. 155501.

[27] Wei Wei et al. "Many-body effects in silicene, silicane, germanene and germanane". In: *Physical Chemistry Chemical Physics* 15.22 (2013), pp. 8789–8794.

[28] Qi Yang et al. "Recent Progress of MX ene-Based Nanomaterials in Flexible Energy Storage and Electronic Devices". In: *Energy & Environmental Materials* 1.4 (2018), pp. 183–195.

[29] Santosh Kumar Radha et al. "Ultrathin 2D-oxides: A perspective on fabrication, structure, defect, transport, electron, and phonon properties". In: *Journal of Applied Physics* 129.22 (2021), p. 220903.

[30] A Chaves et al. "Bandgap engineering of two-dimensional semiconductor materials". In: *npj 2D Materials and Applications* 4.1 (2020), pp. 1–21.

[31] Agnieszka Kuc, Thomas Heine, and Andras Kis. "Electronic properties of transition-metal dichalcogenides". In: *MRS bulletin* 40.7 (2015), pp. 577–584.

[32] Sajedeh Manzeli et al. "2D transition metal dichalcogenides". In: *Nature Reviews Materials* 2.8 (2017), pp. 1–15.

[33] Roscoe G Dickinson and Linus Pauling. "The crystal structure of molybdenite". In: *Journal of the American Chemical Society* 45.6 (1923), pp. 1466–1471.

[34] Jl A Wilson and AD Yoffe. "The transition metal dichalcogenides discussion and interpretation of the observed optical, electrical and structural properties". In: *Advances in Physics* 18.73 (1969), pp. 193–335.

[35] Zhiyuan Zeng et al. "Single-layer semiconducting nanosheets: high-yield preparation and device fabrication". In: *Angewandte Chemie* 123.47 (2011), pp. 11289–11293.

[36] Kin Fai Mak et al. "Atomically thin MoS 2: a new direct-gap semiconductor". In: *Physical review letters* 105.13 (2010), p. 136805.

[37] Agnieszka Kuc, Nourdine Zibouche, and Thomas Heine. "Influence of quantum confinement on the electronic structure of the transition metal sulfide T S 2". In: *Physical Review B* 83.24 (2011), p. 245213.

[38] Cameron Robert Thurston. "Band Gap Engineering Of Titania Systems Purposed For Photocatalytic Activity". In: (2017).

[39] Wenzhong Bao et al. "High mobility ambipolar MoS2 field-effect transistors: Substrate and dielectric effects". In: *Applied Physics Letters* 102.4 (2013), p. 042104.

[40] GL Frey et al. "Optical-absorption spectra of inorganic fullerenelike M S 2 (M= Mo, W)". In: *Physical Review B* 57.11 (1998), p. 6666.

[41] Muhammad R Islam et al. "Tuning the electrical property via defect engineering of single layer MoS 2 by oxygen plasma". In: *Nanoscale* 6.17 (2014), pp. 10033–10039.

[42] Nitin Choudhary et al. "Two-dimensional lateral heterojunction through bandgap engineering of MoS2 via oxygen plasma". In: *Journal of Physics: Condensed Matter* 28.36 (2016), p. 364002.

[43] Rajesh Kappera et al. "Phase-engineered low-resistance contacts for ultrathin MoS2 transistors". In: *Nature materials* 13.12 (2014), pp. 1128–1134.

[44] Damien Voiry, Aditya Mohite, and Manish Chhowalla. "Phase engineering of transition metal dichalcogenides". In: *Chemical Society Reviews* 44.9 (2015), pp. 2702–2712.

[45] Liang Zhang et al. "Tracking the chemical and structural evolution of the TiS2 electrode in the lithium-ion cell using operando x-ray absorption spectroscopy". In: *Nano letters* 18.7 (2018), pp. 4506–4515.

[46] Hidetaka Kasai et al. "X-ray electron density investigation of chemical bonding in van der Waals materials". In: *Nature materials* 17.3 (2018), pp. 249–252.

[47] *Top and side view*. `https://www.ossila.com/en-us/products/titanium-disulfide`.

[48] PC Klipstein et al. "Stoichiometry dependence of the transport properties of TiS2". In: *Journal of Physics C: Solid State Physics* 14.28 (1981), p. 4067.

[49] JACOPO RANALLI. "Dimensionality effect of titanium disulphide nanosheets on its vibrational properties measured via Raman spectroscopy". In: (2016).

[50] AH Thompson, FR Gamble, and CR Symon. "The verification of the existence of TiS2". In: *Materials Research Bulletin* 10.9 (1975), pp. 915–919.

[51] J Dahn and RR Haering. "Lithium intercalation in TiS2". In: *Materials Research Bulletin* 14.10 (1979), pp. 1259–1262.

[52] M Stanley Whittingham. "Electrical energy storage and intercalation chemistry". In: *Science* 192.4244 (1976), pp. 1126–1127.

[53] Evgeny A Suslov et al. "Lithium intercalation into TiS2 cathode material: phase equilibria in a Li–TiS2 system". In: *Ionics* 22.4 (2016), pp. 503–514.

[54] Yang Ye et al. "Enhanced thermoelectric performance of xMoS2–TiS2 nanocomposites". In: *Journal of Alloys and Compounds* 666 (2016), pp. 346–351.

[55] Viljami Pore, Mikko Ritala, and Markku Leskelä. "Atomic layer deposition of titanium disulfide thin films". In: *Chemical Vapor Deposition* 13.4 (2007), pp. 163–168.

[56] Guillaume A Muller et al. "High performance pseudocapacitor based on 2D layered metal chalcogenide nanocrystals". In: *Nano letters* 15.3 (2015), pp. 1911–1917.

[57] Mariam Barawi et al. "Hydrogen storage by titanium based sulfides: nanoribbons (TiS3) and nanoplates (TiS2)". In: *J. Electr. Eng* 3 (2015), pp. 24–29.

[58] Jae Hyo Han et al. "Unveiling chemical reactivity and structural transformation of two-dimensional layered nanocrystals". In: *Journal of the American Chemical Society* 135.10 (2013), pp. 3736–3739.

[59] Juhyun Lee et al. "Improved electrical properties of atomic layer deposited tin disulfide at low temperatures using ZrO2 layer". In: *AIP Advances* 7.2 (2017), p. 025311.

[60] Jung Joon Pyeon et al. "Low-temperature wafer-scale synthesis of two-dimensional SnS 2". In: *Nanoscale* 10.37 (2018), pp. 17712–17721.

[61] B Pałosz, W Steurer, and H Schulz. "Refinement of SnS2 polytypes 2H, 4H and 18R". In: *Acta Crystallographica Section B: Structural Science* 46.4 (1990), pp. 449–455.

[62] Miika Mattinen et al. "Low-temperature wafer-scale deposition of continuous 2D SnS2 films". In: *Small* 14.21 (2018), p. 1800547.

[63] Lee A Burton et al. "Synthesis, characterization, and electronic structure of single-crystal SnS, Sn2S3, and SnS2". In: *Chemistry of Materials* 25.24 (2013), pp. 4908–4916.

[64] RMA Lieth, HJM Heijligers, and CWM vd Heijden. "The P-T-X phase diagram of the system Ga-S". In: *Journal of the Electrochemical Society* 113.8 (1966), p. 798.

[65] Xiangbo Meng et al. "Atomic layer deposition of gallium sulfide films using hexakis (dimethylamido) digallium and hydrogen sulfide". In: *Chemistry of Materials* 26.2 (2014), pp. 1029–1039.

[66] C Sanz, C Guillen, and MT Gutierrez. "Influence of the synthesis conditions on gallium sulfide thin films prepared by modulated flux deposition". In: *Journal of Physics D: Applied Physics* 42.8 (2009), p. 085108.

[67] *Top and side view*. `https://www.ossila.com/products/gallium-sulfide-gas-powder-and-crystals`.

[68] Hüseyin Ertap et al. "Structural and optical properties of gallium sulfide thin film". In: *Turkish Journal of Physics* 40.3 (2016), pp. 297–303.

[69] Xian-an Cao et al. "Passivation of the GaAs (100) surface with a vapor-deposited GaS film". In: *Journal of Vacuum Science & Technology B: Microelectronics and Nanometer Structures Processing, Measurement, and Phenomena* 16.5 (1998), pp. 2656–2659.

[70] Xiangbo Meng et al. "Gallium sulfide–single-walled carbon nanotube composites: high-performance anodes for lithium-ion batteries". In: *Advanced Functional Materials* 24.34 (2014), pp. 5435–5442.

[71] Dattatray J Late et al. "GaS and GaSe ultrathin layer transistors". In: *Advanced materials* 24.26 (2012), pp. 3549–3554.

[72] Marilena I Zappia et al. "Two-Dimensional Gallium Sulfide Nanoflakes for UV-Selective Photoelectrochemical-type Photodetectors". In: *The Journal of Physical Chemistry C* 125.22 (2021), pp. 11857–11866.

[73] E Cuculescu et al. "Optical and photoelectrical properties of GaS and CdTe thin FILMS, components of GaS/CdTe heterojunctions". In: *Journal of Optoelectronics and Advanced Materials* 8.3 (2006), p. 1077.

[74] AF Qasrawi and Olfat A Omareya. "Characterization of the Al/Ge/In2Se3/Ga2S3/Al hybrid tunneling barriers designed for Gigahertz/Terahertz applications". In: *Thin Solid Films* 660 (2018), pp. 276–281.

[75] SE Al Garni and AF Qasrawi. "TUNABLE Au/Ga 2 S 3/Yb VARACTOR DIODES DESIGNED FOR HIGH FREQUENCY APPLICATIONS." In: *Chalcogenide Letters* 14.9 (2017).

[76] Nan Zhou et al. "Nonlayered two-dimensional defective semiconductor γ-Ga2S3 toward broadband photodetection". In: *ACS nano* 13.6 (2019), pp. 6297–6307.

[77] Manal MYA Alsaif et al. "Atomically thin Ga2S3 from skin of liquid metals for electrical, optical, and sensing applications". In: *ACS Applied Nano Materials* 2.7 (2019), pp. 4665–4672.

[78] Yaowei Wei et al. "Fabrication of in-situ Ti-doped CuGaS2 thin films for intermediate band solar cell applications by sputtering with CuGaS2: Ti targets". In: *Vacuum* 169 (2019), p. 108921.

[79] Lei Hu and Dongshan Wei. "Janus group-III chalcogenide monolayers and derivative type-II heterojunctions as water-splitting photocatalysts with strong visible-light absorbance". In: *The Journal of Physical Chemistry C* 122.49 (2018), pp. 27795–27802.

[80] Killian Denoue et al. "Mechanochemical synthesis and structural characterization of gallium sulfide Ga2S3". In: *Journal of Solid State Chemistry* 292 (2020), p. 121743.

[81] Ruben Mas-Balleste et al. "2D materials: to graphene and beyond". In: *Nanoscale* 3.1 (2011), pp. 20–30.

[82] Jonathan N Coleman et al. "Two-dimensional nanosheets produced by liquid exfoliation of layered materials". In: *Science* 331.6017 (2011), pp. 568–571.

[83] E Benavente et al. "Intercalation chemistry of molybdenum disulfide". In: *Coordination chemistry reviews* 224.1-2 (2002), pp. 87–109.

[84] Edward P Randviir, Dale AC Brownson, and Craig E Banks. "A decade of graphene research: production, applications and outlook". In: *Materials Today* 17.9 (2014), pp. 426–432.

[85] Hugh O Pierson. *Handbook of chemical vapor deposition: principles, technology and applications*. William Andrew, 1999.

[86] Ruitao Lv et al. "Transition metal dichalcogenides and beyond: synthesis, properties, and applications of single-and few-layer nanosheets". In: *Accounts of chemical research* 48.1 (2015), pp. 56–64.

[87] Danielle M Hamann, Erik C Hadland, and David C Johnson. "Heterostructures containing dichalcogenides-new materials with predictable nanoarchitectures and novel emergent properties". In: *Semiconductor Science and Technology* 32.9 (2017), p. 093004.

[88] Dongil Chu and Eun Kyu Kim. "Recent advances in synthesis and assembly of van der Waals materials". In: *Journal of the Korean Physical Society* 73.6 (2018), pp. 805–816.

[89] Rie Shimanouchi et al. "Plasma-enhanced chemical vapor deposition of titanium sulfides". In: *Chemistry Letters* 14.9 (1985), pp. 1323–1326.

[90] Yi-Hsien Lee et al. "Synthesis of large-area MoS2 atomic layers with chemical vapor deposition". In: *Advanced materials* 24.17 (2012), pp. 2320–2325.

[91] Luca Seravalli and Matteo Bosi. "A review on chemical vapour deposition of two-dimensional MoS2 flakes". In: *Materials* 14.24 (2021), p. 7590.

[92] Kibum Kang et al. "High-mobility three-atom-thick semiconducting films with wafer-scale homogeneity". In: *Nature* 520.7549 (2015), pp. 656–660.

[93] Steven M George. "Atomic layer deposition: an overview". In: *Chemical reviews* 110.1 (2010), pp. 111–131.

[94] Tuomo Suntola and Jorma Antson. *Method for producing compound thin films*. US Patent 4,058,430. Nov. 1977.

[95] Gregory N Parsons et al. "History of atomic layer deposition and its relationship with the American Vacuum Society". In: *Journal of Vacuum Science & Technology A: Vacuum, Surfaces, and Films* 31.5 (2013), p. 050818.

[96] Tommi Kääriäinen et al. *Atomic layer deposition: principles, characteristics, and nanotechnology applications*. John Wiley & Sons, 2013.

[97] Saleem Hashmi. *Comprehensive materials processing*. Newnes, 2014.

[98] Mikko Ritala and Jaakko Niinistö. "Industrial applications of atomic layer deposition". In: *ECS transactions* 25.8 (2009), p. 641.

[99] Ivo J Raaijmakers. "Current and future applications of ALD in micro-electronics". In: *ECS Transactions* 41.2 (2011), p. 3.

[100] Mikko Ritala and Markku Leskela. "Handbook of thin film materials". In: *Deposition and processing of thin films* 1 (2002), p. 103.

[101] Anthony C Jones and Michael L Hitchman. *Chemical vapour deposition: precursors, processes and applications*. Royal society of chemistry, 2009.

[102] Kaizad Mistry et al. "A 45nm logic technology with high-k+ metal gate transistors, strained silicon, 9 Cu interconnect layers, 193nm dry patterning, and 100% Pb-free packaging". In: *2007 IEEE International Electron Devices Meeting*. IEEE. 2007, pp. 247–250.

[103] Md Anower Hossain et al. "Atomic layer deposition enabling higher efficiency solar cells: A review". In: *Nano Materials Science* 2.3 (2020), pp. 204–226.

[104] Jeong-Gyu Song et al. "Layer-controlled, wafer-scale, and conformal synthesis of tungsten disulfide nanosheets using atomic layer deposition". In: *ACS nano* 7.12 (2013), pp. 11333–11340.

[105] Bhobnibhit Chatmaneerungcharoen et al. "Synthesis of In-Plane Oriented Tin Sulfides by Organosulfur-Mediated Sulfurization of Ultrathin SnO2 Films". In: *Chemistry of Materials* 34.13 (2022), pp. 5842–5851.

[106] Jolien Dendooven and Christophe Detavernier. "Basics of atomic layer deposition: growth characteristics and conformality". In: *Atomic layer deposition in energy conversion applications* (2017), pp. 1–40.

[107] Harm CM Knoops et al. "Atomic layer deposition". In: *Handbook of Crystal Growth*. Elsevier, 2015, pp. 1101–1134.

[108] Miika Mattinen, Markku Leskelä, and Mikko Ritala. "Atomic layer deposition of 2D metal dichalcogenides for electronics, catalysis, energy storage, and beyond". In: *Advanced Materials Interfaces* 8.6 (2021), p. 2001677.

[109] Jiyu Cai et al. "Atomic layer deposition of two-dimensional layered materials: processes, growth mechanisms, and characteristics". In: *Matter* 2.3 (2020), pp. 587–630.

[110] Youngjun Kim et al. "Atomic-Layer-Deposition-Based 2D Transition Metal Chalcogenides: Synthesis, Modulation, and Applications". In: *Advanced Materials* 33.47 (2021), p. 2005907.

[111] Gyu-Hyeon Park, Kornelius Nielsch, and Andy Thomas. "2D transition metal dichalcogenide thin films obtained by chemical gas phase deposition techniques". In: *Advanced Materials Interfaces* 6.3 (2019), p. 1800688.

[112] Haodong Zhang et al. "Nucleation and growth mechanism of 2D SnS2 by chemical vapor deposition: Initial 3D growth followed by 2D lateral growth". In: *2D Materials* 5.3 (2018), p. 035006.

[113] Jenna Multia and Maarit Karppinen. "Atomic/Molecular Layer Deposition for Designer's Functional Metal–Organic Materials". In: *Advanced Materials Interfaces* 9.15 (2022), p. 2200210.

[114] Yang Zhao et al. "Atomic/molecular layer deposition for energy storage and conversion". In: *Chemical Society Reviews* 50.6 (2021), pp. 3889–3956.

[115] Xiangbo Meng. "An overview of molecular layer deposition for organic and organic–inorganic hybrid materials: mechanisms, growth characteristics, and promising applications". In: *Journal of Materials Chemistry A* 5.35 (2017), pp. 18326–18378.

[116] Pia Sundberg and Maarit Karppinen. "Organic and inorganic–organic thin film structures by molecular layer deposition: A review". In: *Beilstein journal of nanotechnology* 5.1 (2014), pp. 1104–1136.

[117] Petros Abi Younes et al. "Elaboration of porous alumina nanofibers by electrospinning and molecular layer deposition for organic pollutant removal". In: *Colloids and Surfaces A: Physicochemical and Engineering Aspects* 628 (2021), p. 127274.

[118] Kevin Van de Kerckhove, Jolien Dendooven, and Christophe Detavernier. "Annealing of thin "Tincone" films, a tin-based hybrid material deposited by molecular layer deposition, in reducing, inert, and oxidizing atmospheres". In: *Journal of Vacuum Science & Technology A: Vacuum, Surfaces, and Films* 36.5 (2018), p. 051506.

[119] Kevin Van de Kerckhove et al. "Molecular layer deposition of "vanadicone", a vanadium-based hybrid material, as an electrode for lithium-ion batteries". In: *Dalton Transactions* 46.14 (2017), pp. 4542–4553.

[120] Stéphane Cadot et al. "A novel 2-step ALD route to ultra-thin MoS 2 films on SiO 2 through a surface organometallic intermediate". In: *Nanoscale* 9.2 (2017), pp. 538–546.

[121] Neha Mahuli and Shaibal K Sarkar. "Atomic layer deposition of titanium sulfide and its application in extremely thin absorber solar cells". In: *Journal of Vacuum Science & Technology A: Vacuum, Surfaces, and Films* 33.1 (2015), 01A150.

[122] Farheen N Sayed et al. "Li and Na-ion diffusion and intercalation characteristics in vertically aligned TiS2 nanowall network grown using atomic layer deposition". In: *Materials Research Express* 6.11 (2019), p. 115549.

[123] Gyeong Taek Lim and Do-Heyoung Kim. "Characteristics of TiOx films prepared by chemical vapor deposition using tetrakis-dimethyl-amido-titanium and water". In: *Thin Solid Films* 498.1-2 (2006), pp. 254–258.

[124] Hochul Nam et al. "Semiconducting TiO2- xSx thin films by atomic layer deposition of TiS2 and its oxidation in ambient". In: *Journal of Vacuum Science & Technology A: Vacuum, Surfaces, and Films* 37.2 (2019), p. 020916.

[125] Neil P Dasgupta et al. "Atomic layer deposition of metal sulfide materials". In: *Accounts of chemical research* 48.2 (2015), pp. 341–348.

[126] Emily S Peters, Claire J Carmalt, and Ivan P Parkin. "Dual-source chemical vapour deposition of titanium sulfide thin films from tetrakisdimethylamidotitanium and sulfur precursors". In: *Journal of Materials Chemistry* 14.23 (2004), pp. 3474–3477.

[127] Robert G Palgrave and Ivan P Parkin. "Chemical vapour deposition of titanium chalcogenides and pnictides and tungsten oxide thin films". In: *New Journal of Chemistry* 30.4 (2006), pp. 505–514.

[128] Claire J Carmalt, Ivan P Parkin, and Emily S Peters. "Atmospheric pressure chemical vapour deposition of TiS2 thin films on glass". In: *Polyhedron* 22.9 (2003), pp. 1263–1269.

[129] Claire J Carmalt et al. "Titanium sulfide thin films from the aerosol-assisted chemical vapour deposition of [Ti (SBu t) 4]". In: *Journal of Materials Chemistry* 14.5 (2004), pp. 830–834.

[130] Keiichi Kanehori et al. "Titanium disulfide films fabricated by plasma CVD". In: *Solid State Ionics* 18 (1986), pp. 818–822.

[131] Jinwoo Cheon, John E Gozum, and Gregory S Girolami. "Chemical Vapor Deposition of MoS2 and TiS2 Films From the Metal- Organic Precursors Mo (S-t-Bu) 4 and Ti (S-t-Bu) 4". In: *Chemistry of materials* 9.8 (1997), pp. 1847–1853.

[132] Peter C Sherrell et al. "Thickness-dependent characterization of chemically exfoliated TiS2 nanosheets". In: *ACS omega* 3.8 (2018), pp. 8655–8662.

[133] Vladimir V Plashnitsa et al. "Synthetic strategy and structural and optical characterization of thin highly crystalline titanium disulfide nanosheets". In: *The journal of physical chemistry letters* 3.11 (2012), pp. 1554–1558.

[134] Abdalaziz Aljabour et al. "Active sulfur sites in semimetallic titanium disulfide enable CO2 electroreduction". In: *ACS Catalysis* 10.1 (2019), pp. 66–72.

[135] Xining Zang et al. "Titanium disulfide coated carbon nanotube hybrid electrodes enable high energy density symmetric pseudocapacitors". In: *Advanced materials* 30.5 (2018), p. 1704754.

[136] Saravana Balaji Basuvalingam et al. "Low-temperature phase-controlled synthesis of titanium di-and tri-sulfide by atomic layer deposition". In: *Chemistry of Materials* 31.22 (2019), pp. 9354–9362.

[137] Miika Mattinen et al. "Atomic Layer Deposition of Large-Area Polycrystalline Transition Metal Dichalcogenides from 100° C through Control of Plasma Chemistry". In: *Chemistry of Materials* (2022).

[138] Jeroen GA van Kasteren et al. "Growth Mechanism and Film Properties of Atomic-Layer-Deposited Titanium Oxysulfide". In: *Chemistry of Materials* (2022).

[139] Patrick J Pernot and Andrew R Barron. "Photo-assisted chemical vapor deposition of gallium sulfide thin films". In: *Chemical Vapor Deposition* 1.3 (1995), pp. 75–78.

[140] Andrea Keys, Simon G Bott, and Andrew R Barron. "MOCVD growth of gallium sulfide using Di-tert-butyl gallium dithiocarbamate precursors: formation of a metastable phase of GaS". In: *Chemistry of materials* 11.12 (1999), pp. 3578–3587.

[141] Graeme A Horley, Mike R Lazell, and Paul O'Brien. "Deposition of Thin Films of Gallium Sulfide from a Novel Liquid Single-Source Precursor, Ga (SOCNEt2) 3, by Aerosol-Assisted CVD". In: *Chemical Vapor Deposition* 5.5 (1999), pp. 203–205.

[142] Guihua Shang, Mark J Hampden-Smith, and Eileen N Duesler. "Synthesis and characterization of gallium thiocarboxylates as novel single-source precursors to gallium sulfide thin films by aerosol-assisted CVD". In: *Chemical Communications* 15 (1996), pp. 1733–1734.

[143] Mike R Lazell et al. "Deposition of Thin Films of Gallium Sulfide from a Novel Single-Source Precursor, Ga (S2CNMeHex) 3, by Low-Pressure Metal- Organic Chemical Vapor Deposition". In: *Chemistry of materials* 11.12 (1999), pp. 3430–3432.

[144] Seigi Suh and David M Hoffman. "Chemical vapor deposition of gallium sulfide thin films". In: *Chemistry of materials* 12.9 (2000), pp. 2794–2797.

[145] Xiaochen Wang et al. "Chemical vapor deposition growth of two-dimensional monolayer gallium sulfide crystals using hydrogen reduction of Ga2S3". In: *ACS omega* 3.7 (2018), pp. 7897–7903.

[146] Charles Goehry and Nathanaelle Schneider. "Chemical processes involved in atomic layer deposition of gallium sulfide: insights from theory". In: *The Journal of Physical Chemistry C* 121.11 (2017), pp. 5871–5881.

[147] Nathanaelle Schneider et al. "Gallium-containing sulfide binary and ternary materials by atomic layer deposition: precursor reactivities and growth fine chemistries". In: *Materials today chemistry* 10 (2018), pp. 142–152.

[148] Jakob Kuhs, Zeger Hens, and Christophe Detavernier. "Plasma enhanced atomic layer deposition of gallium sulfide thin films". In: *Journal of Vacuum Science & Technology A: Vacuum, Surfaces, and Films* 37.2 (2019), p. 020915.

[149] Evgeniy V Skopin et al. "The initial stages of ZnO atomic layer deposition on atomically flat In 0.53 Ga 0.47 As substrates". In: *Nanoscale* 10.24 (2018), pp. 11585–11596.

[150] Evgeniy V Skopin, Jean-Luc Deschanvres, and Hubert Renevier. "In situ ellipsometry study of the early stage of ZnO atomic layer deposition on In0. 53Ga0. 47As". In: *physica status solidi (a)* 217.8 (2020), p. 1900831.

[151] EV Skopin et al. "In situ x-ray studies of the incipient ZnO atomic layer deposition on In 0.53 Ga 0.47 As". In: *Physical Review Materials* 4.4 (2020), p. 043403.

[152] EV Skopin et al. "In situ ellipsometry monitoring of TiO2 atomic layer deposition from tetrakis (dimethylamido) titanium (IV) and H2O precursors on Si and In0. 53Ga0. 47As substrates". In: *Thin Solid Films* 723 (2021), p. 138591.

[153] R Boichot et al. "Evolution of crystal structure during the initial stages of ZnO atomic layer deposition". In: *Chemistry of Materials* 28.2 (2016), pp. 592–600.

[154] Manh Hung Chu et al. "An Atomistic View of the Incipient Growth of Zinc Oxide Nanolayers". In: *Crystal Growth & Design* 16.9 (2016), pp. 5339–5348.

[155] Manh-Hung Chu et al. "Evaluation of Alternative Atomistic Models for the Incipient Growth of ZnO by Atomic Layer Deposition". In: *Journal of Electronic Materials* 46.6 (2017), pp. 3512–3517.

[156] Kjell Knapas and Mikko Ritala. "In situ studies on reaction mechanisms in atomic layer deposition". In: *Critical reviews in solid state and materials sciences* 38.3 (2013), pp. 167–202.

[157] R Methaapanon et al. "Portable atomic layer deposition reactor for in situ synchrotron photoemission studies". In: *Review of Scientific Instruments* 84.1 (2013), p. 015104.

[158] Scott M Geyer et al. "An atomic layer deposition chamber for in situ x-ray diffraction and scattering analysis". In: *Review of Scientific Instruments* 85.5 (2014), p. 055116.

[159] Kilian Devloo-Casier et al. "In situ synchrotron based x-ray techniques as monitoring tools for atomic layer deposition". In: *Journal of Vacuum Science & Technology A: Vacuum, Surfaces, and Films* 32.1 (2014), p. 010801.

[160] Massimo Tallarida, Konstantin Karavaev, and Dieter Schmeisser. "The initial atomic layer deposition of Hf O 2/ Si (001) as followed in situ by synchrotron radiation photoelectron spectroscopy". In: *Journal of Applied Physics* 104.6 (2008), p. 064116.

[161] DD Fong et al. "In situ synchrotron x-ray characterization of ZnO atomic layer deposition". In: *Applied Physics Letters* 97.19 (2010), p. 191904.

[162] Jolien Dendooven et al. "In situ X-ray fluorescence measurements during atomic layer deposition: nucleation and growth of TiO2 on planar substrates and in nanoporous films". In: *The Journal of Physical Chemistry C* 115.14 (2011), pp. 6605–6610.

[163] Hanfei Yan et al. "Takagi-Taupin description of x-ray dynamical diffraction from diffractive optics with large numerical aperture". In: *Physical Review B* 76.11 (2007), p. 115438.

[164] Kilian Devloo-Casier et al. "In situ synchrotron based x-ray fluorescence and scattering measurements during atomic layer deposition: Initial growth of HfO 2 on Si and Ge substrates". In: *Applied Physics Letters* 98.23 (2011), p. 231905.

[165] Krzysztof Kolanek et al. "Atomic layer deposition reactor for fabrication of metal oxides". In: *physica status solidi c* 8.4 (2011), pp. 1287–1292.

[166] Massimo Tallarida and Dieter Schmeisser. "In situ ALD experiments with synchrotron radiation photoelectron spectroscopy". In: *Semiconductor Science and Technology* 27.7 (2012), p. 074010.

[167] Scott M Geyer et al. "In vacuo photoemission studies of platinum atomic layer deposition using synchrotron radiation". In: *The Journal of Physical Chemistry Letters* 4.1 (2013), pp. 176–179.

[168] Jeffrey A Klug et al. "A modular reactor design for in situ synchrotron x-ray investigation of atomic layer deposition processes". In: *Review of Scientific Instruments* 86.11 (2015), p. 113901.

[169] Jolien Dendooven et al. "Mobile setup for synchrotron based in situ characterization during thermal and plasma-enhanced atomic layer deposition". In: *Review of Scientific Instruments* 87.11 (2016), p. 113905.

[170] Kilian Devloo-Casier et al. "A case study of ALD encapsulation of quantum dots: embedding supported CdSe/CdS/ZnS quantum dots in a ZnO matrix". In: *The Journal of Physical Chemistry C* 120.32 (2016), pp. 18039–18045.

[171] Jan Knudsen, Jesper N Andersen, and Joachim Schnadt. "A versatile instrument for ambient pressure x-ray photoelectron spectroscopy: The Lund cell approach". In: *Surface Science* 646 (2016), pp. 160–169.

[172] Adam S Hoffman et al. "In situ observation of phase changes of a silica-supported cobalt catalyst for the Fischer–Tropsch process by the development of a synchrotron-compatible in situ/operando powder X-ray diffraction cell". In: *Journal of synchrotron radiation* 25.6 (2018), pp. 1673–1682.

[173] James M LeBeau et al. "Stoichiometry optimization of homoepitaxial oxide thin films using x-ray diffraction". In: *Applied Physics Letters* 95.14 (2009), p. 142905.

[174] G Ciatto et al. "SIRIUS: A new beamline for in situ X-ray diffraction and spectroscopy studies of advanced materials and nanostructures at the SOLEIL Synchrotron". In: *Thin Solid Films* 617 (2016), pp. 48–54.

[175] Evgenii Skopin. "Visualising the incipient Atomic Layer Deposition of ZnO ultrathin film on In0, 53Ga0, 47As, for tailoring contact resistivity". PhD thesis. Université Grenoble Alpes, 2018.

[176] Dhruv Shah et al. “Installation of an FS-1 in situ Ellipsometer on an Atomic Layer Deposition (ALD) System. Part 1.” In: ().

[177] Richard J Lewis and N Sax. “Sax’s dangerous properties of industrial materials”. In: *New York* 3 (1996).

[178] Pierre Birnal. “Films minces micro/nanostructurés: synthèse par ALD de composites associant opales inverses de TiO2 et nanoparticules d’or pour des applicationsphotocatalytiques.” PhD thesis. Bourgogne Franche-Comté, 2021.

[179] Fabien Piallat. “Plasma assisted chemical deposi-tion (CVD/ALD) and integration of Ti (Al) N and Ta (Al) N for sub-20 nm metal gate”. PhD thesis. Université de Grenoble, 2014.

[180] Serge Zhuiykov et al. “Data set for fabrication of conformal two-dimensional TiO2 by atomic layer deposition using tetrakis (dimethylamino) titanium (TDMAT) and H2O precursors”. In: *Data in brief* 13 (2017), pp. 401–407.

[181] Stéphane Cadot. “Élaboration de monocouches de dichalcogénures de métaux de transition du groupe (VI) par chimie organométallique de surface”. PhD thesis. Lyon, 2016.

[182] Medet Zhukush. “Chimie organométallique de surface pour la croissance ALD de films ultra-minces de WS2 et leurs performances photo (électro) catalytiques”. PhD thesis. Lyon, 2021.

[183] Mathias Fraccaroli. “Synthèse par CVD/ALD sur grandes surfaces d’un sulfure de vanadium transparent et conducteur”. PhD thesis. Université Grenoble Alpes [2020-....], 2020.

[184] Joaquin L Brito, Marcel Ilija, and Petra Hernández. “Thermal and reductive decomposition of ammonium thiomolybdates”. In: *Thermochimica Acta* 256.2 (1995), pp. 325–338.

[185] Jeffrey W Elam et al. “Atomic layer deposition of tin oxide films using tetrakis (dimethylamino) tin”. In: *Journal of Vacuum Science & Technology A: Vacuum, Surfaces, and Films* 26.2 (2008), pp. 244–252.

[186] *TDMASn pressure*. `https://ereztech.com/product/tetrakisdimethylaminotiniv-1066-77-9/`.

[187] *TDMASn pressure*. https://ereztech.com/product/trisdimethylamidogalliumiii-57731-40-5/.

[188] Dana Cialla-May, Michael Schmitt, and Jürgen Popp. "Theoretical principles of Raman spectroscopy". In: *Physical Sciences Reviews* 4.6 (2019).

[189] Taylor Bure et al. "Assessing Advanced Methods in Xps and Haxpes for Determining the Thicknesses of High-K Oxide Materials: From Ultra-Thin Layers to Deeply Buried Interfaces". In: *Available at SSRN 4056716* ().

[190] Sebastian Siol et al. "Concepts for chemical state analysis at constant probing depth by lab-based XPS/HAXPES combining soft and hard X-ray sources". In: *Surface and Interface Analysis* 52.12 (2020), pp. 802–810.

[191] CR Brundle, Giuseppina Conti, and Paul Mack. "XPS and angle resolved XPS, in the semiconductor industry: Characterization and metrology control of ultra-thin films". In: *Journal of Electron Spectroscopy and Related Phenomena* 178 (2010), pp. 433–448.

[192] William K Istone. "X-ray photoelectron spectroscopy (XPS)". In: *Surface analysis of paper*. CRC Press, 2020, pp. 235–268.

[193] Jill Chastain and Roger C King Jr. "Handbook of X-ray photoelectron spectroscopy". In: *Perkin-Elmer Corporation* 40 (1992), p. 221.

[194] Ke Wang, Benjamin Ecker, and Yongli Gao. "Photoemission Studies on the Environmental Stability of Thermal Evaporated MAPbI3 Thin Films and MAPbBr3 Single Crystals". In: *Energies* 14.7 (2021), p. 2005.

[195] Hiroshi Shinotsuka, Shigeo Tanuma, and Cedric J Powell. "Calculations of electron inelastic mean free paths. XIII. Data for 14 organic compounds and water over the 50 eV to 200 keV range with the relativistic full Penn algorithm". In: *Surface and Interface Analysis* 54.5 (2022), pp. 534–560.

[196] Florian Flamary-Mespoulie et al. "Lithium-rich layered titanium sulfides: Cobalt-and Nickel-free high capacity cathode materials for lithium-ion batteries". In: *Energy Storage Materials* 26 (2020), pp. 213–222.

[197] *HAXPES*. https://www.spectraresearch.com/product/phi-quantes-scanning-xps-haxpes-microprobe/.

[198] Miho Yasaka et al. “X-ray thin-film measurement techniques”. In: *The Rigaku Journal* 26.2 (2010), pp. 1–9.

[199] JK Srivastava, M Prasad, and JB Wagner. “Electrical conductivity of silicon dioxide thermally grown on silicon”. In: *Journal of The Electrochemical Society* 132.4 (1985), p. 955.

[200] Akshay Singh et al. “Near-infrared optical properties and proposed phase-change usefulness of transition metal disulfides”. In: *Applied Physics Letters* 115.16 (2019), p. 161902.

[201] J Tauc and A Menth. “States in the gap”. In: *Journal of non-crystalline solids* 8 (1972), pp. 569–585.

[202] G Ciatto et al. “FORTE–a multipurpose high-vacuum diffractometer for tender X-ray diffraction and spectroscopy at the SIRIUS beamline of Synchrotron SOLEIL”. In: *Journal of Synchrotron Radiation* 26.4 (2019), pp. 1374–1387.

[203] Petros Abi Younes et al. “Transition Metal Dichalcogenide TiS2 Prepared by Hybrid Atomic Layer Deposition/Molecular Layer Deposition: Atomic-Level Insights with In Situ Synchrotron X-ray Studies and Molecular Surface Chemistry”. In: *Chemistry of Materials* (2022).

[204] Sabine Van Doorslaer et al. “Continuous wave and pulse EPR as a tool for the characterization of monocyclopentadienyl Ti (III) catalysts”. In: *Journal of Organometallic Chemistry* 634.2 (2001), pp. 185–192.

[205] ZY Wu et al. “Interpretation of preedge features in the Ti and S K-edge x-ray-absorption near-edge spectrain the layered disulfides TiS 2 and TaS 2”. In: *Physical Review B* 55.15 (1997), p. 9508.

[206] Chenwen Lin et al. “Hydrogen-incorporated TiS2 ultrathin nanosheets with ultrahigh conductivity for stamp-transferrable electrodes”. In: *Journal of the American Chemical Society* 135.13 (2013), pp. 5144–5151.

[207] A Dużyńska et al. “Temperature-induced phonon behavior in titanium disulfide (TiS2) nanosheets”. In: *Journal of Raman Spectroscopy* 50.8 (2019), pp. 1114–1119.

[208] M Hangyo et al. “Raman scattering from the misfit-layer compounds SnNbS 3, PbNbS 3, and PbTiS 3”. In: *Physical Review B* 48.15 (1993), p. 11291.

[209] M Ishii, M Saeki, and I Kawada. "Raman Study of Non-Stoichiometric Titanium Sulfides". In: *physica status solidi (b)* 124.2 (1984), K109–K112.

[210] Alexandru L Let et al. "Thio sol–gel synthesis of titanium disulfide thin films and powders using titanium alkoxide precursors". In: *Journal of non-crystalline solids* 354.15-16 (2008), pp. 1801–1807.

[211] Alexandru L Let et al. "Thio sol–gel synthesis of titanium disulfide thin films and nanoparticles using titanium (IV) alkoxide precursors". In: *Journal of Physics and Chemistry of Solids* 68.7 (2007), pp. 1428–1435.

[212] Hervé Martinez et al. "Studies of 1T TiS2 by STM, AFM and XPS: the mechanism of hydrolysis in air". In: *Applied surface science* 93.3 (1996), pp. 231–235.

[213] S Tanuma, CJ Powell, and DR Penn. "Calculations of electron inelastic mean free paths. IX. Data for 41 elemental solids over the 50 eV to 30 keV range". In: *Surface and interface analysis* 43.3 (2011), pp. 689–713.

[214] Julia E Fulghum. "Determination of overlayer thickness by angle-resolved XPS: A comparison of algorithms". In: *Surface and interface analysis* 20.2 (1993), pp. 161–173.

[215] Jean-Charles Dupin et al. "Amorphous oxysulfide thin films MOySz (M= W, Mo, Ti) XPS characterization: structural and electronic pecularities". In: *Applied surface science* 173.1-2 (2001), pp. 140–150.

[216] Marie-Hélène Lindic et al. "XPS investigations of TiOySz amorphous thin films used as positive electrode in lithium microbatteries". In: *Solid State Ionics* 176.17-18 (2005), pp. 1529–1537.

[217] Marie-Hélène Lindic et al. "Characterization of rf sputtered TiOySz thin films". In: *Thin Solid Films* 484.1-2 (2005), pp. 113–123.

[218] Vincent Dubois et al. "Dual cation-and anion-based redox process in lithium titanium oxysulfide thin film cathodes for all-solid-state lithium-ion batteries". In: *ACS Applied Materials & Interfaces* 9.3 (2017), pp. 2275–2284.

[219] J Richard et al. "Charge transfer mechanism into the chevrel phase Mo6S8 during Mg intercalation". In: *The Journal of Physical Chemistry C* 121.32 (2017), pp. 17096–17103.

[220] Hervé Martinez et al. “Influence of the cation nature of high sulfur content oxysulfide thin films MOySz (M= W, Ti) studied by XPS”. In: *Applied surface science* 236.1-4 (2004), pp. 377–386.

[221] D Gonbeau et al. “XPS study of thin films of titanium oxysulfides”. In: *Surface Science* 254.1-3 (1991), pp. 81–89.

[222] DA Verner et al. “Atomic data for astrophysics. II. New analytic fits for photoionization cross sections of atoms and ions”. In: *arXiv preprint astro-ph/9601009* (1996).

[223] Gerhard Betz. “Alloy sputtering”. In: *Surface Science* 92.1 (1980), pp. 283–309.

[224] Ph Holliger, F Laugier, and JC Dupuy. “SIMS depth profiling of ultrashallow P, Ge and As implants in Si using MCs2+ ions”. In: *Surface and Interface Analysis: An International Journal devoted to the development and application of techniques for the analysis of surfaces, interfaces and thin films* 34.1 (2002), pp. 472–476.

[225] Nicolas Gauthier et al. “Impact of the cycling temperature on electrode/electrolyte interfaces within Li4Ti5O12 vs LiMn2O4 cells”. In: *Journal of Power Sources* 448 (2020), p. 227573.

[226] Yi-Hsin Liu, Spencer H Porter, and Joshua E Goldberger. “Dimensional reduction of a layered metal chalcogenide into a 1D near-IR direct band gap semiconductor”. In: *Journal of the American Chemical Society* 134.11 (2012), pp. 5044–5047.

[227] Ofer Sneh and Steven M George. “Thermal stability of hydroxyl groups on a well-defined silica surface”. In: *The Journal of physical chemistry* 99.13 (1995), pp. 4639–4647.

[228] Christophe Coperet et al. “Surface organometallic and coordination chemistry toward single-site heterogeneous catalysts: strategies, methods, structures, and activities”. In: *Chemical reviews* 116.2 (2016), pp. 323–421.

[229] Arthur Roussey et al. “Cu nanoparticles on 2D and 3D silica substrates: controlled size and density, and critical size in catalytic silicon nanowire growth”. In: *Journal of Materials Chemistry C* 1.8 (2013), pp. 1583–1587.

[230] Laurent Mathey et al. “Functionalization of silica nanoparticles and native silicon oxide with tailored boron-molecular precursors for efficient and predictive p-doping of silicon”. In: *The Journal of Physical Chemistry C* 119.24 (2015), pp. 13750–13757.

[231] Thibault Alphazan et al. “Monolayer doping of silicon through grafting a tailored molecular phosphorus precursor onto oxide-passivated silicon surfaces”. In: *Chemistry of Materials* 28.11 (2016), pp. 3634–3640.

[232] Gary M Diamond, Richard F Jordan, and Jeffrey L Petersen. “Synthesis of Group 4 Metal rac-(EBI) M (NR2) 2 Complexes by Amine Elimination. Scope and Limitations”. In: *Organometallics* 15.19 (1996), pp. 4030–4037.

[233] Haibin Lin et al. “Electrocatalysis of polysulfide conversion by sulfur-deficient MoS_2 nanoflakes for lithium–sulfur batteries”. In: *Energy & Environmental Science* 10.6 (2017), pp. 1476–1486.

[234] Y Altowairqi et al. “The effect of annealing conditions: temperature, time, ramping rate and atmosphere on nanocrystal Cu2ZnSnS4 (CZTS) thin film solar cell properties”. In: *Materials Today: Proceedings* 18 (2019), pp. 473–486.

[235] MP Seah et al. “Simple method of depth profiling (stratifying) contamination layers, illustrated by studies on stainless steel”. In: *Surface and interface analysis* 21.6-7 (1994), pp. 336–341.

[236] Casey G Hawkins and Luisa Whittaker-Brooks. “Controlling sulfur vacancies in TiS2–x cathode insertion hosts via the conversion of TiS3 nanobelts for energy-storage applications”. In: *ACS Applied Nano Materials* 1.2 (2018), pp. 851–859.

[237] E Guilmeau et al. “On the effects of substitution, intercalation, non-stoichiometry and block layer concept in TiS 2 based thermoelectrics”. In: *Physical Chemistry Chemical Physics* 17.38 (2015), pp. 24541–24555.

[238] Han Wang et al. “Semimetal or semiconductor: the nature of high intrinsic electrical conductivity in TiS2”. In: *The journal of physical chemistry letters* 10.22 (2019), pp. 6996–7001.

[239] Hossein Rokni and Wei Lu. “Direct measurements of interfacial adhesion in 2D materials and van der Waals heterostructures in ambient air”. In: *Nature Communications* 11.1 (2020), p. 5607.

[240] Tom Iung et al. “Synthesis of metal chalcogenides GaSx by a Atomic Layer Deposition/Molecular Layer Deposition route”. In: (2022).

[241] M Isik, NM Gasanly, and L Gasanova. "Spectroscopic ellipsometry investigation of optical properties of β-Ga2S3 single crystals". In: *Optical Materials* 86 (2018), pp. 95–99.

[242] *Ga-S bonds*. https://materialsproject.org/materials/mp-2507?chemsys=S-Ga.

[243] Carlo Lamberti et al. "EXAFS studies on MFI-type gallosilicate molecular sieves". In: *Catalysis letters* 63.3 (1999), pp. 213–216.

[244] *Ga-O bonds*. https://materialsproject.org/materials/mp-1183990?chemsys=O-Ga.

[245] Hiroshi Senoh et al. "Gallium (III) sulfide as an active material in lithium secondary batteries". In: *Journal of Power Sources* 196.13 (2011), pp. 5631–5636.

[246] Jannise J Buckley et al. "Dissolution of Sn, SnO, and SnS in a thiol–amine solvent mixture: insights into the identity of the molecular solutes for solution-processed SnS". In: *Inorganic Chemistry* 55.6 (2016), pp. 3175–3180.

[247] David Edeler et al. "Delivery of [Ru (η6-p-cymene) Cl2 {Ph2P (CH2) 3SPh-κP}] using unfunctionalized and mercapto functionalized SBA-15 mesoporous silica: Preparation, characterization and in vitro study". In: *Journal of Inorganic Biochemistry* 180 (2018), pp. 155–162.

[248] ID Olekseyuk, IV Dudchak, and LV Piskach. "Phase equilibria in the Cu2S–ZnS–SnS2 system". In: *Journal of alloys and compounds* 368.1-2 (2004), pp. 135–143.

[249] Parag Vasekar et al. "Synthesis of zinc sulfide by chemical vapor deposition using an organometallic precursor: Di-tertiary-butyl-disulfide". In: *Thin Solid Films* 524 (2012), pp. 86–92.

[250] *lattice ZnO*. https://materialsproject.org/materials/mp-2133?chemsys=O-Zn.

[251] *lattice ZnS sulf*. https://materialsproject.org/materials/mp-9946?_skip=135&formula=ZnS.

[252] Jun Lin et al. "Large-area growth of MoS2 at temperatures compatible with integrating back-end-of-line functionality". In: *2D Materials* 8.2 (2020), p. 025008.

[253] LM Epstein and Darel K Straub. "Mössbauer Spectra of Tin Dithiolates". In: *Inorganic Chemistry* 4.11 (1965), pp. 1551–1554.

[254] Joanne L Murray. "Phase Diagrams of Binary Titanium Alloys'(ASM International". In: *Metals Park, OH* (1987).

[255] Kenji Hirata et al. "Thermodynamic assessment of Fe–Ti–S ternary phase diagram". In: *Calphad* 57 (2017), pp. 62–77.

[256] Kapildeb Dolui and Stefano Sanvito. "Dimensionality-driven phonon softening and incipient charge density wave instability in TiS2". In: *EPL (Europhysics Letters)* 115.4 (2016), p. 47001.

Appendices

Appendix A

Process details

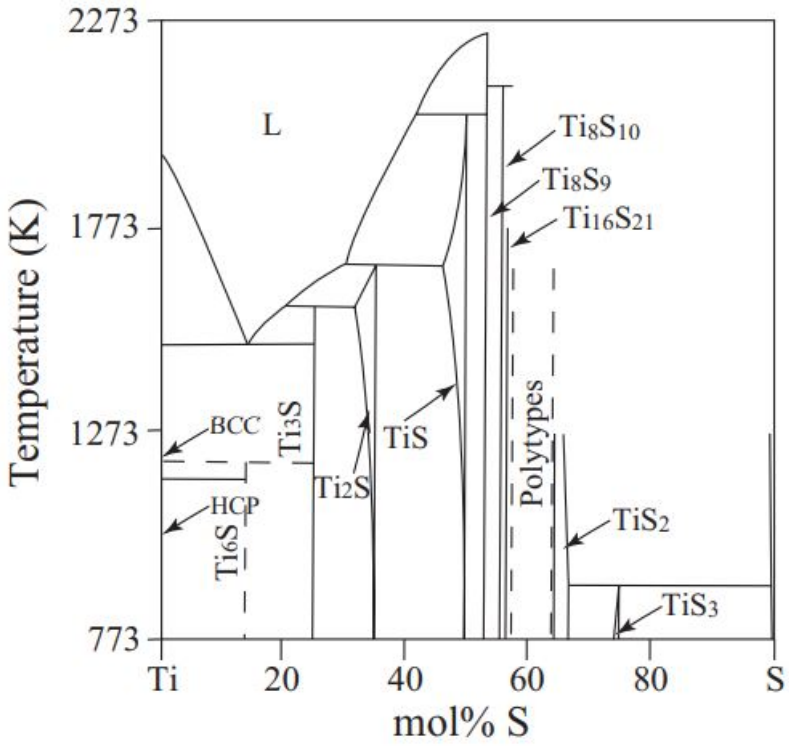

Figure A.1: The experimental Ti–S binary phase diagram by Murray. [254, 255]

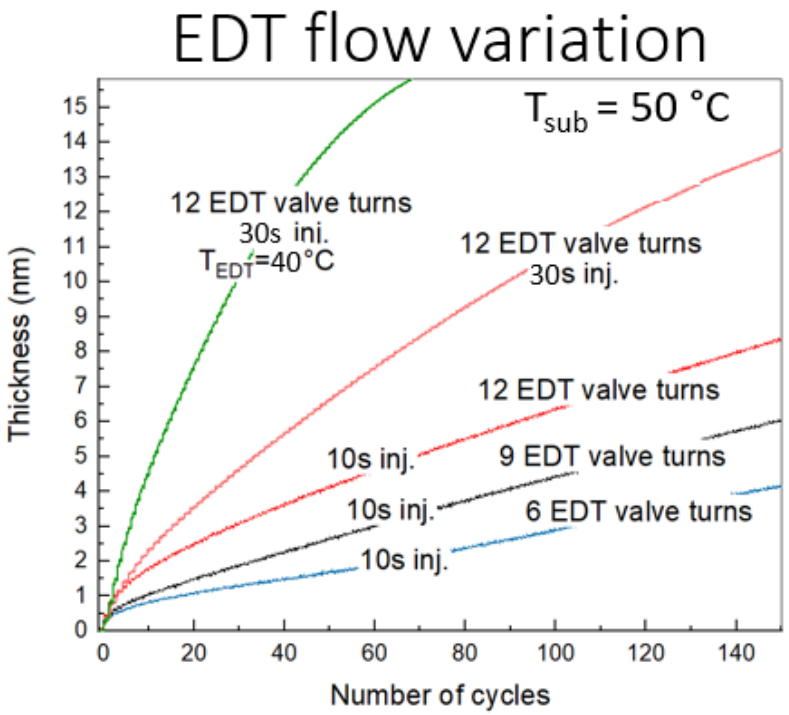

Figure A.2: EDT flow variation measured by in situ ellipsometry for different turns of the manual needle valve (opening).

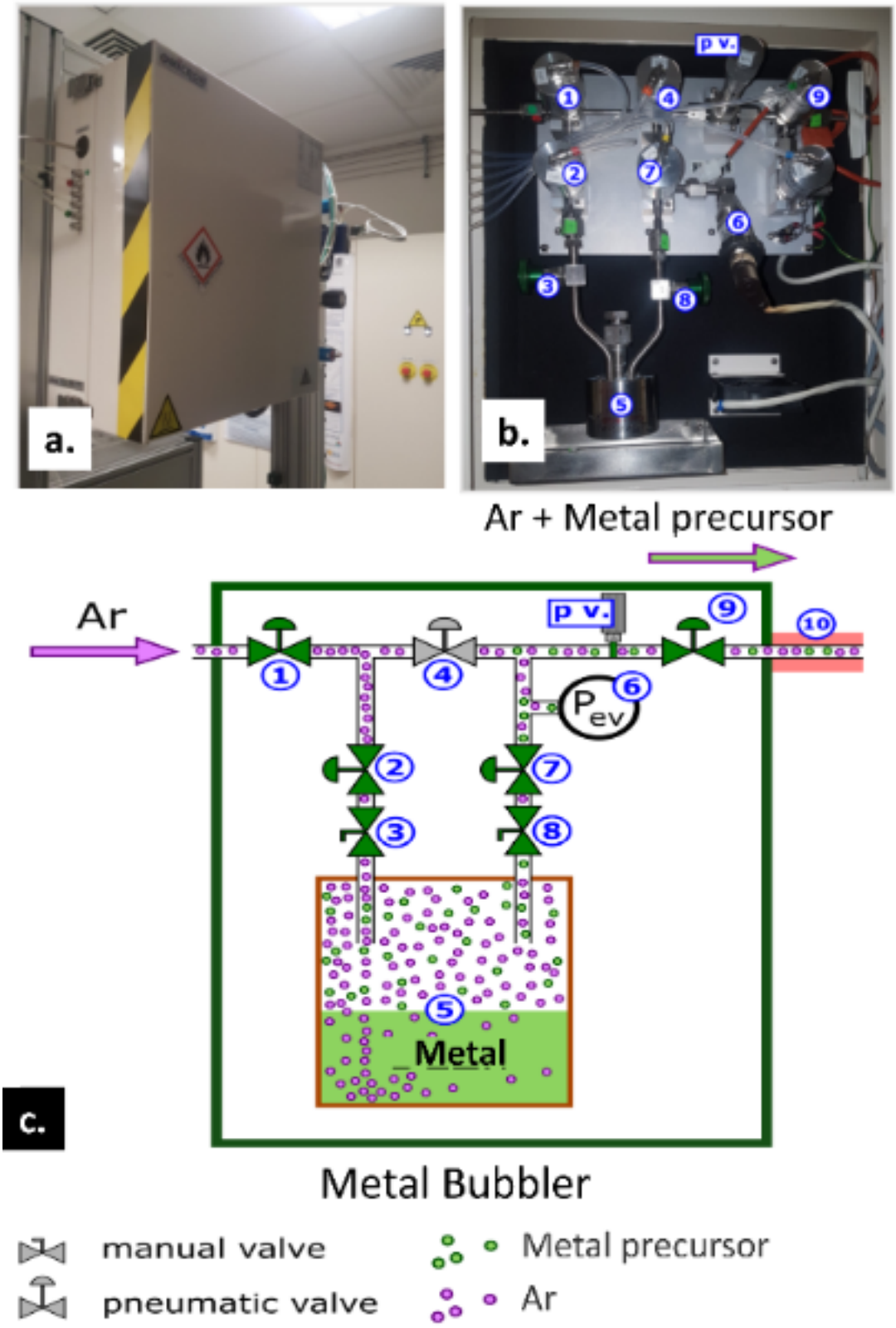

Figure A.3: (a) Thermally insulated bubbler box with two parts: fixed base and a lid for closing the box once all preparations step are finished to maintain the heating of the precursor constant. (b) A picture of the bubbler box. The box comprises pneumatic valves (1,2,4,7,9); manual valves (3,8); bubbler pressure gauge(6); manual needle valve(pv.) to control the pressure inside the bubbler. c) Schematic representation of the mixture of Ar with the metal molecules into the reactor chamber.(adapted from [175])

Appendix B

Supplementary materials (Chapter 3)

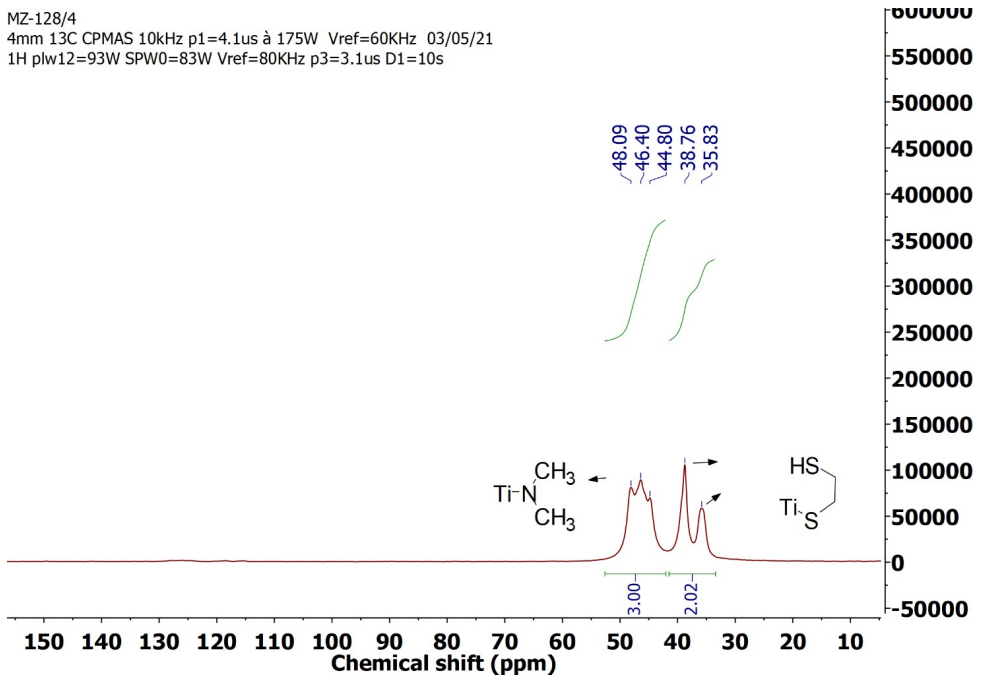

Figure B.1: Solid-state ^{13}C NMR spectrum recorded for the orange solid product of the reaction between TDMAT and EDT in pentane.

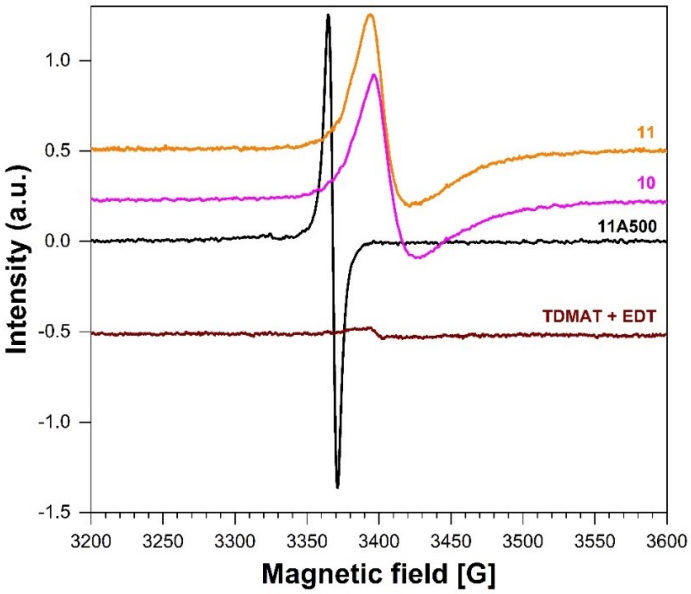

Figure B.2: EPR spectra of solid products obtained by TDMAT's reaction with EDT (brown line), 5 full ALD/MLD cycles and metal pulse on silica nanobeads (10, pink line), 6 full ALD/MLD cycles on silica nanobeads before (11, orange line) and after annealing at 500 °C (11A500, black line) recorded at room temperature.

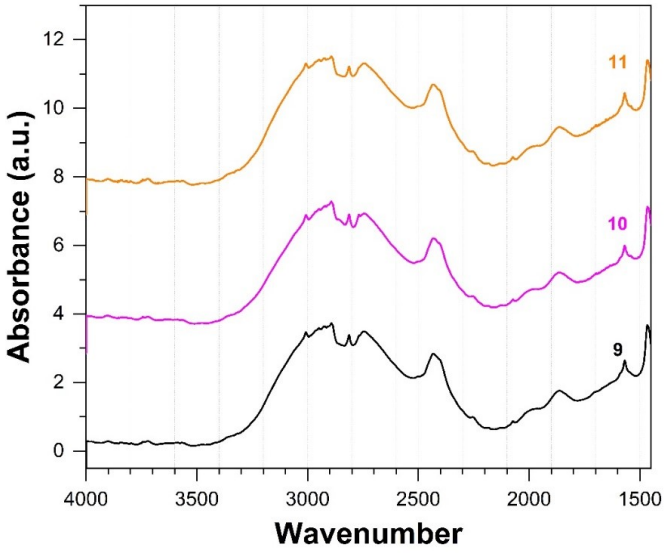

Figure B.3: IR absorbance spectra recorded after 5 full ALD/MLD cycles on silica nanobeads SiO_{2-700} (spectrum of 9, black); after 5 cycles and one pulse of TDMAT (spectrum of 10, pink); after 6 full cycles (spectrum of 11 , orange).

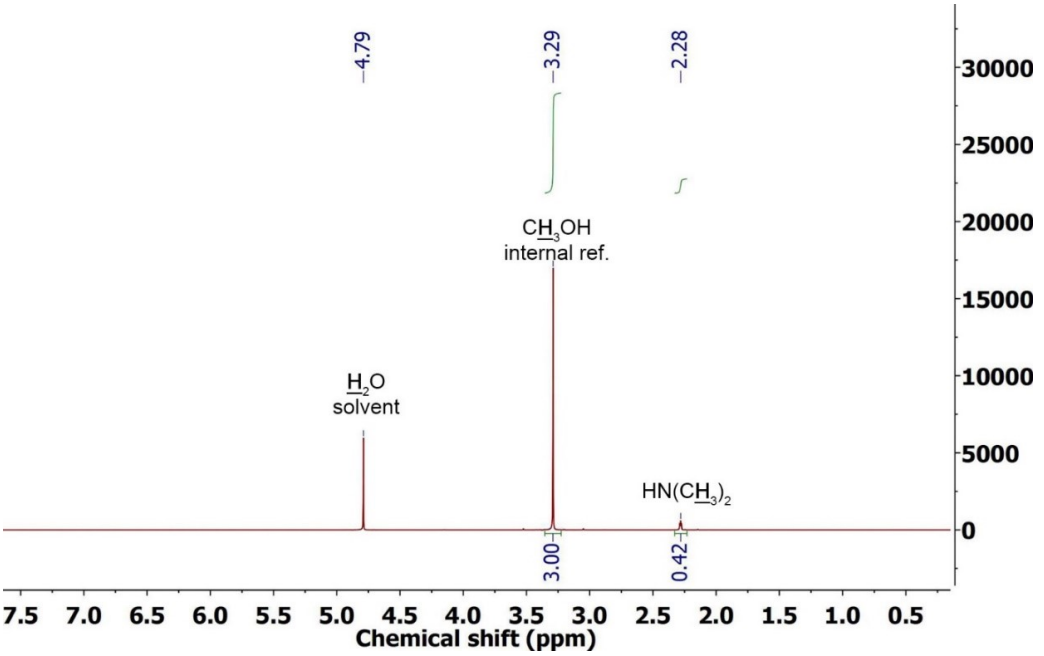

Figure B.4: Solution ^1H NMR spectrum recorded for the trapped volatile by-products of the reaction of the 2nd Ti pulse on silica nanobeads.

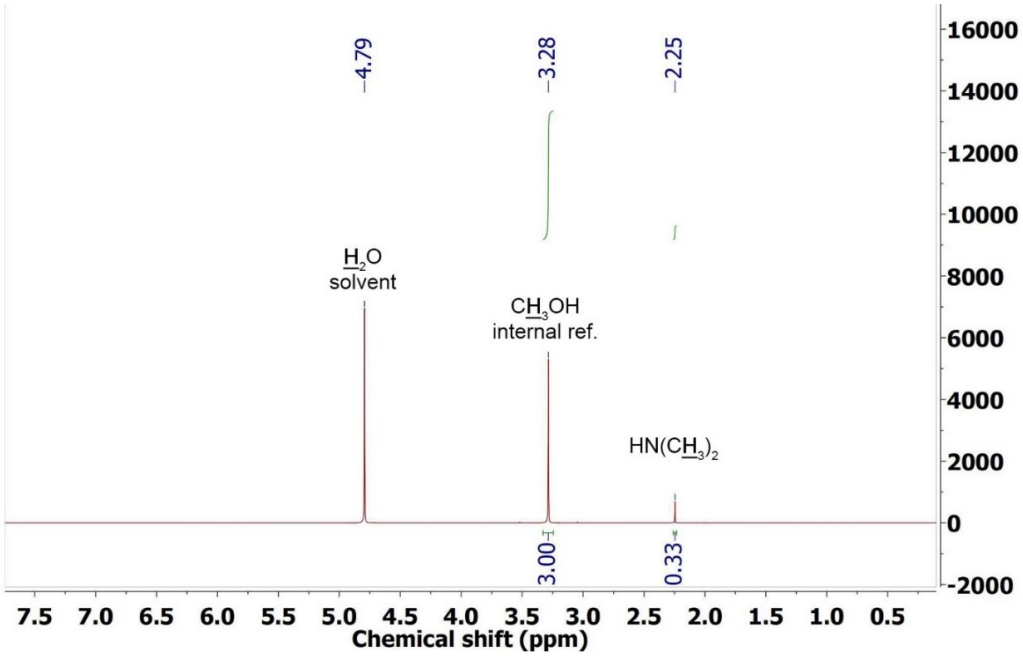

Figure B.5: Solution ^1H NMR spectrum recorded for the trapped volatile by-products of the reaction between SiO-Ti$(NMe_2)_3$ and EDT vapors.

B.1 X-Ray reflectivity and growth rate : Growth Per cycle (GPC) study

The Reflected Beam Intensity (RBI) was measured *in situ* during the growth of 40 ALD/MLD cycles. Figure B.6(a) shows RBI as a function of cycle number for the cycles 0-40. RBI is a periodical function, it has a decrease (around cycle 10) due to destructive interference at the growing layer and then an increase (around cycle 19) due to the constructive interference and so on. If the thickness of the ALD/MLD layer increases linearly, the period of RBI function is constant and the function is smooth. During one cycle, RBI function decreases and increases due to the layer thickness evolution upon injections and purges as well. We show here that knowing RBI as a number of cycle function and final thickness after cycle 40, and assuming that the growth is linear (Growth Per Cycle (GPC) is constant), it is possible to plot thickness as a function of cycle number. To do this, first, we calculated the mean RBI intensity measured during EDT purge for every cycle. For calculation, we chose a plateau intensity region (Grey region in Figure B.6(a). Figure B.6(b) shows mean RBI values for every cycle as a function of cycle number. This function is smooth. Assuming that the thickness per cycle is constant (according to *in situ* XRF measurements, in Figure 3.3 (c,d)), we can normalize the last point of RBI function (40 cycles), to the final thickness. Figure B.6(c) shows X-ray Reflectometry (XRR) curve measured after cycle 40 (black line) and the its simulation (blue line). The simulated XRR curve corresponds to the ALD/MLD layer thickness of 13.3 nm. This thickness of 13.3nm for 40 cycles was used for normalization of the RBI curve (see Figure B.6(b) – RBI as a function of thickness (values on the top)). RBI thickness function was used as a calibration curve to determine thickness as a function of cycle number. Figure B.6(d) shows measured RBI as a function of cycle number for the cycle range [11-17] : RBI (cycle) curve, and figure B.6(e) shows mean RBI as a function of thickness for the cycle range [11-17] : RBI (thickness) curve. The points of the RBI(thickness) curve were fit by polynomial function to obtain a calibration curve (line in the Figure B.6(e)). Then, we took one by one point from the RBI(cycle) curve with a coordinates cycle number; intensity and compared “intensity” with the value of intensity on the RBI(thickness) curve (thickness; intensity). After the comparison, we assigned the “thickness” value to the cycle number; intensity coordinate and obtained cycle number; thickness coordinate. Using the same type of calculations for every point, we plotted thickness as a cycle number function

(as shown in Figure 3.3-b)

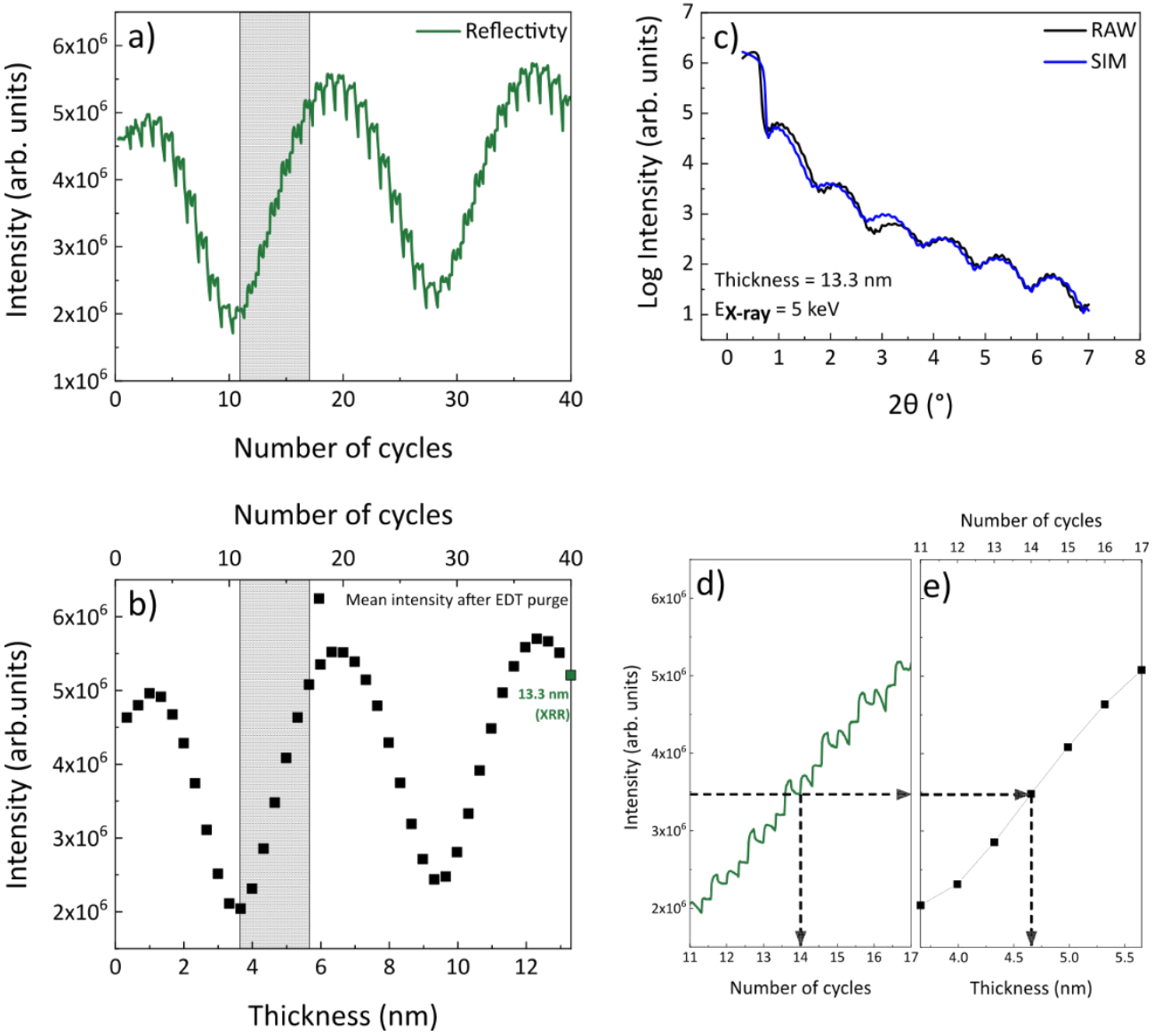

Figure B.6: a) Reflected Beam Intensity (RBI) as a function of the number of cycles; (b) mean RBI as a function of the number of cycles (top) and thickness (bottom); (c) x-ray reflectivity curve measured by the end of the growth after cycle 40; (d) RBI as the function of a number of cycles and (e) mean RBI as a function of thickness.

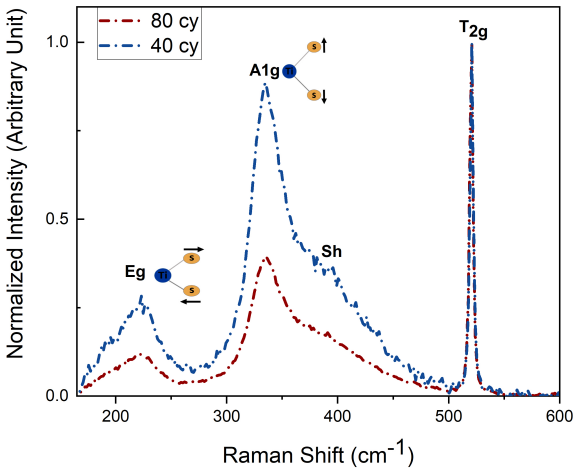

Figure B.7: Raman spectra (dashed lines) of samples resulting from 40 and 80 ALD/MLD cycles and an annealing at 450°C for 30 min under Ar(96%)/H2(4%) gas. Raman spectra were normalized to the intensity of the T2g Si peak.

B.2 Evalutation of upper oxide layer thickness by TPP2M calculations model

To determine the TiO_x thickness, we used the attenuation law of the Ti signal, considering the Ti 1s core level at around 4968 eV after the formation of TiO_x oxide. The relative intensity of the Ti 1s core level before and after the formation of TiO_x oxide was defined as:

I_{rel} **= at:%(TiS_2)/at:%(Ti1s)**; where at:%(TiS_2) and at:%(Ti1s) are the atomic percentages of Ti for attributed to TiS_2 and considered oxidised on the surface and for the total Ti1s without any oxidation, respectively. Those values were determined from XPS spectra quantification. Assuming a simple model where the TiO_x layer was considered as homogeneous in thickness (d) with no porosity and with an average composition, the layer thickness (2.1nm) was then estimated from: I_{rel} **= exp(-d/(λ*sin(θ)))** ; where θ is the take-off angle and λ is the Inelastic Mean Free Path (IMFP) of electrons emitted from the material, estimated by using the TPP2M equation based on the Bethe equation for inelastic scattering of electrons in matter in the 50-2000 eV energy range.[213] This procedure yielded Lambda = 15.9 Å in the TiS_2 layer for the photoelectron kinetic energy of 450 eV (Ti 1s) considered in this study.

Table B.1: Binding energies (BE) and atomic percentages (at.%) of the different chemical environments identified by ARXPS at the surface of a 80-cycle ALD/MLD thiolate annealed in Ar(96%)/H_2(4%) for 30 min at 450 °C.

Angle	Element	Attribution	Position (eV)	Atomic Percentage (%)
85°	**Ti 2p**	TiS_2 2p3/2	457.1	4.5
		TiS_2 2p1/2	462.8	2.2
		TiO_2 2p3/2	459.3	10.9
		TiO_2 2p1/2	465.0	5.4
	S 2p	TiS_2 2p3/2	161.4	8.6
		TiS_2 2p1/2	162.5	4.3
		$TiO_xS_y/(S_n)^{2-}$/C-S 2p3/2	163.4	2.6
		$TiO_xS_y/(S_n)^{2-}$/C-S 2p1/2	164.5	1.3
		SO_4^{2-}	169.5	0.3
		SO_4^{2-}	170.6	0.1
	N 1s	NO_x / $C_xN_yH_x$	400.8	0.7
	O 1s	TiO_2	530.8	30.3
		SO_4^{2-} / C-O / O-C=O	531.9	7.8
	C 1s	C-C / C-H	285.0	17.5
		C-O / C-S / C-N	286.6	2.8
		O-C=O	289.1	0.7
45°	**Ti 2p**	TiS_2 2p3/2	456.8	3.0
		TiS_2 2p1/2	462.5	1.5
		TiO_2 2p3/2	459.0	12.0
		TiO_2 2p1/2	464.7	6.0
	S 2p	TiS_2 2p3/2	161.2	6.3
		TiS_2 2p1/2	162.4	3.2
		$TiO_xS_y/(S_n)^{2-}$/C-S 2p3/2	163.4	2.0
		$TiO_xS_y/(S_n)^{2-}$/C-S 2p1/2	164.5	1.0
		SO_4^{2-}	169.0	0.1
		SO_4^{2-}	170.2	0.1
	N 1s	NO_x / $C_xN_yH_x$	399.9	1.0
	O 1s	TiO_2	530.6	32.9
		SO_4^{2-} / C-O / O-C=O	531.8	8.8
	C 1s	C-C / C-H	284.8	16.9
		C-O / C-S / C-N	286.0	4.5
		O-C=O	289.3	0.6
15°	**Ti 2p**	TiS_2 2p3/2	457.0	1.7
		TiS_2 2p1/2	462.7	0.9
		TiO_2 2p3/2	458.9	10.8
		TiO_2 2p1/2	464.6	5.4
	S 2p	TiS_2 2p3/2	161.1	3.3
		TiS_2 2p1/2	162.2	1.7
		$TiO_xS_y/(S_n)^{2-}$/C-S 2p3/2	163.4	1.7
		$TiO_xS_y/(S_n)^{2-}$/C-S 2p1/2	164.5	0.8
		SO_4^{2-}	168.8	0.3
		SO_4^{2-}	169.9	0.2
	N 1s	NO_x / $C_xN_yH_x$	400.4	2.2
	O 1s	TiO_2	530.4	28.5
		SO_4^{2-} / C-O / O-C=O	531.8	10.5
	C 1s	C-C / C-H	284.8	26.3
		C-O / C-S / C-N	286.1	4.9
		O-C=O	289.0	0.8

Appendix C

XPS Quantitative chemical composition

Table C.2: Binding energies (BE) and atomic percentages (at.%) of the different chemical environments identified by XPS for a reference powder of TiS_2 purchased from $Merck_{TM}$ (CAS number: [12039-13-3]).

Element	Attribution	Position (eV)	Percentage (%)
Ti 2p	TiS_2 2p3/2	456.9	9.6
	TiS_2 2p1/2	462.8	4.8
	TiO_xS_y / TiO_2 2p3/2	459.0	4.9
	TiO_xS_y / TiO_2 2p1/2	464.7	2.4
S 2p	TiS_2 2p3/2	161.4	22.4
	TiS_2 2p1/2	162.6	11.2
	$TiO_xS_y/(S_n)^{2-}$/C-S 2p3/2	162.9	3.9
	$TiO_xS_y/(S_n)^{2-}$/C-S 2p1/2	164.0	1.9
O 1s	TiO_2	530.8	8.3
	C-O / O-C=O	532.4	6.6
C 1s	C-C / C-H	284.8	17.9
	C-O / C-S	286.5	4.1
	O-C=O	289.5	1.9

The obtained values ars actually the same for a reference crystalline stoichiometric TiS_2 powder as shown in this table, which indicates that the deposited film of TiS_2 is close to the stoichiometric one.

Table C.1: Binding energies (BE) and atomic percentages (at.%) of the different chemical environments identified by ARXPS at the surface of a 60-cycle ALD/MLD Ti-thiolate annealed using annealing strategy A under $Ar/H_2(5\%)$. The presence of nitrogen content is likely to originate from the residue of the TDMAT precursor.

Angle	Element	Attribution	Position (eV)	Atomic Percentage (%)
90°	**Ti 2p**	TiS_2 2p3/2	457.0	4.8
		TiS_2 2p1/2	462.7	2.4
		TiO_2 2p3/2	458.8	6.4
		TiO_2 2p1/2	464.5	3.2
	S 2p	TiS_2 2p3/2	161.2	9.0
		TiS_2 2p1/2	162.3	4.5
		$TiO_xS_y/(S_n)^{2-}$/C-S 2p3/2	162.8	4.5
		$TiO_xS_y/(S_n)^{2-}$/C-S 2p1/2	164.0	2.3
	N 1s	NO_x / $C_xN_yH_x$	401.0	1.4
	O 1s	TiO_2	530.4	19.8
		C-O / O-C=O	531.7	5.3
		C- O - C	533.1	1.7
	C 1s	C-C / C-H	284.8	27.8
		C-O / C-S / C-N	286.2	5.0
		O-C=O	288.8	1.7
45°	**Ti 2p**	TiS_2 2p3/2	457.1	4.0
		TiS_2 2p1/2	462.8	2.0
		TiO_2 2p3/2	458.8	6.6
		TiO_2 2p1/2	464.5	3.3
	S 2p	TiS_2 2p3/2	161.2	7.4
		TiS_2 2p1/2	162.3	3.7
		$TiO_xS_y/(S_n)^{2-}$/C-S 2p3/2	162.9	3.6
		$TiO_xS_y/(S_n)^{2-}$/C-S 2p1/2	164.0	1.8
	N 1s	NO_x / $C_xN_yH_x$	401.0	1.3
	O 1s	TiO_2	530.5	20.8
		C-O / O-C=O	531.8	5.5
		C- O - C	533.1	1.7
	C 1s	C-C / C-H	284.8	31.3
		C-O / C-S / C-N	286.2	5.4
		O-C=O	288.7	1.5
15°	**Ti 2p**	TiS_2 2p3/2	457.1	2.6
		TiS_2 2p1/2	462.8	1.3
		TiO_2 2p3/2	458.8	5.6
		TiO_2 2p1/2	464.5	2.8
	S 2p	TiS_2 2p3/2	161.2	5.2
		TiS_2 2p1/2	162.3	2.6
		$TiO_xS_y/(S_n)^{2-}$/C-S 2p3/2	163.1	2.7
		$TiO_xS_y/(S_n)^{2-}$/C-S 2p1/2	164.2	1.3
	N 1s	NO_x / $C_xN_yH_x$	400.7	1.1
	O 1s	TiO_2	530.5	16.8
		C-O / O-C=O	531.9	5.0
		C- O - C	533.1	1.2
	C 1s	C-C / C-H	284.8	43.8
		C-O / C-S / C-N	286.2	6.3
		O-C=O	288.7	1.8

Table C.3: Binding energies (BE) and atomic percentages (at.%) of the different chemical environments identified by HAXPES at the surface of a 40-cycle ALD/MLD Ti-thiolate annealed using annealing strategy A under $Ar/H_2(5\%)$.

Element	Attribution	Position (eV)	Percentage (%)
Ti 2p	TiS_2 2p3/2	456.6	6.3
	TiS_2 2p1/2	462.3	3.1
	TiO_2 2p3/2	458.6	4.0
	TiO_2 2p1/2	464.3	2.0
S 2p	TiS_2 2p3/2	160.8	14.5
	TiS_2 2p1/2	162.0	7.3
	$TiO_xS_y/(S_n)^{2-}$/C-S 2p3/2	162.6	7.8
	$TiO_xS_y/(S_n)^{2-}$/C-S 2p1/2	163.7	3.9
O 1s	TiO_2	530.3	13.5
	C-O/O-C=O/SiO_2	532.7	11.3
C 1s	C-C/C-H	284.8	19.2
	C-O/C-S	288.2	5.1
Si 1s	SiO_2	1843.9	2.0

Table C.4: Binding energies (BE) and atomic percentages (at.%) of the different chemical environments identified by HAXPES at the surface of a 40-cycle ALD/MLD Ti-thiolate annealed using annealing strategy B under $Ar/H_2(5\%)$.

Element	Attribution	Position (eV)	Percentage (%)
Ti 2p	TiS_2 2p3/2	456.7	6.4
	TiS_2 2p1/2	462.4	3.2
	TiO_2 2p3/2	458.8	4.6
	TiO_2 2p1/2	464.5	2.3
S 2p	TiS_2 2p3/2	160.8	14.5
	TiS_2 2p1/2	162.0	7.3
	$TiO_xS_y/(S_n)^{2-}$/C-S 2p3/2	162.6	6.3
	$TiO_xS_y/(S_n)^{2-}$/C-S 2p1/2	163.7	3.2
O 1s	TiO_2	530.4	16.0
	C-O/O-C=O/SiO_2	532.4	9.8
C 1s	C-C/C-H	284.8	21.4
	C-O/C-S	287.0	3.8
Si 1s	SiO_2	1843.9	1.2

Table C.5: Binding energies (BE) and atomic percentages (at.%) of the different chemical environments identified by HAXPES at the surface of a 20-cycle ALD/MLD Ti-thiolate annealed using annealing strategy B under $Ar/H_2(5\%)$.

Element	Attribution	Position (eV)	Percentage (%)
Ti 2p	TiS_2 2p3/2	456.7	3.3
	TiS_2 2p1/2	462.4	1.7
	TiO_2 2p3/2	458.8	4.1
	TiO_2 2p1/2	464.5	2.1
S 2p	TiS_2 2p3/2	160.8	7.6
	TiS_2 2p1/2	162.0	3.8
	$TiO_xS_y/(S_n)^{2-}$/C-S 2p3/2	162.6	5.1
	$TiO_xS_y/(S_n)^{2-}$/C-S 2p1/2	163.7	2.6
O 1s	TiO_2	530.4	14.4
	C-O/O-C=O/SiO_2	532.4	32.0
C 1s	C-C/C-H	284.8	12.7
	C-O/C-S	287.0	2.0
Si 1s	SiO_2	1843.9	8.6

Table C.6: Binding energies (BE) and atomic percentages (at.%) of the different chemical environments identified by HAXPES at the surface of a 40-cycle ALD/MLD Ti-thiolate with 60s of EDT injection upon the annealing under $Ar/H_2(5\%)$ using annealing strategy B.

Element	Attribution	Position (eV)	Percentage (%)
Ti 2p	TiS_2 2p3/2	456.6	7.7
	TiS_2 2p1/2	462.3	3.8
	TiO_2 2p3/2	458.7	2.7
	TiO_2 2p1/2	464.4	1.4
S 2p	TiS_2 2p3/2	160.9	19.3
	TiS_2 2p1/2	162.0	9.6
	$TiO_xS_y/(S_n)^{2-}$/C-S 2p3/2	162.8	9.3
	$TiO_xS_y/(S_n)^{2-}$/C-S 2p1/2	164.0	4.6
O 1s	TiO_2	530.3	10.6
	C-O/O-C=O/SiO_2	532.3	5.0
C 1s	C-C/C-H	284.8	21.0
	C-O/C-S	288.5	4.6
Si 1s	SiO_2	1843.8	0.5

Table C.7: Binding energies (BE) and atomic percentages (at.%) of the different chemical environments identified by HAXPES at the surface of a 20-cycle ALD/MLD Ti-thiolate with 60s of EDT injection upon the annealing under Ar/H_2(5%) using annealing strategy B.

Element	Attribution	Position (eV)	Percentage (%)
Ti 2p	TiS_2 2p3/2	456.6	5.7
	TiS_2 2p1/2	462.3	2.8
	TiO_2 2p3/2	458.6	3.9
	TiO_2 2p1/2	464.3	2.0
S 2p	TiS_2 2p3/2	160.8	14.2
	TiS_2 2p1/2	162.0	7.1
	$TiO_xS_y/(S_n)^{2-}$/C-S 2p3/2	162.7	5.9
	$TiO_xS_y/(S_n)^{2-}$/C-S 2p1/2	163.9	3.0
O 1s	TiO_2	530.3	16.7
	C-O/O-C=O/SiO_2	532.8	16.3
C 1s	C-C/C-H	284.8	16.0
	C-O/C-S	288.1	3.0
Si 1s	SiO_2	1843.9	3.3

Table C.8: Binding energies (BE) and atomic percentages (at.%) of the different chemical environments identified by HAXPES at the surface of a 20-cycle ALD/MLD Ti-thiolate with 60s of EDT injection upon the annealing under Ar/H_2(5%) using annealing strategy A.

Element	Attribution	Position (eV)	Percentage (%)
Ti 2p	TiS_2 2p3/2	456.7	4.0
	TiS_2 2p1/2	462.4	2.0
	TiO_2 2p3/2	458.6	4.5
	TiO_2 2p1/2	464.3	2.2
S 2p	TiS_2 2p3/2	160.9	3.4
	TiS_2 2p1/2	162.1	4.7
	$TiO_xS_y/(S_n)^{2-}$/C-S 2p3/2	163.1	4.5
	$TiO_xS_y/(S_n)^{2-}$/C-S 2p1/2	164.3	2.3
O 1s	TiO_2	530.3	16.6
	C-O/O-C=O/SiO_2	532.7	13.6
C 1s	C-C/C-H	284.8	22.5
	C-O/C-S	287.8	3.4
Si 1s	SiO_2	1843.9	4.4

Appendix D

Supplementary materials (Chapter 4)

D.1 Operando DRIFT coupled GC-MS monitoring of the annealing step

The operando DRIFT experiment was carried out in an integrated system comprising Brooks mass flow controllers, Harrick's high-temperature reaction chamber with ZnSe windows, Nicolet FTIR 6700 spectrophotometer equipped with MCT detector and online GC-MS (Agilent 6850/5975C); as decribed elsewhere.[120] (see Figure D.1).

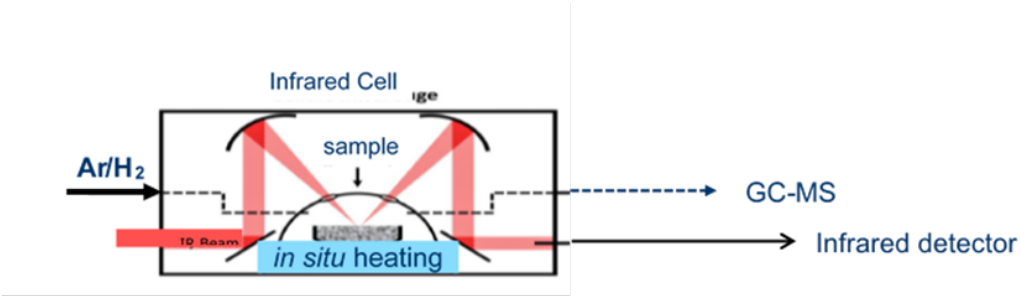

Figure D.1: Schematic representation of the experimental setup used for *in-situ* DRIFT and GC-MS monitoring of the thermal decomposition of our ALD-deposited molybdenum thiolate on silica nano-beads.[120]

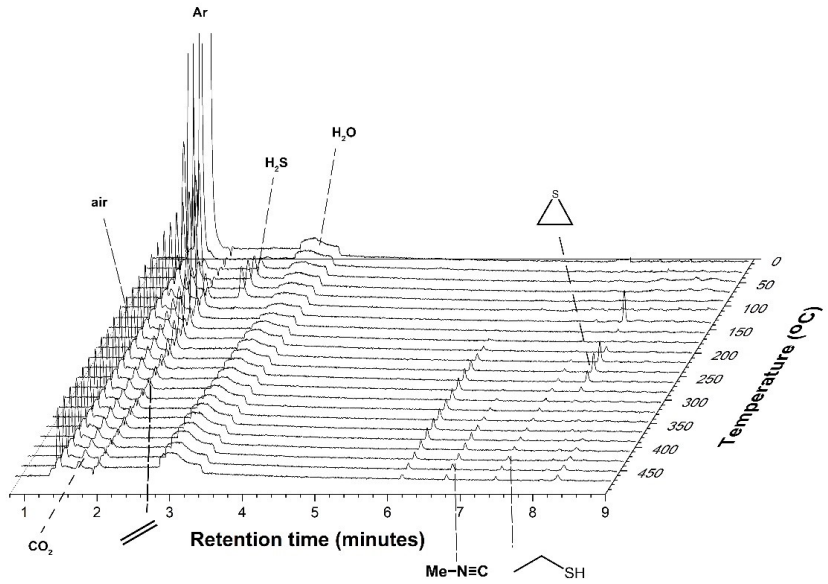

Figure D.2: *In situ* GC-MS spectra of volatile by-products released upon heating silica nanobeads-supported Ti thiolate obtained by 2 ALD cycles, from 20 °C to 500 °C.

The stack plot of the gas chromatograms acquired over time is reported in Figure D.2. H_2S evolution is observed between 60 and 140 °C. This is followed by a large production of C_2H_4 from 140 °C to about 280 °C though traces of ethylene are still observed until the end of heating. Hydrogen disulfide, methylisocyanide, thiirane, and ethanethiol are also observed. N_2, CO_2 and H_2O are detected with a stable intensity throughout the entire heating, and are impurities in the GC column which were observed for other samples too. The large argon originates from the glovebox where the sample was loaded.

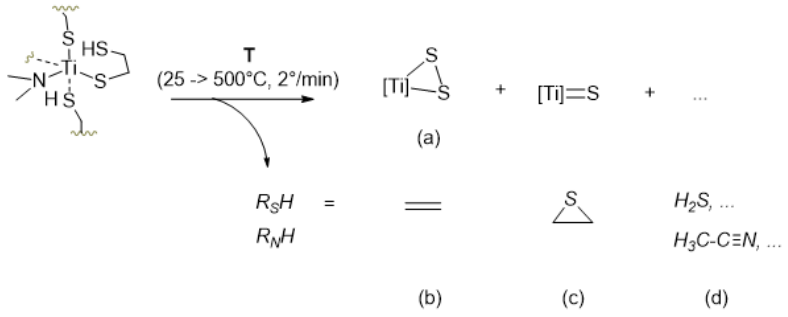

Figure D.3: Schematic presentation examples of possible surface reactions occurring during annealing step of the as deposited thiolate during annealing toward the targeted TiS_2 phase.

D.2 XRR of annealed samples

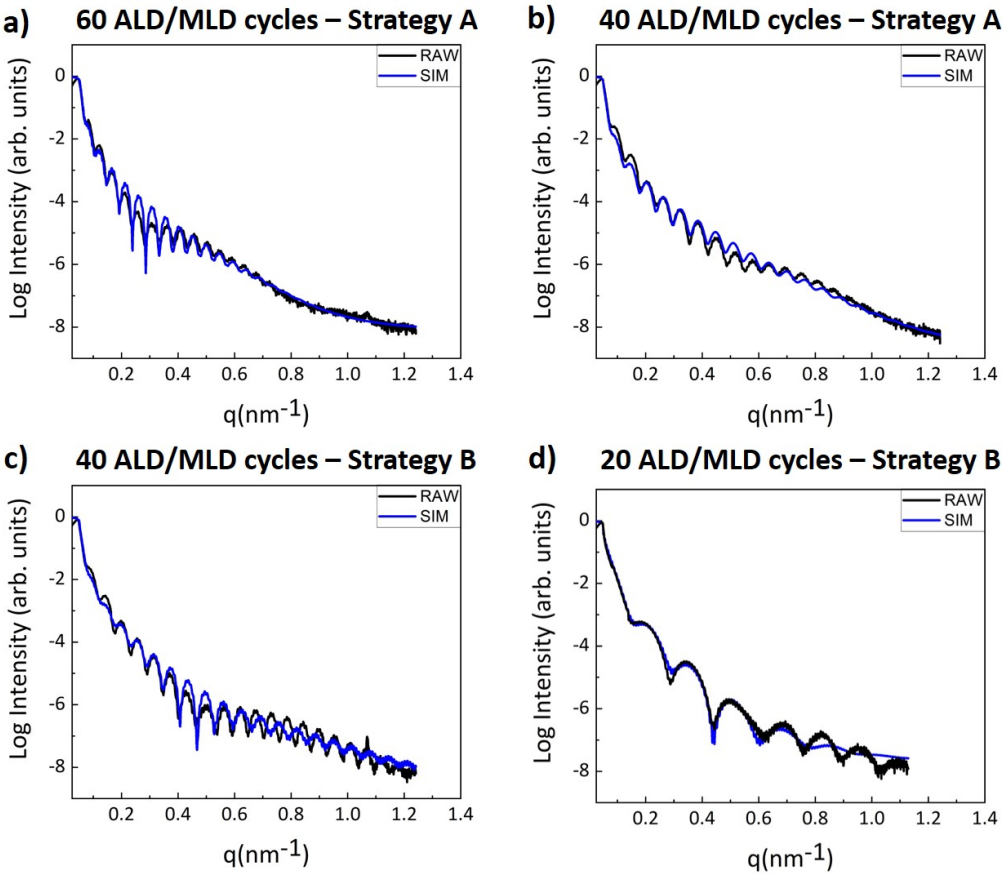

Figure D.4: Simulated XRR plots: reflected intensity as a function of the scattering modulus q for: a) 60- and b) 40- ALD/MLD annealed with strategy A. c) 40- and d) 20- ALD/MLD annealed with strategy B.

D.3 Raman spectrum analysis

In chapter 4, a series of raman spectra were shown for different thicknesses. The Raman spectra exhibit the presence of the vibrationnal modes associated to 1T-TiS_2. In this section, we will focus in details on the difference in the TiS_2 Raman spectra as a function of thickness.

Both Eg and A1g have been considered as the associated vibrationnal modes to confirm the presence of 1T-TiS_2 phase. The positions of this two modes were noticed to be changing from a spectrum to another. However since errors due to the calibration of the spectrometer are to be expected, the relevant parameter that should be taken into consideration is the

frequency difference between them noted hereafter ΔW= A1g-Eg. In this study, the Raman spectrum related to various TiS_2 thin films ranging from 5.5 nm to 19.4 nm were presented. the presented spectrum of different layer thickness were normalized to the intensity of T2g vibrational mode originating from the contribution of the silicon substrate.

We can clearly observe from Figure D.5 that the intensity of vibrationnal modes of TiS_2 increases with respect to the thickness of TiS_2 layer, since the contribution of the silicon substrate decreases and *vice versa*. In this context Figure D.5 confirmed the dispersion of different spectrum with respect to the thickness of TiS_2 layer.

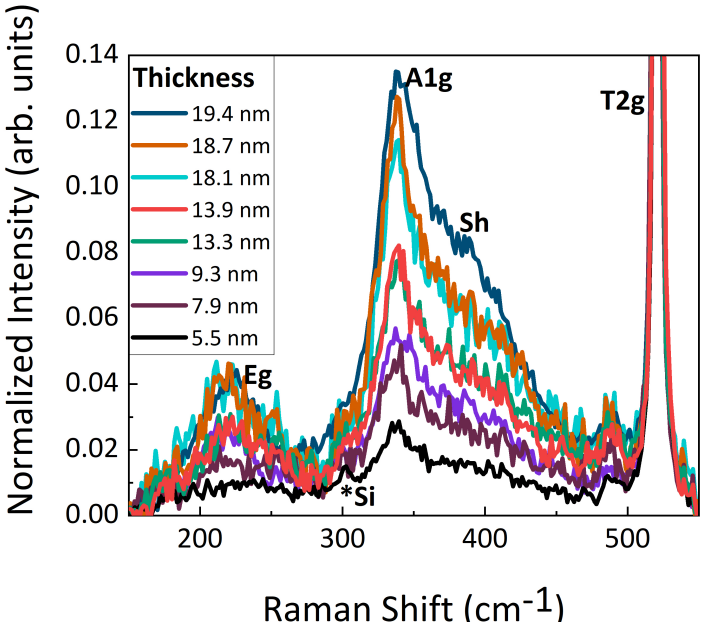

Figure D.5: Raman spectra for all samples with different thicknesses. Raman spectra were normalized to the intensity T2g of the silicon substrate.

Additionally, the previously shown raman spectrum along chapter sections were normalising with respect to the A1g peak. Moreover, they were fitted with Lorentzian curves (A1g mode and when presented *Si mode) and Gaussian-Lorentzian curves (Eg and Sh modes). All previous spectrum showed the presence of additional mode the Shoulder mode that increases with the layer thickness. In this section will explain its importance and additional explanations will be provided.

The fitted curves of various samples were used to perform such analysis, the position of the modes on the x-axis, area, intensity and Full Width at Half Maximum (FWHM) were

taken as a mean to compare the gathered data. From fitted data we can see two main information: The increasing of the shoulder intensity and the increases of the frequency shift between the Eg and A1g peaks with increasing thickness of TiS_2 layer. Below, in Table D.1 we summarize all the samples differentiated by their thickness, along with the values found for the relevant trends considered for the subsequent discussion. For each sample was measured more than three times and mean calculations were taken into account to check error difference and statistical variation in each sample.

Table D.1: Summary of various samples thickness in term of relevant parameters with their Standard Error of Mean in brackets.

Thickness (nm)	**Area ratio: Sh/A1g**	**Peak Shift (cm^{-1}):A1g - Eg**
5.5	1.041 ($\pm$0.065)	102.79 ($\pm$0.39)
7.9	1.268 ($\pm$0.045)	103.11 ($\pm$1.64)
9.3	1.340 ($\pm$0.088)	111.10 ($\pm$3.3)
13.3	1.759 ($\pm$0.023)	113.30 ($\pm$0.72)
13.9	1.856 ($\pm$0.082)	114.92 ($\pm$0.92)
18.1	2.162 ($\pm$0.023)	116.76 ($\pm$0.98)
18.7	2.212 ($\pm$0.018)	116.92 ($\pm$0.86)
19.4	2.236 ($\pm$0.120)	118.62 ($\pm$0.94)

Figure D.6-a displays the variation in the shift between the positions of the Eg and A1g peaks with respect to the thickness of TiS_2 layer. We can see that the frequency difference ΔW increases when the thickness of TiS_2 was increasing, even if this increasing didn't show any linear behaviour or slope. In fact, such trend has been previously encountered in the characterisation of different transtion metal dichalcogenides such as (MoS_2) showing a similar peak shift variation for the peaks corresponding to the in-plane and out-of-plane vibrational modes.[120]

In the presented study the Eg peak displays a frequency shift while the A1g peak remains relatively unchanged in frequency with increasing of layer thickness. The frequency shift of the Eg mode even if it was not familiar, but it can be referred to the presence of an excess of titanium atoms intercalated between two monolayers, increasing the interlayer interactions,thus stiffening the in-plane Eg mode. In other words stiffening the in-plane Eg mode can be reached through the introduction of vacancies in the perfect crystalline structure.

[209] Even if the frequency of the A1g out-of-plane mode was not influenced by the increasing of layer thickness, but intercalated atoms are capable to exhibit their effect on the A1g peak with a local stiffening of the phonon resulting in the appearance of the Shoulder mode at higher frequencies.[132] However, due to a significant asymmetry in the fitted curve of the Eg mode profile, the determination of the frequency difference with high precision remains difficult. [132] For this reason, the A1g mode and the better-defined Sh-shoulder mode should rather be used for the determination of the number of layers. Indeed, it has been observed in the literature that the shoulder mode (Sh) appears being more pronounced for multilayers than for a monolayer. Such explanation were confirmed through various gathered performed raman spectroscopy analysis, whereas a significant decrease of the Sh mode was noticed once approaching to monolayer structure (see Figure D.5).

To systematically interpret this information, the analysed parameter was chosen as the ratio between the area fitted curve of the shoulder and the A1g peak (Sh/A1g). On Figure D.6-b, the ratio of Sh/A1g is decreasing with the decreasing of the layer thickness and the Sh mode as well. The almost linear plot confirms the interpretation of data. The Sh mode showed its potential role in the determination of the thickness layer, however many explanations were attributed to explain its existence, we will present them, thus the most suitable explanation must be confirmed through the studied data.

- The Shoulder mode coincide with IR active active mode A2u: the A2u vibrational mode was reported to exist at frequencies corresponding to 372 cm^{-1} in titanium disulfide.[256] The appearance of a peak related to an IR active mode in a Raman spectrum can be attributed to a variation of out-of-plane symmetry going from bulk to monolayer structure. However, such behaviour was not observed in our data while decreasing down to monolayer structure. Since the appearance of Shoulder mode decreased once we approach to monolayer structure and not the opposite. So it's not possible to relate the presence of Shoulder mode with the A2u vibrationnal mode.

- Presence of stress on the deposited film generating defects: These kind of defects could be generated during the heating and cooling steps, between the deposited material and the substrate due to their difference in thermal expansion coefficients. However, generated defects due to a lattice mismatch between the substrate and deposited layer could cause a slight change in peak positions but not the appearance of a shoulder.

- Local stiffening of A1g phonon: resulting with an excess of titanium atoms intercalated

between two monolayers, increasing the interlayer interactions,which in turn causes a stiffening of the phonon modes. If this holds, the shoulder peak should appear more pronounced for multilayers versus monolayers,[48, 132] which was observed and confirmed by the obtained data from various spectrum. For the reason, the local stiffening of the A1g phonon found to be the most reasonable explanation for the shoulder appearance.

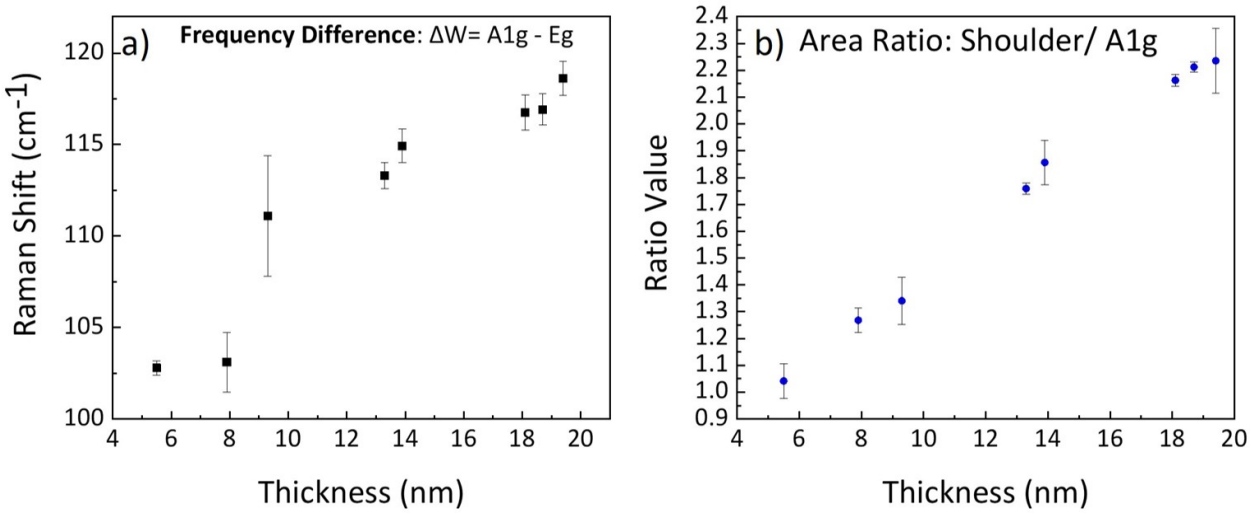

Figure D.6: a) Frequency difference between the Gaussian fitting of the Eg peak and the Lorentzian fitting of the A1g peak plotted with respect to the number of layers and b) Ratio between the area of the Shoulder peak and the A1g peak plotted in function of the thickness. Error bars represent the standard deviation.

In summary, we can conclude that Raman spectroscopy has the ability to compare the thickness of various deposited TiS_2 films (as confirmed by the variation in the relative area between the A1g peak and its shoulder, in addition to the information obtained from the positional shift between the Eg and A1g peaks).

Appendix E

Supplementary materials (Chapter 5)

E.1 *Ex situ* XRF

The deposited samples mentioned above, were measured by *ex situ* XRF. The XRF measurements were performed on the two grown series of samples with an injection time of the EDT of either 30s or 15s. The use of *ex situ* XRF permits to define a GPC as mass concentration of a given atom deposited per cycle. However, we did not carry out the elemental quantitative analysis yet.

Even though quantitative analysis was not possible, we was able to see the evolution of the raw intensity of the gallium and sulfur K_α peaks so we are interested in the S/Ga ratio which may still reveal some information. Figure E.1 shows such a ratio for an injection time of EDT for 30s and 15s. In the case of EDT injection time equal to 30s, a constant ratio is found in the temperature range of [200 °C; 300 °C], while such a region was found within a temperature range of [200 °C; 250 °C] in the case of 15s of EDT injection. To sum up XRF measurements are in agreement with *in situ* ellipsometry measurements.

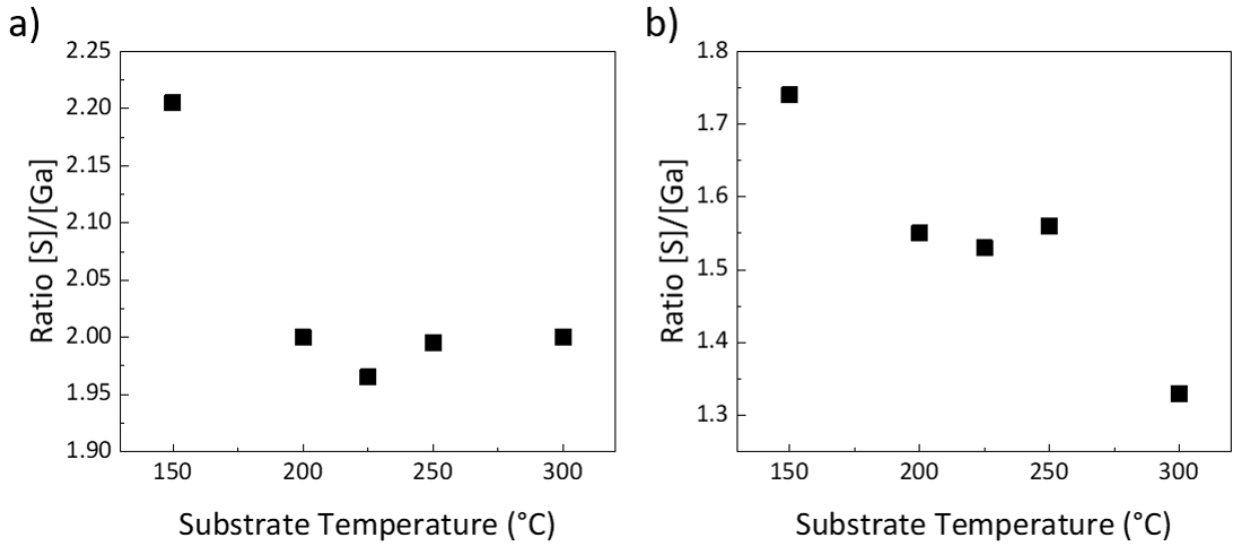

Figure E.1: [S]/[Ga] ratio obtained from *ex situ* XRF measurements for a) 30s and b) 15s of the EDT injection time.

E.2 *Ex situ* XRR

Table E.1: Films structure obtained from simulated XRR curves for the as-deposited thin films at various substrate temperature.

Tsub (°C)	**GaSx thickness (nm)**	**GaOxSy thickness (nm)**
150	2.59	2.13
200	4.76	1.33
225	3.47	2.8
250	5.37	1.29
300	5.68	6.72

E.3 *ToF SIMS*

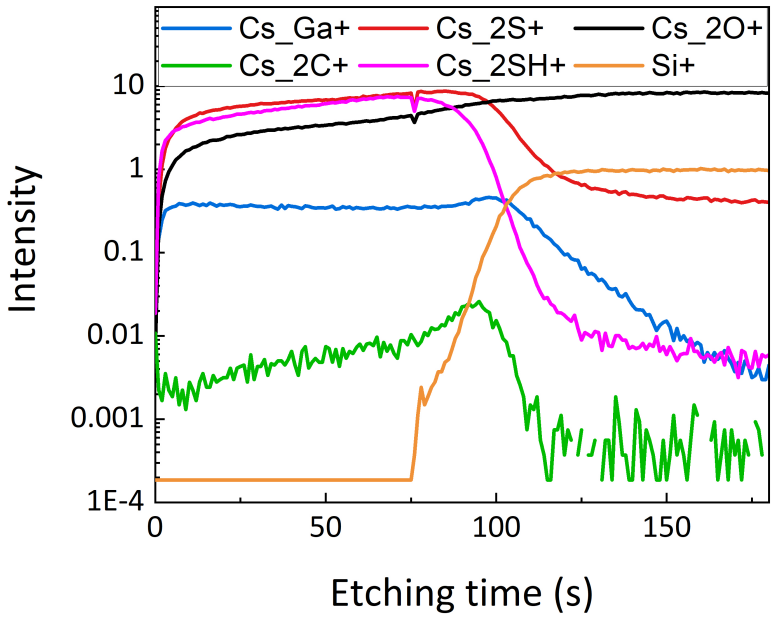

Figure E.2: ToF-SIMS depth profiles of Cs Ga^+,Cs $2S^+$,Cs $2O^+$, Cs $2C^+$, Cs $2SH^+$ and Si^+ ions in positive polarity as a function of etching time for a GaS_x film obtained from a 40 ALD/MLD cycles at 250 °C.

Scientific Contributions

List of Publications

1. **Abi Younes, P.** & Skopin, E.V. & Zhukush, M. & Rapenne, L.& Roussel, H. & Aubert, N. & Khrouz, L. & Licitra, C. & Camp, C. & Richard, M.I. & Schneider, N. & Ciatto, G. & Gauthier,N. & Rouchon, D. & Quadrelli, E.A. & Renevier, H. (2022). "Transition Metal Dichalcogenide TiS_2 Prepared by Hybrid Atomic Layer Deposition/Molecular Layer Deposition: Atomic-Level Insights With *in situ* Synchrotron X-ray Studies And Molecular Surface Chemistry.". In: *Chemistry of materials* `https://pubs.acs.org/doi/10.1021/acs.chemmater.2c02369`

2. **Abi Younes, P.** & Yadav, A.K. & Zhukush, M. & Le, V-H. & Richard, M.I. & Camp, C. & Szeto, K. & Ciatto, G. & Schneider, N. & Quadrelli, E.A. & Gauthier,N. & Renevier, H. (2023). "Investigation Of The Transition Of Amorphous Ti-thiolate prepared by Hybrid Atomic Layer Deposition/Molecular Layer Deposition Into Titanium Disulphide Ultra-Thin Film". In: *Under final revision in JVST A*

3. Skopin, E.V. & Abdukayumov, K. & **Abi Younes, P.** & Anikin, M. & Roussel, H.& Deschanvres, J. L. & Renevier, H. (2021). "*In situ* ellipsometry monitoring of TiO_2 atomic layer deposition from Tetrakis (dimethylamido) titanium (IV) and H_2O precursors on Si and $In_{0.53}Ga_{0.47}As$ substrates". In: *Thin Solid Films*. `https://doi.org/10.1016/j.tsf.2021.138591`

Presentations in Conferences

- **Abi Younes, P.** & Skopin, E.V. & Aubert, N. & Zhukush, M. & Camp, C. & Richard, M.I & Ciatto, G. & Schneider, N.& Quadrelli, E.A. & Gauthier,N. & Rouchon, D. & Renevier, H. **Oral presentation**, ALD/ALE 2022,Ghent,Belgium, June 2022

- **Abi Younes, P.** & Skopin, E.V. & Aubert, N. & Zhukush, M. & Camp, C. & Richard, M.I & Ciatto, G. & Quadrelli, E.A. & Gauthier,N. & Rouchon, D. & Renevier, H. **Poster presentation**, RX et Matière,Aix-en-Provence,France, November 2021

- **Abi Younes, P.** & Skopin, E.V. & Aubert, N. & Zhukush, M. & Camp, C. & Richard, M.I & Ciatto, G. & Quadrelli, E.A. & Gauthier,N. & Rouchon, D. & Renevier, H. **Oral presentation**, RAFALD 2021, Marseille,France, November 2021

- **Abi Younes, P.** & Skopin, E.V. & Aubert, N. & Camp, C. & Richard, M.I & Ciatto, G. & Gauthier,N. & Quadrelli, E.A. & Rouchon, D. & Renevier, H. **Oral presentation**, EuroMat2021, Virtual, September 2021

- **Abi Younes, P.** & Skopin, E.V. & Aubert, N. & Richard, M.I & Ciatto, G.& Quadrelli, E.A. & Rouchon, D. & Renevier, H. **Oral presentation**, RAFALD 2020, Virtual, November 2020

Collaborations

Le, V-H & Ramos, R. & Licitra, C. & Saghi, Z.

Skopin, E.V. & Iung, T. & Menez, H. & Roussel, H & Chatmaneerungcharoen, B. & Rapenne, L.

Zukush, M. & Quadrelli, E.A.

Szeto, K. & Camp, C.

Yadav, A-K. & Aubert, N. & Ciatto, G.

Schneider, N. & Weiliang, M-A.

Richard, M.-I.